

FACULTY FOR PHYSICS AND ASTRONOMY

UNIVERSITY OF HEIDELBERG

Diploma Thesis

in Physics

submitted by

Clemens Haltebourg

born in Ostfildern-Ruit

2008

Implementation of the ALICE TRD TRAP-chip into AliRoot

This diploma thesis has been carried out by Clemens Haltebourg at the
Physikalisches Institut
under the supervision of
Prof. Dr. Johanna Stachel

Implementation of the ALICE TRD TRAP chip into AliRoot

The trigger functionality of the Tracklet Processing (TRAP) chip, which is integrated into the Transition Radiation Detector of the heavy ion experiment ALICE at LHC (CERN), has been implemented into the object orientated detector simulation framework AliRoot.

The trigger calculates a linear fit (tracklet) to the section of a particle track in each layer of the detector. This segmentation allows for a fast parallel reconstruction of the track by the integrated electronics.

The implemented TRAP chip simulator is a detailed model of the real TRAP chip, respecting precisely the data formats as well as the applied algorithms. The reconstruction capability of the tracklet simulator has been successfully tested by exploiting the Monte Carlo information, which is available in AliRoot.

Within this diploma thesis, the signal path from its creation in the detector to analog and digital processing by the electronics is described. Based on that, the tracklet algorithm is presented and a selection of performance results is discussed. Finally, possible solutions to some issues, concerning the implementation of an electron-pion separation mechanism on TRAP basis, are presented.

Detailgetreue AliRoot-Implementierung des ALICE TRD TRAP-Chips

Im Rahmen der Diplomarbeit wurde die Trigger-Funktionalität des Tracklet Processing (TRAP) Chips in die objektorientierte Simulationsumgebung des ALICE-Detektors, AliRoot, eingebunden.

Der Trigger nähert den Ausschnitt einer Teilchenspur innerhalb einer Detektorebene durch einen linearen Fit an, welcher "tracklet" genannt wird. Die Aufteilung der Berechnung auf insgesamt sechs Detektorebenen erlaubt eine schnelle parallele Rekonstruktion der Teilchenspur durch die direkt am Detektor angebrachte Elektronik.

Der implementierte TRAP Chip Simulator ist eine detailgetreue Umsetzung des wirklichen TRAP Chips, wobei insbesondere auf eine genaue Einhaltung der Datenformate sowie des in der Hardware verwendeten Algorithmus Wert gelegt wurde. Die Fähigkeit des TRAP-Simulators, anhand der tracklets Ausschnitte der Teilchenspur zu rekonstruieren, wurde mit Hilfe der in AliRoot zur Verfügung stehenden Monte Carlo Informationen erfolgreich nachgewiesen.

In dieser Diplomarbeit wird der Signalweg von der Entstehung im Detektor bis zur analogen und digitalen elektronischen Verarbeitung dargestellt. Auf dieser Grundlage aufbauend wird der zur Berechnung der tracklets verwendete Algorithmus vorgestellt. Eine Auswahl der Ergebnisse, die durch Vergleich der tracklets mit Monte Carlo Informationen zustande kamen, wird diskutiert. Schließlich werden Lösungsvorschläge zu einigen Problemen präsentiert, welche bei der Implementierung einer Elektron-Wahrscheinlichkeit auf TRAP Basis auftreten können.

Contents

1	Physics Overview	1
1.1	The Standard Model	1
1.1.1	Strong Interactions	2
1.1.2	The Quark Gluon Plasma and the QCD Phase Diagram	5
1.2	Heavy Ion Collisions	11
1.2.1	Basic Quantities and Features	11
1.2.2	Fireball and Probes for Medium Modifications	13
1.2.3	Quarkonia and Deconfinement	15
2	The ALICE Experiment	17
2.1	The Large Hadron Collider	17
2.2	The ALICE Experiment	18
2.2.1	Design Considerations	19
2.2.2	The Detector System	19
3	The Transition Radiation Detector	22
3.1	Physics With the TRD	22
3.2	TRD Design Considerations	22
3.3	The TRD Layout	23
3.4	The Front End Electronics	27
3.4.1	Requirements	27
3.4.2	Structure of the Front End Electronics	28
3.5	The GTU	33
3.6	Zero Suppression	33
4	The Trigger System	36
4.1	The ALICE Trigger System	36
4.1.1	Overview	36
4.1.2	Trigger Logic	37
4.2	The TRD Trigger	39
4.2.1	Requirements	39
4.2.2	Purposes	39
4.2.3	Realization	39
4.2.4	The TRD Trigger States	40
4.3	Connection Between the TRD and the ALICE Trigger System	42
5	Signal Creation and Signal Processing	46
5.1	Interaction of Charged Particles with Matter	46
5.1.1	Physics Overview	46

5.1.2	Properties of the Electromagnetic Processes	49
5.1.3	Photo Absorption Ionization Model	52
5.1.4	Transition Radiation	53
5.1.5	Energy Loss	55
5.1.6	Bremsstrahlung	59
5.2	Signal Generation	60
5.2.1	Energy Loss and Cluster Creation	60
5.2.2	Diffusion	63
5.2.3	Multiple Scattering	65
5.2.4	Recombination and Electron Attachment	67
5.2.5	Electron Drift in Electric Fields	68
5.2.6	Electron Drift in Electric and Magnetic Fields	71
5.2.7	Gas Gain	73
5.3	Signal Processing	79
5.3.1	The Way to Raw Data	80
6	Tracklet Calculation	103
6.1	The Principle	103
6.2	Preprocessing	110
6.2.1	Cluster Detection	112
6.2.2	Cluster Selection	114
6.3	Processing	119
6.3.1	Avoidance of Submission of Double Tracklets	121
6.3.2	Merging of the Fit Sums of Channel Pairs	123
6.3.3	Calculation of Offset and Slope	123
6.3.4	Electron Probability	124
6.3.5	Preparing for GTU	126
6.4	Lorentz Angle Correction	129
6.5	Tilted Pads Correction	131
6.6	Sending of the Tracklet Words	133
6.6.1	Cut on the Transverse Momentum	135
6.6.2	Structure of a Tracklet Word	140
7	Implementation and Results	141
7.1	Implementation Issues	142
7.2	Offset Correction	147
7.2.1	Offset Lorentz Correction	149
7.2.2	Offset Tilted Pads Correction	152
7.3	Results	153
7.3.1	General Results	156
7.3.2	Performance Results	164
7.3.3	Efficiency Results	174
8	Electron Probability Measure and Pion Rejection Capability	184
8.1	Electron Probability and Likelihood	184
8.1.1	1D Likelihood Approach for TRAP	184

8.1.2	1D Likelihood Approach Offline	189
8.1.3	2D Likelihood Approach Offline	190
8.2	The Energy Loss Distribution	191
8.2.1	Average Pulse Height Spectrum and Electron Pion Separation Power	192
8.2.2	Some Features Influencing the Mean Cluster Charge Distributions .	193
8.3	Proposal for the Implementation of a Likelihood Measure into the TRAP .	197
8.3.1	Technical Conditions	197
8.3.2	The Reference Distribution	197
8.3.3	Tracklet Length Correction	199
8.3.4	Implementation	206
8.3.5	Assigning Momentum to Deflection	207
8.3.6	Mean Cluster Charge Distributions and Likelihood Distributions in view of the Quantization Issue	211
8.4	Recipe for an Electron Probability	216
A	Appendix	220
A.1	Kinematics	220
A.1.1	Collision and Decay	220
A.1.2	Observables	221
A.2	The Maximum Energy Transfer to a Scattered Electron	224
A.3	Sum of Two Poisson Distributed Variables	225
A.4	How the Kinematics Tree is built	226
A.5	Two-Complement Representation	226

1 Physics Overview

In this chapter a short overview of the physics, that will be investigated by the ALICE experiment, shall be given.

A comprehensive introduction into particle physics is published in [PRSZ04]. Particle properties are summarized in [PDG02]. An overview over the current situation concerning the phase diagram of strongly interacting matter can be found in [BMW07]. In [Kra06], an introduction to the QGP and its messengers is given. [ALI04] provides the theoretical background to ALICE physics. Some issues concerning electrodynamic plasmas (e.g. the Debye length) are discussed in [Hun04]. After an introduction, [Y⁺05] deals with advanced topics concerning the Quark Gluon Plasma.

1.1 The Standard Model

With the increasing accessible energy-range in collider experiments also the number of found particles and resonances increased. However, in the framework of the Standard Model all directly observable matter is built up by a limited number of elementary particles. The interactions between these particles are mediated by exchange bosons. Up to now the Standard Model has proved very successful in explaining and predicting experimental observations and results. One distinguishes between two particle species, bosons and fermions. Leptons and quarks are elementary spin 1/2 fermions. Baryons which consist of three quarks are also fermions whereas mesons (built by two quarks) are bosons. The mediators of the interactions are bosons.

Table 1.1: The elementary particles

particle family	particles	charge (Q/ e)	color charge
leptons	ν_e ν_μ ν_τ	0	-
	e μ τ	-1	-
quarks	u c t	+2/3	r,g,b
	d s d	-1/3	r,g,b

In table 1.1 the three generations of leptons and quarks are shown along with their electric- and color-charge. There are four known elementary forces and to each type of interaction belongs a special type of charge. The exchange bosons of an interaction can only couple to particles carrying the corresponding type of charge. The electromagnetic force, whose mediator is the photon, acts only between particles carrying electric charge. Since the photon is massless, its lifetime is not restricted by the uncertainty principle and the range of the electromagnetic interaction is infinite. The same is true for the range of

the gravitational force. Therefore these two forces are experienced on macroscopic scales, although the coupling of the gravitation is very weak. In contrast, because of the large mass of the mediators of the electroweak interactions, W^\pm and Z^0 , these virtual exchange bosons can only exist for a very short time due to the uncertainty principle:

$$\Delta E \cdot \Delta t \leq \hbar/2 \tag{1.1}$$

Hence, the range of the electroweak interaction is limited to very short distances (table 1.2).

Table 1.2: The four forces and their mediators

interaction	particles affected	exchange bosons	mass (GeV/c ²)	range (m)	relative strength
gravitation	all	graviton	0	∞	$5 \cdot 10^{-40}$
weak	quarks, leptons	W^\pm, Z^0	$\approx 10^2$	10^{-18}	$1.2 \cdot 10^{-5}$
electromagnetic	electrically charged	γ	0	∞	$\frac{1}{137}$
strong	quarks, gluons	eight colored gluons	0	10^{-18}	≤ 1

1.1.1 Strong Interactions

The strong interaction is responsible for the binding of protons and neutrons into nuclei and also for forming hadrons out of quarks and gluons. It is described by Quantum Chromodynamics (QCD), a relativistic, non Abelian quantum field theory in which massive fermionic matter fields (quarks) interact with massless, pointlike bosonic gauge fields (gluons), realized in SU(3). Currently six quark flavors are known. Quarks carry color-charge (red, green, blue) additionally to fractional electric charge and spin. Yet, if a hadron is formed, color neutrality (white) must be ensured. Also the exchange bosons, the gluons, are colored, carrying one out of eight possible color combinations, e.g.:

$$r\bar{g}, r\bar{b}, g\bar{b}, g\bar{r}, b\bar{r}, b\bar{g}, \sqrt{\frac{1}{2}}(r\bar{r} - g\bar{g}), \sqrt{\frac{1}{6}}(r\bar{r} + g\bar{g} - 2b\bar{b}).$$

This leads to a peculiarity: In contrast to the exchange bosons of the other interactions, gluons can self-interact. Therefore the four elementary interaction vertices of QCD (figure 1.1) incorporate gluon self coupling (gluon-splitting into two gluons, gluon-gluon-scattering) besides the gluon radiation by a quark and the gluon-splitting into a $q\bar{q}$ -pair. As a consequence, despite $m = 0$, the range of the strong interaction is finite. When trying to separate a quark-antiquark pair ($q\bar{q}$ -pair), a gluon-field with increasing energy content would evolve, leading to the formation of new $q\bar{q}$ -pairs from the vacuum (once the field energy is large enough) in a way, that in total color-neutrality is conserved. Thus free quarks have never been observed, color charges are always confined within hadrons. For the description of the potential between a $q\bar{q}$ -pair one can use (figure 1.2)

$$V(r) = -\frac{4}{3} \cdot \frac{\alpha_s(r)}{r} + kr \tag{1.2}$$

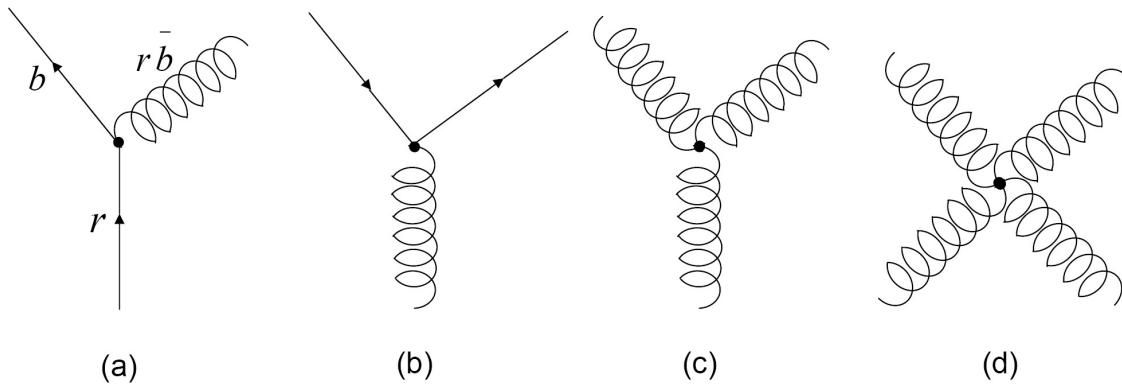


Figure 1.1: The four elementary QCD vertices: (a): gluon radiation off a quark, (b) splitting of a gluon into a $q\bar{q}$ -pair, (c) and (d): self-couplings of the gluons. Color charge must be conserved at the vertices, which is symbolized in (a).

where r is the distance between two quarks, k the string tension of the gluon field and α_s the strong coupling constant (which in fact is no constant, see below). The potential is a superposition of a Coulomb-like term and a linear increase, which is responsible for the confinement of quarks into color-neutral objects.

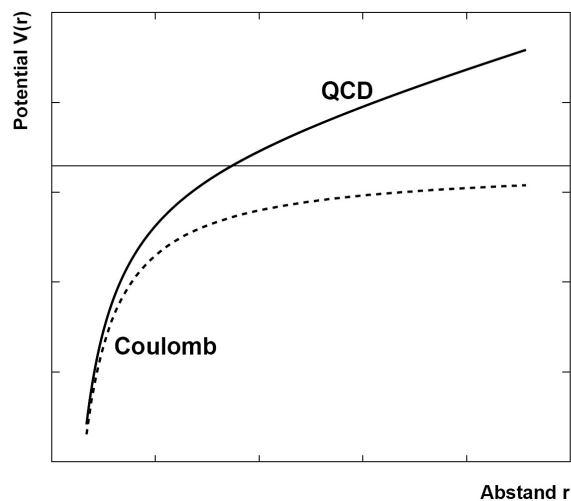


Figure 1.2: The quark anti-quark potential [Kra06]

The color-neutrality manifests itself in always binding quarks into a baryon or a meson. Baryons consist of three quarks or anti quarks of three different colors such that in sum it is color neutral ($r + g + b = \text{white}$). In mesons color-neutrality is achieved by putting together a colored quark and its anti quark with opposite (anti-)color. An example for baryons in ground state are protons and neutrons. It is also possible to excite baryons. Due to the large energy needed for excitation those resonances are usually treated as independent particles.

The maximum possible spatial extent that still can be resolved, decreases with increasing

momentum transfer Q . Analogously, the resolution of an usual microscope is physically limited by the wavelength of the used light. To be able to see smaller structures, the wavelength has to be decreased (e.g. the de Broglie wavelength of particles can be used). Decrease of wavelength means increase of energy. In high energy physics it was possible to penetrate into matter deeper and deeper by increasing the energy of the probe. Once the energy becomes comparable to the binding energy of a subatomic structure, it can break apart and can be detected by measuring inelastic cross sections. Like that the size of the observed particles shrunk with increasing energy. One now observes that the strong coupling constant α_s , which determines the strength of the coupling of a gluon to a quark and thus the strength of the strong interaction, depends on the momentum transfer Q and thus on the spatial resolution. In leading order the running of α_s with Q^2 can be described by (figure 1.3)

$$\alpha_s(Q^2) = \frac{12\pi}{(32 - 2N_f) \ln(Q^2/\Lambda_{QCD})}, Q^2 \gg \Lambda_{QCD} \quad (1.3)$$

with $\Lambda_{QCD} \approx 200\text{MeV}$ being the fundamental QCD scale parameter and N_f the number of active quarks flavors. Since virtual heavy $q\bar{q}$ -pairs have a very short lifetime due to the uncertainty principle, the distance they can gain is very short and thus they are only resolvable at large values of Q . At low Q they do not affect interactions and thus do not count into α_s . So $N_f(Q) = 3.6$.

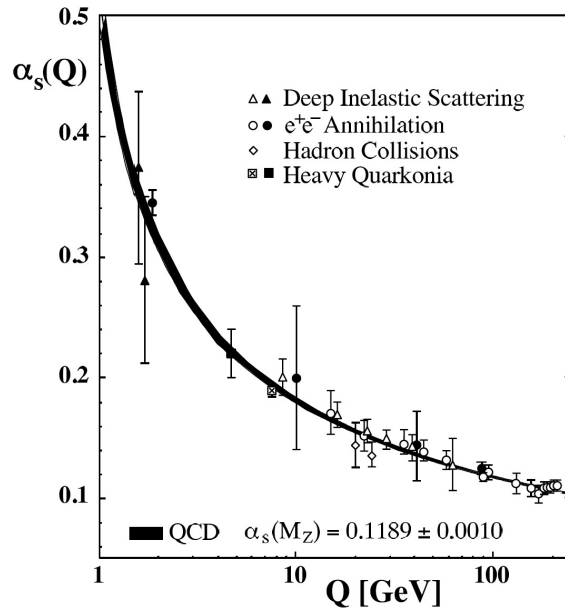


Figure 1.3: Running of the QCD coupling constant with momentum transfer Q [BMW07]

For large Q^2 the coupling constant becomes very small, which implies that for short distances quarks can almost be considered free (asymptotic freedom) since the interaction between them becomes very small. For lower Q^2 and larger distances however, α_s grows and the interaction becomes stronger. This is also expressed by the form of the $q\bar{q}$ potential, dominated at large distances by a linear increase.

In a simple picture one can 'explain' the running of α_s by thinking of a color charge sitting in the origin. As a quark can irradiate and absorb gluons (according to the QCD interaction vertices), which in turn can split into $q\bar{q}$ -pairs or into other gluons, this dilutes the charge spatially. At increasing Q^2 , one resolves shrinking distances and zooms through a non-focused cloud of gluons toward the quark in the origin. Hence, the single gluon irradiations and absorptions become detectable. This means, that only in a short fraction of time the quark is seen with its original color. If the frequency of charge changes is larger than the time resolution, the quark effectively appears color neutral. Decreasing Q^2 means, that due to the worsening resolution not every single quark-gluon interaction is visible any more. Coarsely spoken, the observed charge is an average over the focused volume. Therefore also the fluctuation of the observed charge with time decreases and its effective value increases. Hence, by lowering Q^2 an increasing fraction of the incident charge of the quark in the origin is detected. Thus, the QCD vacuum is also called an anti-screening medium.

In QED on the other hand, a bare charge will be screened by virtual polarized e^+e^- -pairs, occurring from the splitting of virtual photons, radiated from the bare charge in the origin. Hence, the fact that photons do not carry charge yields, that the effective charge and field strength decrease with decreasing Q (looking at the charge from further away). In this sense, the QED vacuum is a screening medium. The running of the fine structure constant α is opposite to α_s and much less pronounced.

By this picture also scaling violation in QCD can be explained qualitatively. If Q increases, also the number of resolved partons of a hadron increases and the hadron momentum is distributed to more partons (making the momentum fraction of an individual parton decrease). Investigating the valence quark distribution function $q(x, Q^2)$ (measure for the probability to find a quark) at different portions of the particle momentum x for momentum transfers Q_0 and $Q > Q_0$, the following observation becomes qualitatively understandable: At low x , $q(x, Q^2)$ becomes larger than $q(x, Q_0^2)$ and smaller at large x , $q(x, Q^2) < q(x, Q_0^2)$. Thus for low x , $q(x, Q^2)$ will increase with Q^2 whereas a decrease occurs at larger momentum fractions x .

Alike in the electromagnetic regime, also strongly interacting matter can appear in different phases. The thermodynamical state in which quarks are bound into hadrons is only one of many possible phases. Another one is the Quark Gluon Plasma which is of particular interest in heavy ion physics, as the creation of this state of matter lies within experimental prospects.

1.1.2 The Quark Gluon Plasma and the QCD Phase Diagram

Under extreme conditions strongly interacting matter can undergo a transition from the hadronic state to a deconfined plasma state. Graphically spoken, the distance between quarks becomes very small such that quarks only feel the short-ranging Coulomb part of the strong potential, whereas the long-ranging part is screened. It is supposed that the early universe at around $10\mu s$ after the big bang underwent a phase transition from a QGP to hadronic matter state at small chemical potential.

In the following, all quantities will be given in units with $c = \hbar = 1$. A model to describe the plasma transition, accounting for confinement, is the Bag Model. There it is assumed that the QCD vacuum is a perfect paramagnet ($\mu_0^c = \infty$, $\epsilon_0^c = 0$, c symbolizes that

color-electric charges are regarded).¹ A hadron emerges by cutting a small bag out of the vacuum and by filling it with three quarks for baryons and with a $q\bar{q}$ -pair for mesons. All the color fields are confined within this hadron. Inside the bag the strong interaction between the quarks is assumed to be only weak (the quarks are separated by small distances only) and $\epsilon_0^c = \mu_0^c = 1$. Like that, the bag model divides space into the two extreme regions of very weak interaction (inside bag, $\alpha_s \approx 0$, perturbation theory applicable) and strong interaction (non perturbative vacuum with large α_s). There are then two ways to obtain a QGP:

- The first is by heating (hot plasma, figure 1.4). If the temperature of a box in the vacuum is raised, thermal creation of light hadrons (pions) becomes considerable, once the energy for producing the according bag is provided. The bags of those hadrons finally overlap with each other and with the bags of the original hadrons. A network of cones is built which, beyond some critical temperature $T_C \approx 150$ to $190 MeV$, fills the entire volume and the quarks, antiquarks and gluons can (almost) freely move about inside these zones as the interaction is small (the vacuum is filled out by the bags which superimpose their properties: $\epsilon_0^c = \mu_0^c = 1$). Their mean free path becomes much larger than the size of a hadron and thus the association of a quark to a hadron is no longer possible. Due to confinement at $T < T_C$ a rather sharp transition to the QGP is expected. The feature of a QGP obtained in this way is, that the number of quarks would approximately equal the number of anti-quarks, $N_q \approx N_{\bar{q}}$. Hence most of the particles are mesons, the net baryon density is small. As the temperature is large, α_s is small and some properties could be calculated by perturbative methods.

It is assumed that matter of the early universe (after $\approx 10\mu s$ after the big bang) was in such a hot QGP state for a short while, before expansion and cooling lead to a transition to hadronic matter.

- The other way is to compress matter adiabatically (one may think of matter in a cylinder with a piston. The volume is compressed fast, so that no heat exchange can take place) until the nucleons overlap from a critical number density n_c on (cold plasma, figure 1.5). Models predict that the density of such a cold QGP exceeds

¹In QED, a photon can create virtual e^+e^- pairs which partially screen a charged particle. This way the vacuum reduces an incident electric field, meaning $\epsilon_0 > 1$. Since $\epsilon_0 \cdot \mu_0 = 1$ (Lorentz invariance) $\epsilon_0 > 1$ leads to $\mu_0 < 1$, thus the QED vacuum is diamagnetic. Note the form of the Coulomb force: $F \propto \frac{1}{\epsilon_0} \frac{QQ'}{r^2}$. If $\epsilon_0 > 1$, the vacuum reduces the action of the charges. The reaction of the vacuum to a magnetic excitation H is described by $B \propto \mu_0 H$. The action of H is reduced, if $\mu_0 < 1$.

In QCD however, instead of screening a color charge by $q\bar{q}$ -pairs (which would lead to a diamagnetic vacuum reaction) gluons can self-interact due to their color charge and lead to an effective anti-screening. This causes a magnetization of the vacuum which wins over the diamagnetic screening part, such that $\mu_0^c > 1$ and $\epsilon_0^c < 1$. The color electric field is thus enhanced as a reaction to a color charge, which was already mentioned when explaining the running of α_s . This anti-screening property of the QCD vacuum makes it a paramagnetic medium. (The paramagnetism of an electron gas can serve as a comparison: The diamagnetic contribution evolves from electrons circling around the kernel and producing a current, such that the associated magnetic field counteracts a possible external field. The paramagnetic contribution coming from spin alignment under the external action, just overwhelms the diamagnetic effect). For large Q^2 and vanishing distances, the incident color charge is not screened, thus $\epsilon_0^c \uparrow 1, \mu_0^c \downarrow 1$ for $r \rightarrow 0$ or, equivalently, $\alpha_s(Q^2) \rightarrow 0$ for $Q^2 \rightarrow \infty$ (meaning no interaction).

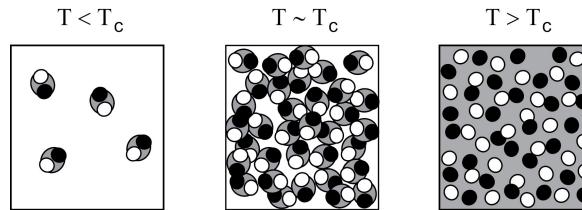


Figure 1.4: QGP by heating [Kra06]

the density in a nuclei of normal nuclear matter by a factor 10. In this way, a cold degenerate QGP is created with a high net baryon density, $N_q \gg N_{\bar{q}}$. However such a QGP at low temperatures will not be achievable in experiments but it is assumed that in the core of neutron stars matter could be in this state. Experiments might realize a transition to a QGP at intermediate temperatures and high baryon density.

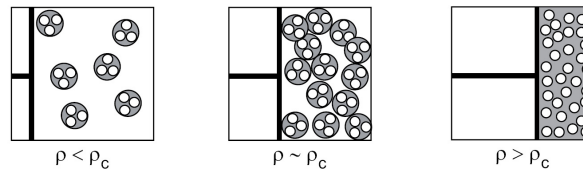


Figure 1.5: QGP by compression [Kra06]

If the quark hadron transition is a thermodynamical state transition of first order (as predicted by the Bag Model), the phase boundary can be obtained by requiring the pressure of the QGP state being equal to the pressure of the hadronic state at the boundary and for given T or μ .² Theoretical predictions of the phase diagram together with the way of the early universe are shown in figure 1.6.

Chiral Symmetry Breaking

In strong interactions, chiral symmetry is spontaneously broken in the QCD vacuum, resulting from the increase of α_s at low momenta Q (chiral symmetry conservation is a feature of weak interactions and is only exact for massless particles moving with velocity of light). When observing a hadron at low momentum Q , the interaction among its constituents is strong, leading to a strong gluon field and hence many virtual $q\bar{q}$ -pairs. The vacuum expectation value $\langle q\bar{q} \rangle$ becomes non vanishing and the mass of this condensate (the sea quarks) will increase the observed mass of the constituent quarks at this Q (the mass of the virtual $q\bar{q}$ -pairs is added to the Higgs masses of the valence quarks. See figure 1.7). As chiral symmetry is exact only in case of massless particles (thus for bare up and down quarks it is already quite well satisfied), this means that decreasing Q^2 (increasing α_s) leads to

²The chemical potential is used rather than the particle number density since the density is not conserved in relativistic systems. In order to obtain thermodynamical quantities the grand-canonical partition function has to be calculated.

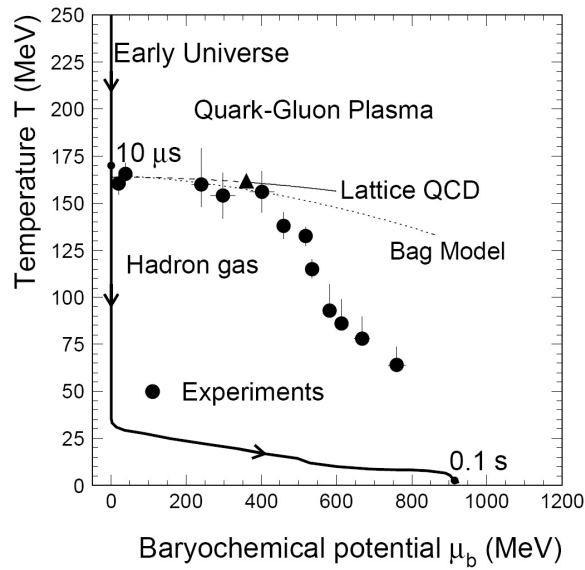


Figure 1.6: The phase diagram as predicted by lattice QCD and the bag model. The full dots are experimental data from chemical freeze-out (see 1.2.2) [BMW07]

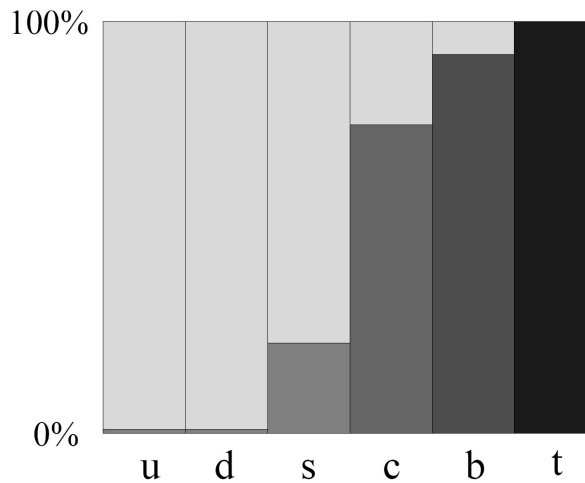


Figure 1.7: The fraction of the quark masses made up by the Higgs-mechanism (dark grey) and by dynamical mass generation (light grey) [BMW07]

stronger violation of chiral symmetry. In a case, where chiral symmetry is perfectly fulfilled, left-handed and right-handed particles cannot interact.

The bag-model violates chiral symmetry since quarks with low mass may flip their helicity at the boundary. In vacuum, due to its anti-screening property, their dynamical quark masses are enhanced (non vanishing $\langle q\bar{q} \rangle$) and chiral symmetry is broken. Thus one cannot speak of left-handed or right-handed quarks anymore. All the quarks may interact with each other. Inside the bag however, where no interactions and no residual quark condensate $q\bar{q}$ is assumed, chiral symmetry becomes almost exact for the light quarks, i.e. their spin is aligned parallel or anti-parallel to their momentum direction.

The chiral symmetry breaking can thus be connected to the condensation of $q\bar{q}$ -pairs . In the vacuum, $\langle q\bar{q} \rangle \neq 0$ (usually the quark condensate of the vacuum is referred to as virtual sea-quarks which only contribute to mass but not to effective quantum numbers).

In the theory of superconductivity, where electrons can pair despite the Coulomb repulsion through the interaction with lattice phonons, as a consequence an energy gap for the excitation of a Cooper pair (and thus their break-up) occurs. Also in the case of condensed $q\bar{q}$ -pairs , an energy gap should emerge. This energy gap can be interpreted as giving dynamical mass to quarks. In this way the large mass of a nucleon ($\approx 1\text{GeV}$) can be explained, although the bare masses of the light u and d quarks are below 10MeV , if one considers the nucleon to be an excited vacuum state.

However, then the questions arises why the mass of the pion is only below 140MeV . This is explained by a comparison with a collective phenomenon in condensed matter physics, also emerging from spontaneous symmetry breaking. There it is known that spin waves occur with infinite wavelength which are due to the simultaneous rotation of all spins. This excitation does not cost energy. Similarly, because of spontaneous chiral symmetry breaking, massless excitations of the vacuum should exist, the Goldstone modes. It is supposed that the lightest meson, the pion, is a realization of such a Goldstone mode. Correspondingly, light quarks and gluons can be seen as the massless excitations of a QGP.

The link to the phase diagram is provided by the prediction, that with increasing T and μ chiral symmetry for light quarks becomes restored. That means, that the vacuum expectation value $\langle q\bar{q} \rangle$ of virtual $q\bar{q}$ -pairs vanishes at some critical temperature T_C and quarks thus lose their dynamical mass. Therefore also the mass of vector mesons should decrease, which might be observable by reconstructing the invariant mass of their leptonic decay products.

As can be seen from the predicted development of the condensate ratio with chemical potential and temperature (figure 1.8), the transition is smooth along T but for lower T discontinuous along μ . This first order transition line finally ends in a critical endpoint (CEP) where the transition is of second order and might be continued toward lower μ by a line indicating a smooth crossover rather than an abrupt transition. The critical temperature T_C cannot be calculated from perturbative methods because $\alpha_s \approx 1$ in this regime. The dependence of the energy density from temperature has instead been obtained from lattice QCD (figure 1.9 shows some results). There, space-time is discretized, quarks are set to the lattice points and gluons to the links between these points. These calculations from first principles (limited in accuracy by the coarseness of the lattice), performed at vanishing chemical potential μ , yield a critical temperature in the range $T_C \approx 150 - 190\text{MeV}$, where the reduced energy density ϵ/T^4 experiences a rapid variation corresponding to the quick transition from the hadronic state to the QGP. However at $\mu \approx 0$ this transition might be

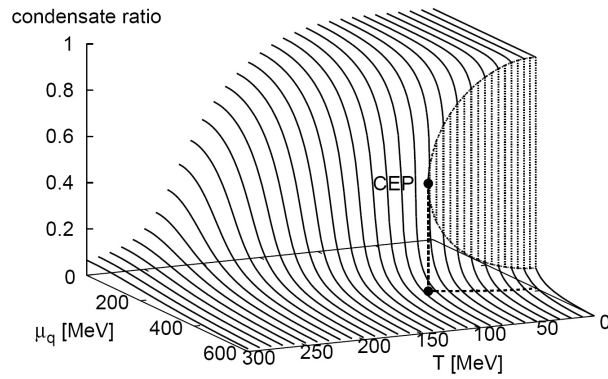


Figure 1.8: The condensate ratio $\langle q\bar{q} \rangle_{T,\mu} / \langle q\bar{q} \rangle$ as function of temperature and chemical potential. Prediction of the NJL (Nambu and Jona-Lasinio) model, a relativistic field theory for interacting point-like nucleons of vanishing mass [BMW07]

a rapid crossover taking place in a narrow temperature interval, rather than a first order transition, resulting in a smooth dependence of the energy density on T . In a crossover, the order parameter of the transition (e.g. the chiral condensate $\langle q\bar{q} \rangle$) changes fast but smoothly. With the LHC, where in the fireball the chemical potential μ is small, one will presumably observe a crossover. The energy density at T_C of around $700 \text{ MeV}/\text{fm}^3$ is around five times higher than the energy density inside heavy nuclei ($\approx 160 \text{ MeV}/\text{fm}^3$). Finally also the chiral condensate $\langle q\bar{q} \rangle$ vanishes rapidly at T_C , thus the critical temperatures of chiral symmetry restoration and plasma transition might correspond.

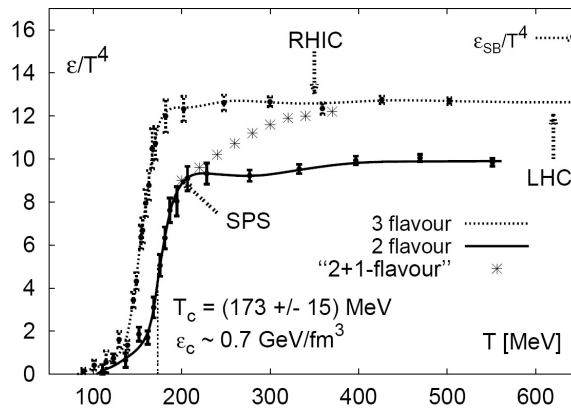


Figure 1.9: The energy density dependence on temperature, obtained by lattice QCD calculations. The results correspond to different numbers of involved light quarks (2 flavor and 3 flavor) and a case, where two light quarks and a third, heavier strange quark are involved ("2+1-flavor") [BMW07]

1.2 Heavy Ion Collisions

At the Large Hadron Collider (LHC) at CERN (Geneva), runs with colliding protons as well as runs with Pb-Pb collisions will be performed. This section gives an overview of quantities and conditions in heavy ion collisions.

1.2.1 Basic Quantities and Features

In order to calculate the momentum that an accelerated particle obtains inside a circular beam line, the centripetal force has to be equal to the Lorentz force $\frac{d\vec{p}}{dt} = e\vec{v} \times \vec{B}$ (where $c = 1$ and v is given as a fraction of c):

$$F_C = F_L \Rightarrow m \frac{v^2}{r} = evB \quad (1.4)$$

where m is the relativistic mass of the accelerated proton ($m = \gamma m_p$), e the elementary charge, r the radius of the beam line and B the magnetic field. In case of accelerated nuclei, the mass has to be multiplied by the number of nucleons A (assuming $m_n \approx m_p$) and the charge by the number of protons Z :

$$mA \frac{v^2}{r} = eZvB \Rightarrow p = \frac{Z}{A} eBr. \quad (1.5)$$

Since many particles are collimated to bunches, which are accelerated and collided at different interaction points, another important quantity is the Luminosity. It is defined as

$$L = \frac{N_a \cdot N_b \cdot j \cdot \nu}{A} \quad (1.6)$$

where N_a , N_b are the number of particles in the colliding bunches, respectively, j is the number of colliding bunches, ν the revolution frequency and A the interaction area, which can be written as $A = 4\pi\sigma_x\sigma_y$, if the particles of a bunch are distributed in Gaussian shape along the x and y direction, perpendicular to the tangent to the beam (z -direction). The cross section σ is a measure for the probability of a collision between two particles. The number of interesting signals per unit time is then given by the product of the luminosity with the cross section σ of the signal at the collision energy:

$$N = L \cdot \sigma. \quad (1.7)$$

The cross section for an interaction is given by $\sigma = A$, hence $N = L \cdot A$ gives the collision rate.

At LHC, a center of mass energy of $\sqrt{s_{NN}} = 14TeV$ will be reached for colliding protons ($A = Z = 1$) and $\sqrt{s_{NN}} = 5.52TeV$ per colliding nucleon pair at PbPb-run. Also large luminosities will be reached. For pp the luminosity is intended to be of the order of $L \approx 10^{34} cm^{-2} s^{-1}$ and $L \approx 10^{27} cm^{-2} s^{-1}$ in case of PbPb.

The energy density at the interaction point is influenced by a number of quantities. When bunches are crossing each other (figure 1.10), the longitudinal momenta of the particles are partly transferred to transversal momenta, leading to nuclear stopping. In case of low collision energies ($\sqrt{s_{NN}} \ll 100GeV$), the particles are efficiently stopped and high baryon

densities are reached at midrapidity, however at moderate temperatures. If the collision energies become larger, the bunches are Lorentz contracted (become narrower in z , pan cake shape) and tend to penetrate each other, leaving an area of low baryon density and high temperatures around midrapidity. Both cases could in principle lead to the formation of a QGP, by crossing the phase transition line at different points (high temperature and lower chemical potential or high chemical potential and lower temperature). As a measure for

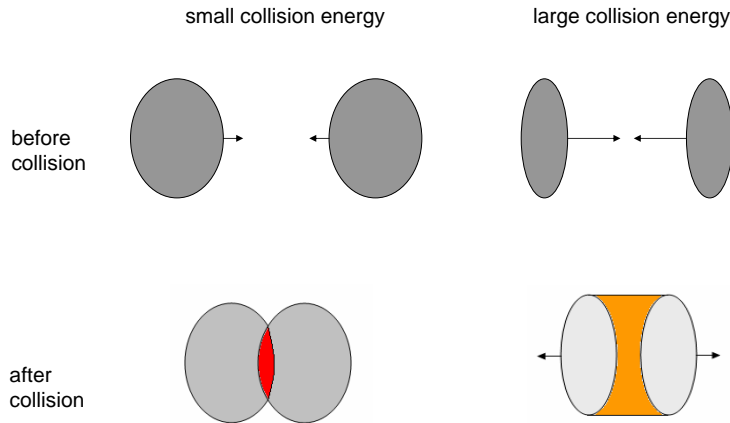


Figure 1.10: Collisions of Lorentz contracted nuclei at different collision energies. Regions of low baryon densities after the collision are signaled in orange, large densities in red.

the energy density at the collision point, the produced transversal energy E_t as a function of rapidity y could serve. A spatially sensitive calorimeter placed around the beam line at some radius would provide an estimate for E_t .

Another quantity influencing the energy density, is the impact parameter of the collision (figure 1.11). Here, one distinguishes between central collisions with the impact parameter being approximately 0, $b \approx 0$, and peripheral collisions for which $0 < b < 2R$ holds, with R being the radius of a nucleus. In case of $b > 2R$ (ultra peripheral collisions), the nuclei can only interact electromagnetically. At high beam energies one can further discriminate between participators and spectators. Participators are nucleons which hit other nucleons during the collision, whereas spectators continue flying in beam direction almost unbiased, due to their large momenta (de Broglie wave-length is very small, wave-like nature of the nucleons can be neglected). The number of spectators is not measured at LHC, however the remaining number of participants influences the event multiplicity, which in turn can be used as measure for the centrality of the collision.

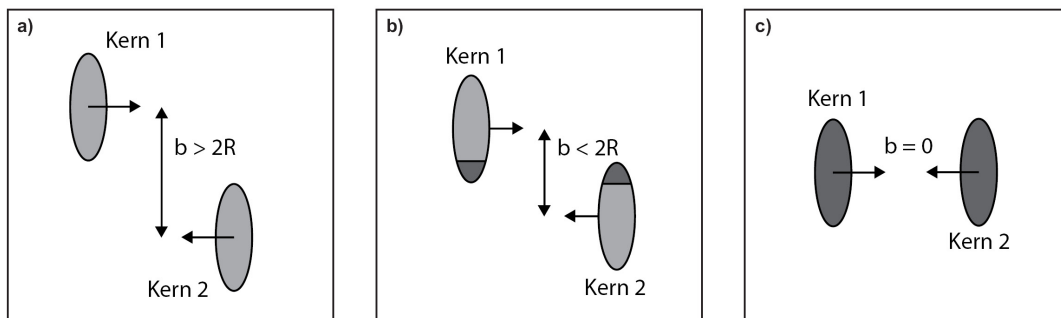


Figure 1.11: Impact parameter of collisions. a) ultra peripheral, b) peripheral and c) central collisions. R denotes the radius of the large axis of the Lorentz contracted, ellipse-like shape of the nuclei [Kra06]

1.2.2 Fireball and Probes for Medium Modifications

Once equilibrium³ has set in after a collision (happening very rapidly), a hot and dense fireball is formed. In case of peripheral collisions, the collision zone is geometrically very anisotropic, resulting in large pressure gradients inside the fireball, which lead to the formation of flows of the quark gluon matter. Hydrodynamically, these can best be described by a liquid model with negligible shear viscosity (ideal fluid, if the constituent particles interact strongly enough). Finally, due to expansion, the fireball cools down, such that at first chemical freeze out is reached, where the particle composition, evolving with inelastic scattering, does not change any more. At still lower temperatures also the phase space distributions remain unchanged since elastic scattering events become rare. This is called thermal freeze out. The fireball finally falls apart into many hadrons. Jets⁴, dileptons and photons carry important information about the history of the fireball and the initial conditions. Thus, these particles can also serve as messengers of a possible QGP created in the fireball medium.

Because of the high density inside the fireball, quarks and gluons with large momenta cannot leave the area without being subject to strong rescattering, e.g. through elastic parton parton collisions and gluon radiation. At the stage of hadronization (cooling of the fireball), this leads to a strong suppression of hadrons with large transverse momenta as compared to the number of such hadrons, that would be expected from scaling the number of binary collisions in nucleon nucleon runs to that in heavy ion runs. As a measure for the suppression, one can investigate the behavior of the nuclear suppression factor

$$R_{AA} = \frac{dN_{AA}}{dN_{pp} \cdot \langle N_{coll} \rangle} \quad (1.8)$$

as a function of p_t , centrality or N_{coll} (figure 1.12). Here N_{coll} means the number of binary collisions, that are expected from scaling the number of collisions in a pp event (with $N_{part} = 2$) up to the heavy ion case (where N_{part} depends on the centrality of the collision). N_{AA} and N_{pp} are the number of interesting events (e.g. number or rate of J/Ψ) in heavy

³Only in an equilibrium state temperature is defined.

⁴A jet is built during the hadronization of very energetic partons (quarks, gluons). A jet consists of a number of hadrons, that are collimated spatially (spray of collimated hadrons).

ion collisions and in pp collisions, respectively. If N counts the number of direct photons created in a collision, which are not subject to strong interaction and thus to the effects of a denser medium, their number N_{AA} should simply scale with the number of collisions N_{coll} , resulting in $R_{AA} \approx 1$.

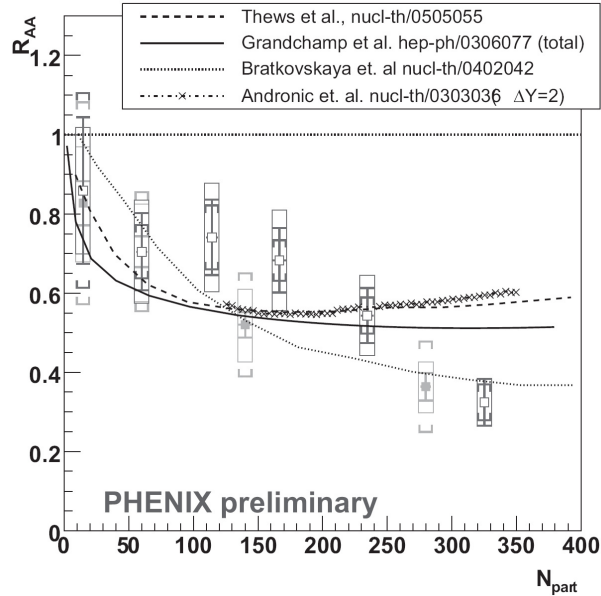


Figure 1.12: Results from PHENIX for the dependence of the nuclear modification factor of the number of participants. Shown are results for gold gold collisions at rapidities $y=0$ (open squares) and $y=1.7$ (filled squares) [Kra06]

Also the modification of the jet-structure with changing centrality of the collision can give insight into changes of the fireball medium. When investigating the angle distribution of jet particles with momenta p_t beyond some threshold (angle relative to the leading particle with the largest p_t), one finds two maxima: one at 0° (near-side jet) and one at 180° (away-side jet). If the centrality of the collisions is increased, also the density of the fireball and thus the impact of the medium on the jet partons traversing it after their hard scattering, increases. This influences the hadronization of the partons to the observed jet particles, resulting in a suppression of the away-side maximum and a modification of its shape.

Increasing the collision rate also opens new decay channels for hadrons, resulting in larger widths. This can be probed by the leptonic decay of those hadrons, because leptons and especially photons have a relatively large mean free path, even in very hot and dense fireballs (they are not subject to strong interaction. For photons the mean free path is of the order of $10^3 fm$, which largely exceeds the size of the fireball). In this way, leptonic signals carry information about the state of the fireball before chemical freeze out. Calculation of the production rates yields, that for the abundance of di-leptons predominantly the pion annihilation channel

$$\pi^+\pi^- \rightarrow \rho \rightarrow e^+e^- \quad (1.9)$$

is responsible in case of a hadronic phase, and quark annihilation

$$q\bar{q} \rightarrow e^+e^- \quad (1.10)$$

in a plasma phase. Comparisons of di-lepton data from central nucleus nucleus collisions with data from peripheral collisions (resembling rather nucleon nucleon collisions due to the smaller number of participants) or with the expectations from the electromagnetic decay of hadrons at chemical freeze-out, yield a strong enhancement of the di-lepton rates in nucleus nucleus collisions. This points toward an increased decay width of the ρ -meson in the dense fireball [BMW07].

1.2.3 Quarkonia and Deconfinement

Quarkonia are bound states of heavy $q\bar{q}$ -pairs, e.g. $c\bar{c}$ or $b\bar{b}$, whose masses are primarily made up of the electro-weak Higgs-masses (the portions added by the $\langle q\bar{q} \rangle$ condensate can be neglected). That's why the mass of the hadron (the quarkonium) is given by the sum of the bare-masses of its constituent quarks. As in the e^-e^+ -system, the quarkonia can be excited to different energy states. Due to its large mass, the lifetime of a t -quark is very short. Thus the condensation of $t\bar{t}$ quarkonia is not observed.

Maybe the J/Ψ meson is the most prominent quarkonia-system. It consists of a $c\bar{c}$ -pair in the ground state and has the same spin and parity as the photon $J^P = 1^-$. Its lifetime τ is uncommonly high, as the favorite strong decay-channel to a $D\bar{D}$ -pair ($|D\rangle = |c\bar{u}\rangle$) is energetically impossible, since $2m_D > 2m_{J/\Psi}$ (the necessary light $q\bar{q}$ -pairs would have to be created from the excitation energy of the quarkonia) and the annihilation of the $c\bar{c}$ -pair is suppressed due to the branch rule (annihilation requires the exchange of three gluons in strong decays due to color neutrality and parity conservation, or the creation of leptons or hadrons through an electromagnetic decay, which is suppressed due to the low e.m. coupling constant α). Because in the strong decay channel three gluons have to be produced (decay-probability $\sim \alpha_s^3$), the J/Ψ decays in about 30% of the cases electromagnetically into a lepton-pair through a virtual photon.

At first glance one might assume that in a QGP with high particle densities quarkonia should be destroyed or even be prevented from being formed because color-charges are screened effectively by the freely movable partons (Debye screening). Because of their large mass (slow motion, velocity considerably smaller than the speed of light), the energy levels of quarkonia can be calculated in the non-relativistic limit, using the Schrödinger-equation. Using the potential for the color field,

$$V(r) = k \cdot r - \frac{\kappa}{r} \quad (1.11)$$

one finds for the mean distance between the two quarks of the meson,

$$\langle r_i \rangle = \frac{\int dr r \Psi_i(r)}{\int dr \Psi_i(r)} \quad (1.12)$$

(i denotes the state with energy E_i and wave function Ψ_i), a value much larger than the Debye length λ_D . In an electromagnetic plasma, the Debye length is given as $\lambda_{D,e.m.} = \sqrt{\frac{2\varepsilon_0 k_B T_F}{3n_e e^2}}$, where n_e is the electron number density and T_F the Fermi temperature of the material. The effective color potential (resulting from screening) in a dense plasma

$$V_{eff} \sim -\frac{e^{-r/\lambda_D}}{r}, \quad (1.13)$$

is supposed to have the same structure as in an electromagnetic plasma. The range of the color charges is significantly reduced as compared to a Coulomb like potential. In case of a QGP, additionally the long ranging linear part of the $q\bar{q}$ potential, which is responsible for confinement, is omitted. The surrounding of the heavy quarks with light quarks, in case $\lambda_D < \langle r_i \rangle$, should then prevent the recombination of quarkonia to a large extent. The suppression of quarkonia therefore was originally considered a possible signal for QGP formation. However the experimental data, suggesting suppression of J/Ψ , can also be explained by normal absorption of $c\bar{c}$ in the dense nuclear medium or by a break-up due to energetic hadrons produced during the collision.

Statistical models now predict even an enhancement of the J/Ψ yield at LHC energies, as there will be many more heavy quarks created (order of 100) in one collision event than in former experiments at lower energies. If a QGP is formed, the quarks should then be able to effectively travel large distances and like that a heavy quark that originally may have been bound in quarkonia and was then broken-up can recombine statistically with any other available heavy (anti)quark in the plasma. In this way the abundance of quarkonia (growing quadratically with the number of produced heavy quarks), following the hadronization of a QGP, could even exceed the expected value from scaling pp-collisions. This would result in the nuclear modification factor for the J/Ψ -yield, $R_{AA}^{J/\Psi}$, to become greater than one. If LHC verified this prediction of non-suppression, it would provide a very strong hint toward the existence of a QGP.

2 The ALICE Experiment

In this chapter first a short overview of the ALICE detector system at the Large Hadron Collider (LHC) is given. In the next chapter, physical requirements and the design of the Transition Radiation Detector (TRD) are explained in some more detail.

More about the ALICE detector system in general and its components can be found in [ALI04] and [ALI08]. The TRD layout is described in detail in [ALI01]. Concerning the Front End Electronics of the TRD, especially the TRAP chip, more information can be found in [Gut02], [Gut06], [ALI01], [TRA06]. For more details about data acquisition issues, including a description of Zero Suppression, refer to [Gut06]. The architecture and implementation of the GTU is developed in [dC03]. Technical aspects and the current development concerning the TRD can be found on the TRD Wiki pages [WIK].

2.1 The Large Hadron Collider

The Large Hadron Collider (LHC) is intended to collide protons at a center of mass energy of 14TeV and lead ions at 5TeV per nucleon pair, resulting in a total center of mass energy of the order of 1150TeV . LHC will reach high luminosities by focusing the particle bunches to small diameters. In order to hold particles on a circle, 1232 dipoles have been installed producing peak magnetic fields of $B = 8.3\text{T}$. The accelerator ring is situated in the former Large Electron Positron Collider (LEP) tunnel near Geneva, Switzerland.

Table 2.1: LHC parameters for Pb run

Beam Energy (maximum)	$2.76\text{TeV}/\text{nucleon}$
Luminosity	$10^{27}\text{cm}^{-2}\text{s}^{-1}$
Interaction Rate (minimum bias)	8kHz
Interaction Rate (central, impact parameter $< 5\text{fm}$)	0.8kHz
Bunch Length	7.94cm
Beam Radius	$15.9\mu\text{m}$
Number of Particles per Bunch	$7 \cdot 10^7$

Some parameters for LHC during PbPb-run can be found in table 2.1.

Before particles are injected into the LHC ring they are pre-accelerated in two smaller synchrotrons. After having reached the final energy, the protons or ions are collided at four interaction points where the four LHC experiments are situated. The protons stem from a duoplasmatron proton-source and are accelerated in several steps. Lead ions come from an electron cyclotron resonance source. They are bunched, preaccelerated and selected, if they are in the charge state Pb^{27+} . After further acceleration, they are stripped by several foils and selected according to their charge state, such that finally Pb^{82+} is obtained. These

fully ionized lead ions are then accelerated by SPS to $177\text{GeV}/\text{nucleon}$, before they are injected into the LHC, where they gain a final energy of $2.76\text{TeV}/\text{nucleon}$.

The mass region in which the Higgs Boson is supposed to be found is accessible by the LHC. ATLAS (A Toroidal LHC Apparatus) and CMS (Compact Muon Solenoid) will therefore exploit the pp-run for their search for the Higgs-Boson, which is needed to complement the Standard Model. The Higgs mechanism is expected to produce the masses of charged leptons and the bare-masses of quarks. Also theoretical approaches reaching beyond the Standard Model will be addressed by these experiments. A third experiment is LHCb (LHC Beauty Experiment) with which the CP violation in B-meson systems will be investigated, thus contributing to the understanding, why there is the obvious unbalance of matter and antimatter in the universe. ALICE (A Large Ion Collider Experiment) will identify and characterize the Quark Gluon Plasma, a state of strongly interacting matter that the early universe is supposed to have gone through until the first microseconds of its existence, when quarks combined into hadrons. In very energetic heavy ion collisions such a plasma is supposed to be established for a short time. For an overview refer to chapter one.

2.2 The ALICE Experiment

ALICE is the dedicated heavy ion detector at LHC, addressing the physics of strongly interacting matter and the quark gluon plasma (QGP) at extreme values of energy density ϵ and temperature T . As the center of mass energy of a nucleon pair is in the order of 5.5TeV during PbPb-run, it is supposed that a hot and long-living QGP forms. Due to its high gluon density and the fast equilibration of the gluons, large energy densities and temperatures will be reached. The ALICE experiment is designed to study the properties of such a hot QGP. Besides its dynamical evolution and the hadronization, also the evolution of the hadronic state until chemical freeze-out is of strong interest. Therefore a huge set of observables will be measured covering a large phase-space volume.

During PbPb-runs very high particle multiplicities will be reached. Although there is strong evidence from data of former heavy ion experiments that a maximum multiplicity of about 2000 charged particles per unit interval of rapidity around midrapidity ($dN_{ch}/dy|_{y=0} = 2000$) emerging directly from the collision (not including secondary particles) can be expected. However, as there was no relying theoretical prediction for the multiplicity when the detector was designed, the detector systems are able to cope with multiplicities of up to $dN_{ch}/dy \approx 8000$ (this results in about 16000 charged particles alone inside the TRD volume, including secondary particles that are created in the more inner detectors and inside other material. For example the decay of K_s^0 within 5cm of the primary vertex enhances the charged particle yield by more than 10%). Lately, a peak multiplicity of around $dN_{ch}/dy \approx 2500$ is expected. The pp-runs serve as a source for getting reference data for the heavy ion physics program as well as for adjustment and aligning of the detectors. The overall dimensions of the ALICE experiment are 26m in length, 16m in width and height and its weight is about 10000t .

2.2.1 Design Considerations

As was already mentioned, the ALICE detector is able to cope even with the largest anticipated particle multiplicities however it is optimized for $dN_{ch}/dy \approx 4000$. In this region a robust tracking of the particles entering the detectors must be accomplished, for which three dimensional hit information is necessary. In order to make particle identification possible, a magnetic field of $B \approx 0.5T$ is applied, so that the bending of charged particles in it yields information about their transverse momentum p_t . The momentum reconstruction must work in the range of $\propto 100MeV/c$ (resonances) up to $100GeV/c$ (jet physics). In order to reduce Bremsstrahlung and multiple scattering at low p_t , the material budget is very limited. It corresponds to about 13% of a radiation length X_0 until the outer radius of the TPC. For the particle identification many different methods are combined, such as specific energy loss, time of flight, transition radiation, Cherenkov radiation as well as electromagnetic calorimeter measurements and muon filters.

2.2.2 The Detector System

A part of the detector system is embedded in a large solenoid magnet (L3 magnet) which is able to provide a rather homogeneous magnetic field of $B = 0.5T$. These detectors, which surround the beam-pipe cylindrically, are called central barrel. The polar angle acceptance of these detectors comprises the range $45^\circ < \theta < 135^\circ$, corresponding to rapidities from $y = -0.9$ to $y = 0.9$. Due to the cylindrical shape, there is full azimuthal coverage (except for dead-regions of the individual detectors). At smaller polar angles (2° to 9°) outside the L3 magnet, the forward muon arm is situated together with a large dipole magnet and absorbers. See figure 2.1 for a schematic drawing of the ALICE detector system.

The Inner Barrel Detectors

Here a short overview over the central barrel detectors is given. It begins with the detector closest to the interaction vertex, increasing the radius gradually.

- The innermost detector being closest to the beam and the interaction vertex is the Inner Tracking System (ITS). It is able to reconstruct the secondary vertices from hyperon and heavy quark decays. Furthermore it serves as a tracker for low- p_t particles and improves the overall momentum resolution when combined with the other central barrel detectors, that provide momentum reconstruction (especially TPC). Furthermore the ITS provides particle identification capabilities which makes it a stand-alone particle spectrometer at low p_t . In order to keep the occupancy low enough to ensure robust and unambiguous tracking, the number of detector pixels is chosen as large as possible (hence their size becomes small, reducing the $\frac{S}{N}$ ratio of a pixel). A large number of pixels on the other hand increases readout and calculation time and reduces the overall speed of tracking. A time limit is set by the collision frequency, which, at a luminosity of $L = 10^{24}cm^{-2}s^{-1}$, is low enough to allow for a fine detector granularity. The ITS consists of six high resolution detector barrels. The innermost detectors at radii where the particle density is very high, are silicon pixel and silicon drift detectors, providing a very good two dimensional spatial resolution. The outer layers are made of silicon micro-strip detectors.

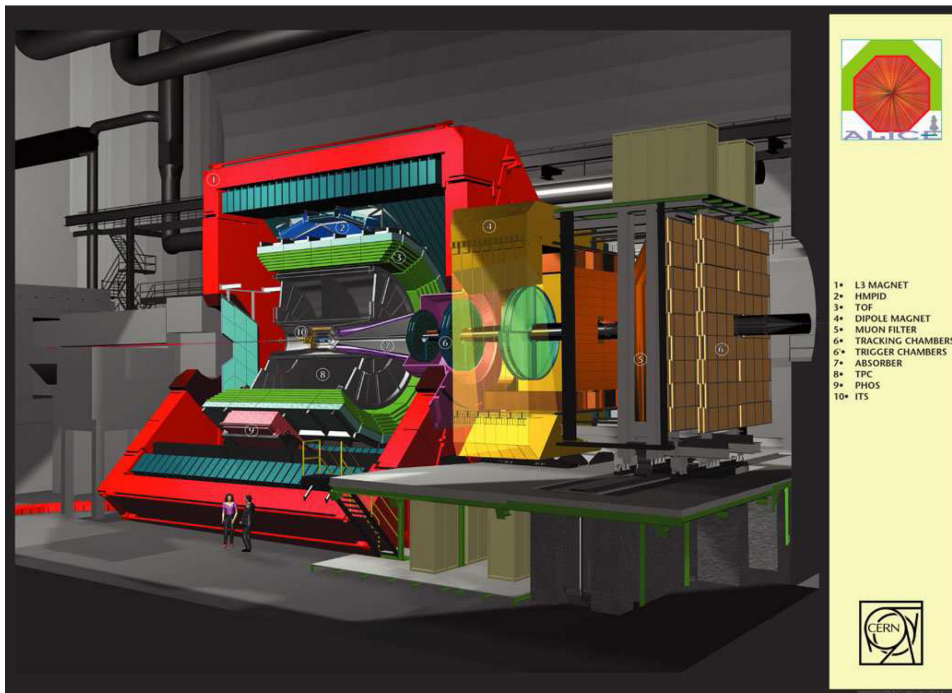


Figure 2.1: The ALICE detector system [ALI01]

- The detector system following at increasing radius is the Time Projection Chamber (TPC). It is the largest detector and provides robust and efficient tracking of up to 10000 charged particles in its acceptance volume. Therefore the TPC also is the slowest detector of the ALICE-detector system which can be afforded since the event rate of 8000 minimum-bias collisions per second (of which 5% are most central events) is low enough. Its inner radius of 85cm is chosen such that the hit-density is below a critical threshold that is driven by the detector granularity and the anticipated tracking efficiency. The maximum radius of 250cm is required to have enough length in which a particle can produce hits, so that the resolution of the dE/dx determination is better than 7%. In this way the TPC provides PID information at momenta in the region of the relativistic rise and up to $50\text{GeV}/c$.
- The Transition Radiation Detector (TRD) is supposed to detect electrons at high transversal momenta ($p_t > 1\text{GeV}/c$) and to provide efficient electron-pion separation. By its trigger capabilities it supports measurements of the production rates of quarkonia and heavy quarks near midrapidity and contributes to jet physics. The TRD in some more detail will be the topic of the next section.
- The Time Of Flight (TOF) detector uses as means of particle identification the flight time of a particle through a defined length. It is able to provide PID at intermediate momenta (up to $2.5\text{GeV}/c$ for pions and kaons and $4\text{GeV}/c$ for protons) thus leading to the possibility to distinguish between pions and kaons and between kaons and protons. The occupancy (number of occupied cells) should be below 10% in order to guarantee that TOF works efficiently also at large multiplicities. Therefore the number of cells will be as large as 150000. The time resolution then falls below 100ps .

Not mentioned in the above list is the High Momentum Particle Identification Detector (HMPID), consisting of a ring imaging Cherenkov counter, which extends the hadron identification capability at larger momenta. PHOS and EMCAL, two electromagnetic calorimeters, will also be installed inside the L3-magnet, providing energy information of photons (ranging from thermal photons to photons emerging from hard QCD-processes) and neutral mesons (PHOS) as well as information about jet production rates (EMCAL).

Further Detectors

- The Muon Spectrometer, which is situated outside the L3 magnet at more forward pseudorapidities ($2.5 < \eta < 4.0$), will measure the production of heavy quark resonances by their muonic decay channel with good enough mass resolution ($100\text{MeV}/c^2$ at $10\text{GeV}/c^2$ di-muon invariant mass) to be able to disentangle the different states ($J/\Psi, \Psi', \Upsilon, \Upsilon', \Upsilon'', \Phi$ -meson). This allows for a determination of the production rate, depending on centrality of the collision or on transverse momentum. Moreover, the measurement of the muon continuum, which mainly emerges from the semi-leptonic decay of open charm and open beauty at LHC energies, allows for the study of heavy quark production, which is a crucial measure, e.g. for the existence and the properties of a QGP. In order to be able to detect muons, the large flux of hadrons has to be absorbed by applying a muon filter with much material. Therefore, muon identification is done for total momenta larger than $4\text{GeV}/c$ and in addition at large rapidities, in order to measure low- p_t charmonia. A dipole magnet with a large field integral is applied, in order to achieve the desired mass resolution.
- There are a number of smaller detectors for obtaining information of global interest about the event, that are used as triggers, for example for the event time (measured by T0 with 25ps accuracy), the event multiplicity (measured by FMD for charged particles, by PMD for photons) or the impact parameter of the collision (obtained by ZDC).

3 The Transition Radiation Detector

As this diploma thesis is mainly concerned with the Transition Radiation Detector, its purposes and design shall be discussed in a little more detail. Here the emphasis is not put on the signal creation because this topic will be part of an own chapter.

3.1 Physics With the TRD

The main task of the TRD is to provide electron identification in a highly relativistic (for electrons) momentum range of $p > 1\text{GeV}/c$. At these momenta the specific energy loss of pions rises (relativistic rise), approaching the electronic energy loss. Thus the e/π separation power of the TPC-PID, which is based on the specific energy loss only, decreases. Transition Radiation is an efficient way to improve the separation power in the high-momentum range. Complementary to the measurement of quarkonia at forward rapidities in the di-muon channel, together with TPC and ITS the TRD provides measurements of the production of light and heavy vector-meson resonances via their di-electron decay channel. Moreover, the dilepton continuum in pp and PbPb collisions shall be measured and the TRD shall ease the ITS reconstruction of hadrons with open charm and open beauty in their leptonic decay channels.

Another important feature of the TRD is its trigger capability. It provides a L1 trigger for high momentum particles thus enhancing for example the Υ -statistics or the J/Ψ -yield. The trigger can also be employed in jet physics by requiring three or more high- p_t tracks (3 to $5\text{GeV}/c$) in a cone-volume of specified size. This constellation could then define a jet candidate. A candidate could be combined with another jet candidate back to back or with two close high momentum electrons. A candidate opposite to PHOS could also be combined with a high momentum photon, thus also including PHOS into the trigger. Finally a trigger could reduce the data volume by only reading out the TPC-region to which a detected high- p_t electron tracks to (region of interest).

3.2 TRD Design Considerations

The TRD is designed to provide a pion rejection capability of 100 at an electron efficiency of 90% for particles with momenta larger than $3\text{GeV}/c$. This means that in a sample of investigated electrons and pions only one in a hundred pions are allowed to be misidentified as an electron whereas at the same time 90% of all electrons must be inferred as electrons. Due to the large pion background, this is a challenging task which is however substantial for measurements of the J/Ψ production and its p_t dependence in the e^+e^- channel. These measurements are carried out by reconstructing the invariant mass of unlike-sign electrons (combining e^- with e^+ under some additional cuts), and therefore the combinatorial background obtained in a mass spectrum depends crucially on the signal over background ($\frac{S}{N}$)

ratio. A pion misidentified as an electron would increase the background and worsen the distinctness of the signal sitting upon the background structure.

Another important issue is the position and momentum resolution which should match to the TPC. In order to not worsen the TPC performance, the reconstruction of a track inside the TRD should lead to a pointing resolution toward the TPC that is a fraction of a TPC pad-width. The combined momentum resolution determines (together with the time-of-flight information from TOF) the mass resolution which should be in the order of $100\text{MeV}/c^2$ at the Υ mass scale (with an applied magnetic field of $B = 0.4T$). In order to reduce energy loss by Bremsstrahlung which would lead to incorrect momentum determination at least on trigger level (where undisturbed particles originating from the primary vertex are supposed), the amount of material should be reduced to a minimum. The smaller the radiation length the smaller is also the probability of photon conversions, which lead to more background and increasing pixel occupancy and therefore can deteriorate the position resolution of track reconstruction (e.g by assigning wrong clusters). The size of the pads (on which the read out signal is induced) in the particle-bending plane inside the magnetic field, defines the granularity of the position resolution and thus also the momentum resolution. The pad-dimensions are chosen small enough, such that a tracking efficiency (number of reconstructed tracks over number of trackable tracks with hits in at least the outermost three detector layers) of 80% is achieved, even at the highest multiplicities. This means that the occupancy (number of detector pixels including time-bins that have a non-noise signal) at these multiplicities should not exceed 35%.

3.3 The TRD Layout

The above mentioned design considerations have driven the choice of the final TRD layout. The TRD is built cylindrically along the beam-line, which defines the z-axis and the direction of the magnetic field $\vec{B} = B \cdot \vec{e}_z$. It is centered around the interaction point defining also the origin of the ALICE coordinate system. Its orientation is such that the positive z-axis points toward the muon arm. The azimuthal angle ϕ defines the deflection angle in the magnetic field. The polar angle θ is defined as the angle with respect to the beam-line in a plane that contains the z-axis. Since all the TRD-chambers are flat, a local coordinate system for each sector is defined by keeping the z-axis but introducing a local y-axis in direction of the wires (in bending direction) and an x-axis in drift-direction parallel to the chamber normal. This local coordinate system is thus obtained by rotating the ALICE system around the z-axis, until the x-axis points parallel to the direction of the chamber normal of the considered sector. The polar angle coverage of the TRD is $35^\circ < \theta < 145^\circ$ or $|\eta| < 0.9$ in terms of pseudorapidity. It is situated between TPC and TOF.

The TRD is subdivided into 18 individual sectors in ϕ which are called supermodules and which together cover the whole azimuthal angle range of 360° . Each supermodule consists of six individual layers. This segmentation is necessary in order to reduce the individual drift time and provide a fast trigger. Additionally, an electron passes six radiators, increasing e/π separation capability. In z-direction the supermodule is subdivided into five stacks. So in total there are $5 \cdot 6 = 30$ independent chambers making up one supermodule and $18 \cdot 5 \cdot 6 = 540$ chambers of which the TRD consists.

Each module (chamber) is a multiwire proportional readout chamber with an additional

drift region and a radiator at the entrance of the module. A particle traversing the radiator can produce transition radiation (TR) (in the next chapter, this is discussed in more detail). Since the onset for transition radiation in the TRD lies at $\gamma \approx 1000$, only electron tracks will produce a measurable TR signal in the momentum range $p \leq 100 \text{ GeV}/c$. The radiator is a carbon fiber laminated Rohacell/polypropylene fiber sandwich of 48 mm thickness, allowing for enough material-transitions and along with low absorption for a yield of X-ray transition radiation, sufficient for the anticipated e/π separation. Due to the carbon fiber structure enough rigidity is achieved in order to not exceed the deformation of the chamber over 1 mm at an overpressure (gravity, flow of the Xe/CO_2 gas mixture) of up to 1 mbar . Additionally this solution is more efficient than a stack of foils in terms of mass contribution. Transition radiation is released for incident particles with $\gamma \geq 1000$ thus allowing for an efficient distinction between electrons and pions (figure 3.1). The inset of TR emission thus is at an electron momenta of $p_e \approx 0.5 \text{ GeV}/c$ and it saturates at $p_e \approx 2 \text{ GeV}/c$. Per such incident electron around 1.45 TR photons are released of which on average 1.25 are detected. The

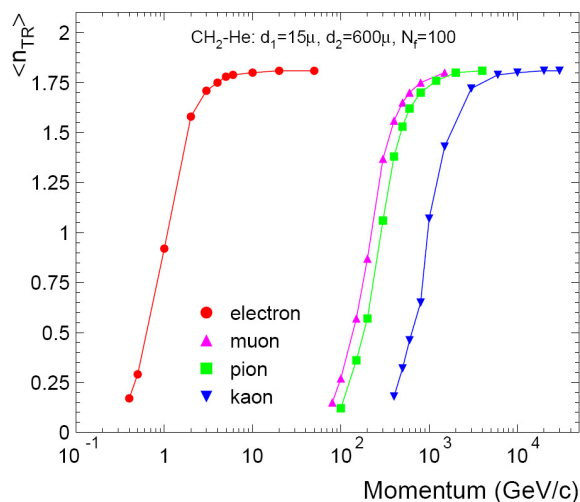


Figure 3.1: Mean number of Transition Radiation photons as a function of momentum for different particle species [And]

TR photons are in the X-ray range, having energies from 1 keV to 30 keV and in the high Z gas of the drift-chamber they are preferentially converted to electron clusters via photo absorption at the entrance of the drift region (late drift-times).

Behind the radiator, a drift region of 30 mm follows which is filled with a gas mixture of Xe and CO_2 in the proportion $85 : 15$. A minimum ionizing particle liberates on average 275 electrons per centimeter. The drift-time amounts to $2 \mu\text{s}$ at a drift velocity of $1.5 \text{ cm}/\mu\text{s}$ in an electrical field strength of $0.7 \text{ kV}/\text{cm}$. There is only little diffusion. Due to the magnetic field the drift-direction is inclined with respect to the chamber normal as a consequence of the simultaneous impact of the electrical drift-field and the magnetic field. This $\vec{E} \times \vec{B}$ effect results in an inclination angle (Lorentz-angle) of $\Psi_L \approx 8^\circ$ at $B = 0.4 \text{ T}$. The amplification in a multiwire proportional chamber of 7 mm height induces a signal on the pad-plane, which is placed on top of the chamber. The gas gain will be of the order of 5000, meaning that the original charge from an electron cluster that is amplified in the vicinity of the anode wire, creates an avalanche charge being around 5000 times larger than the original

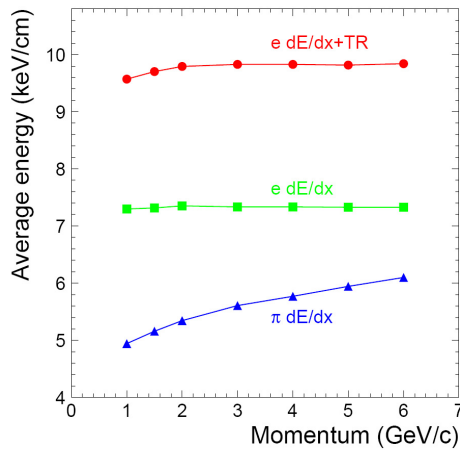


Figure 3.2: The influence of Transition Radiation on the average energy deposit per distance as function of momentum. The increase for pions is due to the relativistic rise of energy loss. In the shown momentum range, pions do not produce Transition Radiation. For electrons, which are already on the Fermi Plateau of energy loss, Transition Radiation enhances the average energy deposit substantially [And]

cluster charge (the average pulse height spectrum is shown in figure 3.3). The pad-plane of each chamber consists of 144 pads in bending ($r\phi$) direction and of 12 to 16 pad-rows in z-direction, depending on the stack position and the layer. The pad-sizes differ from layer to layer and also on a pad-plane the length of pads from the border pad-rows may vary. In total the $1.18 \cdot 10^6$ pads cover an area of about $716m^2$.

The TRD geometry is shown in figure 3.4. The layout of the detector with radiator, drift and readout along with a sketch on the signal creation, is pictured in figure 3.5.

The signal on the pads is read out by the front end electronics which is mounted directly on the chamber. The readout samples the signal with a frequency of $10MHz$. The time-bin length of $100ns$ corresponds to $1.5mm$ of drift length. Signals in lower time-bins correspond to clusters from early drift-times and positions near the anode wire. Furthermore the signal amplitude is digitized and turned into a 10Bit number.

The position resolution reached with this layout is $\sigma_y \approx 400\mu m$ for $p_t \approx 1GeV/c$ at low multiplicity. To obtain a good y-resolution (which is mandatory for a good momentum resolution since the momentum measurement makes use of the bending of a charged track in the magnetic field by looking at its deflection in y-direction) extensive use of charge sharing between pads in y-direction is made whereas the position resolution in z-direction is limited by the pad-length since there is almost no charge sharing between pad rows. Also the time information is limited by the sampling rate at readout. The momentum resolution consists of a constant term and a linear term depending on multiplicity: $\frac{\sigma_p}{p} = 2.5\% + \frac{0.5\%}{GeV/c} \cdot p[GeV/c]$ for low multiplicity and $\frac{\sigma_p}{p} = 2.5\% + \frac{0.8\%}{GeV/c} \cdot p[GeV/c]$ for full multiplicity.

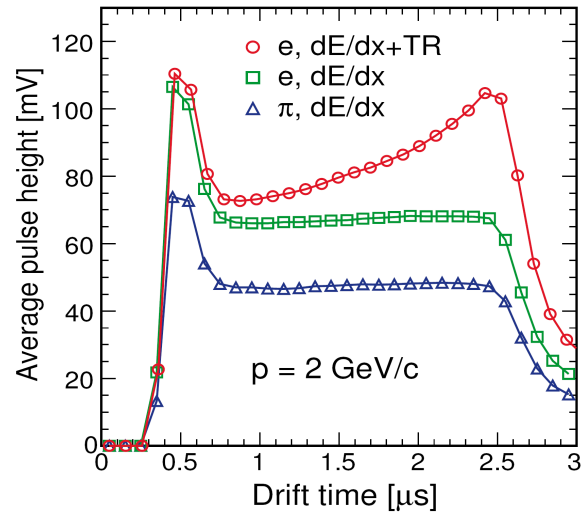


Figure 3.3: Average pulse height spectrum as function of the drift time. The large peak at early time bins in the amplification region is due to charge clusters arriving from two sides at the anode wire. For electrons with Transition Radiation contribution, one can observe a clear increase of the average signal toward later time bins, due to the absorption of Transition Radiation photons in the drift gas [Pos04]

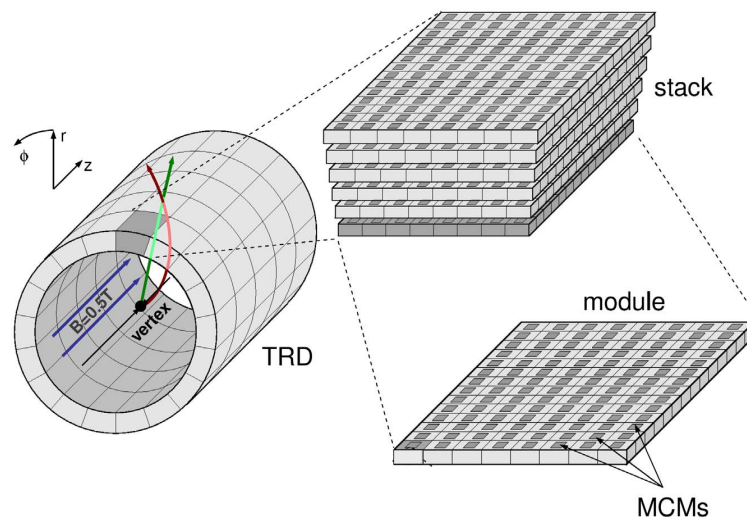


Figure 3.4: The TRD detector geometry [Gut06]

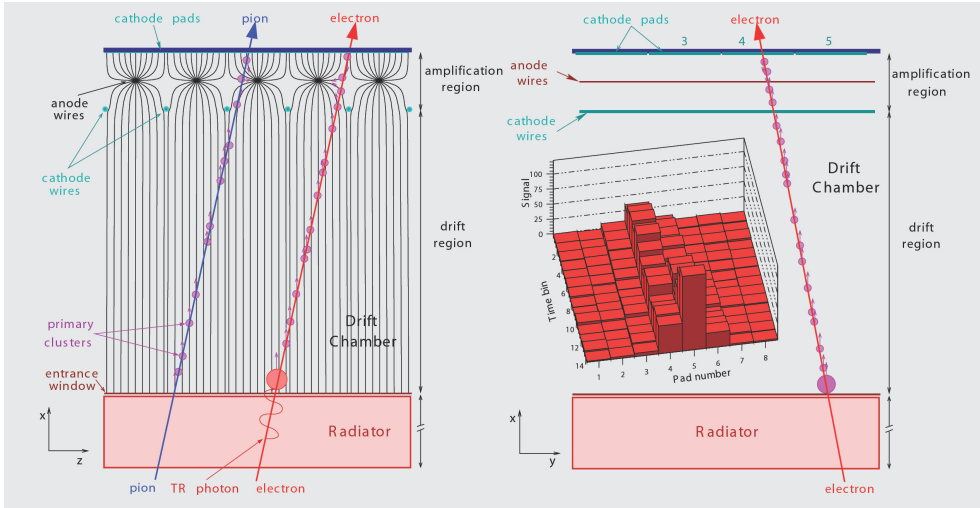


Figure 3.5: The TRD detector layout and creation of a signal [ALI01]

3.4 The Front End Electronics

Since the implementation of part of the front-end electronics (FEE) (namely the trigger calculation of the TRAP-chip, see below) into AliRoot was task of this thesis, in this section and the following chapter a closer look to it and its functionality in the trigger-system shall be taken.

3.4.1 Requirements

The FEE sits directly on the TRD chambers in order to save the latency, that would be introduced by shipping data away from the detector for calculation and back again. The FEE is supposed to perform fast particle tracking in order to obtain a guess on the particle's transverse momentum and its identity. In order to achieve enough accuracy on the results, there are a number of requirements. As the momentum resolution is based on the position resolution in y -direction (along a pad-row), the position estimation due to the charge deposit on the pads must be more accurate than the width of the actual pad. Therefore the anode-wires are situated a certain distance away from the pad-planes, such that the neighboring channels see about 10% of the mirror charge of the avalanche, in case the incident electron cluster makes a hit centered on one pad. This improves the space-point resolution in case of a signal to noise ratio of $S/N \geq 30$. If the digital output of an ADC ¹ channel is below 30, digitization errors begin to worsen the space-point resolution. For a minimum ionizing particle about $3 \cdot 10^4$ electrons (after amplification) contribute to the signal on the central pad (corresponding to ADC-count 30) which determines the noise to be smaller than 1000 electrons (1 ADC counts) in order to reach $S/N \geq 30$ also in this case. For the electron/pion separation one uses the Transition Radiation (TR) signal, that is significantly induced only by electrons in the considered momentum range. By using a digitization of the signal into a word of 10 bit, the dynamic range is supposed to not limit the e/π -separation. Another important quantity is the digitization rate. Depending on it,

¹Analog Digital Converter. Converts the signal from the PASA into a digital number

Overview

The FEE participates in calculating the TRD trigger decision. Therefore there are strong time-limitations which make it necessary to perform all the calculations on the detector and in a parallel fashion. The idea is to use the separation of the TRD into six layers to perform a straight line fit to the hit points of a track in each of them independently (tracklet). This means, that the required fit parameters can be calculated during the drift-time of $2\mu s$ ³.

Since a stiff (high p_t) track, that comes from the primary vertex (which is always assumed but not always true of course) will in most cases only affect the pixels belonging to two adjacent pads when flying through a TRD layer, a logic chooses the hits of two adjacent channels to perform the fit. This step is performed by four CPUs. The electronics performing these calculations, is called Local Tracking Unit (LTU). After the slope and offset of a tracklet have been calculated, the tracklets of different layers and of one stack (since stiff tracks will not cross stack-borders) have to be combined to tracks. This is accomplished by the GTU (Global Tracking Unit). After $6\mu s$, all the calculations have to be finished and based on the track-content of the event, the trigger-level decision is chosen by the ALICE Central Trigger Processor (CTP).

Structure

The FEE is placed on a chip called MCM (Multi Chip Module) which is a multi-mode chip that has an analog input part consisting of 18 channels of a pad row (so there are 8 MCMs on one pad row) and corresponding PASAs (one for each channel) as well as a digital part. This multi mode approach expects a great deal from the architecture since the analog part easily imposes frequency disturbances on the digital electronics. The digital part, which is of special interest in view of this diploma thesis, is called TRAP chip (tracklet processing chip). It consists of 21 input channels, ADCs, digital filters and event buffers. Furthermore 21 preprocessors (used for the accumulation of hit information) and four CPUs (which calculate the linear fit) are situated on the TRAP. Finally a network interface controls the insertion of the results from the tracklet calculation into the readout tree network, which in turn provides them to the GTU, where they are merged to tracks.

The MCMs are integrated on Readout Boards (ROB). Six to eight ROBs cover one TRD chamber (depending on the position of the chamber). The ROBs are arranged in two rows and three or four columns, respectively. On each ROB 16 usual MCMs (for tracklet calculation) are placed. Moreover there is one MCM per ROB to merge the readout stream of one ROB (Board Merger) and two ROBs carry an additional MCM to put together the data from each half of the chamber (Half Chamber Merger). One ROB per chamber carries a DCS board (Detector Control System), needed for controlling the power, checking supply voltage, humidity and temperature. The DCS also distributes the clock and pre-trigger signals and provides the configuration interface to the TRAP chip. The coverage of a chamber with ROBs and numbering of the constituents is shown in figure 3.7.

Each MCM chip used for data acquisition is directly connected to 18 cathode pads of the chamber, thus covering 1/8 of a pad-row (144 channels). From these channels the induced

³The incident particle is supposed to travel very fast as compared to the drift-velocity of the electron clusters. Thus the latency between production of the clusters in different layers can be neglected as compared to the drift-time.

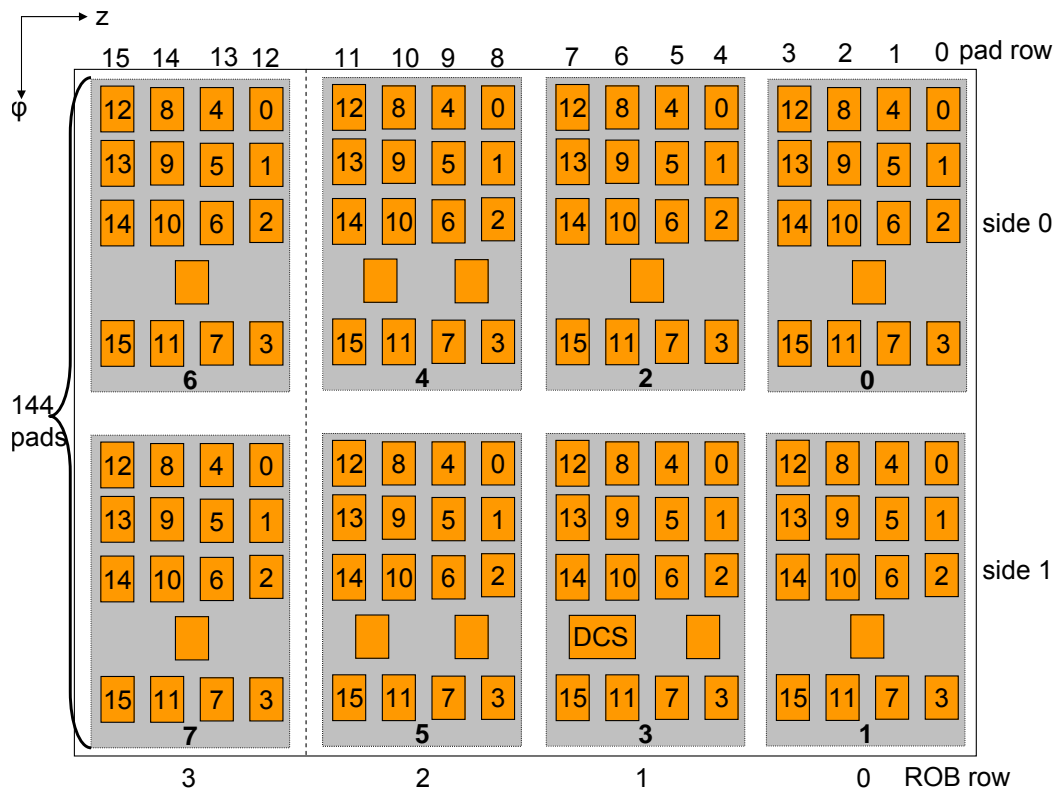


Figure 3.7: The coverage of a readout chamber with 16 ROBs. The orange squares on the ROBs symbolize the MCMs. The counting convention is as follows: Counting starts with 0 and numbers increase in negative z direction, along φ direction counter clockwise and with increasing radius [Gut06] [Ems06]

charge is acquired and given to the PASA, which forms a $120ns$ FWHM Gaussian-like signal with a tail. The conversion gain is $12mV/fC$. These 18 channels and additionally three channels from neighboring MCMs drive the inputs to 21 ADC (Analog Digital Converter) channels. In order to prevent deterioration in the y-position resolution, that is based upon charge-sharing between three channels, the signal of the outer analog channels from the chip border of the two neighboring MCMs, have to be included into the calculation of the actual MCM. The electronics, coming after the PASAs in the signal path, belongs to the digital part of the TRAP chip.

The ADCs are responsible for digitizing the analog signals. The possible conversion gain of the ADCs lies in the range from 2.0 to $2.8mV$ per ADC count. The sampling rate is chosen to be $10MHz$ and the sampled signal is turned to a digital word of 10 bit size. The ADCs are required to have low noise.

To each of the 21 ADC values, a variety of digital filters can be applied, one of which is the tail cancellation filter that was already mentioned and will be discussed in more detail in the signal processing chapter. The filter enlarges the 10 bit ADC words by two additional bits to reduce rounding errors. The filter output distributes the data independently to the event buffers for the later raw-data readout and to the preprocessor for tracklet calculation. In the event buffers, only 11 bit words can be stored. However, the filter output to the preprocessors provides the whole 12 bits, which enter the tracklet calculation. The filter can also be bypassed. Then, just the unfiltered data is put on the event buffers as raw-data. Since the preprocessors have no read access to the event buffers, they need the filter output to get data for tracklet calculation.

The event buffer consists of 21 independent memory-blocks of $64 * 11$ bits each. Thus they provide enough space for storing all the sampled (≥ 20 time bins) 10 bit ADC words. They will in the end be read out by the four CPUs of the MCM chip where the CPUs 0 to 2 will read out 5 event buffer channels each and the last 6 channels are assigned to CPU 3. For test purposes it is also possible for the CPUs to write on the event buffers.

The task of the preprocessor is to parameterize the track segments (tracklets) for 19 channels. The number of 21 channels is reduced to 19, because during preprocessing always three channels are involved in the position reconstruction by charge-sharing. The result is written to the central of the three channels, thus the outer two channels of the MCM chip (whose data comes from neighbored MCMs) are not assigned tracklet parameters. The preprocessing starts as soon as first data arrives. So the active time-period is directly coupled with drift-time.

Within each time bin, a maximum of four tracklets can be processed in parallel. If one assumes that a stiff track affects a maximum of two pads (not considering charge sharing) when traversing a chamber, a clear parameterization in every time bin is only possible if a maximum of four tracks passed the chamber without interfering. In each time-bin the signal of a maximum of 4 pads belongs to one track then (two central affected pads and two pads due to charge-sharing) and hence 4 tracks can be distinguished (18 pads). At normal multiplicity a situation of having more than four tracks in one MCM should happen very rarely (this is due to the choice of the pad granularity).

The fit parameters of each channel (fit sums) are stored in 19 Fit Register Files (FRF) providing 111 bits each. The fit parameters of a maximum of four chosen channels per time bin are updated. During the state, in which the chip prepares for a new data-acquisition cycle, also the FRF is cleared. In order to not disturb the sampling, the preprocessors also

work at a rate of 10MHz .

After the drift-time, when the fit-sums of the channels are filled, a maximum of four tracklet candidates have to be chosen and assigned to the four CPUs for further processing. A tracklet candidate is defined by the fit sums of two adjacent channels (following the idea that a stiff track crosses a maximum of two pads) and is indicated by the lower channel number. Only those channel pairs will be considered a tracklet candidate, whose number of hits (corresponding to the number of entries in the fit-sums) exceeds some threshold values. If there are more than four tracklet candidates on one MCM, the four with the greatest number of hits in both channels together are chosen. A sorting algorithm will then assign the parameters of the tracklet candidates to the four CPUs.

The subsequent processing by the CPUs contains the merging of the two parameter sets of the assigned tracklet candidate pair. Out of these parameters the slope and offset of the tracklet are calculated. The original idea was to also calculate some electron probability measure for the tracklet also, but currently it is under discussion whether this should only be done inside the GTU (where very stringent timing-limits might forbid this). Some corrections (Lorentz angle, tilted pads) are applied and transformations of the calculated quantities performed. Finally all the information is packed into a 32 bit word (tracklet-word) which is then to be sent to the GTU.

The signal path within an MCM is sketched in figure 3.8.

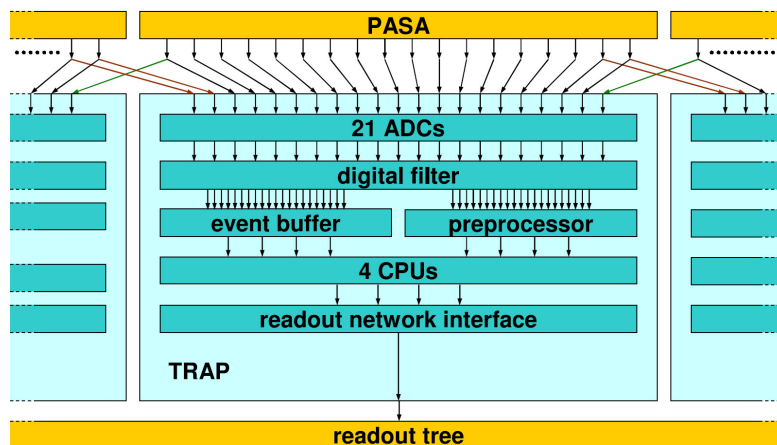


Figure 3.8: The signal path within a MCM [Gut06]

Each CPU has an instruction memory (IMEM) of $4096 * 30$ bits. A quad-ported memory of $1024 * 39$ bits serves as data memory (DMEM). Each data word has a width of $32 + 7$ bits with 7 redundancy bits, allowing for correcting 1 bit errors and detecting up to two bit errors, which improves the radiation resistance of the CPUs.

A CPU can only read the fit parameter registers that it was assigned to. In order to allow communication and fast data transfer between the CPUs, additional registers are available. The CPUs are running at 120MHz and thus are switched off during the TRAP preprocessing state in order to save power and to not disturb the digitization (running at 10MHz) with noise.

Besides the processing of the tracklet candidate data and sending the final tracklet word to the readout network interface of the TRAP, the CPUs are also used for reading data from

the event buffers, thus for raw-data readout. Here, zero suppression mechanisms (see below) can be applied. Therefore a variety of different programs are available, corresponding to the different tasks of the CPUs. An interrupt handler sets the program counter of the CPU to a start address, that is suitable for the current state of the chip.

The readout network interface of the TRAP merges the data stream of the four CPUs. As already mentioned, there are two modi with different requirements. The first one is to send the tracklet information to the GTU. Here, since timing is a severe issue, there is no handshaking between two chips and continuous clocking of the CPUs is required. All incoming data is buffered in FIFO (first in first out) memories. The second mode is raw-data readout, where timing is less tight but the amount of data is larger. The FIFOs are used for buffering the data from the CPUs and thus the CPUs can be switched off during readout (performed with handshaking) to save power.

3.5 The GTU

The GTU will combine the tracklet information of individual layers to tracks, involving tracklets of one TRD stack. Due to the tight time-limitations (less than $1.5\mu s$), the calculations need to be done in a highly parallel fashion with efficient algorithms to be used. Of special interest are the information about p_t and the electron probability, calculated for a merged track out of the tracklet parameters. As already on LTU level a cut on the tracklet- p_t was performed (tracklets with an estimated $p_t > 2.3 GeV/c$ are not sent) and the stacks are arranged cylindrically around the interaction vertex in a projective way, it is highly probable that a stiff track does not cross stack boundaries. Therefore only the tracklets of one stack are considered by one Track Matching Unit (TMU). Their total number ($18 * 5 = 90$) thus corresponds to the total number of stacks within the whole TRD. Each TMU obtains its data by 12 optical links from one stack, each of the links collecting the data from one half-chamber. The GTU expects tracklets that are pre-ordered according to their z-position (row-position). As the readout of the tracklets is performed in an ordered way through the readout tree, the GTU can start its calculations as soon as the first tracklets arrive.

The GTU projects the tracklets of one stack onto a middle plane and looks for tracklets of similar slope inside a spatial window of defined size. If at least four tracklets are found fulfilling the conditions, they are matched together and the track parameters are calculated, using position and slope of the tracklets. Also the local PID information of the tracklets is planned to be used, in order to get a handle on the particle's identity.

See figure 3.9 for a sketch on the GTU projection mechanism.

3.6 Zero Suppression

This short section about zero suppression is just for completeness, since the four CPUs on the TRAP chips are also used for raw-data readout of the event buffers. Each CPU is assigned to a defined set of channels for readout.

For each channel, a set of data comprising $20 * 10$ bit words is stored in its event buffer. However, not each data word contains a true signal but may just be a noisy fluctuation

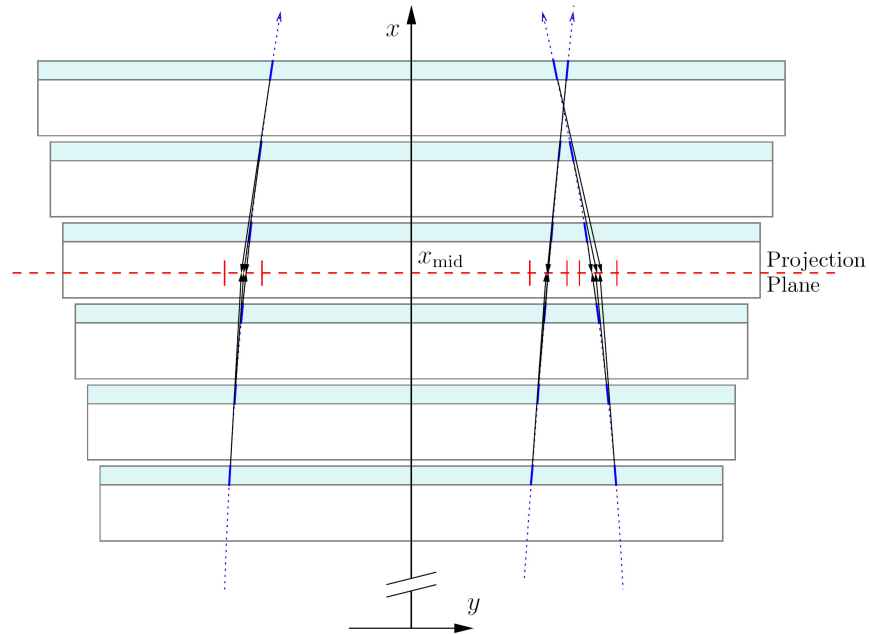


Figure 3.9: The GTU projection of the tracklets from a stack onto a middle plane [dC03]

Table 3.1: assignment of channels to the CPUs

CPU	channels
0	0 to 4
1	5 to 9
2	10 to 14
3	15 to 20

around the baseline. In order to compress the amount of raw-data already on the detector, such channels can be indicated and prevented from being read out (zero suppression). There are a number of criteria as listed in the table below (i denotes the channel number, j the time-bin number, e is the signal height in ADC-counts, where the baseline is subtracted).

Table 3.2: criteria for zero suppression

maximality	$\bar{Z}_j^{0,i} = 0$ if	$e_j^i \geq e_j^{i-1} \wedge e_j^i \geq e_j^{i+1}$
	$\bar{Z}_j^{0,i} = 1$	otherwise
triplet threshold	$\bar{Z}_j^{1,i} = 0$ if	$e_j^i + e_j^{i-1} + e_j^{i+1} \geq T^{triplet}$
	$\bar{Z}_j^{1,i} = 1$	otherwise
single threshold	$\bar{Z}_j^{2,i} = 0$ if	$e_j^i \geq T^{single}$
	$\bar{Z}_j^{2,i} = 1$	otherwise

It should be noted that in general all thresholds (here: T^{single} , $T^{triplet}$) are given for "naked" ADC values without baseline or pedestal. Hence the baseline must be subtracted from e_j^i first, before comparing it with thresholds. More on the problematic of baseline subtraction can be found in the chapter "Signal Creation and Signal Processing" in the section dealing with digital filters.

The indicator bit for a channel i at time-bin j is then given by the value of a lookup table (LUT), based upon a set of three criteria b :

$$\tilde{d}_j^i = LUT(\{\bar{Z}_j^{b,i}\}_{b \in \{0,1,2\}}). \quad (3.1)$$

There is also the possibility to take the neighbor channels into account. The final indicator bit is then built by:

$$d_j^i = \tilde{d}_j^{i-1} \wedge \tilde{d}_j^i \wedge \tilde{d}_j^{i+1}. \quad (3.2)$$

Without neighbor sensitivity, d_j^i is simply given by \tilde{d}_j^i .

4 The Trigger System

In the first part of this chapter a look at the ALICE trigger system is taken. Then the TRD front end electronics will be revisited in terms of the TRD trigger, e.g. timing limitations are mentioned, the different trigger issues discussed, the corresponding states of the TRAP chip investigated. The last part is concerned with the connection of the TRD trigger to the ALICE trigger system.

Additional information about the ALICE trigger system in general can be found in [ALI08] and in [ALI04]. Issues concerning the TRD trigger and its timing limitations are discussed for example in [ALI01], [Gut06] and [dC03].

4.1 The ALICE Trigger System

4.1.1 Overview

The anticipated interaction rate at LHC in PbPb mode amounts to $\approx 10^4$ collisions per second ($10k Hz$). Yet only about 100 events per second will contain interesting information (defined by having small impact parameters, low vertex displacement etc.). The idea behind the trigger is to select those interesting events and optimize the use of the data bandwidth of the Data Acquisition System (DAQ). This optimization includes some fair division of the bandwidth between observables with a higher trigger rate and rare events, because it should be made sure that rare events are not rejected because of occupied DAQ bandwidth. Moreover also the acquisition data rate of the High Level Trigger (HLT) system is limited. The HLT performs a software based detailed analysis of the event data to further compress and reduce the amount of data to be permanently stored. The challenge of the trigger system is to make optimal use of the component detectors, which are busy for quite different time scales. Moreover the trigger has to be adjusted to the different running modes since for example the counting rate for pp events is about 30 times smaller than for PbPb interactions.

There are several trigger levels whose signals are available at different time scales and in whose trigger decisions a different amount of information (e.g. due to different stages of the trigger calculation) is included. As the detectors need to be able to cope with the large multiplicities reached in PbPb mode, some of them expect a trigger input already $1.2\mu s$ after the interaction. Therefore the first level (L0) of the trigger arrives at the detectors at the expected time, containing information of the fastest trigger detectors only. As not all the early trigger inputs can be collected in such a short time, the fast trigger signal is split and a second level of the fast trigger (L1) is at the detectors after $6.5\mu s$, containing the remaining fast trigger inputs. The L0 trigger contains information from the Forward Multiplicity Detector (FMD). An event will be accepted at this stage if the multiplicity exceeds a certain threshold, if the interaction point is close to its expected position and

the forward backward distribution of charged particles corresponds to one created by a beam-beam interaction (e.g. to reject cosmic events). The subsequent L1 trigger may contain the TRD trigger decision based upon the reconstruction of e^+e^- -pairs with high p_t . Also information from the Zero Degree Calorimeter (ZDC) and the Muon Spectrometer are available at this time. Their trigger decisions consider centrality of the event, multiplicity and the number of muon pairs with high momentum.

Due to the high multiplicities, events with more than one central collision inside a detector will not be reconstructible. Therefore it is the task of the trigger to protect the detectors from pile-up of earlier or later events with the one under consideration. This is also called past-future protection. In case of a L1 accept trigger signal (L1A), the event is chosen to be further considered and the involved detectors are not cleared and reset. For past-future protection reasons the next level of the trigger (L2) will then only be issued after the slowest of the involved detectors (mostly the TPC) has finished its readout (in case of the TPC after $88\mu s$). During this time a bunch of analysis tasks could already be performed, such as applying cuts on the mass of μ -pairs, looking for J/Ψ signatures or inspecting the data from more detectors, which has become available meanwhile. A L2 trigger accept will then verify, that the event can be taken off the detectors for further analysis on the HLT computing farm. There, a detailed software analysis is performed using specified classes that were already tested on simulated events in AliRoot. It is believed that at this stage the events still contain much more information than needed. Thus the goal is to select a fraction of the data only for permanent storage and to compress it. Therefore a more sophisticated particle-tracking as well as accurate momentum determination is performed. PID cuts and region-of-interest limitations are aimed to reduce the amount of data considerably. In the end, the original input bandwidth to the HLT of about $20GB/s$ will be reduced to an output rate (input to the DAQ) of less than $1GB/s$. Also fake events shall be rejected by means of the HLT, thus improving the statistics of rare events. The DAQ finally writes the data to permanent storage with a bandwidth of $1.25GB/s$, which is distributed between the many different observables.

4.1.2 Trigger Logic

For each trigger level a number of trigger inputs are requested by the Central Trigger Processor (CTP) for finding its decision. Which inputs are expected for which level and from which detectors is defined by the trigger class. Each trigger class determines the logical conditions demanded from the input signals and by this is intended to optimize the use of the available detector systems for the observation of a given physical quantity. It defines the set of detectors that are needed for readout (detector cluster) and the requirements for past-future protection, which depends on the detector cluster. Also a scaling factor that is intended to be applied, can be set in the trigger class. This prevents a frequent event to be taken every time it is triggered in order to give rare events a sure place in the DAQ bandwidth, once they occur. In total there are 50 trigger classes demanding for 24 different trigger inputs for L0, 20 for L1 and 6 for L2. Each input can take one of three states: asserted, negated, not relevant. The inputs are coupled by a logical "And".

In trigger classes, for which TRD triggers or the readout of the TRD are required, the TRD pretrigger signal (see section TRD trigger) serves as its L0 input. By a valid L0 trigger signal it is assured that a proper event has been detected and that the TRD is in

ready state (ready for data acquisition).

The trigger output is returned as a trigger signal to the detectors. In addition with each successful L1 and L2 trigger, also some trigger data is submitted containing information about the event (orbit number, bunch crossing number), the trigger type (physics, software, calibration), the detector set to be read out and the active trigger classes. Moreover, information about the interaction is recorded (primary vertex position, classification of the collision a peripheral or semi-central). This can be used to detect pile-ups, since events, that occur out of time, may point to a different origin position due to a shift of the interaction vertex. Comparing this information with the interaction record, one could remove this event from the data set (for example in cases, when pile-ups are allowed to a certain extent (see below)). So called "scalers" count the number of occurrences for a trigger input for each trigger class and the number of events passing the different trigger levels. This can be used to compare the counting rate of the trigger with the rate expected from the total cross section of the physical quantity under consideration.

Past-Future Protection

Since the LHC luminosity will be very high, pile-up events, that spoil a selected event currently being read out, might occur very frequently. The past-future protection must therefore reject an event under certain conditions. These conditions are influenced for example by the classification of the event into peripheral or semi-central. In case of a semi-central event in PbPb mode, another event taking place within a certain time window which depends on the readout detector cluster, should be rejected and not read out, since it would increase the occupancy inside the detectors beyond the limit, for which both events would be reconstructible. The choice of the time window is driven by the readout time of the slowest detector in the cluster and is the time, within which another event would spoil the one currently read out in this detector. This already shows that the time-future protection needs to incorporate different strategies, depending at least on the detector cluster, the centrality of the interaction, the run mode and the beam luminosity.

As an example, the TPC sensitive time window amounts to $\pm 88\mu s$ corresponding to its drift time of $88\mu s$. A possible past-future protection strategy during PbPb run for detector clusters containing the TPC (which is the slowest of all detectors), could allow up to four additional peripheral events but no additional semi-central event inside the TPC, within a time window of $176\mu s$, which is centered at the starting time of the current event. This guarantees, that no further event is still occupying the drift-region when the event under consideration starts and that this event may only be spoiled by another one, if the reconstruction can still distinguish between the different tracks.

A different approach is needed however in case of pp mode. Here pile-up will almost be certain, due to increased luminosity. Yet, the multiplicities will be much lower than during PbPb run and thus more pile-up of events can be accepted. Here, the fast-future-protection must make sure that all detectors can perform a sensible readout. This takes into account that for inner detectors like the ITS, a pile-up of events is more serious than for outer detectors, since the cluster density inside a detector increases with decreasing radius (neglecting that the secondary charged particle density might increase with radius). Two different time-windows could be applied, e.g. $\pm 10\mu s$ for ITS and $\pm 88\mu s$ for TPC.

4.2 The TRD Trigger

4.2.1 Requirements

The investigation of properties of the QGP requires to take into consideration rare probes with small cross sections ($100\mu b$) and low production probabilities per collision ($\approx 10^{-5}$). Therefore a trigger is needed to enhance the number of read out events that contain such rare signals. Of special interest are electromagnetic probes, since they are not affected by strong interaction and thus allow a direct view onto the interaction process. However, their production cross section is very small. Additionally, electromagnetic decay products of heavy vector mesons (e.g. J/Ψ , Υ) yield information about the conditions in a QGP.

A trigger is also needed in order to obtain differential distributions, expressing the dependence of an observable on p_t or on centrality. Since the abundance of resonances at large p_t is suppressed (and therefore also the number of electro magnetic decay products with large p_t) and since the probability for an interesting signal to be produced decreases at larger impact parameters (due to a smaller reaction volume), the statistics of differential distributions crucially improves by applying a trigger.

However a more technical argument in favor of a TRD trigger is the limited bandwidth of the DAQ system for high- p_t electrons because it must be shared among the different observables. Therefore only interesting events should be selected.

4.2.2 Purposes

From the above requirements the purposes of the trigger can be derived. Some general expectations are, that the trigger works with a high and uniform efficiency for the whole acceptance and p_t range, for which the TRD was designed. Also at the highest multiplicities of $dN_{ch}/dy = 8000$, the system must work well, although it is optimized for lower multiplicities.

In detail, the TRD trigger is supposed to find and select tracks with $p_t > 3GeV/c$ and allow for an efficient separation of electrons from pions. Relying on these capabilities, correlation quantities, like the invariant mass of track pairs or the multiplicity in special spatial regions, are computed.

Due to the application of a TRD trigger, the production rates of Υ and of J/Ψ at large p_t can be studied as well as the dilepton continuum in the invariant mass range between 4 to $9GeV/c^2$. Also jet production at energies beyond $100GeV$ is in the prospect of studies and rare probes can be correlated event wise with the information from other central barrel detectors.

4.2.3 Realization

As the TRD trigger decision influences whether the TPC opens its gating grid for event readout, the calculation has to be accomplished in a very short time as compared to the drift time of the TPC, in order to not cut its available track lengths too much. As the TPC drift time amounts to $88\mu s$, the TRD trigger is given a decision time of $6\mu s$. During this time a fast tracking of up to 20000 charged particles in the TRD acceptance has to be performed. As it is required to pick rare events that have probabilities down to 10^{-5} per

collision, this task can only be fulfilled by a highly parallel computation. As it was already outlined in the section about the Front End Electronics (FEE) of the TRD, the separation of the detector into six layers with a resulting drift time of $2\mu s$ is exploited, by fitting to the hits of one layer a straight line which is called tracklet. This is done independently and in parallel in all detector chambers by the on-chamber electronics. From the obtained fit parameters an estimate on p_t is calculated, assuming that all tracks originate from the primary vertex. Only the data of tracklets that are stiff enough is sent to the GTU, which combines at least four tracklets to a track and performs a cut on its transverse momentum ($p_t \geq 2.7 GeV/c$). The detection of electron tracks embedded into a background of many pions is performed by means of the total energy loss of the particle, involving the Transition Radiation emitted only by electrons. The number of positive and negative tracks within a selected area can be counted and two-particle correlation quantities (e.g. invariant mass) can be calculated. The final result is then sent to the CTP.

4.2.4 The TRD Trigger States

There are a number of different states of the TRAP chip electronics, between which there are transitions, steered by external trigger signals, commands and internal timers. The states and transitions are controlled by the Global State Machine (GSM). The TRD trigger states are shown in figure 4.1, the TRD trigger timing in figure 4.2. After a reset or a low power command, the TRAP chip enters a low power mode. All the components are disabled in this state and only the configuration interface is clocked. Leaving the low power state, the TRAP enters the clear state. This is the starting point of any readout cycle. The ADCs are enabled and clocked together with the digital filters. The preprocessors are reset and the CPUs are started and clocked shortly for clearing their registers. After the clearing procedure has finished, the chip stays in the following state waiting for the pretrigger signal to arrive and wake up the TRAP. Once the pretrigger signal reached the chip, the preprocessors are clocked during the drift time to be able to calculate from the sampled and digitized cluster information the necessary fit sum updates. This is done in parallel to data acquisition, hence, sampling and digitization of the next data set is already ongoing, while the previous data sample is still preprocessed. During preprocessing the CPUs are turned off to save power and not disturb the ADCs and preprocessors, as the CPUs run at a higher frequency (CPU: 120MHz, preprocessor: 10MHz). At the transition to the preprocessing state also a timer was started, expecting a L0 trigger signal after a defined time. Should the L0 signal not occur, this is treated as a L0 reject (L0R) and the whole data acquisition sequence is aborted returning to the clear state.

If a L0 signal occurs (L0 accept, L0A), after the drift time of $2\mu s$ and after the end of digitization and preprocessing ($2.55\mu s$), the chip enters the processing mode where the CPUs are clocked. The digital noise that is produced here does neither affect the TRD, as the data is already stored, nor does it do harm to the TPC, as it has not started digitization yet (waits for the L1 decision before opening the grid). Up to four tracklet candidates are assigned to the four CPUs for further calculation of the necessary 32 bit tracklet words, which then are sent to the GTU through the readout tree and via optical fibers (two per chamber) in the tracklet transmission state. The whole data shipping has to be accomplished $4.5\mu s$ after the pretrigger signal arrived (the first tracklet will be sent after $\approx 4.3\mu s$). Each MCM can provide a maximum of four tracklet words, however a

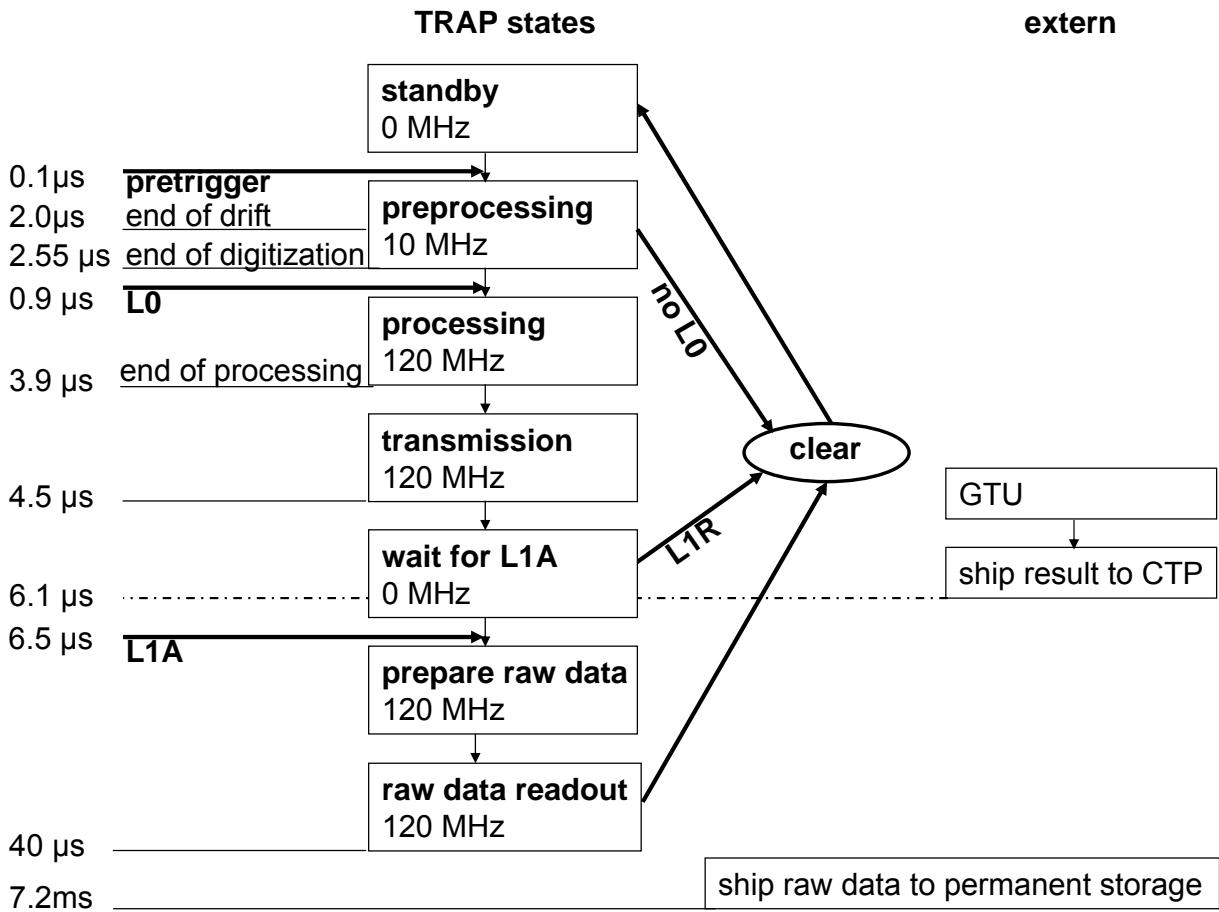


Figure 4.1: The TRD trigger modes and their timing. For the TRAP states the clocking frequency is given. Note that the L0 trigger signal is expected during preprocessing, at 0.9 microseconds.

maximum of 40 tracklets are accepted per chamber (incorporating between 96 and 128 MCMs). Excess tracklets are ignored. Since the tracklet transmission is done in a way, defined by the readout tree (tracklets arrive ordered in increasing pad row number and then sorted according to increasing y coordinate), the GTU can already start its calculations once the first tracklet arrives. After ending with processing, the CPUs are switched off again. After $6.5\mu s$ the GTU has to have sent its results to the CTP and the CTP its decision to the detectors. As the shipping of data to the CTP and the distribution of the trigger from the CTP to the detectors takes about $500ns$, the GTU has about $1.3\mu s$ for the global tracking (assuming that the last tracklet arrives at the GTU after $4.3\mu s$). Another timer, which has been started at the transition to the preprocessing state, awaits the L1 accept trigger signal, which also depends on the results of the GTU calculations. If a L1 reject occurs, all buffers are emptied and the TRAP returns to clear state. In case of an accept however, the CPUs are started again in the raw data preparation state and are set for raw data readout. Then the event buffers are read out by the CPUs via the optical fiber links and the data is fed into the readout network. After completion, the TRAP returns to clear state, preparing for the next data acquisition cycle. The event raw data is now stored in event buffers that are part of the GTU and they are only shipped off the detector in case of a L2 trigger accept. In case of a L2 reject the buffers are cleared.

In case of a L1A, the TRD will not be able to accept any other event (signaled by a TRD BUSY) until the raw data is read out from the TRAP event buffers by the CPUs. This can take up to $40\mu s$. However, the overall dead time of a detector cluster containing the TPC is determined by the TPC drift time of $88\mu s$ and thus the TRD dead time is not crucial. It is important that the TRD derives its trigger decision before the TPC gate opening after about $6.5\mu s$ after the pretrigger. The pretrigger itself is expected at the TRD Point Of Presence (POP) at $100ns$ after the interaction, from where it is spread to all the MCMs to wake them up. This takes another $100ns$, so in total around 10% of the TRD sampling time is lost due to the pretrigger latency. However, the first time bins contain ionization clusters from the amplification region which drift towards the anode wire from two sides and produce on average a signal of almost twice the height as compared to the average signal induced by clusters from the drift region. Using these clusters from the amplification region would spoil the e/π separation, which is based on the mean charge per cluster deposited by the particle (therefore especially the later time bins are of importance, containing the TR clusters, formed at the entrance to the drift volume). Hence, hits from this time region are omitted nevertheless for the tracklet calculation and the trigger decision. On the other hand, using clusters from the amplification region enlarges the lever arm for the track fit and improves the offline reconstruction performance. Therefore, the POP is chosen such, that the pretrigger latency and the cut on the sampling time are as small as possible.

4.3 Connection Between the TRD and the ALICE Trigger System

The TRD pretrigger is a trigger signal that is TRD specific and is not routed via the CTP. It is needed to wake up the TRD and allows the TRD digital components to be in low power state if there is no event to be processed. In order to wake up the TRD in time,

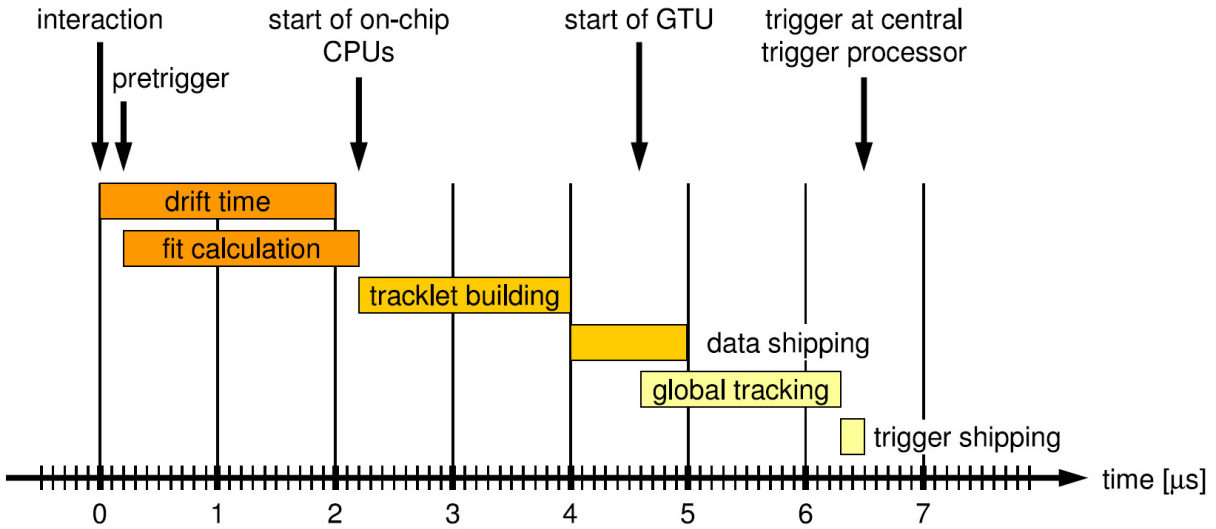


Figure 4.2: The TRD trigger timing ([Gut06])

the pretrigger has to be issued before the L0 trigger signal from the CTP. So the signal is derived from a minimum bias trigger detector and transmitted to the TRD directly with minimum latency. A second copy of the signal is routed to the CTP and contributes there as the L0 input from the TRD. By this input, the CTP assumes that the TRD is in ready state. However, as the pretrigger has been split before the TRD, the CTP does not know if something went wrong with the distribution of the pretrigger to the TRD, its spread to the MCMs or if the switch-on of the FEE has really been successful. This might lead to an inefficiency of trigger classes needing the TRD for readout or needing a higher level trigger decision by the TRD, since the event would be spoiled. At least, the event could be rejected at L1 time after a couple of μs , if the TRD does not send its trigger input. This would prevent the TPC from opening its gate and the detectors from a dead time in the order of $80\mu s$.

There are two cases in which the minimum bias trigger should not lead to a valid pretrigger. If another event has occurred less than $2\mu s$ before (corresponding to the TRD drift time), then the drift volume would be spoiled by clusters from that event, although the TRD does not necessarily read it out. So, although the TRD electronics announces to be idle, the new event must not be read out by the detectors (hence for example the TRD readout electronics must not be started), since the drift volume is not cleared (past protection). In order to ensure this, each minimum bias signal starts another signal with a decay time complying with the TRD drift time. In case a pretrigger arrives at the TRD meeting such a signal (TRD DIRTY), it will not wake up the TRD. The TRD DIRTY state can be reconstructed by the CTP using the copy of the minimum bias signal.

The second case when a minimum bias trigger cannot lead to a valid pretrigger happens, if the TRD electronics is busy. This is signaled by a TRD BUSY state. It is started in case of a valid pretrigger and cleared if an event is rejected (no L0 or L1R) or after the raw data readout upon L1A has finished. Note, that even if the drift volume is cleared, the TRD cannot accept any other event until the raw data of the previous event is shipped off the FEE, since the CPUs are used for the tracklet processing as well as for the raw data

readout. Therefore, the total dead time of the TRD in case of L0 and L1A amounts to about $40\mu\text{s}$.

A further problem concerning past-future protection can occur, if the TRD is currently reading out an event from the drift volume when a new event occurs (within $2\mu\text{s}$ after the first event). The clusters read out from this time on will be spoiled by the new event and must not be considered. Since the expenditure to separate the clusters according to their arrival time at the readout electronics is too large, the whole event needs to be rejected. This is only possible at L1 time ($6.5\mu\text{s}$) by a L1R. The CTP controls this future protection issue by a decay signal ($2\mu\text{s}$ decay time), that starts once the copy of a valid pretrigger arrives (no TRD DIRTY or TRD BUSY encountered). If another event occurs once the drift time for the current one is over, this does not disturb the further processing of the data, since data acquisition finishes with drift time. See figure 4.3 for a summary of the past-future protection steps on pretrigger level.

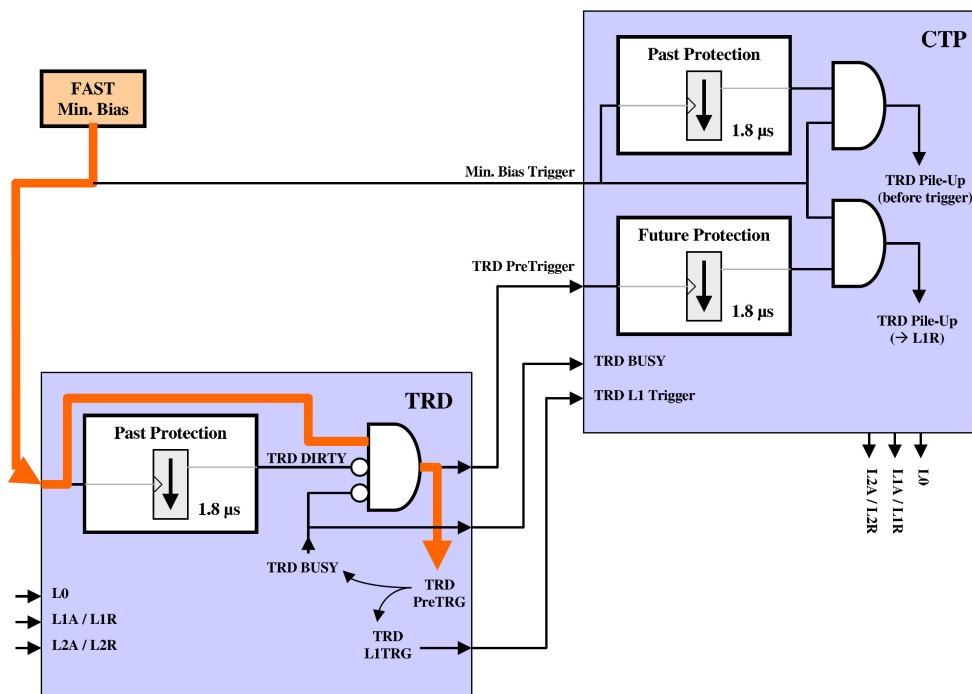


Figure 4.3: Past-future protection on pretrigger level ([ALI01])

In case that a minimum bias trigger does not encounter a TRD DIRTY nor a TRD BUSY, it will become a valid pretrigger waking up the TRD and starting the TRD state machine. The valid pretrigger is forwarded to the CTP where it serves as a valid L0 trigger input that is required for all trigger classes containing the TRD in their detector clusters.

Once a valid pretrigger occurred, the TRD expects a L0 trigger in an appropriate time slot. If no such trigger signal arrives, this causes an abort of the current data acquisition. If the L0 arrives at a different time (maybe caused by a trigger class including the TRD in its detector cluster but without requiring a valid TRD pretrigger as L0 input) error flags are set and the trigger is ignored.

In case a L0 trigger arrives at the right time, the TRD determines its trigger decision and

sends it to the CTP. There the TRD trigger result participates in the L1 trigger decision, depending on the implementation of the trigger class.

In any case the TRD can be forced to abort its event processing only from the outside at L0 and L1 time. It will never abort by itself.

As the past future protection logic is also needed for the TPC (with a drift time of $88\mu s$), the corresponding methods have to be part of the CTP to be able to adjust the signal decay times to the needs of the TPC. This also ensures, that all events can be counted at a central location and a proper cross section calculation can be performed. Otherwise, if the CTP did not know about rejected events by the TRD because of past-protection, this would lead to a biased counting and a wrong estimation of rates. In case a TRD pile-up happens before the L0 trigger was issued, the CTP could also make the decision of not sending a L0. This would have the advantage, that pile-up events were rejected during drift time, even before the power consuming CPUs were started.

In total, the TRD delivers to the trigger system its TRD BUSY state, TRD trigger bits (one bit for each trigger) and a bit mask of $2*36$ bits, marking the region of interest (sector and hemisphere). The TRD BUSY is already included in the TRD pretrigger and not used as input for normal trigger operation since this would prevent any L0 trigger (the TRD BUSY is issued upon each valid pretrigger, hence before the L0 trigger, to which the valid pretrigger serves as input. Note that all inputs are connected by logical "And"). However the CTP needs the knowledge about TRD BUSY in order to count properly the number of events during and after the TRD dead time.

The TRD receives a L0 (which serves as accept; no L0 at given time is interpreted as reject), L1R or L1A and L2R or L2A. The trigger signals arrive at the TRD's point of presence (POP) and are distributed within the TRD from there on.

5 Signal Creation and Signal Processing

In this chapter the creation of signals inside the TRD and the different processing steps are discussed. The first part however deals with the interaction of charged particle with matter which gives rise to three basic processes used by particle detectors: ionisation/excitation of medium atoms, emission of Cherenkov light and Transition Radiation. The second part gives an overview over the subsequent signal processing within the detector.

More physical background about signal creation and particle detectors can be found in [Kle84], [Kol], [FHV05], [Ene03], [Spa04], [Pos04], [Phy06]. An introduction to diffusion can be found in [Dem99]. A basic course on stochastic is presented in [Naw94]. Issues about signal processing in general can be found in [Jae02]. TRD related topics about signal processing are put together in [ALI01], [Gut06]. The digital filters are described in [Gut06] and [Gut02].

5.1 Interaction of Charged Particles with Matter

In this section a phenomenological overview over the possible and in case of the TRD relevant processes, that occur when a charged particle traverses matter, will be given. These processes are mostly used by detectors to identify a particle's track, momentum and its identity and lead to a decrease of the particle's energy. The electromagnetic interaction expresses itself by three processes: ionization/excitation, Cherenkov light and Transition Radiation.

5.1.1 Physics Overview

The conditions for the onset of these processes can be investigated by a simple picture reducing the medium to its dielectric number $\epsilon = \epsilon_1 + i \cdot \epsilon_2$ and its smallest excitation energy $\hbar\omega_0$.

Assuming a charged particle of mass M and velocity $\vec{v} = \vec{\beta} \cdot c$ traveling through a medium with refraction number $n = n_1 - i \cdot n_2$ or dielectric number $\epsilon = \epsilon_1 + i \cdot \epsilon_2$ with $\epsilon_1 = n_1^2$, the electromagnetic interaction is mediated by the emission of a photon with energy $E = \hbar\omega$ and momentum $\vec{p} = \hbar \cdot \vec{k}$. In order to express the photon energy by its momentum and the particle's velocity, the following three 4-vectors are introduced: $p = \begin{pmatrix} E/c \\ \vec{p} \end{pmatrix}$ denotes the 4-momentum of the particle before interaction, $p' = \begin{pmatrix} E'/c \\ \vec{p}' \end{pmatrix}$ the 4-momentum of the particle after interaction and $p_\gamma = \begin{pmatrix} \hbar\omega/c \\ \hbar\vec{k} \end{pmatrix}$ the 4-momentum of the produced photon. As $p_\gamma^2 = m_\gamma^2 = 0$, this yields the dispersion relation in vacuum, $\frac{\omega^2}{c^2} = k^2$. Since $p_\gamma = p - p'$ this

yields

$$\begin{aligned}
 p'^2 &= (p - p_\gamma)^2 \\
 M^2 c^2 &= M^2 c^2 - 2pp_\gamma \\
 2pp_\gamma &= 0 \\
 2\left(\frac{\hbar\omega E}{c^2} - \hbar\vec{p}\vec{k}\right) &= 0
 \end{aligned}$$

$$\begin{aligned}
 \omega &= \vec{p}\vec{k} \frac{c^2}{E} \\
 &= p \cdot k \cdot \cos \theta \cdot \frac{c^2}{E} \\
 &= v \cdot k \cdot \cos \theta \cdot \frac{\gamma M c^2}{E} \\
 &= v \cdot k \cdot \cos \theta
 \end{aligned}$$

where $p = \gamma M v$ and $E = \gamma M c^2$ was used and θ is the angle between the incident direction of the charged particle and the direction of emission of the photon. Thus, the photon frequency can be expressed by $\omega = v \cdot k \cdot \cos \theta$. With the dispersion relation in medium $\omega^2 = \frac{k^2 c'^2}{\epsilon}$, where $c' = \frac{c}{\sqrt{\epsilon}}$ was inserted as the light speed in medium, this allows to derive the following equation:

$$\frac{v}{c} \sqrt{\epsilon} \cos \theta = 1$$

For optically very thin material ($n_1 \approx n$, $n - 1 \ll 1$) the complex refraction number can be expressed as

$$n = 1 + \frac{n_{dipole} e^2}{2\epsilon_0 m (\omega_0^2 - \omega^2 + i\omega\gamma)}$$

The picture used here is, that the atomic electrons oscillate around their positions and have a resonance frequency ω_0 and a damping coefficient γ . The density of the dipoles is denoted by n_{dipole} . The photon emitted by the interaction acts as an electromagnetic wave with frequency ω , which enforces the oscillation of the atomic electrons. The resonance frequency ω_0 corresponds to the (first) excitation energy $\hbar\omega_0$ and thus the photons can be absorbed by exciting the atoms, if they have the right energy¹. As a primary electromagnetic wave with electric field strength $\vec{E}_p = \vec{E}_0 e^{i(\omega t - \vec{k}\vec{x})}$ passes a medium, it induces a dipole oscillation of the electrons against the atomic trunk, which in turn leads to the radiation of e.m. waves of the same frequency. By cutting the material into a discrete number of layers k , the individual e.m. waves \vec{E}_k are characterized by a layer depending phase shift (the finite velocity of the primary e.m. wave affects the layer at increasing times). The superposition

¹Due to the energy time uncertainty principle $\Delta E \Delta \tau \leq \frac{\hbar}{2}$ and the finite lifetime τ of an excited state (the excited electron is described by the model of a damped oscillator, losing energy by irradiating e.m. waves of Lorentz shaped power spectrum. The lifetime of the state is determined by the damping constant), the energy level has a natural width which is additionally enlarged by the interactions between the atoms of the medium and other effects. Thus the photon can be absorbed, although it has not exactly the theoretical excitation energy.

of the primary wave with all the secondary waves at some observer position, yields an overall field strength for the resulting wave: $\vec{E} = \vec{E}_p + \sum_k \vec{E}_k$. Because of the phase shift, the resulting e.m. wave arrives later than an e.m. wave traveling solely through vacuum. This can be described by a reduction of the velocity of light in matter, $c' = \frac{c}{n}$, and a modified wavelength $\lambda' = \frac{\lambda}{n}$ because the frequency $\frac{\omega}{2\pi} = \frac{c}{\lambda}$ is not changed. Therefore, if the primary e.m. wave travels through a medium of thickness Δz in z direction and the observer is situated in a point z outside the medium, the resulting wave can be described effectively by introducing the time shift $\Delta t = t' - t = \Delta z(\frac{1}{c'} - \frac{1}{c}) = \frac{\Delta z}{c}(n-1)$, that expresses the additional time the wave needs, for passing through the medium. Because the wave is observed outside the medium, $k_z = k = \frac{\omega}{c}$ there and the wave can be described by

$$\begin{aligned} \vec{E}(z) &= \vec{E}_0 e^{i[\omega(t-\Delta t)-kz]} &&= \vec{E}_0 e^{i\omega(t-(n-1)\Delta z/c-z/c)} \\ &= \vec{E}_0 e^{i\omega(t-z/c)} \cdot e^{-i\omega(n-1)\Delta z/c} \\ &\approx \vec{E}_0 e^{i\omega(t-z/c)} - i\omega(n-1)\Delta z/c \cdot \vec{E}_0 e^{i\omega(t-z/c)} \\ &= \vec{E}_p + \sum_k \vec{E}_k \end{aligned}$$

where $n-1 \ll 1$ and $e^{-i\phi} \approx 1 - i\phi$ for small ϕ was used. Especially for gases (in the TRD charged particles travel through a medium of Xe/CO₂ gas) the condition for optically thin media with a small dipole density n_{dipole} , $n-1 \ll 1$, is usually fulfilled. The refraction number n is then obtained by comparing the above expression for the electrical field with the results of a microscopic model, which integrates over the electrical field strengths of the e.m. waves, that were emitted by the induced oscillations of the medium dipoles, at the observer's position. The refraction number can be split into a real and an imaginary part, $n = n_1 - i \cdot n_2$, with $\epsilon \approx n^2$ for $n_2 \approx 0$ and $n \approx n_1$.

$$\begin{aligned} n_1 &= 1 + \frac{n_{dipole} e^2}{2\epsilon_0 m} \frac{\omega_0^2 - \omega^2}{(\omega_0^2 - \omega^2)^2 + \omega^2 \gamma^2} \\ n_2 &= \frac{n_{dipole} e^2}{2\epsilon_0 m} \frac{\omega \gamma}{(\omega_0^2 - \omega^2)^2 + \omega^2 \gamma^2} \end{aligned}$$

For the field strength of an e.m. wave traveling along z through a medium of width Δz with refraction number n (depending on the frequency of the wave) one obtains:

$$\begin{aligned} \vec{E}(z) &= \vec{E}_0 e^{i\omega(t-(n-1)\frac{\Delta z}{c}-\frac{z}{c})} \\ &= \vec{E}_0 e^{i(\omega t - k_0 z)} \cdot e^{-i\omega(n_1-1)\frac{\Delta z}{c}} \cdot e^{-\omega n_2 \frac{\Delta z}{c}}. \end{aligned}$$

$k_0 = \frac{\omega}{c}$ was used. From this it can be seen that the real part of n introduces a phase retardation whereas the imaginary part is responsible for absorption.

Depending on the photon energy $\hbar\omega$ one can distinguish different cases:

- If the photon energy is significantly smaller than the excitation energy of the medium atoms $\hbar\omega \ll \hbar\omega_0$, n_2 becomes small and thus ϵ is a real number. Due to (5.1.1), $v = \frac{c}{\sqrt{\epsilon \cos \theta}} \geq \frac{c}{\sqrt{\epsilon}}$ since $\cos \theta \geq 1$. This is the Cherenkov threshold. Since $n_1 > 1$ and

$\epsilon_1 > 1$, the threshold can be exceeded, if the velocity of the particle is larger than the speed of light in the medium. In this case, the photon is emitted as a real photon. The irradiated light is called Cherenkov light.

- In the absorption region, where $\hbar\omega \geq \hbar\omega_0$, one obtains for the refraction numbers $n_1 < 1$ and $n_2 > 0$ and thus the dielectric number ϵ becomes complex. In this region (between approximately $2eV$ to $5keV$), the photon is virtual and mediates the interaction between the charged particle and the medium. As a consequence, the atoms of the medium are excited or ionized by the absorption of the virtual photon and the charged particle loses energy.
- In the X-ray region ($\hbar\omega \geq 5keV$), where $\hbar\omega \ll \hbar\omega_0$, absorption becomes negligible ($n_2 \ll 1$). Since $n_1 < 1$ also $\epsilon_1 < 1$, thus the Cherenkov threshold exceeds the speed of light in vacuum and $v \geq \frac{c}{\sqrt{\epsilon}} > c$ cannot be fulfilled any more. Therefore no Cherenkov light is emitted but in case of discontinuities of the dielectric number, Transition Radiation (TR) can be emitted instead.

5.1.2 Properties of the Electromagnetic Processes

In the following, some properties of the three above mentioned processes are investigated by applying an example. These observations can also explain some properties on the development of the mean energy loss with $\beta\gamma$. However, the Bethe Bloch formula will not be derived here.

In the example, the dielectric number of the medium, ϵ , is used to denote in the course of the discussion the real part ϵ_1 .

If a charged particle moves along the z-direction with velocity $\vec{v} = (0, 0, v)$ in a medium and an observer is situated at $(0, y, z)$ also in the medium, then the wave vector of the e.m. wave detected by the observer is given by $\vec{k}' = (0, k'_y, k'_z)$. Using $\vec{v} \cdot \vec{k}' = vk \cos \theta = \omega = vk'_z$ and the dispersion relation of the e.m. wave in the medium, $\omega^2 = \frac{\vec{k}'^2 c^2}{\epsilon}$ this yields $k'_y = \frac{\omega^2 \epsilon}{c^2} - \frac{\omega^2}{v^2}$ and thus

$$k'_y = \frac{\omega}{v} \sqrt{\frac{v^2}{c^2} \epsilon - 1}.$$

The phase velocity of light in the medium is given by $c' = \frac{c}{\sqrt{\epsilon}}$. By defining $\beta' := \frac{v}{c'}$ and $\gamma' := \frac{1}{\sqrt{1-\beta'^2}}$, k'_y can be expressed by

$$k'_y = \frac{\omega}{v} \sqrt{\beta'^2 - 1}.$$

Now there are two cases:

- If $\beta' > 1$, meaning that the particle velocity exceeds the velocity of light in the medium, k'_y is a real number leading to the emission of a real e.m. wave $\sim e^{i(\vec{k}'\vec{r}-\omega t)}$. This case corresponds to the irradiation of Cherenkov light.

- In the second case, when $\beta' < 1$, $k'_y = i\frac{\omega}{v}\sqrt{1-\beta'^2}$ becomes purely complex. Inserting this yields for the wave phase factor:

$$\begin{aligned} e^{i(\vec{k}'r-\omega t)} &= e^{-i\omega t} e^{i(k'_y y + k'_z z)} \\ &= e^{-i\omega t} e^{i\frac{\omega}{v}z} e^{(iy)(i\frac{\omega}{v}\sqrt{1-\beta'^2})} \\ &= e^{-i\omega t} e^{i\frac{\omega}{v}z} e^{-\frac{y}{y_0}} \end{aligned}$$

with $y_0 = \frac{v}{\omega\sqrt{1-\beta'^2}} = \gamma'\beta'\frac{c'}{\omega}$. By $k' = \frac{\omega}{c}\sqrt{\epsilon}$ the range of the damped transversal component of the electrical field can be expressed as

$$y_0 = \frac{\gamma'\beta'}{k'}.$$

By further arithmetics and using the wave vector in vacuum, $k = \frac{\omega}{c}$, the range can also be brought to the form

$$\begin{aligned} y_0 &= \frac{\beta\sqrt{\epsilon}\frac{1}{\sqrt{1-\beta^2\epsilon}}}{k\sqrt{\epsilon}} \\ &= \frac{\beta}{k} \frac{1}{\sqrt{\frac{1}{\gamma^2} + \beta^2(1-\epsilon)}}. \end{aligned}$$

$\beta' < 1$ can occur for two different ϵ ranges:

- $\epsilon > 1$ corresponds to $n_1 > 1$ and thus implies $\omega < \omega_0$ meaning that the energy of the e.m. wave is below the excitation energy of the medium atoms and the medium is transparent. From $\beta' < 1$ it follows that $v < \frac{c}{\sqrt{\epsilon}}$. In this case the Cherenkov threshold can still be reached by increasing v toward c' , resulting in $\beta' \rightarrow 1$. That leads to an increase of the range y_0 to infinity and at the Cherenkov threshold, when $v \geq c'$, an e.m. wave is released.
- The case $\epsilon < 1$ ($n_1 < 1$) occurs if $\omega > \omega_0$. The photons have enough energy to excite or ionize the atoms and the medium becomes absorbing. Here, $\beta' < 1$ is urged by $c' > c$ ². The range of the electrical field y_0 increases proportional to $\beta'\gamma'$. This also leads to an increase of the energy loss of the primary charged particle due to the relativistic expansion of its electric field. Hereby more electrons (of nearby atoms) are affected and the probability of photon absorption increases.

However, the value of y_0 reaches a plateau (the denominator never becomes 0 for $\epsilon < 1$). Classically, the relativistic expansion of the electric field is stopped once

²Although the phase velocity in the medium, c' , is larger than c , this is not a contradiction. As it was mentioned in the previous section, the photon in the absorption region is virtual and can not spread physical information. In the region where $\hbar\omega \gg \hbar\omega_0$, still $\epsilon < 1$ holds, but again, no real (Cherenkov) photon is emitted. Since the dielectric number $\epsilon = \epsilon(\omega)$ is a function of ω , also the phase velocity is. The relevant velocity for information spread is not the phase velocity but the group velocity of a wave package (superposition of even waves of different frequencies), which is always smaller than the speed of light. The wave package is used to describe the quantum mechanical probability density for localized states such as particles, carrying the information.

its range is comparable to the mean distance between atoms. Their electrons are rearranged in a way, that the electric field is screened and deeper lying atoms don't get in touch with the field any more. This impacts also on the mean energy loss, which saturates at the so called Fermi Plateau. The $\langle dE/dx \rangle$ at the plateau depends on the density of the medium. It is much smaller in solid matter with high density and an effective screening as compared to the value in gases. Rewriting the range as $y_0 = \frac{1}{k} \frac{1}{\sqrt{\frac{1}{(\beta\gamma)^2} + (1-\epsilon)}}$ shows, that for large $\beta\gamma$ the range approaches the plateau value, $y_0 \rightarrow y_{0,max} = \frac{1}{k\sqrt{1-\epsilon}}$ (positive branch of the function in figure 5.1). Differentiating the range yields: $\frac{dy_0}{d(\beta\gamma)} = \frac{1}{k(1+(1-\epsilon)x^2)^{3/2}} > 0$ ($\epsilon < 1$). Therefore, y_0 approaches the plateau from beneath. Already at $\beta\gamma \sim \frac{1}{\sqrt{1-\epsilon}}$, the value of y_0 is $\frac{1}{\sqrt{2}} \cdot y_{0,max}$. It is $1 - \epsilon \approx 1 - n^2$. In the absorption area, where $\omega \geq \omega_0$, one can set $n = 1 + x$ with $x < 0$ and $|x| \ll 1$, hence $n^2 = 1 + 2x + x^2 \approx 1 + 2x$. Therefore $1 - \epsilon \approx -2x > 0$. Because $x \sim n_{dipole}$ (see previous section), $1 - \epsilon \sim n_{dipole}$. The plateau value is mainly influenced by the density of dipoles n_{dipole} and thus by the atomic density ρ : $y_{0,max} \sim \frac{1}{\sqrt{\rho}}$. The larger the density, the lower the plateau of the range and with that the mean energy loss of the particle at the Fermi Plateau. Also the onset of the Fermi Plateau at $\beta\gamma \sim \frac{1}{\sqrt{1-\epsilon}} \sim \frac{1}{\sqrt{\rho}}$ starts earlier, the larger the density is.

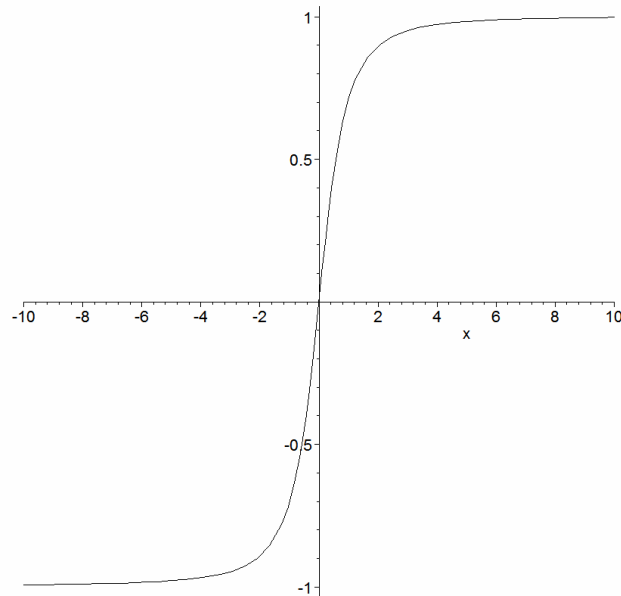


Figure 5.1: The function $f(x) = \frac{x}{\sqrt{1+x^2}}$

5.1.3 Photo Absorption Ionization Model

The differential cross section per medium electron and per energy loss dE of the charged particle is calculated within the photo-absorption-ionization model:

$$\begin{aligned} \frac{d\sigma}{dE} = & \frac{\alpha}{\beta^2\pi} \frac{\sigma_\gamma(E)}{EZ} \ln [(1 - \beta^2\epsilon_1)^2 + \beta^4\epsilon_2^2]^{-\frac{1}{2}} + \\ & \frac{\alpha}{\beta^2\pi} \frac{\sigma_\gamma(E)}{EZ} \ln \frac{2mc^2\beta^2}{E} + \\ & \frac{\alpha}{\beta^2\pi} \frac{1}{e^2} \int_0^E \frac{\sigma_\gamma(E')}{Z} dE' + \\ & \frac{\alpha}{\beta^2\pi} \frac{1}{Znhc} (\beta^2 - \frac{\epsilon_1}{|\epsilon|^2}) \end{aligned} \quad (5.1)$$

$\alpha = \frac{e^2}{4\pi\epsilon_0\hbar c} = 1/137$ is the fine structure constant, Z the number of electrons per atom, $n = \frac{N_A\rho}{A}$ (N_A : Avogadro number, A : weight of N_A atoms, i.e. of 1Mol) the atomic density, $\sigma_\gamma(E)$ the cross section for the absorption of a photon with energy E by the atoms.

For optical photon energies, i.e. $\omega < \omega_0$ the medium is transparent and $\sigma_\gamma = 0$. Therefore the creation of Cherenkov light is determined by the fourth term in the above cross section (5.1) which is independent of σ_γ . As $n_1 \gg n_2$, $\epsilon \approx \epsilon_1$ and the differential cross section becomes

$$\frac{d\sigma}{dE} = \frac{\alpha}{\pi Znhc} \left(1 - \frac{1}{\epsilon\beta^2}\right).$$

Now the cross section per target particle is given by

$$\sigma_b = \frac{\dot{M}}{\Phi_a N_b}$$

where σ_b has the dimension of an area and can in some cases be interpreted as the scattering area that one target particle "b" provides to a beam particle "a". \dot{M} is the number of reactions per unit time, here the rate of produced photons. The flux of beam particles Φ_a is given by $\Phi_a = \frac{\dot{N}_a}{A} = n_a v_a$ and is a measure for the number of beam particles per area and per time that hit the target. N_b is the number of target particles. If N_a and N_b are given for a target volume V , one can write $\Phi_a = \frac{N_a}{V} v_a$ and $\frac{N_b}{V} = Zn$ with Zn being the electron density of the medium. So the beam particle corresponds to the charged particle ($N_a = 1$) and the target particles to the medium electrons and the cross section is proportional to the probability to produce a photon per target electron. Hence, $\frac{d\sigma}{dE} = \frac{d\sigma_b}{dE}$. Exploiting this yields

$$\frac{d\sigma}{dE} \cdot Zn = \frac{d}{dE} \left(\frac{\dot{M}}{N_a v_a} \right).$$

With the flight distance $L = v_a \cdot \Delta t$ of the incident particle (L short enough to assume v_a

to be constant) this turns into

$$\begin{aligned}
 \frac{d\sigma}{dE} \cdot Zn \cdot L &= \frac{d}{dE}(\dot{M}) \frac{1}{n_a} \Delta t \\
 &= \frac{d}{dE} \left(\frac{\dot{M}}{A'} \right) \cdot A' \Delta t \\
 &= \frac{d}{dE} \left(\frac{\dot{M}}{A'} \right) \cdot A' \Delta t \\
 &= \frac{d\Phi_\gamma}{dE} W'
 \end{aligned}$$

where Φ_γ is the photon flux through an area A' and $W' = A' \Delta t$ is a normalization factor. It was assumed that the rate \dot{M} is the only energy dependent quantity. Finally, by setting $m := W' \cdot \Phi_\gamma$, where m is dimensionless and directly proportional to the photon flux, one obtains the flux of photons per energy interval $dE = \hbar d\omega$ (energy loss of charged particle due to photon emission) when the charged particle travels a distance L , as a function of β and ϵ :

$$\frac{dm}{\hbar d\omega} = \frac{\alpha}{\pi \hbar c} \left(1 - \frac{1}{\beta^2 \epsilon} \right) \cdot L. \quad (5.2)$$

As β increases also the photon flux emitted per energy interval is enhanced.

For long radiators with $L \gg \lambda$ (λ wavelength of the photons) and in the regime $\omega < \omega_0$ (5.2) yields the intensity of Cherenkov light. For $\omega \ll \omega_0$ and varying ϵ , (5.2) describes the emission of Transition Radiation.

5.1.4 Transition Radiation

Transition radiation (TR) is produced if a charged particle crosses a boundary between two media of different refraction numbers. For example, a charged particle in vacuum forms an electric dipole with its mirror charge in the denser medium. As the particle approaches the boundary, the field strength varies and it vanishes once the particle has entered the medium. A changing dipole field strength with time leads to the emission of electromagnetic radiation (TR). In this section it will be shown that for highly relativistic particles the radiation is peaked at small opening angles $\sim 1/\gamma$ and that the intensity grows with γ . By this and the fact that there is a threshold in γ for the emission of TR, particles of same momentum but different mass, which have the same bending radius in a magnetic field, can be distinguished.

In the following, the quantities are considered in a unit system, where $c = \hbar = 1$.

For short radiators ($L \ll \lambda$), small angles of emission Θ and $\beta \sim 1$, from (5.2) the number of transition radiation photons in the X-ray range can be obtained. Introducing the energy density W of the irradiated photon field, the density of electrons in a medium $n_e = n \cdot Z$ (n : atomic number density), the plasma frequency $\omega_p = \sqrt{\frac{4\pi\alpha n_e}{m_e}}$ and the squared fraction of plasma frequency to photon frequency, $\zeta = \frac{\omega_p^2}{\omega^2} = 1 - \epsilon(\omega)$, the energy density spectrum of photons irradiated at polar angle Θ can be calculated for the transition of a charged particle with Lorentz factor γ between two media of different dielectric numbers ϵ_1 and ϵ_2 and thus with different electron densities n_e . The following expression for the

energy density spectrum is valid for $\gamma \gg 1$, $\Theta \ll 1$, $\zeta_i^2 \ll 1$ meaning $1 - \epsilon_i \ll 1$ and for a single interface transition:

$$\left(\frac{d^2W}{d\omega d\Omega}\right)_{interface} = \frac{\alpha}{\pi^2} \Theta^2 \left(\frac{1}{\gamma^{-2} + \Theta^2 + \zeta_1^2} - \frac{1}{\gamma^{-2} + \Theta^2 + \zeta_2^2} \right)^2 \quad (5.3)$$

For $\zeta^2 \ll \gamma^{-2}$ (which is a condition to obtain a measurable yield), the emission is peaked at $\Theta \sim \gamma^{-1}$ ³. Also the yield in energy density grows quadratically with γ . This is the reason why electrons produce a significant amount of TR photons at a momentum of $3GeV/c$ ($\gamma \approx 6000$) whereas pions of the same momentum hardly have a measurable TR yield ($\gamma \approx 20$). As the plasma frequency is in the order of some eV and the threshold for the onset of TR emission lies at γ around 1000, the energies of the TR photons will be in the X-ray range (1 to $30keV$) ($\zeta^2 \ll \gamma^{-2}$, thus $\omega \gg \omega_p \cdot \gamma$). Moreover, the average energy of a TR photon depends on γ which, together with the TR threshold for γ , can be used to distinguish between electrons and background particles, such as pions, in the low GeV/c momentum range.

As the emission angle is very small ($\Theta \sim \gamma^{-1}$) the double differential spectrum for the single interface transition can be integrated over the solid angle $d\Omega$: $\int \frac{d^2W}{d\omega d\Omega} d\Omega = 2\pi \int \frac{d^2W}{d\omega d\Omega} \sin \Theta d\Theta \approx 2\pi \int \frac{d^2W}{d\omega d\Omega} \Theta d\Theta$. This yields the differential energy density spectrum for the one-interface transition:

$$\left(\frac{dW}{d\omega}\right)_{interface} = \frac{\alpha}{\pi} \left(\frac{\zeta_1^2 + \zeta_2^2 + 2\gamma^{-2}}{\zeta_1^2 - \zeta_2^2} \ln \frac{\gamma^{-2} + \zeta_1^2}{\gamma^{-2} + \zeta_2^2} - 2 \right).$$

If the transition of a foil is regarded, then two interfaces have to be taken into account leading to interference effects. Thus the double differential cross section for a foil is given by the cross section for one interface and an additional interference factor which depends on the length of the foil, l_1 :

$$\left(\frac{d^2W}{d\omega d\Omega}\right)_{foil} = \left(\frac{d^2W}{d\omega d\Omega}\right)_{interface} \cdot 4 \sin^2 \left(\frac{\phi_1}{2} \right).$$

$\phi_1 \approx (\gamma^{-2} + \Theta^2 + \zeta_1^2) \frac{\omega l_1}{2}$ is the phase retardation of the TR from the second interface (charged particle leaving the foil) with respect to the first one. If there is a whole stack of foils, all the interferences at all interfaces have to be considered.

In the following some features of the TR production are mentioned:

- The distance $z_i = (\gamma^{-2} + \Theta^2 + \zeta_i^2)^{-\frac{2}{\omega}}$ (note that distances have the dimension GeV^{-1}) after which the particle and the emitted photon are separated by the photon wave length. In case $l_i \ll z_i$ one observes a suppression of the photon yield (formation zone effect) whereas interference can be neglected if $l_i \gg z_i$ and then $\left(\frac{d^2W}{d\omega d\Omega}\right)_{foil} = 2 \left(\frac{d^2W}{d\omega d\Omega}\right)_{interface}$.
- The TR spectrum has a maximum at a frequency of $\omega_{max} = \frac{l_1 \omega_{p,1}^2}{2\pi}$. By varying ω_p with the choice of the material (n_e) and by varying the length of the radiator, the

³Practically the direction of the photon coincides with the particle direction. However in media the speed of light is reduced but not the speed of the high relativistic incident particle flying almost at c and therefore faster than the produced photons.

position of this maximum can be influenced. However, in order to have a measurable yield at ω_{max} for TR from electrons in the low GeV/c momentum range ($\gamma \geq 1000$), also $\frac{\omega_{max}}{\omega_p} \gg \gamma$ has to be assured.

- At high γ the yield of TR saturates due to multiple foil interferences.
- The position of the absorption of the TR photons is determined by the mass attenuation coefficient μ/ρ (μ : absorption coefficient, ρ : density of medium) at the energy of the TR photon. Furthermore, due to the small radiation angle, the direction of the incoming particle with respect to the radiator normal direction, influences the position of absorption (inclination leads to a longer way inside the radiator). As one must be able to detect the TR photons, the absorption probability inside the radiator should be small. The absorption cross section by photo effect is proportional to Z^5/E_γ . That's why the radiator is usually built of material with low Z whereas in the (TRD) drift volume, the TR encounters Xe gas with high Z and thus is preferentially absorbed near the entrance of the drift region.

5.1.5 Energy Loss

The first three terms of equation (5.1) describe the energy loss by ionization where the third term is responsible for the creation of energetic delta electrons (δ -e) and from the first two one can obtain the mean energy loss $\langle \frac{dE}{dx} \rangle$. For the ionization region, $\hbar\omega \geq \hbar\omega_0$ must hold for the virtual photons that mediate the interactions. $\sigma(E)$ is the probability for an energy loss E of the particle per medium electron. The energy loss occurs by irradiating a (virtual) photon with energy E , which is absorbed by the medium electron (leading to ionization or energy loss). The differential cross section $\frac{d\sigma(E)}{dE}(E)$ is a measure for the rate of change of the cross section with energy, given at a transmitted photon energy E . The mean energy loss $\langle \delta E \rangle$ per medium electron is obtained by integrating the differential cross section over the possible range of energy transfers:

$$\langle \delta E \rangle \sim \int_I^{E_{max}} \frac{d\sigma}{dE} dE$$

where I ($I \geq \hbar\omega_0$) is the mean ionization potential of the atoms and $E_{max} = 2m_e c^2 \beta^2 \gamma^2$ is the maximum possible energy transfer to a scattered electron (see Appendix). By introducing a mean distance δx between electrons ($\delta x \approx (\frac{N_e}{n_e})^{1/3}$, $n_e = \frac{N_e}{V}$), the mean energy loss per medium electron can be scaled to a mean energy loss per unit distance, $\frac{dE}{dx}$. This yields the Bethe Bloch formula, an approximation for the mean energy loss by ionization of a charged particle traversing a medium and interacting electromagnetically with it:

$$\langle \frac{dE}{dx} \rangle = - \frac{8\pi r_e^2 m_e c^2 N_A Z z^2}{A \beta^2} \cdot (\ln \frac{2m_e c^2 \beta^2}{(1 - \beta^2)I} - \beta^2) \quad (5.4)$$

with N_A : Avogadro number, Z : number of atomic electrons, A : atomic mol mass, ze : charge of the incident particle, $v = \beta c$: velocity of the particle, I : effective ionization potential, $r_e = \frac{e^2}{8\pi\epsilon_0 m_e c^2} \approx 2.8 fm$: classical electron radius (obtained by requiring that the rest mass energy of the electron is equal to the electrostatic energy of a sphere with charge e and

radius $r_e: \frac{e}{8\pi\epsilon_0 r_e} = m_e c^2$). Usually instead of using the thickness of the traveled material, x , the Bethe Bloch formula is expressed in terms of the quantity $X = x \cdot \rho$ where ρ is the density of the medium:

$$\frac{dE}{dX} = \frac{1}{\rho} \frac{dE}{dx}.$$

For the first ionization of Xe one needs $I_0 I \approx .12.1eV$. The Bethe Bloch curve for Xe at small $\beta\gamma$ is shown in figure 5.2. As the formula (5.4) shows, the mean energy loss

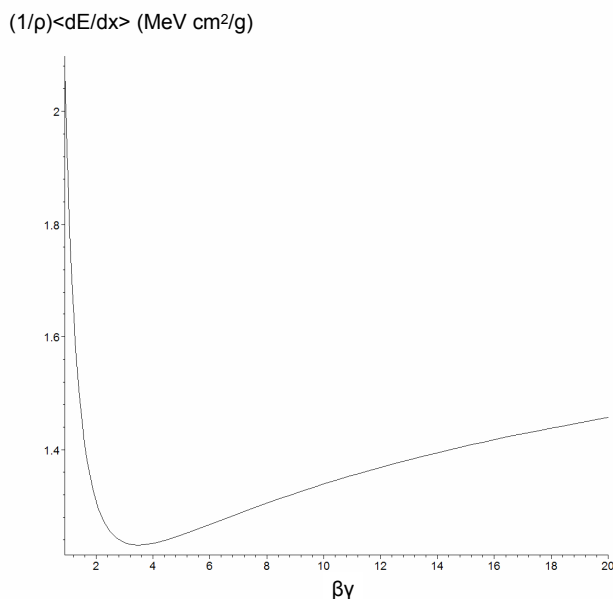


Figure 5.2: The Bethe Bloch curve for Xe

is independent of the mass of the incident charged particle and is influenced only by its velocity $v = \beta c$. To emphasize this independence of the particle species, the mean energy loss is usually plotted against $\beta\gamma = \frac{p}{m_e c}$. However the formula is not true for light particles (e.g. electrons) as it is assumed that a scattering process does not influence the direction of the incident particle. If an electron scatters against an electron this is no more the case. For small values of β , the mean energy loss is $\sim \frac{1}{\beta^2}$. It has a minimum for $\beta\gamma \approx 4$. Such a particle is also called minimum ionizing (MIP). Its $\frac{dE}{dX}$ amounts to roughly $1MeVcm^2/g$ to $2MeVcm^2/g$. For high relativistic electrons with relativistic mass $\gamma m_e \gg m_e$, the Bethe Bloch formula can be applied at least for large values of $\beta\gamma$.

Not taken into account in (5.4) is the shell correction which occurs at particle velocities in the region of the velocities of the atomic electrons. It describes a reduction of the mean energy loss at the corresponding particle velocity due to the shielding of its Coulomb field inside the atom at inner shells by outer shell electrons. So the charged particle does not see the whole atomic charge Z but rather an effective fraction of it. Other features of the mean energy loss distributions have already been mentioned in previous sections.

So as a summary, a primary charged particle excites and ionizes the medium atoms and thus creates electron ion pairs. The energy distribution of the ionized electrons is $\sim \frac{1}{E^2}$.

Electrons that gained kinetic energies $\geq 100eV$ can then ionize other atoms in secondary processes. The energy equilibration happening in this way occurs in a short time after the primary ionization and the charge clusters are concentrated around the track of the primary particle. If the total energy loss in the material was ΔE , the number of produced ions n_T can roughly be estimated by $n_T \approx \frac{\Delta E}{W_i}$ where W_i is the mean energy needed to create an electron ion pair and in xenon amounts to $W_i \approx 22eV$. In gases, $W_i \geq I_0$ ⁴. Usually n_T is 2 to 7 times the number of primary electron pion pairs, n_p .

Since energy loss is a statistical process (the number of ionizations in a thickness Δx is Poisson distributed) one could assume that the range of different particles with the same incident energy should be spread out inside material. The mean range can be calculated by $\langle R \rangle = - \int_{E_0}^0 \frac{dE}{dE/dx(E)}$ with E_0 being the original energy of the particles. However, as the particles slow down due to previous energy losses also their mean energy loss increases and the deceleration becomes quicker. Then only a few energy losses are enough to stop the particle which leads to a narrow distribution of the range around the mean $\langle R \rangle$. Consequently, also the particle density at $\langle R \rangle$ is enhanced (Bragg peak).

Statistical Fluctuations of dE/dx

The Bethe Bloch formula gives the mean energy loss per distance $\langle \frac{dE}{dx} \rangle$ at a given $\beta\gamma$. As the energy loss is a statistical process, for large distances Δx the total energy loss

$$\Delta E(\Delta x) = \sum_{n=1}^N \delta E_n \quad (5.5)$$

will be approximately normally distributed due to the central limit theorem and the large number of energy transfers N . Here it is assumed that the individual energy transfers δE_n are statistically independent of each other. The total number of energy transfers N is Poisson distributed ⁵

Also the size of the individual energy losses δE is subject to fluctuations. The δE distribution follows approximately $\frac{1}{(\delta E)^2}$ between $\delta E_{min} \approx I$ and $\delta E_{max} \approx 2m_e\beta^2\gamma^2c^2$ with the mean individual energy transfer $\langle \delta E \rangle$ being close to E_{min} .

Combining this, the total energy loss (5.5) for thin layers Δx is Landau distributed (figure 5.3) with a tail toward high energy losses (δ -e) ⁶. The distribution is peaked at the most probable energy loss $\Delta E_{m.p.}$ and due to the tail the mean energy loss ΔE_{mean} , which

⁴The cross section for excitation is negligible as compared to the ionization cross section. Not in all ionizations the electron with the lowest ionization potential is kicked out. Moreover, a charged particle in the vicinity of a gas atom (e.g. an electron that is to ionize it) can influence the electron shell configuration of the gas atom and shift the ionization potential. Additional energy can be transferred to kinetic energy of the ionized electron or the gas atom. In latter case, the gas volume would be heated. Or an ionization and an excitation happen during the same process, increasing the inner energy of the gas atom, etc.

⁵one can think of Δx as being cut into sufficiently small slices of size δx , $\Delta x = M\delta x$, M large, inside which one can assume a binomial process: either there is one or no energy loss. If the probability for an energy loss becomes $p_{success} \ll p_{failure}$, then the mean number of energy losses in Δx is given by $\bar{N} = MP_{success}$.

⁶which makes the distribution asymmetric since the lower value for the energy transfer is limited by 0 whereas the upper value is limited by the particle energy E , where mostly $\Delta E \ll E$.

corresponds to the energy loss obtained by the Bethe Bloch formula when neglecting the change in $\beta\gamma$ inside Δx , is larger than $\Delta E_{m.p.}$.

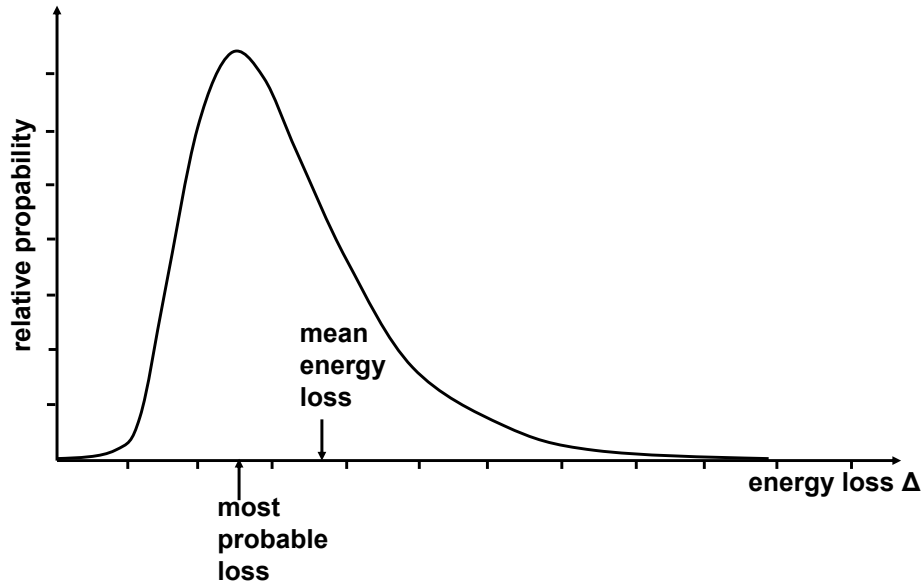


Figure 5.3: Shape of the Landau distribution ([Phy06])

The approximate resolution of a measured ΔE , $\frac{\sigma(\Delta E)}{\Delta E} \approx \frac{1}{\sqrt{N}}$ can be obtained by assuming that $N \approx \bar{N}$ and thus $\Delta E \approx \langle \Delta E \rangle \approx \bar{N} \langle \delta E \rangle$. Due to the Poisson distributed total number of energy transfers N , $\sigma(N) = \sqrt{\bar{N}}$ and hence $\sigma(\Delta E) \approx \sqrt{\bar{N}} \langle \delta E \rangle$. So $\frac{\sigma(\Delta E)}{\Delta E} \approx \frac{\sigma(\Delta E)}{\langle \Delta E \rangle} = \frac{1}{\sqrt{\bar{N}}} \approx \frac{1}{\sqrt{N}}$.

The fluctuations of the energy loss reduces the resolution of

- the particle identification via particle mass: If the momentum of the charged particle is known (bending in B-field) together with the mean value $\langle \frac{dE}{dx} \rangle$, the particle velocity and thus its mass can be derived. However, in order to obtain $\langle \frac{dE}{dx} \rangle$, the mean over the released energy in many thin layers has to be calculated. Due to the Landau tail and the limited number of statistics, one usually finds the mean not to converge to a stable value. By neglecting a fraction r (e.g. 30%) of the measurements with the largest values (cutting on the Landau tail), one can obtain a more stable estimation of the mean out of m measurements (truncated mean): $\langle \Delta E \rangle = \frac{1}{(1-r)m} \sum_i \Delta E_i$ where i runs over the fraction $(1-r)$ of the measurements with smallest values.
- the spatial track reconstruction. Due to the creation of energetic δ -electrons which move away from the primary track and may produce own clusters, it becomes difficult

to associate the right clusters to the primary track and exclude the δ -e. As δ -e still have much less energy and momentum than the primary particle their track can be curled up in the magnetic field of a detector and might not reach other layers or hits the current layer more than once. By combining several layers and requiring that a track hits a minimum number of layers, delta electrons can be excluded to a large extent.

5.1.6 Bremsstrahlung

In case electrons are the primary charged particles, the mean energy loss is not given by the Bethe Bloch formula any more as it was already mentioned in the previous section. However in the case of high relativistic electrons with $\beta \approx 1$ and $E \gg m_e c^2$, the direction of the electron when scattering at atomic electrons will not be influenced a lot, since the relativistic mass $\gamma m_e c^2 \gg m_e c^2$. Thus for large $\beta\gamma$ the Bethe Bloch formula may be applied also for electrons. Then the mean energy loss by ionization is given by

$$\left(\frac{dE}{dx}\right)_{ion} = -4\pi N_A \frac{Z}{A} r_e^2 m_e c^2 \left(\ln \frac{2mv^2\gamma^2}{I} - 1\right).$$

However there is a second process, dominating the energy loss of electrons at high electron energies, Bremsstrahlung:

$$\left(\frac{dE}{dx}\right)_{brems} = -4\pi N_A \frac{Z^2}{A} r_e^2 E \left(\ln \frac{183}{Z^{1/3}}\right) = \frac{E}{X_0},$$

X_0 is the radiation length, defined as the distance, after which the energy decreased to the fraction $1/e$. Bremsstrahlung occurs, if a charged particle is decelerated and deflected in the vicinity of the electric field of an atomic nucleus. Part of the electron's kinetic energy is then irradiated by the release of a photon. As the Bremsstrahlung energy loss per distance dx is finite and $\sim \frac{E}{m^2}$, Bremsstrahlung for energies below $100 GeV$ is only of relevance for electrons (e^- and e^+). Because $\frac{dN_\gamma}{dE_\gamma} \sim \frac{1}{E_\gamma}$, the irradiated photons will be concentrated at lower energies.

The energy loss at low electron energies is dominated by ionization whereas at higher energies Bremsstrahlung is the dominant effect. The critical energy where

$$R = \frac{\left(\frac{dE}{dx}\right)_{Bremsstrahlung}}{\left(\frac{dE}{dx}\right)_{ionization}} \approx \frac{ZE}{580 MeV} = 1$$

is given by $E_c \sim \frac{580 MeV}{Z}$. For Xe gas with $Z = 54$, $E_c \approx 10 MeV$. Hence, for GeV electrons, inspected within the TRD, Bremsstrahlung is the dominant process for energy loss. However, as the energy loss by an individual Bremsstrahlung process is more efficient compared to an individual energy transfer by ionization (meaning that the average number of processes needed for a total energy loss ΔE is smaller for Bremsstrahlung than for ionization or, vice versa, the mean free path for Bremsstrahlung is much larger than for ionization) and moreover the material thickness of the TRD is only about $15\% X_0$, the probability for an energy loss by ionization is much higher than via Bremsstrahlung. This is the reason why tracking of electrons is possible at all in this momentum range.

5.2 Signal Generation

In this section the physical effects are considered influencing the signal that is finally observed with the detector. In the following it is assumed that a charged particle flies through the detector and creates electron ion pairs. The succeeding charge clusters are subject to a homogeneous electric field forcing them to drift inside a $Xe/CO_2(85 : 15)$ gas mixture. Since electrons drift significantly faster than the positive ions and in opposite direction, the probability for direct recombination is low. The electron clusters drift toward an anode wire plane, where the electric field increases (the equipotential surfaces form cylinders around the wires). Here, the cluster electrons (which are assumed to be energetically equilibrated) are accelerated, thus producing electron ion pairs. The additional electrons themselves are amplified and in the end each original cluster electron releases on average a large number of additional electrons in an avalanche process (gas gain). Like that a measurable signal is produced, whose height is proportional to the number of cluster electrons and thus to the original energy release by the particle track.

5.2.1 Energy Loss and Cluster Creation

Cluster Creation by a Charged Particle

As was already discussed in previous sections, the interaction of a charged particle releases in a primary process electrons from atoms of the TRD gas. The probability for such a primary ionization as a function of the traveled distance s (since the last ionization process) is assumed to follow an exponential distribution:

$$P(s) = \frac{1}{D} \exp\left(-\frac{s}{D}\right). \quad (5.6)$$

Here D denotes the mean distance between the primary ionizations. If the mean energy deposit per distance is written as $\langle \frac{dE}{dx} \rangle \approx \langle N_{prim} \rangle \frac{dx}{1cm} \cdot (\delta E)_{mean}$ with the mean number of primary ionizations per cm , $\langle N_{prim} \rangle$ and the mean energy deposit per ionization $(\delta E)_{mean}$ and if $(\delta E)_{mean}$ does not change much with $\beta\gamma^7$, then the Bethe Bloch curve, normalized to MIP values, is given by

$$f(\beta\gamma) \approx \frac{\langle N_{prim} \rangle (\delta E)_{mean}}{\langle N_{prim,MIP} \rangle (\delta E)_{mean}} = \frac{\langle N_{prim} \rangle}{\langle N_{prim,MIP} \rangle}.$$

Thus D becomes

$$D = \frac{1}{\langle N_{prim} \rangle} = \frac{1}{\langle N_{prim,MIP} \rangle f(\beta\gamma)}.$$

So, in a detector with thickness Δ (in cm units, Δ small), on average there will be $\langle N_{\Delta} \rangle = \langle N_{prim} \rangle \cdot \Delta = \langle N_{prim,MIP} \rangle f(\beta\gamma) \Delta = \frac{\Delta}{D}$ primary energy losses (hits). For a specific track, the actual number of hits is obtained in the simulation by sampling a Poisson distribution with mean $\langle N_{\Delta} \rangle$. When assuming that the energy transfer δE of a single process is distributed

⁷since the energy transfer per ionization is distributed $\sim \frac{1}{\delta E^2}$, a change in the maximal energy transfer $2m_e c^2 \beta^2 \gamma^2$ at already large γ ($\beta \approx 1$) in the GeV/c momentum range, will not change the mean value much any more

$\sim \frac{1}{\delta E^2}$ and if Δ is sufficiently small, the energy loss of tracks in the detector, $\Delta E = \sum_{i=0}^{N_\Delta} \delta E_i$ will follow a Landau distribution.

According to the distribution in (5.6), the step size (distance between the release of clusters) in the simulation of the detector is calculated. The mean step size amounts to D .

In order to obtain the number of electrons in a cluster, the energy spectrum of the primary electrons must be known. For the rate of inelastic collisions per cm with an energy transfer above δE one obtains

$$\left(\frac{dN}{dx}\right)_{>\delta E} = \int_{\delta E}^{\infty} \frac{d^2N}{dx d(\delta E')} d\delta E'. \quad (5.7)$$

Assuming $\frac{dN}{d\delta E} \sim \frac{1}{\delta E^2}$ as the distribution for a single energy transfer and further, that an energy transfer (ionization) occurs every distance D (hence, $P(s) \sim \delta(s - D)$), one would get

$$\left(\frac{dN}{dx}\right)_{>\delta E} \sim \frac{1}{D} \int_{\delta E}^{\infty} \frac{1}{\delta E'^2} d(\delta E') \sim \frac{1}{D} \frac{1}{\delta E}.$$

Since (5.6) is not a delta function, the simple $\frac{1}{\delta E}$ scaling is modified.

The energy transfer δE needs to exceed the ionization potential of Xe, $\delta E_{min} = I_{pot} = 12.1eV$ in order to produce a cluster electron. If the energy release is above $\sim 10keV$ this δ -ray is treated as a stand-alone track and is stepped through the detector itself if its average step size D_δ is smaller than the distance to the border of the tracking volume. The number of electrons in a cluster, N_{tot} , is determined by the energy transfer δE via

$$N_{tot} = \frac{\delta E - I_{pot}}{W} + 1$$

where W is the effective energy needed to produce a free electron in Xe, $W \approx 22eV$. It is assumed that the primary electrons, whose energy exceeds W , will very rapidly release their energy by producing further electron ion pairs in the vicinity of the cluster (not deteriorating spatial resolution much). By scattering, equilibration in energy and thermal motion is achieved and the cluster electrons are supposed to all gain the same drift velocity within a very short time.

Cluster Creation by Transition Radiation

If a TR photon enters the drift volume, it is preferentially absorbed after short distances. The first released electron by the photo absorption of the photon has the energy $E_{TR} - I_{pot}$ and creates further charges by ionization. In total $N_{tot}^{TR} = \frac{E_{TR} - I_{pot}}{W} + 1$ charges in a cluster are created.

Although the TR photon yield is peaked at an angle $\frac{1}{\gamma}$ (for large γ) around the incident particle track and thus cannot be separated from it (the TR clusters are added to the track clusters), often TR is responsible for a smearing of the clusters, leading to a deterioration of track reconstruction:

- The photo electron which was originally bound inside the Xe atom with a binding energy of E_S , has an energy of $E_e = E_{TR} - E_S$ after release and is emitted with high probability (at X-ray energies) in a plane perpendicular to the direction of the

incoming photon. The range $R(E_e)$ of the electron in a gas (subject to elastic and inelastic collisions) can be parameterized by

$$R(E_e) = AE_e \left(1 - \frac{B}{1 + CE_e}\right) \frac{1}{\rho} \quad (5.8)$$

where A,B,C are constants to be determined experimentally and ρ is the density of the gas. In Xe gas the range of a $10keV$ electron is about $0.5mm$.

- The hole that is left in the shell by the emission of the photo electron can be filled by other atomic electrons leading to the emission of an Auger electron or of fluorescence photons. If the second shell involved in the transition has the binding energy E_T , a fluorescence photon will have the energy $E_S - E_T$. Depending on the energy, the absorption length in the gas can be very large, such that these photons can produce a remote cluster.

If the energy of the transition is transformed to the release of another shell electron with binding energy E_B , the kinetic energy of this Auger electron is $E_e = E_S - E_T - E_B$. Its range can be calculated by the above formula.

Cluster Creation by Delta Rays

The tail of the Landau distribution for energy loss suggests, that there is a significant probability for the production of energetic electrons in a primary collision. If a δ -electron is produced (the definition of when a particle is considered to be a δ -particle, is arbitrary) its range is calculated using (5.8). If the range is larger than the remaining length of the incident track inside the detector, then the δ -electron is tracked itself. If no magnetic field is applied, it can be assumed that the energetic δ -electron moves along the track of the incident particle and its energy-loss clusters are added to those of the parent track.

Concerning the energy loss distribution, one has to distinguish between δ -electrons that are absorbed inside the detectors and those that escape the detector. Of course in both cases they occur from a energy loss of the incident particle, however measurable is only the energy deposit inside the detector (which is never larger than the energy loss). In the case of an absorbed δ -ray, energy loss and energy deposit (the measurable part of the energy loss) are equal, whereas in the escape case, energy deposit is smaller than the energy loss.

The energy loss distribution of tracks that produce at least one escaped δ -electron, is rather flat. The probability for the production of δ -electrons decreases as their energy increases, however high energetic δ -rays have a large probability to escape, independently from where they were produced. The escape is the condition, that the parent track with is inserted into the energy loss distribution (at large values of the energy loss). The enhancement of low-energetic δ -rays is suppressed in the distribution by the lower probability that they escape⁸, and thus only a fraction of tracks with the corresponding energy losses is counted in the distribution.

The distribution of tracks without δ -electrons will hardly have a tail (depending of course on the definition of a δ -electron) and be rather symmetric (Gaussian).

⁸assuming, that there is no preferred place for producing low energetic δ -rays in the detector. Then only a fraction, that is produced close enough to the chamber border, can escape

The sum of the above two contributions, together with the energy loss distribution of tracks, whose δ -electrons are all contained inside the detectors (Landau distribution), yields the total energy loss distribution inside the detector which is again of Landau shape, since the detector thickness is small enough.

The above explanations are only valid if no magnetic field is applied. In case of a magnetic field, low energetic δ -rays become curled up. In general it is no longer true that δ -rays move close to the incident track. Thus, in most cases, the energy loss of the δ -ray will not be added to the energy loss of the incident particle. Then only the energy deposit due to ionization in the "normal" energy range and not the energy loss is measured.

5.2.2 Diffusion

In this section diffusion effects (along and transversal to electric and magnetic fields) are shortly considered.

Diffusion Without Field

If an electron cloud is placed in the origin at time $t = 0$ (δ peak) inside a gas then the gradient in the electron density is reduced by diffusion. Due to scattering processes with the surrounding gas⁹, the electron peak broadens isotropically, which in one coordinate direction is described by a time dependent Gaussian profile with width $\sigma = \sqrt{2Dt}$:

$$\frac{dN}{N_0}(t) = \frac{1}{\sqrt{4\pi Dt}} e^{-\frac{x^2}{4Dt}} dx \quad (5.9)$$

with N_0 being the total number of electrons. The term on the right side of the equation is a probability density: The probability to find an electron in the interval $[x, x + dx]$, which is given by the fraction of electrons in this interval to the total number of electrons, $\frac{dN}{N_0}$.

The diffusion constant without field, D , is given by $D = \frac{u\lambda}{3}$, where u is the mean thermal velocity of an electron and λ is the mean free path of an electron in the surrounding gas¹⁰. Assuming equilibration, i.e., that the (ideal) electron gas has the same temperature as the surrounding gas, the mean thermal velocity of an electron, u , is given by the mean of a Maxwell-Boltzmann velocity distribution: $u = \sqrt{\frac{8kT}{\pi m_e}}$. For the mean free path, one can write $\lambda = \lambda(\epsilon) = \frac{1}{n\sigma(\epsilon)}$, where n is the number density of the surrounding gas, $\sigma(\epsilon)$ the cross section for an electron of energy ϵ to collide with a gas molecule. Using the equation of state for an ideal gas (the TRD gas consists to 85% of the noble gas Xe), $p = nkT$, where p is the pressure of the gas, the diffusion constant D can be expressed as $D = \frac{2\sqrt{2}}{3\sqrt{\pi}} \frac{1}{p\sigma(\epsilon)} \left[\frac{(kt)^3}{m_e} \right]^{\frac{1}{2}}$.

⁹A particle with f degrees of freedom ($f = 3$ if only translation, ideal gas) has a mean thermal energy of $\epsilon_t = f/2kT$ (for ideal gases the mean kinetic energy is $\langle \epsilon_t \rangle = 3/2kT$)

¹⁰For diffusion, especially the scattering processes of electrons at the border of the electron cloud are responsible for the broadening of the peak and hence only the mean free path in the gas environment is considered. Moreover, due to the small electron radius, the cross section for collisions of electrons with other electrons can be neglected as compared to the probability for a collision of an electron with a particle of the surrounding gas.

Diffusion With Field

Here two cases are considered:

- Applying an electric field (in absence of a magnetic field) leads to non isotropic diffusion, which is superimposed on a drift. If $\vec{E} = (E_x, 0, 0)$, the component D_x usually is changed, $D_x \vec{E} \neq D$, whereas the transversal components remain unchanged. If L denotes the drift length, v_D the drift velocity ($\vec{v}_D \parallel \vec{E}$, drift is parallel to electric field, and $L = v_D \cdot t$) and u the mean velocity of the electrons, then the widths of the transversal diffusions become $\sigma_y^{\vec{E}} = \sigma_z^{\vec{E}} = \sqrt{\frac{2L}{v_D} \frac{u\lambda}{3}}$, where the time t was replaced by the needed time for a drift distance L , $\frac{L}{v_d}$. Thus small values of the mean free path (e.g. in CO_2) help to reduce the perpendicular smearing of the charge clusters away from the track until the end of the drift time.
- If a magnetic field $\vec{B} = (0, 0, B_z)$ is applied, the diffusion coefficients in transversal direction with respect to \vec{B} are declined, the diffusion coefficient along \vec{B} remains unchanged: $D_z^{\vec{B}} = D$, $D_x^{\vec{B}} = D_y^{\vec{B}} = \frac{D}{1+\omega^2\tau^2} < D$. If $|u_{\perp}| = u_{\perp}$ is the mean thermal velocity of the electrons in the plane perpendicular to \vec{B} ($u^2 = u_{\perp}^2 + u_{\parallel}^2$), the average revolution frequency ω of an electron in the magnetic field can be expressed by $\omega = \frac{u_{\perp}}{r}$. τ is the mean time between two collisions, $\tau = \frac{\lambda}{u}$. Hence, $D_x^{\vec{B}} = D_y^{\vec{B}} = \frac{D}{1+\frac{u_{\perp}^2}{u^2} \frac{\lambda^2}{r^2}}$.

Assuming $u_z = 0$, $\vec{u} \perp \vec{B}$, this becomes $D_x^{\vec{B}} = D_y^{\vec{B}} = \frac{D}{1+\frac{\lambda^2}{r^2}}$. The reduction in transverse diffusion is large if $\omega\tau \gg 1$ or $r \ll \lambda$. The revolution of the electrons around the magnetic field suppresses diffusion transversal to the field direction efficiently if the radius is small as compared to the mean free path λ . Note that this is in some sense opposite to the case with electric field, where small values of the mean free path were helpful to reduce transversal diffusion.

If additionally a parallel electric field is applied, $\vec{E} \parallel \vec{B}$, one obtains for the width in perpendicular directions: $\sigma_x^{\vec{B},\vec{E}} = \sigma_x^{\vec{B},\vec{E}} = \sqrt{\frac{2L}{3v_D}} \sqrt{\frac{u\lambda}{1+\omega^2\frac{\lambda^2}{u^2}}}$.

In case of the TRD, the more complicated case with perpendicular electric and magnetic field, $\vec{E} \perp \vec{B}$, is realized.

The three dimensional diffusion profile of a sharp charge cluster, released at (x_0, y_0, z_0) , upon a drift in x direction is described by

$$P(x, y, z) = \frac{\exp\left(-\frac{(x-(x_0+L_{drift}/v_D))^2}{4D_L L_{drift}/v_D}\right)}{\sqrt{4\pi D_L L_{drift}/v_D}} \cdot \frac{\exp\left(-\frac{(y-y_0)^2}{4D_{T,y} L_{drift}/v_D}\right)}{\sqrt{4\pi D_{T,y} L_{drift}/v_D}} \cdot \frac{\exp\left(-\frac{(z-z_0)^2}{4D_{T,z} L_{drift}/v_D}\right)}{\sqrt{4\pi D_{T,z} L_{drift}/v_D}}$$

with D_L and D_T the longitudinal and transversal diffusion coefficients relative to the electric field, respectively. Here a constant drift velocity fulfilling $L_{drift} = v_D \cdot t$ is assumed. Note, that $D_L = D_x$ is influenced by the electric field, since it is the longitudinal coefficient, and by the magnetic field as a transversal coefficient. $D_{T,y}$ is influenced as transversal component by both, the electric and magnetic field. $D_{T,z}$ finally is only influenced by the electric field as transverse component, whereas the magnetic field leaves it unchanged as its longitudinal component.

Of course in general one can state, that a lower drift time will result in less smearing of the clusters.

5.2.3 Multiple Scattering

After having discussed the spatial distribution of a bunch of electrons (concentrated on a spot originally) as a consequence of statistical scattering processes of the electrons in the previous section, here the Coulomb multiple scattering of a single charged particle, namely the incident particle traversing the detector, is shortly discussed for completeness.

For fast particles, scattering off shell electrons is negligible compared to the interaction with the Coulomb field of the nucleus. For the high relativistic incident particles even the scattering on the nucleus has not a large effect because the interaction time is very short. However when increasing the accuracy of track reconstruction, multiple scattering becomes an issue.

The incident particle is assumed to pass through material of thickness x such that it is scattered multiple times. This leads to a statistical distribution of the angle between incident and final particle direction.

The Coulomb scattering upon a single nucleus is described by the Rutherford cross section if the nucleus is assumed to be point-like. The potential has the form (Coulomb potential) $V(r) \sim \frac{1}{r}$ and the force acting on the incident particle $\vec{F} = -\vec{\nabla}V(r) \sim \frac{1}{r^2}\hat{r}$ (\hat{r} is a unity vector in \vec{r} direction). The cross section becomes:

$$\left(\frac{d\sigma}{d\Omega}\right)_{Rutherford} = z^2 Z^2 \alpha^2 \hbar^2 \frac{1}{\beta^2 p^2} \frac{1}{\sin^4\left(\frac{\theta}{2}\right)}. \quad (5.10)$$

Ze is the charge of the nucleus, ze that of the incident particle; β is the velocity, p the momentum of the incident particle; θ is the scattering angle due to one single process. The effectiveness of the scattering process is suppressed by $\frac{1}{\beta^2 p^2}$ which is due to the short interaction time of fast particles and the inertia of heavy or relativistic particles ($p = \gamma mv$).

In case of light particles (such as incident electrons) the scattering will most likely result in a change of direction with only small energy transfer. As there is no preferred orientation of the scattering angle θ , one can project θ onto an arbitrary plane resulting in the projected angle θ_{proj} . If the thickness x is large enough such that a significant number of scatterings occurs, the angle distribution is described by a Molière distribution. Due to the central limit theorem, at increasing number of interactions, the distribution approaches a normal distribution. The distribution at an intermediate number of scatterings (≥ 10) can already be approximated by a Gaussian distribution (which underestimates the number of collisions at large angles).

Approximating the distribution function by a Gaussian with standard deviation θ_0 , the probability density for an angle θ_{proj} can be written as

$$f(\theta_{proj})d\theta_{proj} = \frac{1}{\sqrt{2\pi}\theta_0} \exp\left(-\frac{\theta_{proj}^2}{2\theta_0^2}\right)d\theta_{proj}, \quad (5.11)$$

where θ_{proj} can have positive and negative values. θ_0 is approximately given by $\theta_0 \approx \frac{13.6MeV/c}{\beta p} z \sqrt{\frac{x}{x_0} \left(1 + 0.038 \ln\left(\frac{x}{x_0}\right)\right)}$, where x is the thickness of the scattering material and

x_0 is its radiation length, characterizing processes in the Coulomb field of a nucleus (e.g. Bremsstrahlung).

For the distribution of the angle θ between incident and final direction of the particle, one finds (C is a normalization factor):

$$f(\theta)d\Omega = \frac{1}{Z} \exp\left(-\frac{\theta^2}{2\theta_0^2}\right)d\Omega,$$

with $d\Omega = \sin\theta d\theta d\phi$. Since $\exp\left(-\frac{\theta^2}{2\theta_0^2}\right)$ vanishes quickly with θ , the integral over θ will only give a significant contribution until a small angle $\tilde{\theta}$. There $d\Omega \approx \theta d\theta d\phi = \frac{1}{2}d\theta^2 d\phi$. Due to the integration over $d\phi$, θ can be restricted to positive values. Moreover the integration boundary can be extended from $\tilde{\theta}$ to ∞ without introducing a significant error. Then for the normalization this yields

$$\begin{aligned} & \frac{1}{C} \int_0^{2\pi} d\phi \int_0^\pi d\theta \sin\theta \exp\left(-\frac{\theta^2}{2\theta_0^2}\right) \\ & \approx \frac{1}{C} \int_0^{2\pi} d\phi \int_0^{\tilde{\theta}} d\theta \theta \exp\left(-\frac{\theta^2}{2\theta_0^2}\right) \\ & \approx \frac{\pi}{C} \int_0^\infty d\theta^2 \exp\left(-\frac{\theta^2}{2\theta_0^2}\right) \\ & = \frac{2\theta_0^2\pi}{C} = 1 \\ C & = 2\pi\theta_0^2 \end{aligned}$$

and for the distribution finally

$$f(\theta)d\theta = \frac{1}{2\pi\theta_0^2} \exp\left(-\frac{\theta^2}{2\theta_0^2}\right)d\Omega. \quad (5.12)$$

As the scattering angle distribution (5.12) is normalized for $0 \leq \theta < \infty$, the mean scattering angle is obtained by $\sqrt{\langle\theta^2\rangle} = 2\pi \int_0^\infty \frac{1}{2}\theta^2 f(\theta)d\theta^2 = \sqrt{2}\theta_0$.

Projecting onto a plane, one obtains for the mean spatial deflection $\langle y_{proj} \rangle$ of a particle between entrance and exit of material of thickness x due to multiple scattering (figure 5.4):

$$\langle y_{proj} \rangle = \frac{1}{\sqrt{3}}x\theta_0.$$

The factor $\frac{1}{\sqrt{3}}$ occurs because in case of multiple scattering the deflection due to one scattering process can be reduced by another one. For small $\frac{x}{x_0}$ ($10^{-3} < \frac{x}{x_0} < 10$, still allowing for a sufficient number of scattering processes because $x \gg \lambda$ with λ being the mean free path), in more than 60% of all cases the real value of y_{proj} lies within a 5% interval of $\langle y_{proj} \rangle$.

Although in radial direction the thickness of the TRD is only about $0.15x_0$, multiple scattering might be of importance when reconstructing tracks together with TPC and ITS hit points with a high spatial resolution or when reconstructing secondary vertices. Especially the front end electronics that is built directly onto the detector chambers, may be a source of multiple scattering.

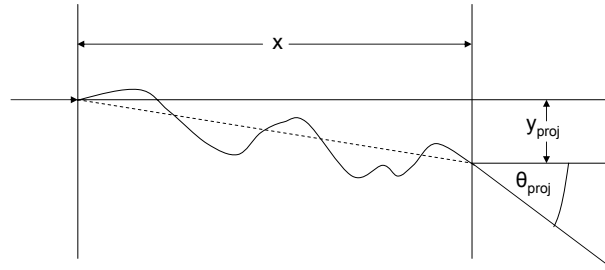


Figure 5.4: Multiple scattering projected onto a plane (idea from [Kol])

5.2.4 Recombination and Electron Attachment

The recombination of electrons and ions may reduce the number of electrons in a cluster substantially. Recombination is possible between electrons and positive ions and between negative and positive ions. If n^+ denotes the number density of positive ions, n^- the number density of negative charges (electrons and negative ions) and α_{rec} the recombination coefficient, then the evolution of the number of positive ions with time is given by $-\frac{dn^+}{n^+} = \alpha \cdot n^- dt$.

Another way to reduce the number of low energetic (eV) electrons is the attachment onto gas molecules. Considering only one scattering process, the probability p_a for the attachment onto an electro-negative molecule is much larger than the probabilities for attachment in case of noble gases or symmetric molecules (CH_4, N_2, \dots). With the average thermal velocity of the electrons $u = \sqrt{\frac{2\bar{\epsilon}}{m_e}} = \sqrt{\langle v^2 \rangle} = \sqrt{\frac{3kT}{m_e}}$ ¹¹ and the mean number of collisions per time $N_c = \frac{u}{\lambda}$ (λ : mean free path), the mean time until attachment occurs becomes $t_a = \frac{1}{p_a N_c}$.

On application of an electric field, the kinetic energy of the electrons increases and by that also the probability p'_a for the attachment in a single collision event, varies with the field strength. If only a fraction f of the gas is electro-negative (in the TRD gas mixture $f = 0.15$ for the CO_2 fraction), the number of collisions per time with these molecules is on average given by $N'_c = f \frac{u}{\lambda}$ (λ mean free path between two collisions of an electron in the

¹¹which one obtains from the Maxwell distribution of the number of electrons with kinetic energies due to thermal motion between ϵ and $\epsilon + d\epsilon$, $\tilde{n}(\epsilon)d\epsilon \sim (kT)^{-\frac{3}{2}} \sqrt{\epsilon} e^{-\frac{\epsilon}{kT}}$. Averaging yields $\bar{\epsilon} = \int_0^\infty \epsilon \tilde{n}(\epsilon) d\epsilon = 3/2kT$. With $\epsilon = \frac{1}{2}m_e v^2$, the distribution $n(v)dv$ for velocities between v and $v + dv$ is obtained, $n(v)dv = \tilde{n}(\epsilon)d\epsilon = \tilde{n}(v) \frac{\partial \epsilon}{\partial v} dv \sim (kT)^{-\frac{3}{2}} v^2 e^{-\frac{m_e v^2}{2kT}} dv$ with which $\sqrt{\langle v^2 \rangle}$ can be calculated

gas mixture¹²). In drift direction (direction of electric field) the mean free drift path until attachment occurs (dominated by the attachment onto the electro-negative molecules) is given by $\lambda'_a = v_D \cdot t'_a = \frac{v_D}{p'_a \cdot N'_c}$. In order to not lose a substantial number of electrons due to recombination, the height of the drift volume d_x should be smaller than λ'_a .

5.2.5 Electron Drift in Electric Fields

The movement of an electron cluster in a gas under the influence of electric and magnetic fields consists of diffusion, superimposed by a drift. The drift is topic of this section. In the following, sometimes the mobility of (positive) ions (μ^+) or electrons (μ^-) in an electric field of strength E will be used. As the drift velocity (v_D^+ for ions, v_D^- for electrons) is proportional to $\frac{E}{p}$, the mobility is defined as the proportional constant,

$$v_D = \mu \cdot E \frac{p_0}{p}$$

with p_0 the pressure under normal conditions. In case of a mixture of n gases with volumic concentration of gas specie k , c_k , and μ_{ik}^+ the mobility of an ion of specie i in gas k , the overall mobility of ions of kind i is given by $\frac{1}{\mu_i^+} = \sum_{k=1}^n \frac{c_k}{\mu_{ik}^+}$.

First a pictorial derivation of the drift velocity is given in the presence of only an electric field. In the last section an additional magnetic field is switched on and the $\vec{E} \times \vec{B}$ contribution to the drift velocity is deduced.

The Drift Velocity

First, it is assumed that there is no electric field. Then, if a bunch of electrons with thermal velocity $u = \sqrt{\frac{2\bar{\epsilon}}{m}}$ and average energy $\bar{\epsilon} = 3/2kT$ is released at a point P they will start to travel away from P isotropically due to their thermal motion. The positions of the first collisions with gas atoms will lie, on average, on a sphere of radius λ (mean free path of electrons in the gas). For a figure see 5.5. Now consider the same process however with an electric field \vec{E} in x direction, $\vec{E} = E_x$. $|\vec{E}|$ is considered to be a sufficiently small disturbance, which changes the velocity of the electrons during the time inside the sphere, τ , only by a small fraction. As it is assumed that there are no collisions inside the sphere, the electrons traveling radially away from P, experience a motion superimposed on their radial movement due to an acceleration in x direction, $a_x = \frac{qE}{m_e}$. This leads to a parabolic movement (parabola opened toward the field direction) of the electrons, which moves their exit points on the sphere as compared to the field-less case. Assuming the effect to be small, one can consider the drift time τ remaining unchanged. The additional distance in x direction is then given by $\Delta x = 1/2a\tau^2$ ($\tau = \frac{\lambda}{u}$). This distance, pointing in x direction, is added to the undisturbed exit point on the sphere (E), leading to a new point E' inside (for the hemisphere opposite to \vec{E} -direction) or outside (for the hemisphere in \vec{E} -direction) the sphere. The electron can be thought to leave the sphere on the projection point of

¹²The collision cross section is assumed to be independent of the gas component. Since the drift velocity ($v_D \approx 1.5 \cdot 10^4 m/s$) is an order of magnitude smaller than the thermal velocity for an electron ($u = \sqrt{\frac{3kT}{m_e}} \approx 1.15 \cdot 10^5 m/s$ at $T = 293K$), it can be assumed that the average number of collisions per time, N'_c , is not influenced by the drift.

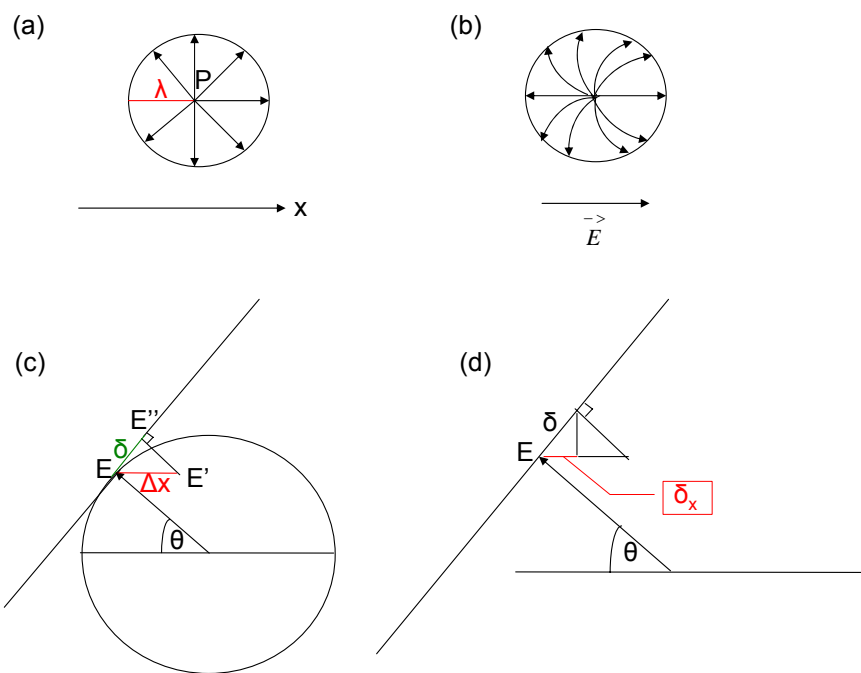


Figure 5.5: Derivation of the drift velocity. The non-scattering sphere. (a): drift without field; (b) parabolic drift with field; (c) new exit point; (d) projection onto the x-axis

E' onto the tangential plane of the sphere through E . As Δx is small as compared to the radius λ , $\Delta x \ll \lambda$, this projection point approximately lies on the sphere and is the new exit point E'' . If θ is the angle between the x axis and the radial direction of the moving electron in the case without field, the distance to the original exit point E is given by the projection length $\delta = 1/2a\tau^2 \sin(\theta)$ (both points are close to each other). In order to calculate the drift velocity in \vec{E} -direction, the distance δ between the two exit points on the sphere without and with field has to be projected back to the x axis. This yields the distance $\delta x = \delta \cdot \sin(\theta) = \Delta x \cdot \sin^2(\theta)$ that an electron in the sphere moves additionally in field direction between two collisions in the time τ , caused by \vec{E} .

Now, in order to get the average effect, the mean of δx is calculated:

$$\langle \delta x \rangle = \frac{1}{2} \frac{qE}{m} \langle \tau^2 \rangle \langle \sin^2(\theta) \rangle$$

$\langle \sin^2 \theta \rangle$ is calculated by averaging over $\cos \theta$:

$$\langle \sin^2 \theta \rangle = \frac{1}{2} \int_{-1}^1 \sin^2(\theta) d(\cos \theta) = \frac{2}{3}$$

thus

$$\langle \delta x \rangle = \frac{1}{3} \frac{qE}{m} \langle \tau^2 \rangle. \quad (5.13)$$

By $\langle \tau^2 \rangle = \frac{\langle s^2 \rangle}{u^2}$ it is enough to calculate the mean of all squared free paths, $\langle s^2 \rangle$, where $\langle s \rangle = \lambda$. If all the electrons were collimated in a beam, their number after a distance s , $N(s)$, would have decreased by $\frac{dN(s)}{N(s)} = -n\sigma ds$ due to scattering (whenever a electron is scattered it is removed from the beam). σ is the scattering cross section (scattering electrons off electrons is neglected due to the small classical electron radius and thus small geometrical cross section) and n the number density of the gas molecules off which the electrons are scattered. Here it is assumed that σ and thus s are independent of u . Integrating yields an exponential decay of the number of unscattered electrons until the distance s : $N(s) = N_0 e^{-n\sigma s}$ (N_0 : initial number of electrons in beam).

The same applies for electrons traveling away radially from P . Once they scatter, they are off the radius s and counted no more. So the probability density to find an electron, that could originally start to travel into any radial direction, between radius s and $s + ds$, is $\sim e^{-n\sigma s} ds$. Regarding also the normalization, $\int_0^\infty e^{-n\sigma s} ds = \frac{1}{n\sigma}$, one obtains for the mean free path

$$\langle s \rangle = n\sigma \int_0^\infty e^{-n\sigma s} s ds = \frac{1}{N_0} \int_0^\infty \left| \frac{dN(s)}{ds} \right| s ds = \frac{1}{n\sigma} = \lambda$$

and the mean of the squared free path

$$\langle s^2 \rangle = \int_0^\infty e^{-n\sigma s} s^2 ds = \frac{2}{(n\sigma)^2} = 2\lambda^2.$$

Inserting this result in 5.13 yields:

$$\langle \delta x \rangle = \frac{2}{3} \frac{qE}{m} \frac{\lambda^2}{u^2}.$$

Finally for the drift velocity one obtains

$$v_D = \frac{\langle \delta x \rangle}{\langle \tau \rangle} = \frac{2}{3} \frac{qE}{m} \frac{\lambda}{u}. \quad (5.14)$$

with $\langle \tau \rangle = \frac{\langle s \rangle}{u} = \frac{\lambda}{u}$. An exact calculation yields a quite similar result:

$$\vec{v}_D = \frac{q\vec{E}}{m} \left(\frac{2}{3} \left\langle \frac{\lambda(u)}{u} \right\rangle + \frac{1}{3} \left\langle \frac{d\lambda(u)}{du} \right\rangle \right).$$

Assuming normal conditions ($p = p_0$) the drift velocity can also be expressed by $v_D = \mu \cdot E$. Comparing this to the equation 5.14 yields for the mobility μ :

$$\mu = \frac{2}{3} \frac{q}{m} \tau.$$

In order to get a constant drift velocity v_D , the energy loss of an electron due to scattering must compensate the energy gain during the time between two scattering processes, $\tau = \langle \frac{s}{u} \rangle$. If $\Delta(\epsilon)$ is the fraction of the whole energy ϵ that is transferred to the molecule or atom at scattering, the following energy equation must approximately hold:

$$qE \cdot v_D \tau = \Delta(\epsilon) \cdot \epsilon.$$

By averaging, this yields

$$qE v_D = \left\langle \frac{\Delta(\epsilon) \epsilon u}{s} \right\rangle.$$

With the kinetic energy $\epsilon = 1/2 m u^2$, by assuming that the energy distribution is a delta peak (only one thermal velocity u) and that $s = \lambda$, this turns into

$$qE v_D = \Delta(\epsilon) \frac{m u^3}{2 \lambda}$$

and finally together with (5.14)

$$v_D \sim \sqrt{\frac{qE}{m}} \lambda \left(\frac{\Delta(\epsilon)}{2} \right)^{\frac{1}{4}}.$$

Above it was always assumed that all scattering processes were elastic collisions. However, in case the gas consists of molecules also inelastic collisions which excite inner degrees of freedom, e.g. oscillator modes of the molecule (0.1..1eV), can occur and become a considerable fraction of the total scattering cross section.

5.2.6 Electron Drift in Electric and Magnetic Fields

If a charged particle (charge q , velocity \vec{v}) moves inside a electric or magnetic field, it experiences the Coulomb force $q\vec{E}$ or Lorentz force $q\vec{v} \times \vec{B}$, respectively. The revolution frequency is obtained by requiring the centripetal power to equal the Lorentz force¹³ and

¹³ $\frac{m v_t^2}{r} = q v_t B$, $\omega = \frac{v}{r}$

is given by $\vec{\omega} = -\frac{q\vec{B}}{m}$. The trajectory in a combined electric and magnetic field is screw-like and can be split into circle-like movement with frequency ω and a translation with drift velocity \vec{v}_D (which does no longer need to be in direction of \vec{E} !).

To obtain \vec{v}_D one has to solve the equation of motion:

$$m\dot{\vec{v}} = q(\vec{E} + \vec{v} \times \vec{B}) + m\vec{A}(t).$$

$m\vec{A}(t)$ is a stochastic force which occurs only in media, e.g. gases, due to collisions with molecules or atoms. As $v_D \sim \frac{qE}{m}\tau$, the mean acceleration of the electrons due to the electric field is given by $\frac{qE}{m} \sim \frac{v_D}{\tau}$ (τ : mean time between two collisions). So in order for the electrons to obtain a constant drift velocity, the average stochastic acceleration must be compensated by the acceleration in the field, $\langle \vec{A}(t) \rangle + \frac{v_D}{\tau} = 0$. By averaging the equation of motion and using $\langle \vec{v} \rangle = \vec{v}_D, \langle \dot{\vec{v}} \rangle = \dot{\vec{v}}_D$ one then obtains

$$\dot{\vec{v}}_D = \frac{q\vec{E}}{m} + \vec{v}_D \times \frac{q}{m}\vec{B} - \frac{\vec{v}_D}{\tau}.$$

As $\vec{E} = \text{const.}$ it follows that $\dot{\vec{v}}_D = 0$ and thus

$$\frac{\vec{v}_D}{\tau} + \frac{q}{m}\vec{B} \times \vec{v}_D = \frac{q\vec{E}}{m}.$$

A solution for this equation is given by

$$\vec{v}_D = \frac{\mu}{1 + \omega^2\tau^2} \left(\vec{E} + \frac{\vec{E} \times \vec{B}}{B} \omega\tau + \frac{(\vec{E} \cdot \vec{B}) \cdot \vec{B}}{B^2} \omega^2\tau^2 \right),$$

where the mobility $\mu = \frac{q}{m}\tau$ was inserted. The drift velocity is a superposition of three vectors: one parallel to \vec{E} , one parallel to \vec{B} ($(\vec{E} \cdot \vec{B}) \cdot \vec{B}$) and one perpendicular to \vec{E} and \vec{B} ($\vec{E} \times \vec{B}$).

To specify the solution for the case of the TRD, the electric field is set along x, $\vec{E} = (E_x, 0, 0)$, and the magnetic field along z, $\vec{B} = (0, 0, B_z)$. Then $\vec{E} \times \vec{B} = (0, -E_x B_z, 0)$. For the components of the drift velocity \vec{v}_D this yields:

$$\begin{aligned} v_{D,x} &= \mu \frac{1}{1 + \omega^2\tau^2} E_x \\ v_{D,y} &= -\mu \frac{\omega\tau}{1 + \omega^2\tau^2} E_x \\ v_{D,z} &= 0. \end{aligned}$$

The total drift velocity is given by

$$v_D = \sqrt{v_{D,x}^2 + v_{D,y}^2} = \mu E_x \frac{1}{\sqrt{1 + \omega^2\tau^2}}.$$

For the angle of \vec{v}_D with respect to the direction of the electric field \vec{E} one obtains:

$$\begin{aligned} \cos \Psi_L &= \frac{\vec{v}_D \cdot \vec{E}}{v_D E_x} = \frac{1}{\sqrt{1 + \omega^2\tau^2}} \\ \sin \Psi_L &= \sqrt{1 - \cos^2 \Psi_L} = \sqrt{\frac{\omega^2\tau^2}{1 + \omega^2\tau^2}} \\ \tan \Psi_L &= \frac{\sin \Psi_L}{\cos \Psi_L} = \omega\tau. \end{aligned}$$

The inclination angle of the drift direction with respect to the electric field direction is called Lorentz angle Ψ_L . If the drift started at (x_0, y_0, z_0) , the y position at a position x is given by

$$y = y_0 + \omega\tau(x - x_0).$$

In the TRD at a magnetic field of $B = 0.4T$, the drift velocity in the region with homogeneous field lines is measured to be $v_D = 1.5cm/\mu s$. From this an Lorentz angle of $\Psi_L = 7.7^\circ$ can be calculated.

The drift velocity however is not constant everywhere. It increases toward the anode wire to values around $3.5cm/\mu s$. In general the relation between drift path and time is given by

$$\vec{x}(t) = \int_0^t \vec{v}_D(t') dt' + \vec{x}_0,$$

where \vec{x}_0 is the spatial position where the charge cluster was created and $\vec{v}_D(t)$ is the local drift velocity at time t . The charge cluster drifts toward the anode wire where it is amplified. The direction of the homogeneous electric field lines (reached by surrounding the drift volume with cathode wires on amplification-side and with a drift-electrode on the opposite side) in the drift volume is in x direction. Setting the origin $x = 0$ to the position of the anode wire and assuming that there is a unique relation between the position of the cluster release, x_0 (being also the distance to the anode wire plane which is perpendicular to \vec{E}), and the drift time t_{drift} the space-time relation can be written as

$$x_0 = \int_0^{t_{drift}} v_{D,x}(t') dt'.$$

In case of constant drift velocity in field direction, $v_{D,x} = const.$, this would turn into

$$x = v_{D,x} t_{drift}.$$

In the TRD, $v_{D,x} = 1.5cm/\mu s$ is almost constant in the drift region. The electron clusters will drift toward the nearest anode wire. As the anode wires have a distance of $0.5mm$ from each other in z direction, this means that charges drifting to this anode wires, can have started traveling at different z positions (the z range for this anode wire is $0.5mm$). This leads to the situation that the drift time is no longer determined only by x_0 but also by z_0 . On the one hand the drift path and thus the drift length varies with z, which alone would not influence t_{drift} if $v_{D,x}$ was constant. However depending on the drift path also regions of different electric field strengths, especially in the amplification region, must be passed. In the region between two anode wires for example the drift field density is reduced whereas an increase of the field strength is observed when charges travel toward the anode wire without a z offset. In this way the drift velocity $v_{D,x}$ changes with the position, which makes the drift time t_{drift} dependent on the drift path and hence on the position of cluster creation (x_0, y_0, z_0) (y_0 does hardly influence the drift time, since the anode wires are collinear to the local SM y axis).

5.2.7 Gas Gain

Once the electron clusters arrive in the amplification region, they will be accelerated and amplified by means of the increasing electric field surrounding the anode wire. By an

avalanche process, each incident electron will be multiplied, creating an avalanche of charge q (figure 5.6). The average amplification charge of an electron, $\langle q \rangle$, is steered by the applied

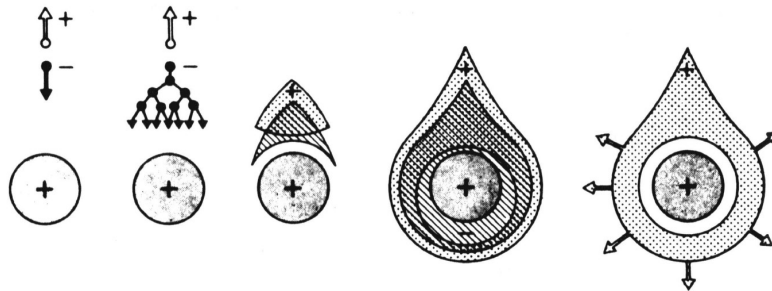


Figure 5.6: Principle of the gas gain at the anode wire [Gut02]

high voltage. The distribution of q is found to be described by an exponential function

$$P(q) = \frac{1}{\langle q \rangle} \exp\left(-\frac{q}{\langle q \rangle}\right)$$

which is used in the simulation to simulate fluctuations of the gas gain.

The gas gain shows an exponential increase as function of the anode-wire voltage. Unless the voltage exceeds some threshold, the charge signal produced by all the electrons of a cluster is proportional to their number. As it was assumed that the electrons were energetically equilibrated and their energy was purely thermal except for the kinetic energy due to their drift, the number of electrons inside a cluster is proportional to the primary energy loss of the incident particle. It follows, that also the height of the charge signal after amplification induced by a cluster, is proportional to the energy loss leading to this cluster.

A larger gas gain does not necessarily lead to a larger signal to noise ratio ($\frac{S}{N}$) of the measured signals. $\frac{S}{N}$ increases by the square root of the original charge in a cluster, which is subject to Poisson statistics. A larger gas gain however enlarges the signal but also the Poisson noise.¹⁴ A larger signal to noise ratio could be obtained by putting independent clusters together (e.g. several clusters per time-bin; the sum of the cluster charges is again Poisson distributed) on cost of position/time resolution. What was neglected in the previous model is a possible error of the digitization, which might be independent of the signal height, thus that the $\frac{S}{N}$ ratio increases with increasing signal. As the signal shall be

¹⁴To see this, the following model for the noise can be applied: Let S be the measured, digitized signal, produced by one cluster. D denotes the "dark signal", meaning the digit that is produced, if no charge is arriving. The fluctuation of D be denoted by σ_D . If the cluster charge before amplification was $q_0 = e \cdot N_e$ (N_e electrons in the cluster) and g is the gas gain, then the charge after amplification is given by $Q = g \cdot q_0$. If k is the transformation factor, which turns charge (via voltage) into a digital number, then the signal is composed by $S = D + k \cdot Q = D + kgeN_e$. It is assumed that k and g are constants with no or only small fluctuations (which is of course not really true for g). The error on the signal, σ_S is then given by $\sigma_S = \sqrt{\left(\frac{\partial S}{\partial D} \sigma_D\right)^2 + \left(\frac{\partial S}{\partial N_e} \sigma_{N_e}\right)^2} = \sqrt{\sigma_D^2 + k^2 g^2 e^2 \sigma_{N_e}^2}$. Assuming that the number N_e of electrons in a cluster is Poisson distributed with $\sigma_{N_e}^2 \approx N_e$, it follows $\sigma_{N_e}^2 = N_e$. Hence $\sigma_S = \sqrt{\sigma_D^2 + k^2 g^2 e^2 N_e}$. This yields for the signal to noise ratio: $\frac{S}{N} = \frac{S}{\sigma_S} = \frac{D + kgeN_e}{\sqrt{\sigma_D^2 + k^2 g^2 e^2 N_e}} \approx \sqrt{N_e}$, if D and σ_D are small. Note, that the quantity $g \cdot N_e$ is not Poisson distributed any more, although N_e is.

proportional to the energy deposit of the incident particle, the gain may nevertheless not be raised unbounded.

Another reason, why one runs at typically low gas gains, is a needed uniformity of the gain. Because electron clusters that were amplified, leave behind a cloud of positive ions (which is denser the larger the gas gain) surrounding the anode wire and drifting away only very slowly due to their small mobility (compared to the electrons which were swallowed quickly by the anode wire), they reduce the effective field that is seen by subsequent electron clusters, by shielding. Hence, also the gas gain decreases. This effect is most pronounced in case of incident tracks entering the chamber at the Lorentz angle Ψ_L (deviation angle with respect to the chamber normal, $\Psi_L = 0$ in case of no magnetic field), when practically all electrons drift toward one spot of the anode wire and also the positive ions are concentrated around this spot. Of course, e.g. due to transversal diffusion and the subsequent different drift path (and drift time) of electrons from one cluster, even at normal incidence of the track, never all electrons (not even of one cluster) will arrive on one spot, but the arrival points will be smeared. However, as this shielding is a local effect depending in addition on the inclination of a track and of the drift time, the gas gain will not be the same any more at different regions of a chamber, for different tracks or different times, which makes the comparison of $\frac{S}{N}$ values or pion rejection efficiencies (which depends on the mean charge per cluster after amplification) very difficult.

Distortions can also occur due to photons that are created during the amplification process. Because the cross section for producing photons is comparable to that of ionization, also energetic photons will be created. These can ionize the gas at some distance from the original cluster. If the ionization occurs in the vicinity of the anode wire, where the electric field starts to be strong enough, such that an electron can gain enough energy between two scattering events to ionize a gas molecule itself, this may lead to an additional avalanche. If the number of electron ion pairs in the gas exceeds some threshold, also the occurrence of sparks becomes likely. Therefore one adds to the drift gas (Xe in the TRD, 85%) a quencher gas, which is an organic gas component (CO_2 for the TRD, 15%) with a large number of degrees of freedom and hence a high cross section for photo absorption, that does not lead to ionization.

To prevent the entrance of the positive ions into the drift volume which would lead to distortions of the homogeneous electric field lines and to an increased recombination rate, a cathode wire plane¹⁵ separates the drift volume from the amplification region. The ions from the amplification processes are collected without influencing much the permeability of the drift electrons. However, still about a third of the produced ions enter the drift volume, leading to a small positive current. Since the TRD has no gating grid, any ionization in the drift volume will lead to an avalanche process and hence to positive ions, drifting back toward the drift volume. The distortions of the electric drift field due to the entering ions is small.

A cluster sees the ion cloud of all its predecessors. The clouds are assumed to drift

¹⁵The cathode wire plane lies on ground. It allows for an independent setting of the negative drift voltage at the drift electrode and the positive anode wire voltage for amplification. The drift voltage is divided by a resistor chain onto several potential strips: The strip closest to the drift electrode lies on full negative potential, whereas the negative potential is lowered at following strips by intermediate resistors, on which the voltage drops. The last resistor is grounded. The cathode wires are therefore only cathodes with respect to the anode wires (but anodes with respect to the drift electrode).

away from the anode wire radially, thus superimposing a cylindrical field to the original field. The ions from one amplification are thus distributed to an increasing surface with increasing time.

Assuming the electric field around the anode wire obeying an exact cylinder symmetry, the undisturbed field strength as a function of radius r ($r > r_a$, r_a the radius of the anode wire) can be written as

$$E_a(r) = \frac{\lambda}{2\pi\epsilon_0 r},$$

where $\lambda = \sigma V$ is the charge density on the wire, σ the wire capacitance (per unit length) and V the anode wire voltage. The ions that are produced during an avalanche process are supposed to drift away radially from the anode wire forming a thin cylinder. If at an instance the radius of this cylinder is R and the charge density λ_{ion} , it will influence the charge density on the wire changing to λ' . Thus, inside the cylinder, $r < R$, the electric field is given by

$$E_{in}(r) = \frac{\lambda'}{2\pi\epsilon_0 r}.$$

This is an effective field accounting for the charge on the cylindrical cover surrounding the anode wire, treated by a reduction of the wire charge density. Outside the cylinder, $r > R$, the field of the cylinder is superimposed on the effective wire field, with the field lines of both fields pointing radially outside thus that the fields can just be summed up:

$$E_{out}(r) = \frac{\lambda' + \lambda_{ion}}{2\pi\epsilon_0 r}.$$

So the charge density on the cylinder, λ_{ion} , reduces the field inside the cylinder (electric field lines opposite to the field from the wire) and amplifies the field of the wire outside (same direction of field lines).

The anode voltage V is the potential between anode wire and cathode and the distance between anode-wire surface and cathode-wire surface is r_{ac} ($r_{ac} \approx 3.5mm$). V is given by integrating the undisturbed electric field over the radius:

$$V = \int_{r_a}^{r_{ac}} E_a(r) dr = \frac{\lambda}{2\pi\epsilon_0} \int_{r_a}^{r_{ac}} \frac{dr}{r}.$$

On the other hand, the total potential difference V in case of a charged cylinder between anode and cathode will remain unchanged, since the system can be seen as a capacitance connected to an external voltage source (the charged medium inside the capacitance reduces the voltage for $r < R$ and increases it for $r > R$). So one can also write:

$$V = \frac{\lambda'}{2\pi\epsilon_0} \int_{r_a}^R \frac{dr}{r} + \frac{\lambda' + \lambda_{ion}}{2\pi\epsilon_0} \int_R^{r_{ac}} \frac{dr}{r}.$$

Evaluating this and resolving for λ' yields:

$$\lambda' = \lambda - \lambda_{ion} \frac{\ln \frac{r_{ac}}{R}}{\ln \frac{r_{ac}}{r_a}}.$$

For the effective reduction of the charge density on the anode wire, which is responsible for the decrease in gas gain (as the electrons see the reduced effective field and are less accelerated) one gets:

$$\frac{d\lambda}{\lambda} = \frac{\lambda - \lambda'}{\lambda} = \frac{\ln \frac{r_{ac}}{R(T)} \lambda_{ion}}{\ln \frac{r_{ac}}{r_a}} \frac{\lambda_{ion}}{\lambda} = \eta(T) \frac{\lambda_{ion}}{\lambda}$$

with the shielding factor $\eta(T)$. Here $R = R(T)$ and thus $\eta = \eta(T)$ because the radius R increases with the ion drift time T and that's why the shielding decreases. The ion cloud is moving away from the wire which means that the drop of the anode wire field decreases.

Assuming that the ions don't see their own effect on the wire field (but only the effect of earlier ion clouds drifting already at larger radii), their drift-time depends only on the wire field from before the avalanche, $\tilde{E}(r) = \frac{\tilde{\lambda}}{2\pi\epsilon_0 r}$. Furthermore it is assumed that the ions begin their drift at the anode wire surface at $t = 0$ and that their drift velocity in vicinity of the electric field $E(r)$ can be written by means of their mobility μ_{ion} in the gas (Xe ion mobility in Xe/CO_2 gas mixture), $v_{D,ion}(r) = \mu_{ion}E(r)$ (drift radially away from the anode wires, along the electric field lines).

$$T = \int_{r_a}^R \frac{dr}{\mu \tilde{E}(r)} = \frac{1}{2} \frac{2\pi\epsilon_0}{\mu \tilde{\lambda}} (R^2 - r_a^2) = \frac{R^2 - r_a^2}{2r_a \mu \tilde{E}(r_a)}$$

To obtain the gas gain drop one has to exploit a dependence between the relative gas gain drop, $\frac{dG}{G}$, and the relative decrease in charge density, $\frac{d\lambda}{\lambda}$.

In order to take into account the gas gain drop due to more than one preceding avalanche, all the contributions to the charge density on the anode wire and thus to the field reduction inside the last ion cylinder have to be added up.

The time dependence of the gas gain for the clusters of one track at normal incidence will differ for electrons and pions. In both cases there will be an early drop in the gas gain due to the clusters from the amplification region that arrive at the anode wires from both sides in one time bin. They produce a large amount of ions shielding the anode wire voltage for later clusters. For pions the charge from the drift volume will approximately arrive at a constant rate and an equilibrium between that rate and the ions moving away from the anode wire turns on. Hence the gas gain drop will level off toward later drift times. In case of electrons, such an equilibrium will not be reached since at later time bins, the cluster charge size increases due to the contribution of Transition Radiation. The gas gain for electrons will show a more marked drop with time than in case of pions.

Signal on the Pads

Once the electron clusters have arrived at the anode wires they are amplified, producing a large amount of electron ion pairs. Because of the large mobility of electrons the ion production process is very fast. The electrons are taken out of the amplification region very quickly by the anode wire and will not produce a considerable signal on the cathode pad plane due (acting as a neutral electrode, capacitance $\approx 20pF$) to its large capacitance (large rise/decay time of the signal $\tau = RC$. Therefore, if the electrons vanish fast, their induced signal on the pad plane is very small). So only the slowly radially drifting ions are left which induce a signal on the pad plane proportional to the number of ions (amount

of charge). Because the ions are created in a short time (ns range) compared to their vanishing by drifting away from the anode wire (μs range), the induced signal on the pad plane has a rather sharp rise (limited only by the rise time of the signal due to $\tau = RC$) and a long fall off, called tail in the following (fall off is governed by the slow ion drift and is much larger than τ)¹⁶. There might be another electron cluster arriving at the anode wire even though the ion clouds of preceding clusters still drift away from it. Then the induced signal by the currently amplified cluster is superimposed on the signal induced by the already drifting ions.

As the anode wires run in $r\phi$ direction (y direction in the local coordinate frame of a sector) and the charge is not arriving on one spot, the spatial extent of the ion cloud in y direction influences the distribution of the charge along one pad row. As it is not possible to take into account all the different positions of one avalanche on the anode wire, for the charge distribution $\rho(y)$ one observes a resulting average effect. It is a good approximation to assume that the whole charge created in one avalanche process is shared between three pads (this is how the pad width ($\approx 7mm$) and the distance to the anode wire ($3.5mm$) were chosen).

In z direction the anode wires are staggered with a pitch of $0.5mm$. Hence, the signal of several anode wires is induced on one pad plane. Since no charge sharing between pad rows is applied, the position resolution in z is limited to pad row granularity.

In y direction however, charge sharing is exploited. The distribution of charge density $\rho(y)$ on pads of a row in case of Multiwire Proportional Chambers (MWPC) (consisting of a cathode wire plane and an anode wire grid), is described by an empirical formula (Mathieson function). This distribution also holds approximately in case of the TRD which consists of a MWPC enlarged by an additional drift volume. The charge on a pad is then considered as the signal response of the pad plane to the avalanche. It is given by the Pad Response Function (PRF):

$$PRF(y) = \int_{y-\frac{W}{2}}^{y+\frac{W}{2}} \rho(y') dy'. \quad (5.15)$$

Here W denotes the width of a pad on this pad plane. If y is the coordinate in the middle of a pad, the PRF gives the fraction of charge distributed on this pad. Otherwise it just sums over the charge that is distributed around half a pad width on either side.

The shape of the PRF resembles a Gaussian distribution (figure 5.7). If a charge cluster arrives at the anode wire at a y position corresponding to the center of a pad, the distribution is peaked at this position and its flanks at distance W are a measure for the charge fraction that is observed on the two neighboring pads. Let $y = 0$ be the center of a pad and assume a charge cluster arriving at the anode wire at $y = 0$ (never mind the incident angle of the track). Then, $PRF(-W) + PRF(0) + PRF(W) = 1$. $PRF(0) \approx 0.8$ and $PRF(W) = PRF(-W) \approx 0.1$, where the symmetry of the PRF was used. 80% of the charge is seen by the central pad, 10% on the neighboring pads, each.

The charge sharing effect will be used by the tracklets for determining the position of a cluster with sub pixel resolution. By determining the central pad (with the largest fraction of charge) and adjusting the PRF (which has been measured in advance) in y according

¹⁶As the ions drift away, the charge density and hence the induced signal decreases until the ions are neutralized when they hit the pad plane or the cathode wire grid. A fraction also enters the drift volume. Their field lines end on the cathode wire plane.

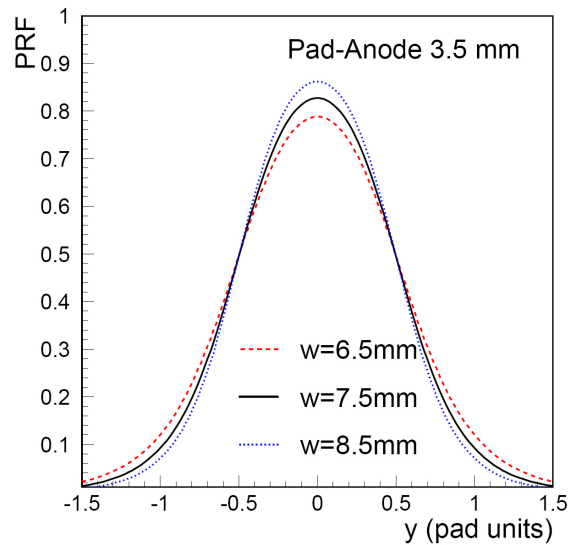


Figure 5.7: Pad Response Function for different widths of pads [ALI01]

to the charge measured on the neighbored pads, one can estimate the y position of the original charge cluster on the anode wire by the peak position of the PRF.

As the length of the pads is in the order of 10cm , charge sharing in z direction is only weak and not exploited for position measurements. So the resolution in z would be restricted by the pad length. However, the pads are inclined with respect to the z direction by the tilting angle $\beta_{\text{tilt}} = \pm 2^\circ$. The sign of the tilting angle is swapped layer by layer. By the tilting of the pads, y and z coordinates are no longer independent of each other. This makes it possible to get information on the z coordinate at a granularity much better than the pad row position. Yet, this is only used in reconstruction algorithms but not on tracklet basis. For the tracklets it is necessary to perform a correction on the slope due to the tilting, which will be discussed later.

5.3 Signal Processing

After having discussed the physical processes involved in the signal creation, the focus is now set to the processing of the signal by the on-chamber electronics. There, two steps have to be distinguished:

- First the signal on the pads is sampled and digitized. Some filter operations can be applied to correct for inefficiencies and distortions. The data that is obtained then is called raw data and is read out upon a valid trigger. This is the data that will be used for the offline reconstruction later on.
- For the calculation of the TRD trigger decision the raw data will be further processed by the on the chamber electronics. The result of this will be the tracklets, that are subsequently sent to the GTU, where they are combined to tracks. The momenta of the tracks, their inclination angle, their PID, etc. can be used to steer the trigger decision of the TRD, depending on the trigger class. The main task here is to perform

all the calculations in a very limited time budget. That's why fast and effective algorithms have to be applied with the cost of accuracy in the parameter determination (position, slope, PID, ...). One could say, that a look on the raw data is taken by the trigger, before it is decided, whether the data is worth being read out.

In the rest of this chapter, the way to the raw data will be followed coarsely. The tracklet reconstruction algorithm will be discussed in some more detail only in the next chapter, because it solely contributes to the trigger but is not needed for track reconstruction.

5.3.1 The Way to Raw Data

In the following the processes on the PASA and ADCs are described. All the processing takes place in parallel on all the channels.

The PASA Contribution

The analog signal on the pad plane is first amplified and shaped by a charge sensitive PASA (Pulse Amplifier and Shaper Amplifier). The time response of the PASA upon an input step function has the shape of a Gaussian with $100ns$ FWHM but being slightly asymmetric (with a tail toward larger times). The PASA turns an incident charge into a voltage with a gain of around $12mV/fC$. Its noise contribution is about 1000 electrons, whereas the signal of an MIP is at 10^4 electrons.

Of special importance is the PASA response upon the signal of an amplified ideal charge cluster with no spatial extent (due to diffusion). The time evolution of the signal on the pads is mainly determined by the slowly moving ions. It has a sharp rise and a decay characterized by a long tail. If $S_{pad}(t)$ denotes the signal evolution on the pads upon a spatially delta shaped charge cluster (the time response of the amplification process) and $S_{PASA}(t)$ is the time response of the PASA upon a time-like delta pulse, then the combined signal that is observable after the PASA and which is called Time Response Function (TRF) is given by the convolution: $TRF(t) = (S_{pad} * S_{PASA})(t) = \int_0^\infty S_{PASA}(t') S_{pad}(t-t') dt'$. This is in some sense the mean of the pad signal weighted with the corresponding amplification by the PASA response¹⁷. Taking into account that $S_{pad}(t < 0) = 0$ (causality: a signal arriving at $t = 0$ cannot impact on times $t < 0$), the TRF can be written as $TRF(t) = \int_0^t S_{PASA}(t') S_{pad}(t-t') dt'$. The tail of the TRF can be approximately described by the sum of two decaying exponential functions.

To obtain the final signal of a realistic charge cluster which is spatially spread due to diffusion, one has to convolute the time dependence of the cluster charge arriving at the anode wire with the TRF. The time dependence is determined by longitudinal diffusion which smears the electrons in drift direction by $\sigma_x(t) = \sqrt{2Dt}$ ($\sigma_x(t)$ is meant to be the width of the Gaussian profile). If the whole charge would be spread along the width only, it would arrive continuously but within a finite time¹⁸(figure 5.9). As the charge is spread

¹⁷Since the TRF at time t is considered, the pad signal height at time t is weighted with the PASA signal height at time 0, the pad signal height at time 0 is multiplied by the PASA signal height at time t . In general, a pad signal, that occurs at time t' contributes to the total TRF signal at time t according to the PASA shaping of the signal at $t - t'$ (that's the lifetime of the pad signal at time t).

¹⁸Let a charge cluster of charge q_i be created at position x_i ($x = 0$ at entrance of drift volume near beam line, $t = 0$ at creation time of the clusters). The cluster drifts with v_D toward the end of the

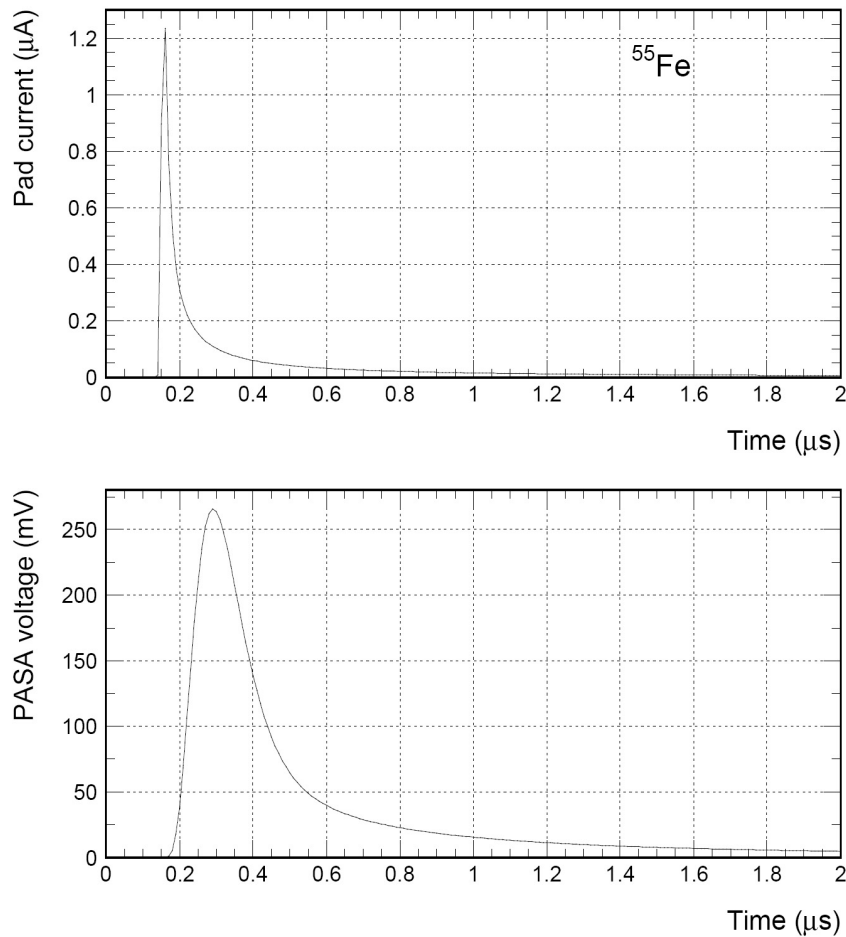


Figure 5.8: The Time Response upon a ^{55}Fe X-ray signal. The charge deposit is almost point like and therefore the signal is very similar to the TRF. In the upper panel the induced signal on the pad without PASA is shown. This corresponds approximately to the amplification response to a pulse. In the lower panel the signal after PASA shaping, hence the Time Response Function, is depicted.[ALI01]

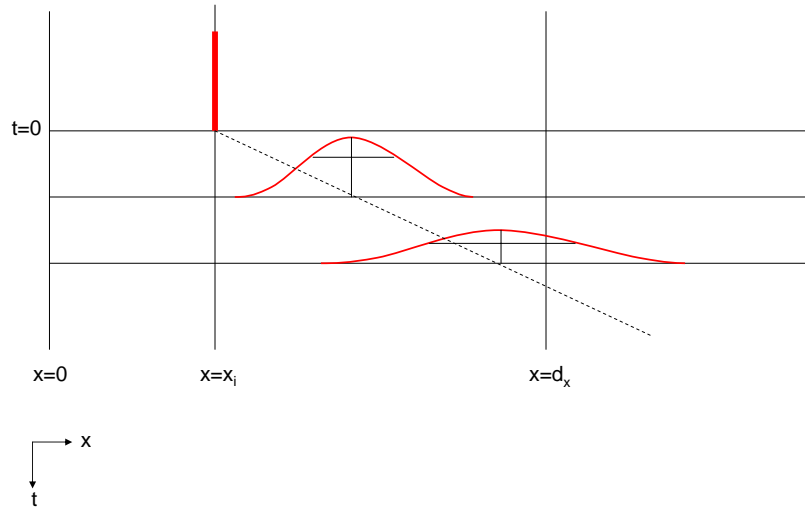


Figure 5.9: Diffusion and drift of a charge peak

according to the Gaussian profile, theoretically it would take infinitely long. In the last section of this chapter, this situation is considered. A cluster that has had a smaller drift path will be smeared less. According to the Gaussian charge distribution, the time dependence of the arriving charge $S_{diffusion}(t)$ is not linear. On average diffusion adds about $50ns$ to the width of the final signal from one cluster $S(t)$. $S(t)$ is given by

$$S(t) = (TRF * S_{diffusion})(t) = (S_{pad} * S_{PASA} * S_{diffusion})(t).$$

The Discretization

The signal $S(t)$ after the action of the PASAs is given to the ADCs (Analog Digital Converter) (in fact, due to the long tail of the amplified cluster signals, there will be overlapping. Refer to the last section for a consideration of this). The PASAs and ADCs are placed on the MCM chip. The digital part of the MCM chip (no PASAs) is called TRAP. There are

drift volume at d_x . It is supposed that no charge is absorbed anywhere (meaning especially, that the whole width during readout is situated at $x \geq 0$). Since all clusters were created instantaneously at $t = 0$, the distance, the cluster has traveled after time t is $v_D \cdot t = x - x_i$. Hence for the width as function of the position: $\sigma(x) = \sqrt{2D \frac{x-x_i}{v}}$. The charge arrives at d_x , if $x + \frac{1}{2}\sigma(x) = d_x$. The position of the cluster (peak) is then: $\tilde{x} = d_x + (\frac{D}{4v_D}) - \sqrt{(d_x + \frac{D}{4v_D})^2 - d_x^2 - \frac{D}{2v_D}x_i}$. This corresponds to a time $\tilde{t} = \frac{\tilde{x}-x_i}{v_D}$. Introducing the readout time t' for $t \geq \tilde{t}$ by $t = \tilde{t} + t'$, the width is given by $\sigma(t') = \sqrt{2D(\tilde{t} + t')}$. The part of the width, situated inside the drift at $x < d_x$ at a time t' is therefore given by $\frac{1}{2}\sigma(t') + (d_x - (\tilde{x} + v_D \cdot t'))$. The position of the starting point of the width at $x < d_x$, $x_{start} = d_x - (\frac{1}{2}\sigma(t') + (d_x - (\tilde{x} + v_D \cdot t')))$ $= (\tilde{x} + v_D \cdot t') - \frac{1}{2}\sigma(t')$. The total time needed, until the whole charge has arrived, is then specified by $x_{end} = d_x$. Solving for t' yields the readout time $\Delta t_{ro} = \frac{1}{2v_D^2} \sqrt{D^2 + 8Dv_D(d_x - x_i)}$.

18 PASA channels and 21 ADC channels placed on one MCM. In order to make position reconstruction via charge sharing also possible on the border of a chip, it is necessary to know about the signal on adjacent pads and thus to share the outer PASA channels between MCMs (always 18 pads of one pad row with 144 pads are assigned to one MCM). This is the reason why 21 ADC channels per MCM are foreseen. Three of them process the analog PASA data from outer channels of neighbored MCMs (the PASA data is split and consequently processed twice in parallel).

First, discretization in the time coordinate is obtained by flashing the signal every $100ns$ or at a rate of $10MHz$. This is done for all ADCs of a MCM with the same clock, hence no phase shift between ADCs should occur. Otherwise different ADCs would be flashed at different times, making their signals not comparable any more. This would deteriorate charge sharing measurements and by this position reconstruction. During the drift time of $2\mu s$, 20 samples are produced (considering also the amplification region, approximately two more samples are needed for its coverage. In the AliRoot simulation 24 time bins are foreseen, thus covering in addition to amplification also times after drift). Assuming the incident particles of an event passing through the detector in time-ranges very small compared to the drift time, all clusters are created instantaneously and one can say that an ADC performs one discretization cycle per event, producing 20 samples.

The whole signal is thus divided into 20 time bins. The value of a time bin before digitization corresponds to the PASA value at sampling time. This value is then digitized by turning it into a 10 bit number, which in the following is called ADC count. The 10 bits are chosen such that the dynamic range of the ADCs, which is coupled to the range of PASA values, is covered.

It can be assumed that almost in any time bin a hit occurs. As the time bin samples are only $100ns$ away from each other but the width of the TRF is already $100ns$ (still enlarged in the final signal by diffusion), the tails of the signal induced by a cluster on the pad plane will reach into the subsequent time bin(s), thus introducing a correlation of the amplitudes in different time bins. Without a tail filter, this would decrease the position reconstruction through charge sharing and additionally enhance the detector occupancy.

Digital Filter

Subsequently the digitized values can be stored in the event buffer and wait for readout or they are filtered. Filtering is performed individually for each ADC channel on the MCM and for each time bin sample. Any of the below mentioned filter steps can be bypassed. During the digital filtering the data word length is enlarged from 10 bits to 12 bits. The two additional bits are added behind the floating point to keep rounding errors below 1 ADC count. The following filter stages are implemented in the order as listed:

- The nonlinearity filter. There is a systematic nonlinearity to the amplification which makes the amplified signal not proportional to the original charge deposit and hence the cluster charge. First, the gas amplification is not totally linear. However, the nonlinearity contribution added by this is negligible as compared to the nonlinearity by the electronics. For example, the amplification in the PASA as well as the conversion to digits within the ADC hide some nonlinearity. The nonlinearity filter is supposed to correct for those influences. Assuming that there exists an unique

mapping between ideally linear distributed signal amplitudes and the disturbed ones for each channel, one can account for the distortions by correcting them with a Look Up Table (LUT). Since the distortion grows only slowly with ADC counts, one correction for a bunch of 16 ADC counts is enough. Therefore there are $2^6 - 1$ correction values. The range of the corrections is $[0, \frac{2^6-1}{2^2}]$, since the last two bits are treated as past-comma bits.

- The pedestal filter. Before the analog signal processing in the PASA starts, a pedestal is added by the PASA to the read out-pad value in order to prevent values below zero from being amplified. This could happen in case the signal on the pad is very small and so, adding the noise of the PASA, the read out value would fluctuate around zero (positive or negative charge). The output of the successive ADC however can only represent non negative digital numbers. The pedestal value changes a lot from channel to channel and also somewhat with time¹⁹. The pedestal value of a PASA is chosen to be some standard deviations of its noise in order to prevent undershoots.

The pedestal filter is designed to detect and subtract the individual pedestal from the signal and add to it a common, configurable baseline, $I_{baseline}$.

If $I(t)$ is the time variation of the input signal, its Fourier transform is given by $\hat{I}(\omega)$. The pedestal is characterized by the Fourier component that is not subject to any oscillations, hence $I_{pedestal} = \hat{I}(0)$. Therefore the goal is to build a low-pass filter whose transfer function approaches a delta function $\delta(\omega)$. It is realized by a relaxation filter with the following discrete recursion equation for the estimated pedestal at time $t + \Delta t$, $P_{est}(t + \Delta t)$:

$$P_{est}(t + \Delta t) = I(t)2^{-\kappa} + P_{est}(t)(1 - 2^{-\kappa}).$$

Here Δt is the time difference between two samplings, $I(t)$ is the flashed signal height at time t and κ is the relaxation constant. By this, the pedestal value of the input signal at the following time sample is estimated, assuming, that it changes only slowly in time. The pedestal for each channel is calculated individually. It is subtracted from the signal and the common baseline is added, in the order of the following operations:

$$O(t) = I(t) + I_{baseline} - P_{est}(t)$$

- The gain filter. The linear amplification also varies from channel to channel. Assuming that the noise is distributed by a Gaussian with the same mean for all channels of a MCM chip, this means that the mean signal to noise ratio $\frac{S}{N}$ is subject to fluctuations. However, within one MCM the charge on the ADC channels must be comparable (same original cluster charge must lead to same signal height) for the tracklet processing, e.g. in order to exploit charge sharing. This is only the case if the overall amplification is the same for all channels of one MCM. The distortions can have many reasons: changes in temperature, pressure, varying distance from the pads to the anode wires due to the sag of the wires (gravitation, high voltage), variations in the anode wire radius (and thus the field strength), inhomogeneous distribution of

¹⁹e.g. because the PASA contribution to the TRF consists partly of pedestal that is added as a tail to later signals. Therefore the fraction of the pedestal on the signal should increase with time

high voltage. But again the main influence comes from the electronics, mostly from variations in the production process. The dynamic range of the ADCs is determined by the range of the PASAs. Thus the pre-amplification and signal shaping in the PASA is the most crucial source for the variations of the linear amplification. To account for this, the filter path contains a gain filter.

The gain factor ρ for each channel has to be pre-calculated by one of the CPUs. Then the input value $I(t)$ is just multiplied by ρ . However the gain filter is applied after the pedestal filter (the reason is discussed later), such that the baseline is multiplied by ρ as well. In order to make the filtered value biased by the baseline $I_{baseline}$ again, a constant has to be added after the multiplication. The obtained output signal after the gain filter, $O(t)$ is then given by $O(t) = I(t)\rho + I_{baseline}(1 - \rho)$, where the constant $I_{baseline}(1 - \rho)$ accounts for the baseline correction ($I(t) = \tilde{I}(t) + I_{baseline}$, $\tilde{I}(t)$: pure, unbiased signal).

The reason why the gain correction is placed after the pedestal correction is, that the correction factor is determined iteratively by comparing the signal amplitude distribution of a channel with an expected reference amplitude distribution. The distribution (corrected for noise) sets on at the pedestal value and is supposed to scale with the gain. A larger gain will bring the higher amplitudes to larger probabilities (although the onset remains at the pedestal). Hence, the idea is to define two amplitudes, T_A and T_B and to count the number of signals I_i for which $T_A \leq I_i < T_B$ (N_A) and $T_B \leq I_i$ (N_B) hold (I_i is a sampled amplitude). Like that also counting noise signals (values around the baseline) is prevented, if T_A is large enough. The two counters are updated with every sample and their fraction $V_i = \frac{N_A}{N_B}$ is supposed to be a measure for the gain shift, if T_A and T_B are set such, that according to the expected reference amplitude distribution their fraction is known (V). The goal is to adjust the fraction in each channel to the desired value V .

- The tail cancellation filter. As was already mentioned, the tail of the TRF, which is mainly due to the slow ion drift, introduces a correlation between time bins. To the signal amplitude of the current cluster, residual signal amplitudes of former clusters are superimposed. This would make position reconstruction based on charge sharing very inexact.

However, the tail of the TRF can be approximated by the sum of two exponential functions. A filter architecture based on continuous signal values, which cuts these tails, can be discretized without changing its general design. This is because the frequency distribution of the input signals to the ADCs have almost a limited bandwidth, such that the loss of information when cutting at the Nyquist frequency $\nu_{Nyquist} = \frac{1}{2}\nu_{sample} = 5MHz$ is negligible. So the whole information can be reconstructed from the sampled values and also the filter can be discretized one to one. The discussion is thus equivalent for the continuous and the discretized case and will be continued for a discretized filter.

The sum of exponentials is given by $g(t) = 1_{t \geq 1} \sum_{n=1}^N \alpha_n e^{-\eta_n t}$, where N is the number of exponentials with which the tail is intended to be approximated and α_n as well as η_n are the corresponding parameters.

Let $f_{PASA}(t)$ be the PASA response function. The observable response of the detector upon a pulse (e.g. induced by a laser) is given by $S(t) = (g * f_{PASA})(t)$. To obtain a measure for the quality of the filter with a given parameter set (α_n, η_n) under detector conditions, first $g(t)$ is calculated with these parameters and applied to $f_{PASA}(t)$. Then the tail filter $F_{tail}^{-1}(t)$ is applied. The result should be similar to the PASA response function, hence have the shape of a Gaussian. A measure for the filter inefficiency could thus be $\int dt [(F_{tail}^{-1} * S)(t) - f_{PASA}(t)]^2$. The result can be evaluated for different parameter sets and different numbers N of used exponential.

For the parameter calibration of the discretized filter, a complete set of sampled data is needed. One can use the average signal that is produced by tracks (e and π) in several events within a chamber. The influence of the tail on the average signal is expressed by an enhancement as compared to the signal without tail, a slight increase of the value in the drift region and a tail for times after the drift (the average signal must be recorded for times larger than the drift time t_{drift}). As it is an average signal, the tail is solely drive by chamber properties, not by individual clusters. Therefore the parameter set can be applied for all tail filters in the chamber. The set of sampled data is given by the average signal $\bar{S}(t)$, $t = k\Delta t$. If this sample is tail filtered, the tail should be declined substantially. Let $\bar{A}(t) = \bar{S}(t) * F_{tail}^{-1}(t)$ the filtered average signal. As an optimization procedure one can try to find the parameter set, for which the

following ratio is minimal: $M = \frac{\sum_{t=t_{drift}}^{t_{end}} \bar{A}(t)^2}{\frac{1}{t_{drift}} \sum_{t=0}^{t_{drift}-1} \bar{A}(t)}$. It is the fraction of the remaining mean tail values after drift (squared in order to enhance their weight) over the mean signal before. The sums run over the sampled values.

Here the tail filter is discussed in some more detail as it is of general importance. In the following first the tail generation process is considered. If $g(t)$ is the continuous time response of the generating filter, the output after convoluting the generator with the time distribution of the incoming signal $I(t)$ is given by

$$O(t) = \int_{-\infty}^t I(t')g(t-t')dt'.$$

Here it was used that $g(t < 0) = 0$ due to causality and hence $t' \leq t$. For an earlier time $t - \tilde{t}$, the output is given by

$$O(t - \tilde{t}) = \int_{-\infty}^{t-\tilde{t}} I(t')g((t - \tilde{t}) - t')dt'.$$

Now this can be simply discretized for sampling times Δt and $t = r\Delta t$ (neglecting a possible time offset):

$$O(t) = \sum_{q=-\infty}^r I(q\Delta t)g((r-q)\Delta t).$$

The output of the filtered signal one sample earlier was

$$O(t - \Delta t) = \sum_{q=-\infty}^{r-1} I(q\Delta t)g((r-q-1)\Delta t).$$

Up to now this was general. Specifying $g(t)$ for the tail generation,

$$g(t) = 1_{t \geq 0} \sum_{n=1}^N \alpha_n e^{-\eta_n t}$$

and taking into account $I(t < 0) = 0$ (hence $q \geq 0$) this yields for the output:

$$\begin{aligned} O(t) &= \sum_{q=0}^r I(q\Delta t) \sum_{n=1}^N \alpha_n e^{-\eta_n(r-q)\Delta t} \\ &= \sum_{n=1}^N \sum_{q=0}^r I(q\Delta t) \alpha_n e^{-\eta_n(r-q)\Delta t}. \end{aligned}$$

For the preceding sample:

$$\begin{aligned} O(t - \Delta t) &= \sum_{q=0}^{r-1} I(q\Delta t) \sum_{n=1}^N \alpha_n e^{-\eta_n(r-q-1)\Delta t} \\ &= \sum_{n=1}^N \sum_{q=0}^{r-1} I(q\Delta t) \alpha_n e^{-\eta_n(r-q)\Delta t} e^{\eta_n \Delta t}. \end{aligned}$$

Let $r_i(t)$ denote the inner sums, thus

$$r_n(t) = \sum_{q=0}^r I(q\Delta t) \alpha_n e^{-\eta_n(r-q)\Delta t}$$

and

$$r_n(t - \Delta t) = e^{\eta_n \Delta t} \sum_{q=0}^{r-1} I(q\Delta t) \alpha_n e^{-\eta_n(r-q)\Delta t}.$$

Then

$$r_n(t) = e^{-\eta_n \Delta t} r_n(t - \Delta t) + I(t) \alpha_n$$

and

$$O(t) = \sum_{n=1}^N (e^{-\eta_n \Delta t} r_n(t - \Delta t) + \alpha_n I(t)).$$

Setting

$$\tilde{r}_n(t) = e^{-\eta_n \Delta t} \cdot r_n(t)$$

yields

$$\begin{aligned} \tilde{r}_n(t - \Delta t) &= e^{-\eta_n \Delta t} \cdot r_n(t - \Delta t) \\ &= \sum_{q=0}^{r-1} I(q\Delta t) \alpha_n e^{-\eta_n(r-q)\Delta t} \end{aligned}$$

and $O(t)$ can be simplified to

$$O(t) = \sum_{n=1}^N (\tilde{r}_n(t - \Delta t) + \alpha_n I(t)).$$

$O(t)$ describes the output signal of the filter at time t with the appropriate contribution of the tail, whereas $I(t)$ is the input signal without tail. In order to get the tail cancellation filter, it is assumed that the input signal has a tail contribution and the output is expected to be tail-free. So one has to reverse the tail generating process by resolving for $I(t)$:

$$I(t) = \frac{1}{\sum_{n=1}^N \alpha_n} (O(t) - \sum_{n=1}^N e^{-\eta_n \Delta t} r_n(t - \Delta t)).$$

The values α_n give the weight for the individual exponential, thus their sum should be unity, $\sum_{n=1}^N \alpha_n = 1$. By renaming $I(t) \rightarrow O(t)$ and $O(t) \rightarrow I(t)$ this finally results in the recursion equation

$$O(t) = (I(t) - \sum_{n=1}^N e^{-\eta_n \Delta t} r_n(t - \Delta t))$$

or

$$O(t) = (I(t) - \sum_{n=1}^N \tilde{r}_n(t - \Delta t))$$

for the tail canceled output. Of course also inside $r(t)$ and $\tilde{r}(t)$, $I(t)$ is renamed by $O(t)$:

$$\begin{aligned} r_n(t) &= e^{-\eta_n \Delta t} r_n(t - \Delta t) + O(t) \alpha_n \\ &= \tilde{r}_n(t - \Delta t) + O(t) \alpha_n; \\ r_n(t - \Delta t) &= e^{\eta_n \Delta t} \sum_{q=0}^{r-1} O(q \Delta t) \alpha_n e^{-\eta_n (r-q) \Delta t}; \\ \tilde{r}_n(t) &= \tilde{r}_n(r \cdot \Delta t) = \sum_{q=0}^r O(q \Delta t) \alpha_n e^{-\eta_n ((r+1)-q) \Delta t} \\ \Rightarrow \tilde{r}_n(t - \Delta t) &= \sum_{q=0}^{r-1} O(q \Delta t) \alpha_n e^{-\eta_n (r-q) \Delta t}. \end{aligned}$$

The recursion of $\tilde{r}_n(t - \Delta t)$,

$$\begin{aligned} \tilde{r}_n(t - \Delta t) &= e^{\eta_n \Delta t} [O(t - \Delta t) \alpha_n + \sum_{q=0}^{r-2} \alpha_n \cdot O(q \cdot \Delta t) \cdot e^{-\eta_n ((r-1)-q) \cdot \Delta t}] \\ &= e^{\eta_n \Delta t} [O(t - \Delta t) \alpha_n + \tilde{r}_n(t - 2\Delta t)] \end{aligned}$$

is used in the simulation for $N = 2$ (hence $\alpha_1 + \alpha_2 = 1$) to calculate

$$O(t) = I(t) - \sum_{n=1}^2 \tilde{r}_n(t - \Delta t).$$

In case $I(t)$ is made up of several contributions $I(t) = I_0(t) + I_1(t) + \dots$, the tail filter output $O(t)$ responds linear and can be split to the output due to the input contributions, $O(t) = O_0(t)[I_0] + O_1(t)[I_1] + \dots$

This becomes important if the original signal height of an ADC value after the tail filter is needed. For this purpose the common baseline must be subtracted. However, as the tail cancellation filter is applied to the signal after the pedestal filter and the baseline is not subtracted at the entrance to the tail filter, the baseline is subject to tail filtering as well. The tail correction, that has to be applied to an input value, is composed by the estimated tail components (exponentially decaying with time) of all previous signals, which all were biased by the baseline. However, the baseline did not belong to the signal, when the tail was added (described by the TRF). The signal, that already contained the tail, was given to the pedestal filter. Thus it is not enough to just subtract the baseline from the signal $O(t)$. The baseline value to be subtracted is time dependent.

To show the linear response of the tail filter first, induction can be used. The first observation is that

$$\begin{aligned} O(0) &= I(0) - \sum_{n=1}^N \tilde{r}_n(-\Delta t), \\ \tilde{r}_n(-\Delta t) &= 0, \\ \Rightarrow O(0) &= I(0) \end{aligned}$$

and

$$\begin{aligned} O(\Delta t) &= I(\Delta t) - \sum_{n=1}^N \tilde{r}_n(0), \\ \tilde{r}_n(0) &= O(0)\alpha_n e^{-\eta_n \Delta t}, \\ \Rightarrow O(\Delta t) &= I(\Delta t) - I(0) \sum_{n=1}^N \alpha_n e^{-\eta_n \Delta t}. \end{aligned}$$

Hence, $O(0)$ and $O(\Delta t)$ are both linear in I . Assuming now that $O(k \cdot \Delta t)$ is linear in I for all $k \leq r$, $O(k \cdot \Delta t)$ can be written as a linear superposition of I :

$$O(k \cdot \Delta t) = \sum_{q=0}^k f_k(N, q) \cdot I(q \cdot \Delta t), \quad 0 \leq k \leq r.$$

$f_k(n, q)$ are prefactors with $f_k(n, k) = 1$. This yields for $O((r + 1) \cdot \Delta t)$:

$$\begin{aligned} O((r + 1) \cdot \Delta t) &= I((r + 1) \cdot \Delta t) - \sum_{n=1}^N \tilde{r}_n(r \cdot \Delta t), \\ \tilde{r}_n(r \cdot \Delta t) &= \sum_{q=0}^r O(q \cdot \Delta t) \alpha_n e^{-\eta_n((r+1)-q)\Delta t} \\ &= \sum_{q=0}^r \sum_{q'=0}^q f_q(N, q') I(q' \cdot \Delta t) \alpha_n e^{-\eta_n((r+1)-q)\Delta t} \\ &= \sum_{q=0}^r g(n, q) \sum_{q'=0}^q f_q(N, q') I(q' \cdot \Delta t) \end{aligned}$$

where $g(n, q) = \alpha_n e^{-\eta_n((r+1)-q)\Delta t}$. By putting everything together, this finally turns into

$$\begin{aligned} O((r + 1) \cdot \Delta t) &= I((r + 1) \cdot \Delta t) - \sum_{n=1}^N \sum_{q=0}^r g(n, q) \sum_{q'=0}^q f_q(N, q') I(q' \cdot \Delta t) \\ &= \sum_{q=0}^{r+1} f_{r+1}(q, N) I(q \cdot \Delta t), \end{aligned}$$

where all terms containing $I(q \cdot \Delta t)$ were collected.

If now $I(t) = \tilde{I}(t) + I_{baseline}$ with $\tilde{I}(t)$ being the "naked" signal and $I_{baseline}$ the common baseline that was added to the signal by the pedestal filter, the filter response can be split in a part $\tilde{O}(t)$, describing the pure signal and $O_{baseline}(t)$ which is the baseline response:

$$\begin{aligned} O(t) = O(r \cdot \Delta t) &= \tilde{O}(t) + O_{baseline}(r \cdot \Delta t) \\ &= \sum_{q=0}^r f_r(q, n) \tilde{I}(r \cdot \Delta t) + I_{baseline} \sum_{q=0}^r f_r(q, n). \end{aligned}$$

In words: The current output signal is made up of the tail corrected non-biased signal and the baseline, corrected for the tail estimates of all previous baselines. This is the reason why the baseline subtraction is time dependent. The tail subtracted non-biased signal is given by $\tilde{O}(t) = O(t) - O_{baseline}(t)$. To obtain the corresponding value of $O_{baseline}(t)$, the tail cancellation has to be applied to the common baseline. It is herefore enough to calculate for each time bin the tail filter response to a unity signal and multiply the result by $I_{baseline}$. These values can be stored in a LUT, whose needed number of entries is limited by the number of time bins.

The time dependent baseline subtraction has to be considered in all cases, in which the unbiased, tail-free signal needs to be extracted from raw data.

- The crosstalk suppression filter. Between adjacent pads there are two dependencies. One is the charge sharing for which no filter is needed as this effect is exploited for

position estimations. The second is capacitive coupling, because the 18 pads are connected to the PASA chip by a ribbon cable. It has been shown that the crosstalk can be described by the slow derivative of the initial signal in the neighboring pads. In the corresponding frequency spectrum the components with $\nu > \nu_{Nyquist}$ can no longer be neglected. Thus there is no exact discrete crosstalk suppression filter but only a filter suppressing an average of the signal between the initial pulse and sampling time (the average does not need to reflect the crosstalk contribution at sampling time).

The discrete crosstalk generator is given by a two dimensional matrix, whose rows handle the pads that are involved and the columns the time bins needed for the averaging process. The crosstalk is mainly limited to the two neighboring pads, hence the matrix has three columns. Depending on the shape of TRD signals that are used for averaging, considering 5 time bins is usually enough.

The crosstalk suppression filter is an approximation to the inverse of the generator matrix and only yields a small suppression of the amplitude but no full correction. The form of the matrix is

$$M = \begin{pmatrix} M_{-2} & 0 & M_{-2} \\ M_{-1} & 0 & M_{-1} \\ M_0 & 1 & M_0 \\ M_1 & 0 & M_1 \\ M_2 & 0 & M_2 \end{pmatrix}$$

It can be seen from the symmetry that neighboring channels are treated equally. By carrying out the two dimensional convolution one obtains the filtered signal at channel ρ and time t :

$$\begin{aligned} O(\rho, t) &= (I * M)(\rho, t) \\ &= \sum_{\zeta=-1}^1 \sum_{\xi=-2}^2 I(\rho - \zeta, t - \xi) M(\xi, \zeta) \\ &= \sum_{\xi} I(\rho + 1, t - \xi) M(\xi, -1) \\ &\quad + \sum_{\xi} I(\rho, t - \xi) M(\xi, 0) \\ &\quad + \sum_{\xi} I(\rho - 1, t - \xi) M(\xi, 1). \end{aligned}$$

As $M(\xi, 0) = \delta(\xi)$ this yields:

$$\begin{aligned} O(\rho, t) &= \sum_{\xi} I(\rho + 1, t - \xi) M(\xi, -1) \\ &\quad + I(\rho, t) \\ &\quad + \sum_{\xi} I(\rho - 1, t - \xi) M(\xi, 1). \end{aligned}$$

Hence the matrix structure with $M(\xi, 0) = \delta(\xi)$ expresses that only a first order correction is applied. Exploiting the symmetry, $M(\xi, \zeta) = M(\xi, -\zeta)$ for all ξ , this

finally leads to

$$O(\rho, t) = I(\rho, t) + \sum_{\xi=-2}^2 M(\xi, 1)(I(\rho + 1, t - \xi) + I(\rho - 1, t - \xi)).$$

The whole crosstalk suppression process needs to be causal. However, as the filter for the correction of the current signal $I(\rho, t)$ uses two inputs from future signals, the output $O(\rho, t)$ has to be delayed by two cycles. The values of five subsequent time bins are stored. The central of these five values is the one to be crosstalk corrected, as it has access to two values of its past (stored earlier) and two of its future (stored later).

In the following the order of the filter stages shall be discussed. The digital filter is mainly intended to correct for distortions within the signal path, that happen from the amplification process on, including effects originating from the electronic signal processing (e.g. nonlinearity and gain distortions are mainly added by the electronics). The distortions to the signal can be quantized by applying the corresponding generator operators F to the ideal signal. Applying the distortion generators considered here in their original order, given by the signal path, yields the operator A :

$$A = F_{nonlinear} \circ F_{gain} \circ F_{pedestal} \circ F_{crosstalk} \circ F_{Tail} \circ G_{PRF}.$$

G_{PRF} denotes the spread of the signal to adjacent pads which is used for the position reconstruction. This contribution to the signal is not to be filtered away.

In the following, the contribution of an incoming charge cluster to the signal on a specific pad is considered. First, the charge is amplified. Since the anode wire is $3.5mm$ away from the pad plane, the ion charge is mirrored not only on the central pad, but also one pad width (either side) in y direction away, affecting also the two neighboring pads with the current signal. This means, that only about 80% of the induced charge is seen on the central pad. The slow movement of the ions introduces a tail. This makes the signal spread also over adjacent time bins. Since the ions are supposed to drift away radially from the anode wire, a part of the ions comes closer to the pad plane with time, another part travels away from the pad plane. Therefore, the tail signal at later time bins would be based on a different fraction of the amplification charge. This is however neglected and it is assumed, that the tail on a pad is due to the fraction of charge, that was mirrored on that pad at creation time. This is an assumption used in the digital tail cancellation and also the reason, why F_{Tail} comes after G_{PRF} . Once the signal is induced on the pads, due to capacitive coupling of the pads of one pad row, the signal is slightly spread over the pads in the neighborhood and over several time bins (due to the slow decay time). Tail and crosstalk have to be corrected for, because otherwise they would influence the charge sharing and deteriorate position reconstruction in y direction.

In a next step, the electronics is involved. The PASA first adds a pedestal to the signal. Then it amplifies and shapes the charge, which influences the overall gain. The subsequent digitization may also add some distortions. Based on the final signal, including pedestal and gain, a characteristic nonlinearity occurs. The nonlinearity is supposed to be pad specific. The electronics adds the largest contribution to it. The assumption is, that the nonlinearity is a monotone function of the measured digit and that therefore the nonlinearity-corrected

digital value is given by an unique mapping of the measured one. Pedestal, gain and nonlinearities change the signal in a nonlinear way. Without correcting for these effects, the final measured signal would no longer be an accurate, proportional measure for the original signal, namely the charge deposit of an incident particle.

If F and F' are linear and shift invariant with respect to time and space, their position in the chain can be interchanged: $F \circ F' = F' \circ F$. Note that for a signal with time and space dimensions the interchanging is only allowed, if the filters are shift invariant w.r.t. those dimensions, they affect and if they respond linear to the input signal. Convolution operators on the other hand are always commutative²⁰. Therefore, their position can be interchanged arbitrarily without influencing the obtained signal. Since $F_{nonlinear}$ does not respond linearly to an input signal ($F_{nonlinear} \circ (c \cdot G) \neq c \cdot F_{nonlinear} \circ G$) its output explicitly depends on the output of the combination of all preceding generators. Its position cannot be interchanged with any of the other generators and the application to a signal can therefore not be described by a convolution. The pedestal filter, which adds a constant to the signal, is not linear either: $F_{pedestal} \circ (G + G') \neq F_{pedestal} \circ G + F_{pedestal} \circ G'$ (in the first case, the pedestal is added once, in the latter case twice). Neither is the gain filter, which multiplies the signal by a factor but also adds a signal-independent value ($O(t) = \rho \cdot I(t) + I_{baseline} \cdot (1 - \rho)$). However, assuming that the pedestal makes up only a small fraction of the signal, for the change of the signal due to gain instabilities the pedestal will not add a considerable effect. Therefore, F_{gain} and $F_{pedestal}$ can be interchanged. F_{tail} and $F_{crosstalk}$ are both linear and shift invariant with respect to time and space and their action is assumed to be described by a convolution. Therefore, they can be interchanged.

Interchanging the position of the generators, respecting the above restrictions, yields:

$$A = F_{nonlinear} \circ F_{pedestal} \circ F_{gain} \circ F_{Tail} \circ F_{crosstalk} \circ G_{PRF}.$$

The combined filter operator D is now supposed to cancel all the distortions F , beginning with the last one, that was added (running through the generator tail in opposite direction). The condition is $D \circ A = G_{PRF}$ (G_{PRF} is not considered a distortion). Thus,

$$D = F_{crosstalk}^{-1} \circ F_{Tail}^{-1} \circ F_{gain}^{-1} \circ F_{pedestal}^{-1} \circ F_{nonlinear}^{-1}.$$

F^{-1} are the inversed generators, thus the filter operators²¹. They are applied in the order as listed above. The modular design allows for example for the bypassing of individual filter steps.

²⁰This can be seen by a transformation to the Fourier domain. For one dimensional, continuous convolution operators (corresponding to a vector with an infinite number of entries), the Fourier Transform of the convolution is given by $(f \hat{*} g)(\omega) = \int e^{-i\omega t} dt \int dt' f(t')g(t - t')$. The Fourier Transform of $g(t - t')$ is given by $\int dt e^{-i\omega t} g(t - t') = \int dt e^{-i\omega(t+t')} g(t) = e^{-i\omega t'} \hat{g}(\omega)$. Therefore $(f \hat{*} t)(\omega) = \int dt' f(t') \int e^{-i\omega t} g(t - t') dt = (\int dt' f(t') e^{-i\omega t'} \hat{g}(\omega) = \hat{f}(\omega) \cdot \hat{g}(\omega) = \hat{g}(\omega) \cdot \hat{f}(\omega) = (g \hat{*} f)(\omega)$. The Fourier Transform of the convolution of two operators is given by the product of their Fourier Transforms. Applying $f * g$ on a signal S yields in time space: $S'(t) = [(f * g) * S](t)$. Going into Fourier domain: $[(f \hat{*} g) * S](\omega) = (f \hat{*} g)(\omega) \cdot \hat{S}(\omega) = \hat{f}(\omega) \cdot \hat{g}(\omega) \cdot \hat{S}(\omega) = (g \hat{*} f)(\omega) \cdot \hat{S}(\omega) = [(g \hat{*} f) * S](\omega)$. Going back into time-space, this yields $S'(t) = ((g \hat{*} f) * S)(t)$.

²¹If F denotes a matrix convolution operator, then the inverse F^{-1} must fulfill the convolution equation $F^{-1} * F = U$, where U is a unity matrix. If G is a signal, U is defined by $U * G = G$ (U is filled by 0 everywhere except for its "origin" position, corresponding to $t = 0$ and $y = 0$; when applied to a pixel of G , U just copies its value to the output matrix). The inversion of the discrete tail generator F_{tail} has been shown above, however without transferring the recursive equation for $O(t)$ into an explicit one depending only on t and $I(t - k\Delta t)$ ($O(t) = O(I(t), I(t - \Delta t), \dots, I(0), t)$). The point spread function

The filtered values are called raw data. They are stored in the event buffers until readout and serve as input to the preprocessors for the further tracklet calculation.

For a more detailed consideration of the generation process, the following picture can be applied: The incoming signal G is given as a matrix with a time and a pad dimension (considering pads of a pad row is enough, since there is no interference expected between pads of different rows), whose entries are denoted by $g_{i,j}$, $0 \leq i < N_{tb}$ (N_{tb} : number of time bins), $0 \leq j < 144$ (144: number of pads in a row). The entries of the incoming signal matrix are the cluster charges arriving at the anode wires at different pads and different time bins. Since a digital filter is applied, the following considerations are restricted to digital values (the cluster charges already translated into digits by performing the PASA transformation and the ADC digitization in advance). It is assumed, that all effects are considered at sampling time and at the readout points of the pads, hence the matrix is discrete in both dimensions. All generators but $F_{nonlinear}$, $F_{pedestal}$ and F_{gain} are linear convolution matrices, which are applied on each entry of the signal matrix. For the convolution, \circ can be replaced by $*$. The dimensions of the overall convolution-generator matrix $\tilde{A} = F_{crosstalk} * F_{Tail} * G_{PRF}$, containing effects that can be described by a convolution, are given by the maximum number of pads involved (5, as determined by $F_{crosstalk}$) and the maximum number of involved time bins (principally as many, as are read out: $N_{tb} + 2$; determined by F_{Tail} and $F_{crosstalk}$). A generator is applied to each entry of the signal matrix by discrete convolution (see [Jae02]) and writes back the result to the same entry after the convolution. This modified signal matrix is the outcome of the current generator and the input to the next one in the chain. The signal at a time i of pad j , that is finally observed after the generation process, is given by $((F_{nonlinear} \circ F_{pedestal} \circ F_{gain}) \circ (\tilde{A} * G))_{ij} = [(F_{nonlinear} \circ F_{pedestal} \circ F_{gain}) \circ (F_{Tail} * F_{crosstalk} * G_{PRF}) * G]_{i,j}$ (figure 5.10)²².

of the tail cancellation operator F_{tail}^{-1} would be given by the vector $(O(0), O(\Delta t), O(2\Delta t), \dots)$ by the explicit form of $O(t)$, when setting $I(0) = I_0 = O(0)$ and $I(k\Delta t) = 0$ for $k > 0$. For the continuous case, the inverse $f^{-1}(t)$ of an operator $f(t)$ is characterized by $(f * f^{-1})(t) = \delta(t)$, hence the equation $\int dt' (f(t') f^{-1}(t - t')) = \delta(t)$ has to be solved.

²²The generators are the point spread functions of a single pixel. Thus they describe, how the pixel evolves with time and space and spreads into the neighboring pixels. The convolution with a generator at a given pixel then weights the values of all pixels, that can be involved by causality, with the value of the point spread function that corresponds to their relative positions. Take for example F_{TRF} . The generator matrix is just a column vector that contains in its time bin entries the corresponding values of the time response function (which is the point spread function in this case): $F_{TRF}(i \cdot \Delta t) = 1_{i \geq 0} \sum_n \alpha_n e^{-\eta_n \cdot i \Delta t}$. The discrete convolution with a signal vector $\vec{g}_j = (g_{0,j}, g_{1,j}, \dots, g_{N_{tb},j})$ yields for the signal at a time i : $g'_{i,j} = (\vec{F}_{TRF} * \vec{g}_j)(i) = \sum_{i'=0}^{\infty} F_{TRF}(i' \cdot \Delta t) \cdot g_{i-i',j}$. The lower boundary of the sum was set to i , since a contribution only occurs for $i' \geq 0$. The upper boundary would only be limited, if $g_{i-i',j} = 0$ from some i' on. The convolution says, that the signal of a pixel from i' time bins in the past (meaning at time $i - i' \leq i$) is weighted with the point spread function at time position i' , hence with $F_{TRF}(i' \cdot \Delta t)$. From this it also becomes clear, that if the value of a pixel has a contribution from pixels of its future ($i - i' > i$ or $i' < 0$), each pixel must be spread into its own past, hence, the point spread function is not causal and has entries at negative times. The crosstalk generation for example, that needs for the evaluation of a pixel value an average over five time bin values, of which two are in the future, therefore requires the generator vector (which is the point spread function) to have two non vanishing entries in the past. Let F be a generator with two additional inputs at negative times, hence $\vec{F} = (F(-2), F(-1), F(0), F(1), \dots)$. Convolution yields (omitting the index j): $g'(i) = (\vec{F} * \vec{g})(i) = \sum_{i'=-\infty}^{\infty} F(i') \cdot g(i - i') = \sum_{i'=-\infty}^{\infty} F(-i') \cdot g(i + i') = \sum_{-\infty}^2 F(-i') \cdot g(i + i')$, the latter because $-i' \geq -2$. This shows, that by equally naming the pixels in the generator vector F and the signal g (same direction of time bin increase), convolution is obtained by laying the mirrored

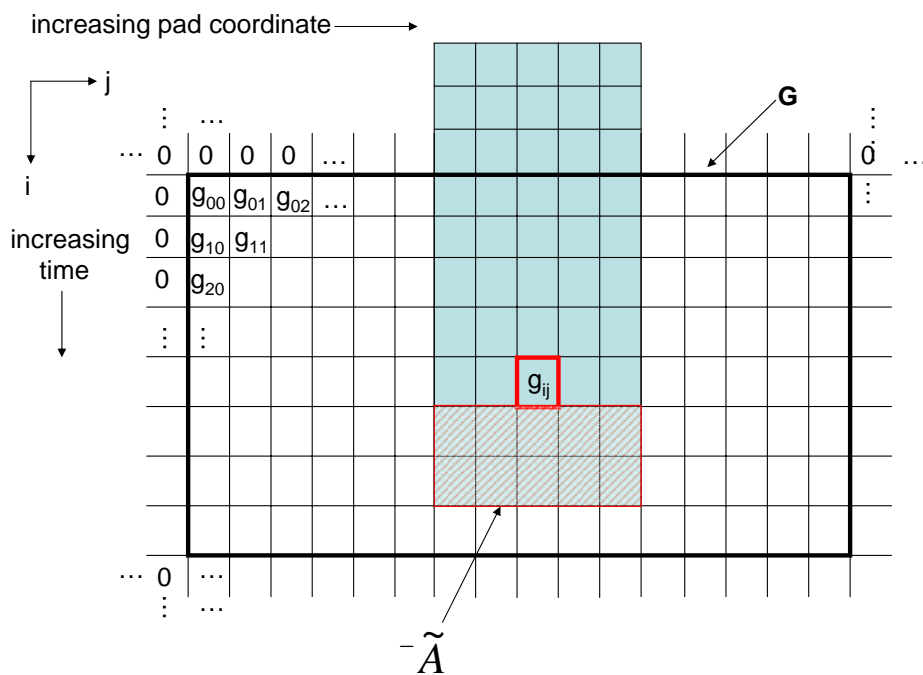


Figure 5.10: Action of the non-symmetric filter chain \tilde{A} on a discrete and sampled signal G , containing the (digital) cluster charges. Here, \tilde{A} is applied on G at position $g_{i,j}$, which yields the signal observed on pad j at time bin i . Note, that due to the crosstalk generator, \tilde{A} acts also upon two time bins in the future. The notation $-\tilde{A}$ symbolizes the mirrored generator \tilde{A} , which is laid upon G at the pixel $g_{i,j}$ in order to calculate the convolution by a direct multiplication of the pixels. The shaded two time bins correspond to the entries of \tilde{A} at negative times.

Let T be the shift operator in time bin direction, $T_k \circ G = G^{T_k}$, with $g_{ij}^{T_k} = g_{i-k,j}$ (it is assumed, that rows with $i < 0$ and $i \geq N_{tb}$ as well as columns with $j < 0$ and $j \geq 144$ of the signal matrix are filled by 0, to prevent boundary effects). S be the shift operator in space direction, $S_k \circ G = G^{S_k}$ with $g_{ij}^{S_k} = g_{i,j-k}$.

When considering only one pad, all generators are independent of time. Hence, they are especially invariant with respect to the sampling time. The action on the input signal is an unique function of the signal value ($F_{pedestal}$ adds a constant, F_{gain} amplifies the signal by a linear factor ρ but also adds a constant, $F_{nonlinearity}$ maps the value to another value in a non-linear way. For the other generators F_{tail} , $F_{crosstalk}$ and G_{PRF} , the output is proportional to the input, as they are linear operators) without explicit time dependence. Respecting the position in the generator chain, this means that $T \circ (F \circ G') = F \circ (T \circ G')$ (F and T commute), if G' denotes the signal that enters the generator F . Therefore the whole signal generation A is invariant with respect to the sampling time and hence also the reversed filter D is.

$F_{Tail} \circ F_{crosstalk} \circ G_{PRF}$ is also supposed to be pad-coordinate invariant (because each of the generators is) and therefore would commute with S (with $F_{crosstalk}$ and G_{PRF} including cluster of pads in the generation process). By that, F_{Tail} , $F_{crosstalk}$ and G_{PRF} each are linear, time and space shift-invariant convolution operators. However, gain, pedestal and the LUT for nonlinearity correction are pad specific and are not invariant under a space shift and therefore also A is not.

A summary of the operator features is shown in table 5.1.

Table 5.1: Features of the signal generators as considered by the digital filters

operator	linear	shift invariance		number of pixels		convolution
		time	space	time	space	
$F_{nonlinear}$	-	✓	-	1	1	-
F_{gain}	-	✓	-	1	1	-
$F_{pedestal}$	-	✓	-	1	1	-
$F_{crosstalk}$	✓	✓	✓	5	3	✓
F_{tail}	✓	✓	✓	all	1	✓
G_{PRF}	✓	✓	✓	1	3	✓

Summary of the Signal Path and Modeling

The different steps between the energy loss of an incident particle to the measured (digital) signal have all to obey one rule: The measured signal in the end must be related to the incident energy deposit. The easiest relation is a proportionality, which requires from each step, that its output is proportional to its input. This is the case, if the contribution of each signal generator step to its input signal can be described by a linear operator.

generator vector over the signal, multiplying the pixel entries, that fall together, add them up and write them to pixel i of the output-signal matrix. Pixel 0 (that corresponds to time bin 0) of the generator vector has to fall together with pixel i of the signal. The same applies for multidimensional generator matrices (pads and time bins), which have to be mirrored in two coordinates.

In this section, the different signal creation and processing steps are investigated in this direction and as an example, a concrete model of the diffusion generator is constructed. The generators are considered as convolution operators exclusively (the non-linearity effects are not taken into account in this section).

- The start of the signal creation and signal processing chain is the energy deposit of an incident particle. The primary energy deposit δE produces an electron, which, in secondary processes of ionization, produces further electron ion pairs in the vicinity of the primary energy deposit. In that way a first transformation from energy to charge is performed. The electrons of this cluster drift toward the anode wire and are subject to the effects, described in this chapter. The detector has to be created such, that the charge of a cluster, that finally arrives at the anode wire, is proportional to the primary energy deposit.
- The amplification of the cluster charge produces in an avalanche process a multiplication of the number of charges in the cluster. The gas gain has to be chosen such, that the charge of the avalanche is a defined multiple of the cluster charge. Note that the signal of the avalanche is due to positive ions, whereas the input were negative electrons.
- Next, the signal, that is mirrored on a pad (which is supposed to be a linear function of the avalanche ion charge), is detected by the electronics. Assuming that the avalanches arrive at separated spots in time, the PASA would convert the charge into voltage, and form a signal whose height is proportional to the voltage and which has a width of $100ns$ FWHM with an additional tail. Although the avalanches arrive separated in time, the signal does not come on a spot but is broadened by longitudinal diffusion and the slow ion movement. Including the resulting tail, the PASA output would be the convolution of all contributions: the PASA response, the tail response, the diffusion response. However, the signals that arrive are not separated enough in time to assume, that they do not interfere. Especially the tail of preceding signals overlap with the current signal. In a model of the signal, that is finally given to the ADCs, all these contributions have to be considered.

The model presented now is based on the assumption, that the effects can be described by generators, whose action on the signal is given by a convolution. Moreover, the generators are supposed to be linear and shift invariant w.r.t. time and space coordinates. Linearity is required already to make the outcoming and measured signal proportional to the input signal (the charge deposits). Since convolution is commutative, the order of the operators can be interchanged.

In the following, $t = 0$ corresponds to the time, when a charged particle enters the detector and starts the readout. $x = 0$ corresponds to the boundary of the drift chamber in direction to the beam line. x is counted positive toward the pad plane along an axis perpendicular to the chamber. The incident particle is so fast, that all clusters are created almost instantaneously at $t = 0$ and that the creation points are an offset to the linear drift length-time correlation.

In an idealization one can assume, that the i^{th} charge cluster was created at one spatial spot x_i . The spatial position of the signal without any additional effects

would then be described by

$$S_{create}(x) = \sum_{i=1}^N q_i \delta(x - x_i)$$

if there were N charge clusters in the detector. Now, drift is switched on. The space response function $f_{drift}(x)$ describes the position of a delta-shaped charge pulse and is given by $f_{drift}(x) = \delta(x - v_D \cdot t)$ (v_D : constant drift velocity). The signal, after switching on drift, $S_{drift}(x)$ (including the creation and the drift), is given by the convolution²³

$$\begin{aligned} S_{drift}(x) &= S_{create}(x) * f_{drift}(x) \\ &= \sum_i q_i \int dx' \delta(x' - x_i) \delta(x - v_D \cdot t - x') \\ &= \sum_i q_i \delta(x - v_D \cdot t - x_i) \\ &= \sum_i q_i \delta(x - v_D(t + t_i)). \end{aligned}$$

Here it was exploited that $x = 0$ for $t = 0$ and thus that the creation position of the i^{th} cluster corresponds to a drift time of $t_i = \frac{v_D}{x_i}$. In the following, all effects that reduce charge (e.g. recombination) are neglected. Although the charge of a cluster is made up of a discrete number of particles, the charge is treated as if it was continuous. Finally it is assumed, that only longitudinal diffusion is responsible for a spread in time of the arriving cluster charge (arriving at the pad plane). Neglecting drift for a moment, the continuous spatial distribution of the cluster charge at a time t is given by equation (5.9). If a delta-like charge cluster q_i was created at $x = 0$, the total accumulated charge (that penetrates a surface) at a position x' and at time t of this cluster, $Q_i(t, x')$ (assuming that all incoming charge is detected), is given by

$$Q_i(t, x') = \int_{x'}^{\infty} dx \frac{q_i}{\sqrt{4Dt}} e^{-\frac{(x)^2}{4Dt}}$$

(figure 5.11). If $f_{diff,q_i}(t, x')$ describes the diffusion response function, i.e. the charge evolution of the cluster at position x' , then

$$Q_i(t, x') = \int_0^t dt' f_{diff,q_i}(t', x').$$

Therefore

$$\begin{aligned} f_{diff,q_i}(t, x') &= \frac{d}{dt} Q_i(t, x') \\ &= \frac{d}{dt} \int_{x'}^{\infty} dx \frac{q_i}{\sqrt{4Dt}} e^{-\frac{(x)^2}{4Dt}}. \end{aligned}$$

²³Note, that the weighting function for the convolution corresponds to the point spread function or, equivalently, to the response function of the considered signal generator

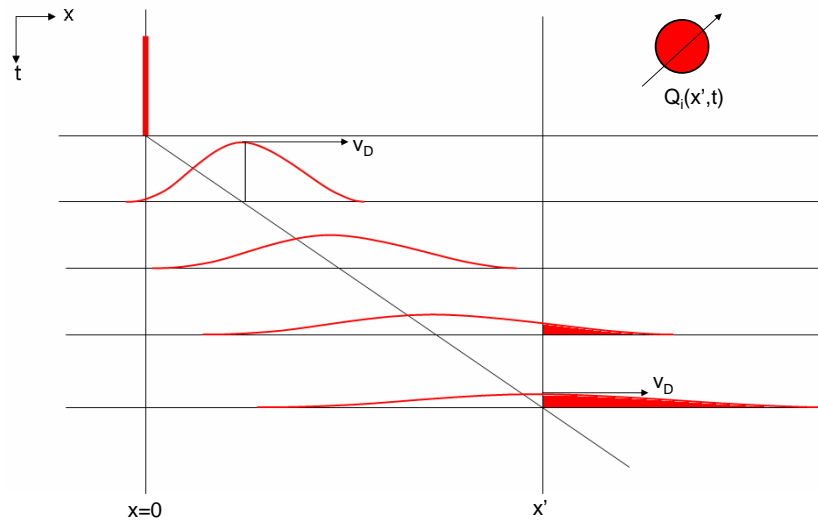


Figure 5.11: Diffusion of a delta peak. The total charge $Q_i(x', t)$ measured at x' , is the integral over the incoming portion of the Gaussian tail.

Since $Q_i(t, x')$ is a monotone increasing function with time for all x' , $f_{diff, q_i}(t, x') \geq 0$ for all t and all x' . If $x' < 0$

$$\begin{aligned} f_{diff, q_i}(t, x') &= \frac{d}{dt} \int_{-\infty}^{x'} dx \frac{q_i}{\sqrt{4Dt}} e^{-\frac{(x)^2}{4Dt}} \\ &= \frac{d}{dt} \int_{|x'|}^{\infty} dx \frac{q_i}{\sqrt{4Dt}} e^{-\frac{(x)^2}{4Dt}}. \end{aligned}$$

In that sense, the following considerations are also valid for negative coordinates. For the following, the normalized response function to unit charge is needed,

$$f_{diff}(t, x') = \frac{d}{dt} \int_{-\infty}^{x'} dx \frac{1}{\sqrt{4Dt}} e^{-\frac{(x)^2}{4Dt}}.$$

Again, the signal after diffusion at a position x , $S_{diff}(x)$, including creation, drift and diffusion, is obtained by convoluting $S_{drift}(x)$ with $f_{diff}(x)$:

$$\begin{aligned} S_{diff}(x, t) &= S_{drift}(x) * f_{diff}(x, t) \\ &= \sum_i q_i \int dx' \frac{d}{dt} \int_{x'}^{\infty} dx'' \frac{1}{\sqrt{4Dt}} e^{-\frac{(x'')^2}{4Dt}} \delta(x - x' - v_D(t + t_i)) \\ &= \sum_i q_i \frac{d}{dt} \int_{x - v_D(t + t_i)}^{\infty} dx'' \frac{1}{\sqrt{4Dt}} e^{-\frac{(x'')^2}{4Dt}} \\ &= \sum_i q_i \frac{d}{dt} \int_0^{\infty} dx'' \frac{1}{\sqrt{4Dt}} e^{-\frac{(x'' + x - v_D(t + t_i))^2}{4Dt}}. \end{aligned}$$

Now, the signal is needed on the pad plane. Let x_{pad} be the coordinate of the pad plane. Then one obtains for the time evolution of the cluster charge arriving at the pad plane:

$$S_{diff}(x_{pad}, t) = \sum_i q_i \frac{d}{dt} \int_0^\infty dx'' \frac{1}{\sqrt{4Dt}} e^{-\frac{(x'' + x_{pad} - v_D(t+t_i))^2}{4Dt}}.$$

It was not really correct to say $S_{diff}(x_{pad}, t)$ was the signal on the pad plane, because the signal on the pad plane is modified by the slow movement of the ions. It is more accurate to define $S_{diff}(x_{anode}, t)$ as the time evolution of the signal on the anode wire. The ion movement only affects the time evolution of the signal (adds a tail to it). Let $f_{ion}(t)$ be the time response function of the avalanche process upon a delta shaped incoming signal on the anode wire. $f_{ion}(t)$ can be described by the sum of exponentially decaying functions, $f_{ion}(t) = 1_{t \geq 0} \sum_{n=1}^N \alpha_n e^{-\eta_n t}$. The actual observed signal on the pad plane is given by

$$\begin{aligned} S_{ion}(t) &= S_{diff}(x_{anode}, t) * f_{ion}(t) \\ &= \sum_i q_i \sum_{n=1}^N \alpha_n \int dt' \left[\frac{d}{dt'} \left(\int_0^\infty dx'' \frac{1}{\sqrt{4Dt'}} e^{-\frac{(x'' + x_{pad} - v_D(t'+t_i))^2}{4Dt'}} \right) \cdot 1_{(t-t') \geq 0} e^{-\eta_n(t-t')} \right]. \end{aligned}$$

$S_{ion}(t)$ contains creation of the clusters, drift, diffusion and tail. Usually, the tail is the most prominent contribution. It can be described by an exponential decay of the signal. The PASA then amplifies and shapes this signal. If the PASA contribution is characterized by the PASA response function (almost Gaussian shaped), $f_{PASA}(t)$, then the final signal $S_{PASA}(t)$ can be written as

$$S_{PASA}(t) = S_{ion}(t) * f_{PASA}(t).$$

Usually, one packs together the contribution of the amplification and the PASA, yielding the Time Response Function (TRF):

$$TRF(t) = f_{ion}(t) * f_{PASA}(t).$$

Since the convolution is associative, $S_{PASA}(t)$ can be written in terms of the TRF:

$$S_{PASA}(t) = S_{diff}(x_{anode}, t) * TRF(t),$$

which means, that the final continuous signal after the PASA is given by the convolution of the detector signal at the anode wire with the TRF.

Things become more complicated, if transversal diffusion is considered. Then, $S_{diff}(x_{anode}, t)$ is distributed in y and z :

$$\begin{aligned} S_{diff,trans}(x_{anode}, y, z, t) &= S_{diff}(x_{anode}, t) \delta(y) \delta(z) *_y f_{diff,trans}(y, t) *_z f_{diff,trans}(z, t) \\ f_{diff,trans}(z, t) &= \frac{d}{dt} \int_z^\infty dz' \frac{1}{\sqrt{4Dt}} e^{-\frac{(z')^2}{4Dt}} \\ f_{diff,trans}(y, t) &= \frac{d}{dt} \int_y^\infty dy' \frac{1}{\sqrt{4Dt}} e^{-\frac{(y')^2}{4Dt}} \end{aligned}$$

where $f_{diff,trans}(y, t)$ and $f_{diff,trans}(z, t)$ are the response functions for transverse diffusion, measured at the positions y (e.g. of a neighbored pad in the same pad row) and z (e.g. of a neighbored pad in an adjacent pad row), if the initial charge is centered at $y = 0$ and $z = 0$. $y = 0, z = 0$ denote the pad under consideration. $*_y$ and $*_z$ symbolize, that the convolution w.r.t. to the y and z coordinate has to be calculated, respectively. $S_{diff,trans}(x_{anode}, 0, 0, t)$ denotes the signal on the pad, including transverse diffusion (which declines $S_{diff,trans}(x_{anode}, 0, 0, t)$ w.r.t. $S_{diff}(x_{anode}, t)$). Normally this is the step, where the TRF starts to act. However, since convolution is commutative, one can first calculate the spread of charge due to the Pad Response Function (PRF) (interchange the order). The PRF distributes the charge of the current pad spatially only in y direction and on average on the two neighbored pads. If $PRF(y)$ is the space response function upon a charge delta-peak at $y = 0$, one obtains:

$$S_{PRF}(x_{anode}, y, z, t) = S_{diff,trans}(x_{anode}, y, z, t) * PRF(y).$$

The contribution of the TRF then yields:

$$S_{TRF}(x_{anode}, y, z, t) = S_{PRF}(x_{anode}, y, z, t) * TRF(t).$$

Let $W_{pad,y}$ be the pad width in y direction and $W_{pad,z}$ the pad length in z direction. If one assumes, that the readout of the charge happens on the center of a pad and $(y = 0, z = 0)$ denotes the center of the current pad, then the TRF also has to be applied to the charge measured on the center of a pad. The above discussions required, that all the clusters were released at $(x_i, y_i = 0, z_i = 0)$ and drifted straight to the pad (no inclination). $S_{PRF}(x_{anode}, y, z, t)$ then gives the time and space evolution of the signal of the N released clusters. Table 5.2 gives the time evolution of the signal due to the considered clusters at the central and its neighboring pads, including the most important effects (drift, diffusion, tail, PASA).

Table 5.2: Measured Signals. S : S_{PRF} , W_y : $W_{pad,y}$, x_a : x_{anode} , $T(t)$: $TRF(t)$

$S(x_a, -W_y, W_z, t) * T(t)$	$S(x_a, 0, W_z, t) * T(t)$	$S(x_a, W_y, W_z, t) * T(t)$
$S(x_a, -W_y, 0, t) * T(t)$	$S(x_a, 0, 0, t) * T(t)$	$S(x_a, W_y, 0, t) * T(t)$
$S(x_a, -W_y, -W_z, t) * T(t)$	$S(x_a, 0, -W_z, t) * T(t)$	$S(x_a, W_y, -W_z, t) * T(t)$

- The signal from the PASA is then sampled every $100ns$. In the minimum ionizing case, on average 48 primary ionizations per cm occur (this is an upper prediction), $\langle N_{prim,MIP} \rangle = 48$. As was shown, the Bethe Bloch curve, normalized to the MIP case, $f(\beta\gamma)$ is given by $f(\beta\gamma) = \frac{\langle N_{prim} \rangle}{\langle N_{prim,MIP} \rangle}$. For the Fermi plateau, with $f((\beta\gamma)_{Fermi}) \approx 1.7$, this yields $\langle N_{prim,Fermi} \rangle \approx \langle N_{prim,MIP} \rangle \cdot 1.7 \approx 80$. This means, that for a high relativistic electron approximately 80 primary ionizations per cm have to be expected. With a drift velocity of $v_{drift} = 1.5cm/\mu s$, this yields about 12 clusters per sampling or time bin.

In order to assure, that the sampled signal is really proportional to the sum of charges in the contained clusters, the FWHM of the formed signal by the PASA has to be

chosen in the order of the sampling width ($100ns$). At sampling time, the signal contains tail contributions from all previous samples. However, due to the FWHM of $100ns$, it is assumed that the contributions of the clusters, that arrived within the last $100ns$, are fully counted (the decay of the signal by a cluster, that arrived $100ns$ before the sampling time and which is therefore counted to the current time bin, is supposed to be negligible, in contrast to clusters, that arrived in advance). In this way, the height of a sampled signal is the superposition of the cluster contributions within this time bin. Beyond that, the signal only contains the tail of all the signals from previous time bins, which decay exponentially. If this tail contribution is subtracted by a tail cancellation filter, the remaining signal is proportional to the sum of the cluster charges of this time bin.

Since the charge of a cluster is spread over three pads by the PRF, a proportionality of the measured signal to the energy deposit is only given, if one adds the sampled signals of the three involved pads. Since the ions are supposed to drift away from the anode wires radially without additional spread, the tail of previous clusters is added to the same pad by the TRF. Therefore, tail cancellation has to be performed pad wise, whereas the signals of three pads are involved, whenever the energy deposit of the primary particle (including TR) is of importance (e.g. electron identification).

What is called "mean cluster charge", is rather a "mean time bin" charge (which is Landau distributed, as will be shown later). Since the charge of a sample is proportional to the charge of its clusters and hence to their energy content, the total measured charge is proportional to the energy deposit of a charged particle in the detector.

- The sampled charge, that is acquired during drift time ($t \leq t_{drift}$), is finally digitized by the ADCs. The PASA gain is set such, that at the known gas gain, also large signal heights can be digitized by a 10 bit value. All the following processing (filter, zero suppression) is based on these digital numbers.
- The digitized values are filtered, to get rid of influences, that are able to worsen the linear dependence of the digit to the original energy deposit. One filter step is a tail cancellation. After the filters, the digital number are supposed to be proportional to the energy contents of the clusters, which contributed to its value.

6 Tracklet Calculation

In this section the algorithm of tracklet preprocessing and processing is presented. Also the corrections applied are discussed here. Details of the implementation, such as bit word lengths, specific difficulties in the implementation, etc. will follow in the next chapter.

The TRAP chip is discussed in [Gut06] and [Gut02]. A manual of the TRAP is published in [TRA06]. Transformation issues, concerning the preparation of the tracklet for the GTU, can be found in [dC03].

6.1 The Principle

As in z direction the position resolution is limited by the pad length ($\approx 10cm$) and the z coordinate is therefore given just by the pad row index, the track reconstruction reduces to a two dimensional problem. In the following the local coordinate system of a sector (SM) is used which is rotated around the z axis with respect to the ALICE global coordinate system, such that the x axis is parallel to the chamber normal. x points in drift direction and y in direction of the anode wires (also called $r\phi$ direction). The x coordinate and the drift time can be identified by $t = \frac{x}{v_{drift,x}}$, where $v_{D,x}$ is the (constant) drift velocity in x direction.

As was already mentioned, raw data will be used for tracklet calculation. For each channel it is stored in the event buffers, ordered according to the sampling position. By comparing data of adjacent channels at corresponding time bins, the sub pixel pad position can be reconstructed by exploiting charge sharing. Hence, by the way of storing it, raw data contains information about time bin and the channel number in a pad row.

However, the tracklets are started to being calculated, once the first raw data arrives, hence already during drift time. So the raw data for the tracklet fitting does not need to be read from the buffers but is obtained directly time bin by time bin.

The space-time points of raw data from one pad row are not distinct in the z coordinate (as if the hits of a track were projected onto a plane perpendicular to the z axis). The intention is therefore to turn the space-time points into time-bin and y coordinates and fit the data in these. This corresponds to a (linear) fit to the incident particle track inside one detector chamber (or, to be more accurate, inside the drift volume of $30mm$ extent belonging to that chamber) and is called tracklet.

A typical sample in a simulated full multiplicity PbPb event ($\frac{dN_{ch}}{dy} = 8000$) is shown in picture 6.1. Here, the sampled ADC counts within one pad row are shown.

Since the drift velocity in the drift volume is assumed to be constant, the time information¹ can be turned to a spatial distance from the cathode wire plane: $\Delta x = v_{drift,x} \cdot n \cdot \Delta t$

¹i.e. which time bin, assuming the range of time bins to cover the whole height of the drift volume from the cathode wire plane to the drift electrode toward the beam line. Some difficulties related to that idealized case will be discussed in the next chapter.

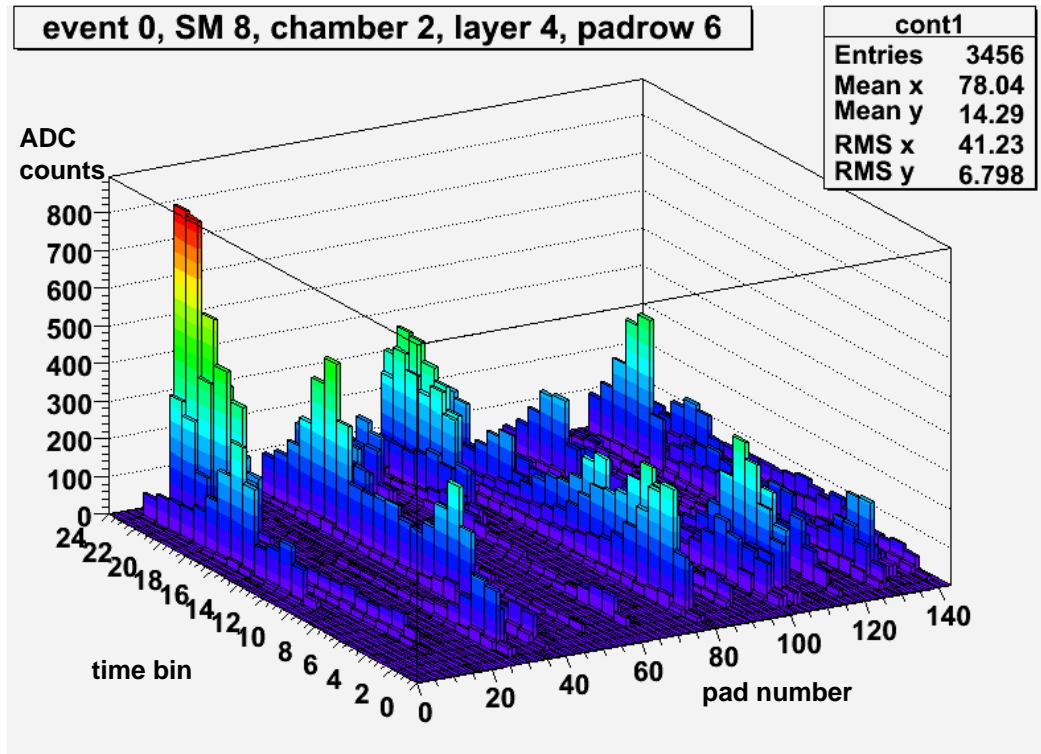


Figure 6.1: Sampled signal in a pad row of a simulated PbPb full multiplicity event. Approximately the first three or four time bins contain clusters from the amplification region. One can clearly see the average enhancement of the ADC counts at these time bins. Also toward later time bins, the signals of some tracks tend to be enhanced. This points toward the Transition Radiation contribution for electron tracks.

with n being the n^{th} time bin counted from the cathode wire plane (the "upper" end of the drift volume) and $\Delta t = 100ns$ the width of one time bin (time between two samples). The spatial x coordinate in the drift volume, belonging to the center of a time bin, is given by $x = x_{cwp} - v_{drift,x} \cdot (n + 1/2) \cdot \Delta t$ (x_{cwp} : radial position of the cathode wire plane).

As the TRAP is intended to fit particles with high transverse momentum p_t , a number of crucial assumptions are made:

- The radius of the track in the magnetic field is so large ($r = \frac{pt}{eB}$), that bending can be neglected when calculating the fit to the track inside one chamber. Therefore the model for the fit is chosen to be just a straight line, resulting in the tracklet. The GTU will then combine the tracklets from different layers to a track. Depending on the layer, tracklets of one track might have slightly different slopes, however it is assumed that even on a stack scale with six layers on top of each other, the bending will not have a great effect and thus the tracklet slopes in the first and the last layer should not differ much.
- All the tracks are assumed to come from the primary vertex which is supposed to be situated around the central z position of the TRD. Only for these tracks the p_t can be estimated by the deflection angle from the vertex direction. Of course this is only an assumption. Bremsstrahlung for example may change the direction of electrons arbitrarily. By running accidentally almost parallel to the vertex direction, a track can pretend to have large p_t . Most of the interesting high p_t electrons at least, will come from the primary vertex or from nearby, e.g. as decay product of a particle or resonance with short decay length $c\tau$ (with the secondary vertex being close to the primary).
- As the tracks are assumed to be stiff, the hits of a track are expected not to be spread over more than two pad widths (and thus they induce a centroid of the charge sharing on a maximum of two pads of one pad row during drift). Assume a track with infinitely high transverse momentum, $p_t = \infty$ (i.e. a straight track, not bent at all), coming from the primary vertex and flying to the edge of a chamber in ϕ direction. Due to the projective geometry of the SM, the maximum possible deflection of the vertex direction with respect to the chamber normal in ϕ (all rays projected onto a plane perpendicular to the z direction through the primary vertex) within the TRD acceptance, amounts to 10° (the total SM is seen under an opening angle of $\Delta\phi = 20^\circ$ from the primary vertex). Looking at a chamber on the innermost layer where the dimensions of the pad width are smallest² ($\approx 6.5mm$), one finds for the maximum deflection of the intersection point on the two outer positions of the drift region (at $x \approx 2970mm$ and $x \approx 3000mm$): $30mm \tan 10^\circ \approx 5.3mm < 6.5mm$. This means that depending on the entry point to the drift volume relative to the pad positions, a maximum of two pads in y are concerned. However, there is an additional deflection angle from the primary vertex direction for particles with finite p_t . Therefore the constraint to not affect more than two pads centrally is only fulfilled for tracks with sufficiently large p_t . A sketch of the projective geometry is shown in figure 6.2.

²due to the projective geometry and the constant number of pads, their size grows with x toward the outer layers

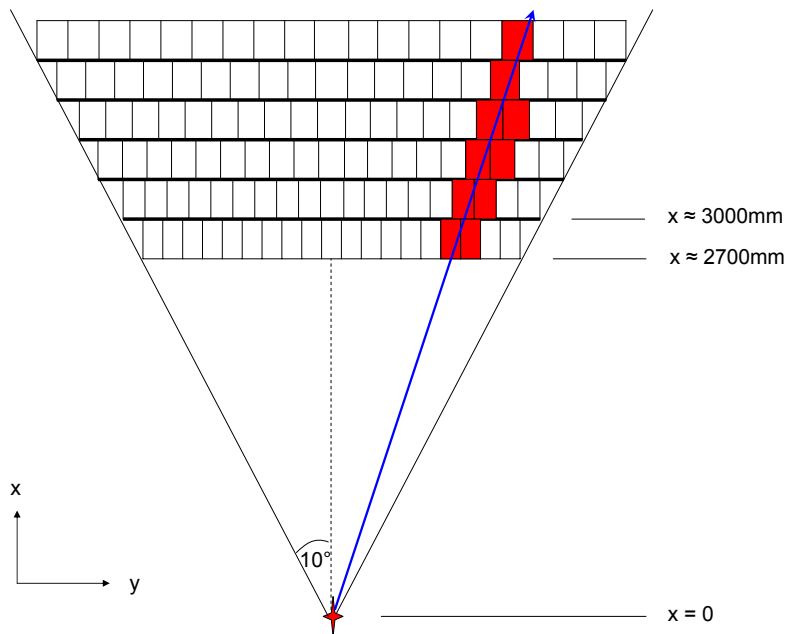


Figure 6.2: The projective geometry of the TRD. Shown is the interaction vertex (red star) and a track with $p_t = \infty$ (blue arrow) passing the six layers. Pads, that are affected by at least one cluster, are marked in red.

Under these assumptions a straight line model for the local fit of the tracks can be applied:

$$y_{fit} = \vartheta \cdot x_{fit} + \hat{y}.$$

(x, y) is the position of a tracklet cluster³, (x_{fit}, y_{fit}) the fitted coordinates. For describing the fit, x denotes in the following the time coordinate as the number of time bin and y the pad position in units of the pad width. θ accordingly is the slope, given in pad widths per time bin. \hat{y} is the offset, given for time bin 0 (hence y position on the cathode wire plane) in units of pad width.

For high p_t tracks the number of pad widths per time bin, thus the slope, is expected to be reasonably small. Hence, fitting by a least squares model should yield quite acceptable results for the parameters θ and \hat{y} . As an error measure, one can use the normalized mean squared deviation of the straight line fit from the real points y ,

$$\begin{aligned} \chi^2 &= \frac{1}{\sigma_y^2} \langle (y - y_{fit})^2 \rangle \\ &= \frac{1}{\sigma_y^2} \langle (y - (\vartheta \cdot x_{fit} + \hat{y}))^2 \rangle. \end{aligned} \quad (6.1)$$

³Here it has to be noted, that by "cluster", the charge measured within a time bin at sampling time is meant. The sampled charge can be assumed to be proportional to the charge sum of the electron clusters, that arrived within $\Delta t = 100ns$ on the anode wire. As was mentioned in the last chapter, there are several electron clusters arriving within one time bins. Therefore "cluster" denotes the measured signal due to them.

σ_y denotes the mean error of the estimated pad position. The optimal parameters for this fit are obtained by minimizing (6.1) with respect to ϑ and \hat{y} , respectively. Differentiating, minimizing and resolving yields

$$\vartheta = \frac{\langle xy \rangle - \langle x \rangle \cdot \langle y \rangle}{\langle x^2 \rangle - \langle x \rangle^2} \quad (6.2)$$

$$\hat{y} = \frac{\langle x^2 \rangle \cdot \langle y \rangle - \langle x \rangle \cdot \langle xy \rangle}{\langle x^2 \rangle - \langle x \rangle^2} \quad (6.3)$$

Inserting this into (6.1) again yields for the estimate on the fit error

$$\sigma_y^2 \chi^2 = \langle (y - \langle y \rangle)^2 \rangle - \frac{[\langle (x - \langle x \rangle)(y - \langle y \rangle) \rangle]^2}{\langle (x - \langle x \rangle)^2 \rangle},$$

where σ_y is unknown, yet independent of the measurement.

Assuming that there are N data points, the mean in the above formulas for the parameters is calculated for these N values. Hence, the following sums have to be accumulated by calculating the position of the clusters, (x_n, y_n) :

$$\begin{aligned} X &= \sum_{n=1}^N x_n \\ Y &= \sum_{n=1}^N y_n \\ XY &= \sum_{n=1}^N x_n y_n \\ \\ X^2 &= \sum_{n=1}^N x_n^2 \\ Y^2 &= \sum_{n=1}^N y_n^2 \\ N &= \sum_{n=1}^N 1. \end{aligned}$$

Then, for example, $\langle xy \rangle$ is given by $\langle xy \rangle = \frac{XY}{N}$. Inserting these relations into (6.2) and (6.3) yields:

$$\vartheta = \frac{N \cdot XY - X \cdot Y}{N \cdot X^2 - X \cdot X} \quad (6.4)$$

$$\hat{y} = \frac{X^2 \cdot Y - X \cdot XY}{N \cdot X^2 - X \cdot X} \quad (6.5)$$

and for the error measure

$$\sigma_y^2 \chi^2 = N \cdot Y^2 - Y \cdot Y - \frac{(N \cdot XY - X \cdot Y)^2}{N \cdot X^2 - X \cdot X}.$$

The error measure will not be investigated further. The TRAP is supposed to calculate the parameters ϑ and \hat{y} . The fit time range, i.e. the time bin range, during which the TRAP uses arriving clusters for the fit and hence for the parameter estimation, can be adjusted to special needs. This becomes important under real conditions, where the first data points that arrive, come from charge clusters in the amplification region. There are several reasons, why to exclude these clusters from the fit:

- In the amplification region, charge clusters arrive on the anode wires from two sides. This leads to an increase of the sampled charge, as if two time bins were put into one. For the electron identification, one uses the mean cluster charge, i.e. the totally measured charge divided by the number of clusters. Its distribution is used as a measure to distinguish between electron and pion tracks. In order to make the mean cluster charge a well defined measure, the amplification time bins, which sample more charge simply for geometrical reasons, should be excluded. One should be able to interpret a deviation from the mean charge with physical reasons (e.g. an enhancement due to Transition Radiation). This is of special importance, if a two dimensional likelihood method (see last chapter) is applied, where the distribution of the time bin position with the largest charge in the fit range is used. Note, that only in an average pulse height distribution one can approximately say, that the amplification samples are on average about twice as high as drift samples. This is not true for an individual sample, therefore the systematically enhanced mean cluster charge in the amplification region cannot be corrected.
- The drift velocity increases in the amplification region toward the anode wires. This means, that more charge arrives at the anode wires (from either side) within the sampling time Δt . Hence, the rate of incoming clusters and therefore the sampled signal is increased⁴ (which makes the amplification peak in the mean pulse height spectrum on average more than twice as high as early drift samples). If one identifies a time bin with the spatial range $\Delta x = v_{drift,x} \cdot \Delta t$, over which it collects its sampling charge, this spatial range Δx increases with the drift time. Therefore the mapping of a time bin onto a spatial position changes. This influences also position reconstruction: Assume for a moment that the drift velocity in the amplification region was on average twice as high as in the drift region. If the y position due to charge sharing is calculated for a sample from the amplification region, one takes into account charge clusters that were spread over a larger radial distance. Charge sharing therefore gives only an average y position for clusters within $\Delta x_{amp} = 2\Delta x$. This reduces the resolution. But even worse, the TRAP does not distinguish between drift and amplification region but assumes an unique drift velocity. Therefore, the calculated y position will be assigned to a spatial width of only Δx . This means, that the TRAP does not consider the loss of accuracy and therefore would calculate a wrong cluster position (x_n, y_n) . Of course, the change in drift velocity also influences the mean cluster charge for amplification time bins. The arguments are the same as in the previous item.

Also samples which belong to clusters from after the drift time (which may give a signal

⁴Because the PASA shapes all incoming charge with a FWHM of $100ns$, the sampled charge for one time bin is approximately proportional to the sum of the cluster charges that arrived at the anode wire within the time bin window of $100ns$.

above baseline e.g. because of the inefficiency of the tail cancellation filter) should not be considered for the fit. Hence it is urgent to have a possibility to set the fit start time and the fit end time. This can be done by setting t_{FS} (linear fit start time) and t_{FE} (linear fit end time) in the configuration (the fit time range then is $[t_{FS}, t_{FE}]$). In the following, if nothing else is mentioned, all sums are built within the fit time range.

In order to be able to separate high p_t electrons from the pion background, the TRAP is intended to calculate an electron probability. Some details about that can be found in the last chapter. However, any electron identification quantity that is under consideration for the TRAP relies on the distribution of the mean charge per cluster (figure 8.1). The

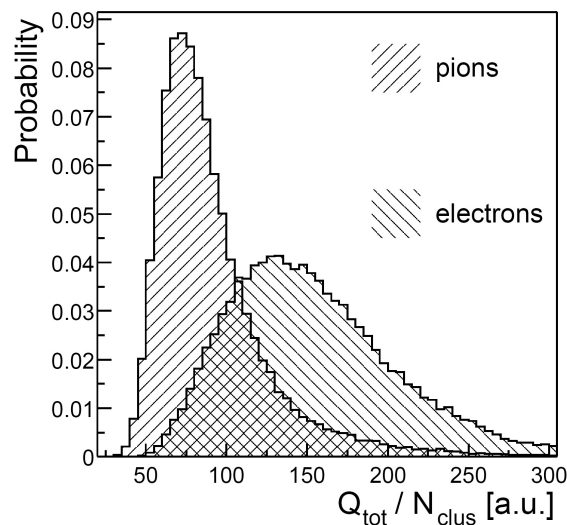


Figure 6.3: Mean cluster charge distribution for electrons and pions for $p_t > 3\text{GeV}/c$ [ALI01]

distribution of electrons and pions differ because electrons are on the Fermi plateau of energy loss whereas pions are in the region of relativistic rise. Moreover, the Transition Radiation clusters add additional charge at later time bins (near the entrance to the drift volume) only for electrons, which increases the mean charge per cluster even more. To have a measure on the mean charge per cluster on TRAP level, the additional quantity

$$\frac{Q}{N} = \frac{1}{N} \sum_{n=1}^N q_n$$

is calculated. q_n is the total charge of the n^{th} cluster, meaning that additionally to the ADC counts of the central channel for a given sample, also the counts of the two neighboring channels at that time bin are added up (which takes charge sharing into account). If $I(\rho, t)$ is the signal height (in ADC counts) of channel ρ (on which the centroid of charge sharing is placed) at time t , q_n can be written as

$$q_n = I(\rho - 1, t) + I(\rho, t) + I(\rho + 1, t).$$

In the TRAP even two charge counters are foreseen. These accumulated charges $Q^{(0)}$ and $Q^{(1)}$ can be configured to individual time bin ranges within the drift time range $[t_{FS}, t_{FE}]$:

$Q^{(0)} : [t_{start}^{(0)}, t_{end}^{(0)}[$ and $Q^{(1)} : [t_{start}^{(1)}, t_{end}^{(1)}[$, in which they accumulate the cluster charge. These time ranges may also overlap⁵.

$$\tilde{Q}^{(0)} = \sum_{n=1}^{N_0} q_n$$

$$\tilde{Q}^{(1)} = \sum_{n=1}^{N_1} q_n$$

where the sums run over all the data points in the according time bin ranges. $\tilde{Q}^{(0,1)}$ denotes the non baseline subtracted accumulated charge. The final accumulated charge $Q^{(0,1)}$ sums up the cluster charges without baseline. If $t_{start}^{(0)} = t_{FS}$, $t_{end}^{(0)} = t_{start}^{(1)}$ and $t_{end}^{(1)} = t_{FE}$, then $N_0 + N_1 = N$ and $Q^{(0)} + Q^{(1)} = Q$.

For each of the 21 channels an individual register, containing the fit sums for this channel, is available. The sums are updated whenever it is affected as the central channel by a cluster.

Assuming that the clusters of a tracklet are not spread over more than two pad widths in y during the drift, for an undisturbed position measurement (no overlapping with clusters of another track) via charge sharing another two channels (left and right neighbors of the two centrally affected channels) are needed. Thus, each tracklet on average occupies four channels in total during drift time. As each TRAP incorporates 18 channels from its own PASAs and 3 channels from neighbored chips, it is possible to have proper charge sharing (including the borrowed channels) for a maximum of five tracklets per TRAP⁶(figure 6.4). This case of five tracklet candidates on one chip would however mean, that the next tracklet candidates on the neighbored MCM channels can only occur from the third channel on (counted from the right for the left MCM, from the left for the right MCM). These two MCMs would then have a maximum of 4 tracklet candidates, each. So on average, not more than four proper tracklets per MCM can occur. The process of fitting is now split into two parts. The first one is the tracklet preprocessing. In this step, which takes place while the clusters are still drifting, for each arriving cluster the coordinates (x_n, y_n) are calculated and with this information the fit sums for the affected central channel are updated. In the second step, the processing, the fit sums of two promising channels are merged and the tracklet information is calculated. The tracklet signal processing steps are sketched in figure 6.5.

6.2 Preprocessing

Here the fit sums of the channel, affected centrally by an arriving cluster, is updated. After the drift time, due to some selection criteria, a maximum of four channel pairs, which are promising tracklet candidates, are selected and assigned to the four CPUs for

⁵However it is supposed that in general $t_{end}^{(0)} \leq t_{start}^{(1)}$. The data width of $Q^{(0)}$ is 15 bit, the width of $Q^{(1)}$ 16 bit. If the time bin ranges are symmetric, $Q^{(1)}$ will on average have larger values due to the TR of electrons toward later time bins

⁶A tracklet is referred to by the left channel of a tracklet candidate pair, whose fit sums are merged. By the way, the channel mapping is done in the course of preprocessing and processing this means, that the left channel pair of all possible tracklet candidates belongs to one of the original channels of a TRAP. See below for details.

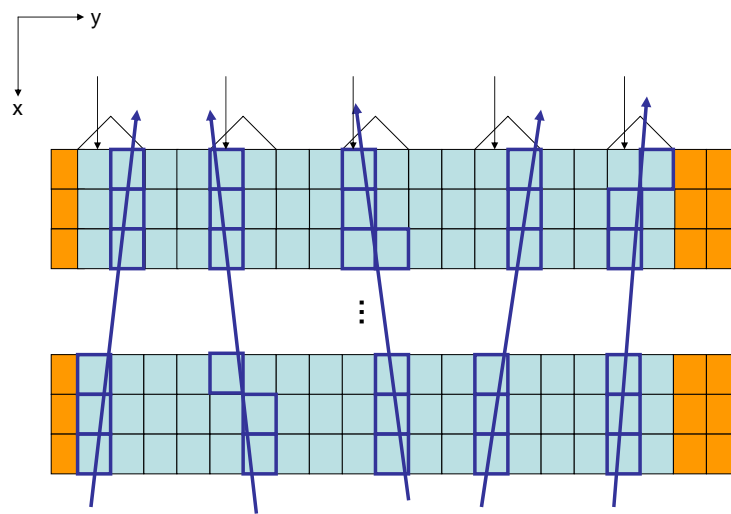


Figure 6.4: Tracklet candidates. The 18 original channels are drawn in blue, the 3 borrowed channels in orange. The triangles above the channels indicate five tracklet candidates. The channels, on which the fit sums would be mapped, are pointed by the black arrows on top. The arrows in dark blue indicate tracks whose clusters affect the bordered pads. This situation shows a constellation to obtain the maximum possible number of clean tracklet candidates.

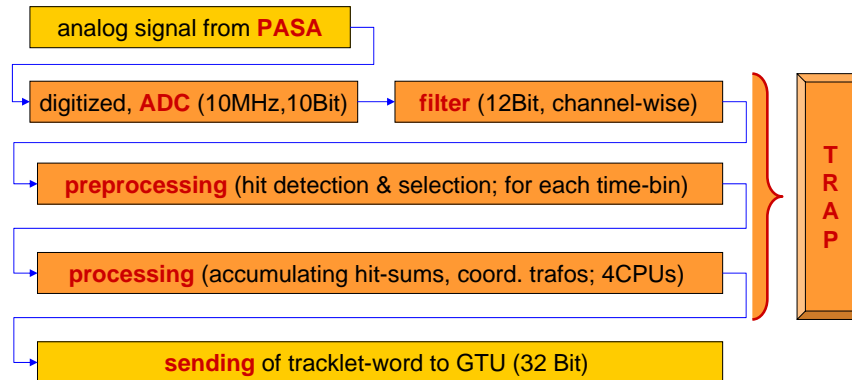


Figure 6.5: Signal processing stages in the TRAP

further processing. The preprocessing can be subdivided into cluster selection and cluster detection.

6.2.1 Cluster Detection

At each time bin and for any of the inner 19 ADC channels (preprocessor channels) a number of quantities are calculated and comparisons performed. Any possible bunch of three adjacent channels is considered a possible cluster candidate and for every channel it is checked, whether it is the centroid of such a candidate. For the centroids of the chosen cluster candidates, the fit sums are updated. This leads to a mapping of the 21 ADC channels to 19 preprocessor channels (figure 6.6). In detail, the following steps are performed:

- Calculate the total charge of a cluster candidate around channel ρ at time t (time bin):

$$h(\rho, t) = I(\rho - 1, t) + I(\rho, t) + I(\rho + 1, t).$$

- Check, if channel ρ is the central channel of a cluster candidate:
 - maximality

$$I(\rho, t) \geq I(\rho - 1, t)$$

$$I(\rho, t) > I(\rho + 1, t)$$

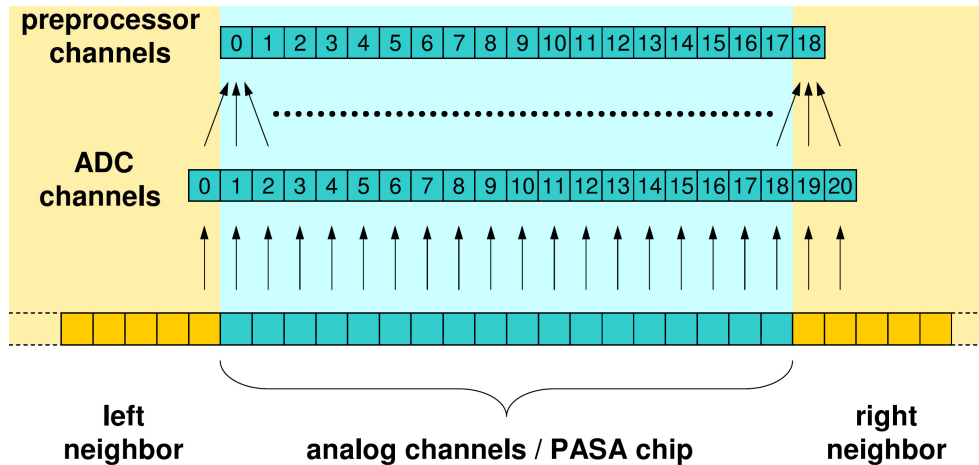


Figure 6.6: The mapping of the 21 ADC channels. In the first step, always three channels are compared and represented by the central channel. This leads to 19 preprocessor channels.

- minimum charge

$$h(\rho, t) \geq T_{Hit} + 3 \cdot I_{baseline}(t)$$

T_{Hit} is the hit charge threshold. As the signal values I contain the common baseline, but T_{Hit} is given for "naked" signal values, one has to account for that by adding the baselines to T_{Hit} (the reason for the time dependence of the baseline was explained in the last chapter).

The comparison with T_{Hit} should ensure for example, that not an accidental fluctuation around the baseline, that fulfills maximality, is considered a cluster. The way, the centroid of clusters is looked for implies, that of three adjacent channels, a maximum of one can be considered a central channel⁷. It has to be noted, that finding a channel to be a centroid does not mean, that all electron clusters of track, that were included in the sample, arrived within one pad width on the anode wire. Since there are several electron clusters arriving within the sampling time, it just means, that most of the charge was mirrored on the central channel. This also shows, that charge sharing can yield at best the mean y position of all the clusters of one time bin. The resolution in y could therefore be improved by shortening the sampling time, such that the average is taken over less clusters. Improving the time bin granularity can therefore improve the y resolution. On the other hand, the relative digitization errors would grow, since the ADC signal would decrease with the number of clusters. To prevent this, the gas gain would have to be enhanced, which would lead to further deteriorations (see previous chapter). Still the time bin width of $\sigma_x = v_{drift,x} \Delta t = 1.5mm$ is considerably smaller than the pad width of around $7mm$. Charge sharing therefore yields a considerable improve and brings the y resolution well inside

⁷If a central channel was found, then its left neighbor cannot be declared central, because its charge is not larger than the charge of the central channel. Also the right channel cannot be a central channel, because its charge is not larger or equal the charge of the central channel.

the sub-pixel regime.

Channels fulfilling these criteria are indicated on a cluster detection mask.

6.2.2 Cluster Selection

Since the neighbors of a central channel cannot be central again, it is assumed for the implementation of the selection algorithm, that a maximum of six clusters (consisting of three channels) per time bin can be found⁸(figure 6.7).

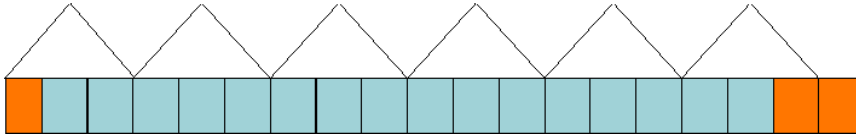


Figure 6.7: Maximum number of preprocessor clusters (containing three channels) in one time bin

The sorting is performed in the following way. Of the channels that are indicated within the 19 bit cluster detection mask only six are compared any further: The first three marked channels on the left and the last three marked channels on the right are chosen. They are sorted according to their total cluster charge $h(\rho, t)$. Here, only the first 8 bits of the 14 bits for $h(\rho, t)$ are considered, for performance reasons. The four channels with the maximum charge are then chosen for fit sum updating. Mostly there will be less than four clusters. If a case occurs, in which there are several channels, whose first 8 bit of the total cluster charge are equal, but not all of the channels can be taken, it depends on the actual implementation of the sorting algorithm which of those channels are finally chosen.

The cluster information of the remaining four channels, i.e. channel number ρ , total cluster charge $h(\rho, t)$, individual channel charge $I(\rho, t)$ and charges of the two neighboring channels, $I(\rho \pm 1, t)$, is processed. Especially the cluster position (x_n, y_n) has to be calculated, where $x_n = t$ is the time bin number (5 bit value). The y coordinate y_n is given in units of a pad width and denotes the shift of the cluster position with respect to the center of the central channel (thus $-\frac{1}{2} \leq y_n \leq \frac{1}{2}$). This sub-pixel resolution is obtained by exploiting charge sharing. For that it is assumed, that all clusters of the current time bin are separated from each other on the chip by at least two pads. Finally, if the cluster passes some quality criterion, the fit sums of the central channels are updated. For the quality measure one needs the individual ADC counts (charges) of the central channel and its neighbored channels, reduced by the common baseline, which still biases the signal heights:

$$\begin{aligned} L &= I(\rho - 1, t) - I_{baseline}(t) \\ C &= I(\rho, t) - I_{baseline}(t) \\ R &= I(\rho + 1, t) - I_{baseline}(t). \end{aligned}$$

⁸It can be expected that on average not more than two tracklets per chip will show up and therefore on average two clusters per time bin will occur. Thus, the probability that they are separated enough to recapitulate their parameters unambiguously, is quite large

Here again, the baseline is time dependent.

The purpose of the quality measure is to not count clusters, that are spoiled by having a contribution from several tracks (overlapping clusters). This would mean that charge sharing as a method for position reconstruction is not applicable. In some sense, overlapping clusters introduce a correlation among channels, such as the long tail of the TRF introduces a correlation among time bins. Of course, also the time-bin correlation would lead to the non-applicability of the charge sharing method, however this correlation was already corrected for by the tail cancellation filter. The correlation among channels is accounted for by enforcing a quality criterion and rejecting clusters, that do not fulfill this criterion. A promising quantity for the cluster quality is

$$Q = \frac{L \cdot R}{C^2}.$$

The distribution of this quantity for overlapping clusters is very broad and reaches up to values near 1. This is because in case of spoiled clusters, neighboring channels can gain signal heights similar to the ones of the central channel. However for clean clusters, the spread of Q is restricted to much lower values which are solely driven by charge sharing. The largest values for such clusters will be reached, when the cluster is centered near the border of two pads (C becomes minimal, $L \cdot R$ maximal) whereas Q will be minimal in case the cluster position is in the center of a pad (figure 6.8). This means that by cutting on a sensible value for Q , T_Q , one can reject a large amount of overlapping clusters by keeping the majority of clean clusters at the same time.

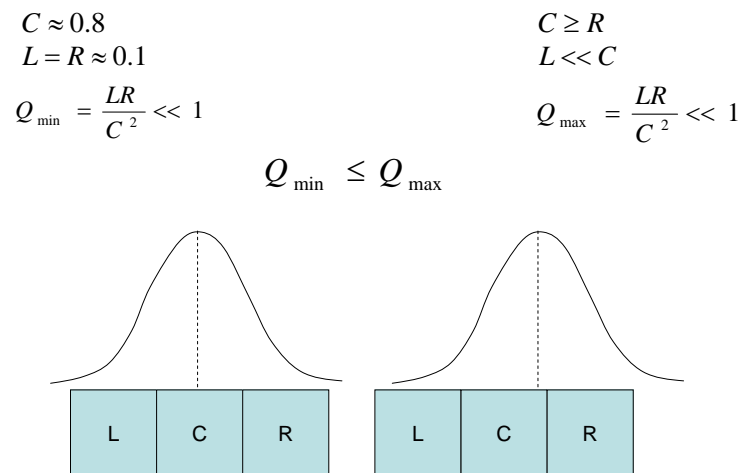


Figure 6.8: Minimum and maximum cluster quality measure for clean clusters. In the left case, the hit is situated in the center of a channel, in the right case near the edge.

Thus a cluster has to fulfill the following condition in order to be accepted:

$$\begin{aligned} \frac{L \cdot R}{C^2} &< T_Q \\ \Leftrightarrow L \cdot R &< T_Q \cdot C \cdot C. \end{aligned}$$

Next, the sub pixel position y_n is calculated, exploiting charge sharing which is described by the PRF. First, an estimated position is calculated:

$$y_n^{est} = \frac{1}{2} \frac{R - L}{C}$$

which is 0 if the charge cluster is placed exactly in the middle of the central pad, positive if it is shifted toward the right neighbor, negative in the other case. The mapping of y_n^{est} to the real position y_n is unique because of the shape of the PRF. Due to the symmetry of the PRF it is enough to investigate the unique mapping

$$|y_n^{est}| \mapsto |y_n|,$$

which can be inverted. If y is the real position of the cluster on the central pad (here y is restricted to positive values and is given in units of a pad width, denoting the shift w.r.t. the center of the channel), L , R and C can be expressed by the PRF. $PRF(\tilde{y})$ gives the integrated charge over a pad width, that is measured a distance \tilde{y} ($0 \leq \tilde{y} \leq 1$) away from the cluster center position at $\tilde{y} = 0$. If the PRF is now peaked at y ($0 \leq y \leq 1$), the fraction of the cluster charge seen on the central pad is $PRF(-y) = PRF(y)$ (symmetry) (figure 6.9), hence

$$C = PRF(y).$$

Accordingly, as the cluster position is $1 - y$ away from the right neighbored channel and $1 + y$ from the left one, the charge measured in these channels can be expressed by

$$\begin{aligned} L &= PRF(y + 1) \\ R &= PRF(1 - y) = PRF(y - 1), \end{aligned}$$

where again the symmetry of the PRF was used. This means for the estimated position as a function of the real position:

$$|y^{est}|(y) = \frac{1}{2} \frac{PRF(y - 1) - PRF(y + 1)}{PRF(y)},$$

which is always ≥ 0 if $y \geq 0$ ($|y - 1| \leq |y + 1|$) (for $y < 0$ the expression on the right side of the equation would become negative). Because of the shape of the PRF, this function is invertible, yielding the real position as a function of the estimated one (figure 6.10):

$$y(|y^{est}|).$$

As can be seen in figure 6.10 the correction to the estimated position $y(|y^{est}|) - |y^{est}| \geq 0$. The LUT, that contains the positive correction values, has 128 entries of 5 bits each. To steer that LUT the quantity $2 \cdot |y_n^{est}| = \frac{|R-L|}{C}$ is built, which consists of one bit before and seven bits after the floating point. The last seven bits are used to select the entry from

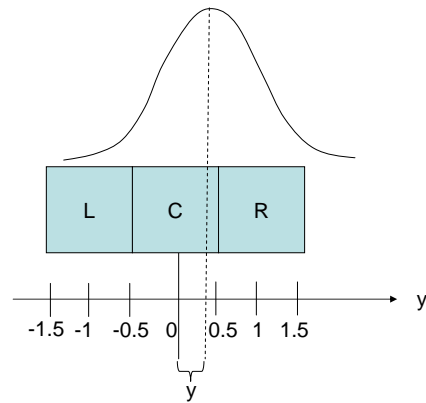


Figure 6.9: The shifted PRF in the coordinate system of the central channel

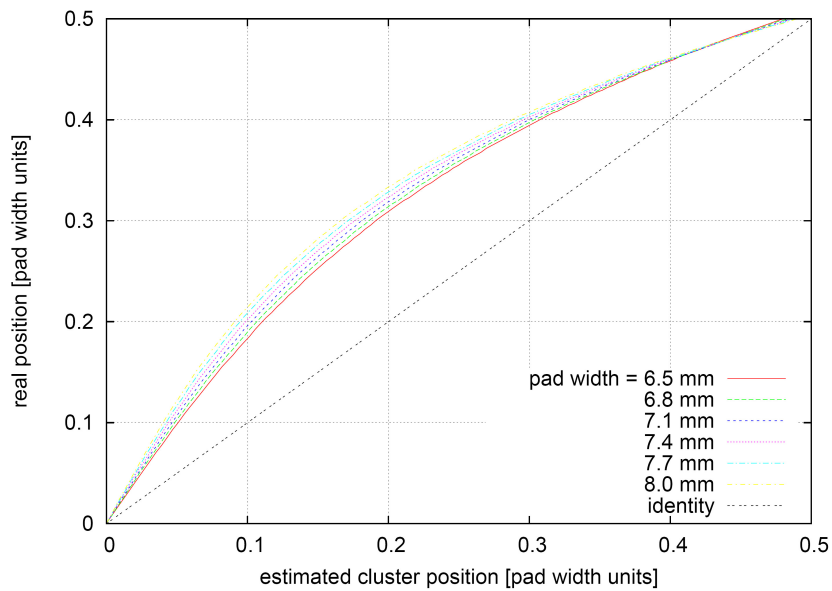


Figure 6.10: Real position as function of the estimated one for the six pad widths of the TRD [Gut06]

the LUT (by multiplying the seven past-comma bits by 2^7 , one gets a value between 0 and $2^7 - 1 = 127$). Finally the cluster position is described by

$$|y_n| = \frac{1}{2} \cdot 2 \cdot |y_n^{est}| + LUT(2|y_n^{est}|).$$

Here the factor $\frac{1}{2}$ shifts the quantity $2 \cdot |y_n^{est}|$ such that it then has 8 bits behind the comma. The five bits of the LUT correction are scaled by 2^{-8} , thus they correspond to the last five of the eight bits after the floating point. For positive values of y_n^{est} the LUT correction is also positive, for negative values negative due to symmetry. If $y_n^{est} = 0$ then $L = R$ and the estimated position is exact, thus $LUT(0) = 0$. That's why the overall sign of y_n is determined already by the sign of y_n^{est} :

$$y_n = \begin{cases} +|y_n|, & \text{if } R \geq L \\ -|y_n|, & \text{if } R < L \end{cases}$$

After the cluster information has been calculated, the fit sums for the chosen channels are updated. For information about the bit format of the data words in general, refer to the next chapter. Here just the increment of the fit sums is given:

$$\begin{aligned} X_N &= X_{N-1} + x_N \\ X_N^2 &= X_{N-1}^2 + (x_N \cdot x_N) \\ Y_N &= Y_{N-1} + y_N \\ Y_N^2 &= Y_{N-1}^2 + (y_N \cdot y_N) \\ XY_N &= XY_{N-1} + (x_N \cdot y_N). \end{aligned}$$

Additionally the following sums are updated:

$$\begin{aligned} Q_N^{(0)} &= Q_{N-1}^{(0)} + \frac{1}{4} h_N \\ Q_N^{(1)} &= Q_{N-1}^{(1)} + \frac{1}{4} h_N \\ N &= N - 1 + 1 \\ ADR &= \rho. \end{aligned}$$

Here ADR denotes the address of the Fit Register File (FRF), in which the fit sums are stored. Access to the register for updating is steered by the address, which in turn is given by the channel number. $h_N = L + C + R = h(\rho, t) - 3 \cdot I_{baseline}(t)$ is the total, baseline corrected cluster charge, where t is the time of the N^{th} cluster. It should be noted that L, C, R are treated as 12 bit integer values with the last two bits being a relict of the filter stage (where the ADC counts were enlarged from 10 bits to 12 bits). Up to now only dimensionless fractions of these quantities were used, thus the real position of the floating point was not important. For the charge sum however, the last two bits have to be treated as past-comma bits and are cut off. This explains the factor $\frac{1}{4}$. Note, that L, C and R are first added up, before their last two bits are cut. By that it is considered, that the sum of the past-comma bits can yield another pre-comma digit. $\frac{1}{4} h_N$ is then a 12 bit integer word that does not overflow even if L, C and R are at their limits.

6.3 Processing

After the end of drift time also preprocessing is finished. The last task of the preprocessor for this event is then to select up to four tracklet candidates and present them to the CPUs which will take over the further processing.

Due to the comparison of the ADC values of always three adjacent channels on preprocessor level, the number of channels that are left for fitting within the preprocessor was reduced from 21 to 19. A tracklet candidate is defined as a pair of channels, whose hit sum counters N fulfill some conditions. Defining tracklet candidates by channel pairs accounts for the fact, that stiff tracks will mostly be spread over two channels in y direction, when passing the drift volume. Therefore, the merged accumulated fit sums of two channels are used to fit a tracklet. Out of the 19 preprocessor channels 18 channel pairs of adjacent channels can be built (figure 6.11). The tracklet candidate is referred to by its left channel. Also the fit sums of the chosen pairs will be projected and transformed to coordinates relative to the left channel of the pair.

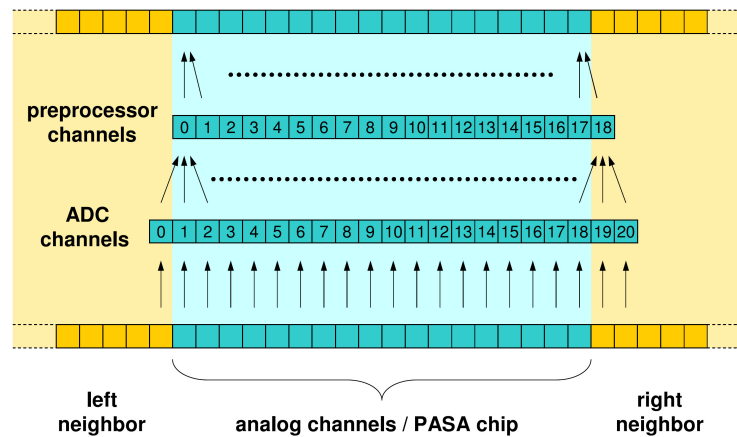


Figure 6.11: Channel mapping. Processing maps the preprocessor channels back to the original PASA channel counting [Gut06]

Like that, a remapping from the preprocessor channels to the original 18-(PASA)channel-grid of this MCM is performed. This also explains that due to the combination of charge sharing, where three channels are involved and due to the tracklet candidate selection with channel pairs, three channels have to be shared with the neighboring MCM chips in order to be able to remap to the original channel array. Sharing three channels (getting two from the right neighbor and one from the left neighbor and giving one channel to the right chip and two to the left chip) also ensures, that the tracklet of a track crossing the two outer pads of an MCM can be reconstructed and will be found on this MCM. Tracklets of tracks crossing one outer pad of one chip and one of a neighbored chip will only be reconstructed on one of the two chips in the ideal case. So each tracklet is processed and only sent once.⁹

⁹Although assuming a track to not cross more the two pads in y , the assumption that each tracklet is only sent once, is in some sense idealistic. Imagine a track crossing the outer left pad of MCM_{middle} and the outer right pad of its left neighbor, MCM_{left} . Then, because MCM_{middle} borrows the outermost right channel of MCM_{left} , this channel is used for charge sharing. A fraction of the total number of clusters formed by this tracklet will be found on MCM_{middle} . By applying the tracklet candidate

The thresholds for a channel pair to be treated as tracklet candidate are characterized by the number of hits in the left channel (N_i) and the total number of hits in the left and the right channel, $N_i + N_{i+1}$:

$$\begin{aligned} N_i &\geq T_{N,left} \\ N_i + N_{i+1} &\geq T_{N,total} \end{aligned}$$

These conditions have to be checked for all original channels $i \in [0, 17]$, to which the merged fit sums are transformed in case of a proper tracklet. The values for the threshold $T_{N,total}$ must be adjusted to the number of time bins included in the current fit time range. In case of 20 time bins, the thresholds are typically set to $T_{N,left} = 1$ (tracklet must involve at least the left channel; standalone tracklet of left channel is possible) and $T_{N,total} = 8$ (hits in at least 40% of the time bins, that were crossed by the track).

The tracklet candidates are then sorted according to their total number of hits. The four candidates with the largest numbers are assigned to the four CPUs for further processing. Alternatively, one could first sort the channel pairs according to their total number of hits and then apply the above tracklet candidate criteria first on the channels with the most hits, until four candidates are found. This might be faster in case of high occupancies (fraction of detector cells (pad and time bin) with ADC values above baseline, i.e. non noise data) with many tracklets expected. The first approach requires a given number of comparisons. The number of found tracklet candidates that have to be sorted increases with multiplicity. In the other case, a constant number of channel pairs has to be sorted. Four valid tracklet candidates will then be found after a small number of comparisons. The current implementation is based on the first method.

The CPUs treat the entries of the fit sum registers as integers, that have to be considered at special scales. Spatial values are given in units of the pad width W_{pad} and time like values in units of the time bin width Δt (time between two samples).

thresholds, the channel pair of the two outermost left (original) channels of MCM_{middle} will form a tracklet candidate, if by chance the track was so stiff that more than 40% of all clusters during the fit time lie on the outermost left channel of MCM_{middle} . This channel then builds a standalone tracklet, to which its right neighbor is assigned just by definition of a tracklet candidate (although it has no hits).

MCM_{left} on the other hand gets the outermost two right channels from MCM_{middle} . Here, in both of the channels that were crossed by the track, charge sharing can be exploited. This time, all the tracklet clusters in both of the channels can be used for fitting. That's why the two affected channels, over which the tracklet clusters are distributed, will build a tracklet candidate, belonging to MCM_{left} (in case the overall number of detected clusters from this tracklet is sufficient). Therefore, MCM_{middle} presents a (standalone) tracklet, projected onto its outermost left, original channel. MCM_{left} will present a tracklet, projected onto its outermost right, original channel.

As a summary one can say that on average a tracklet is found only once. However, in case of standalone tracklets, this is no longer true. It is then possible that two tracklets are built upon the same data points. It should be noted that in the case of standalone tracklets on MCM edges, their submission cannot be avoided, since there is no communication between CPUs of different MCMs. This already shows, that choosing the threshold for the total number of hits/clusters, $T_{N,total}$, properly is of crucial importance: Choosing the threshold too low will introduce a drop in the timing efficiency, since it allows several tracklets of the same data set to be built, which all have to be processed in the TRAP and the GTU and finally at least one of them will have to be removed. It also enhances the chance, that a tracklet is assigned to the wrong track on GTU level. Of course a low threshold will also increase the number of fake tracklets that get to the GTU. If $T_{N,total}$ is chosen too large on the other hand, this might lead to the rejection of real tracklet candidates and thus to a decreasing efficiency in the number of reconstructed tracks.

Table 6.1: Quantities and their scale

quantity	scale	width
i	channels	5
N_i	hits	5
$Q_i^{(0)}$	ADC counts	15
$Q_i^{(1)}$	ADC counts	16
X_i	Δt	9
X_i^2	Δt^2	14
Y_i	$2^{-8} \cdot W_{pad}$	14
XY_i	$2^{-8} \cdot \Delta t \cdot W_{pad}$	21
Y_i^2	$2^{-16} \cdot W_{pad}^2$	21

In the following the tasks of the CPUs will be discussed.

6.3.1 Avoidance of Submission of Double Tracklets

The problem, that two tracklets from the same data set can be sent by two different MCMs, if the outer channels are involved, has already been discussed. However, it is also possible that something similar occurs within one MCM and on arbitrary pads for tracklets distributed over two channels. If the left channel counts at least one hit and the right channel at least 8, then these two channels build a tracklet candidate (referred to as left tracklet candidate in the following). However the right channel also fulfills all the conditions for a tracklet candidate and can build a standalone tracklet (together with its right neighbor, which is not needed but assigned, because a candidate consists of a channel pair). To avoid this, communication between the CPUs is necessary. Each CPU has access to the channel numbers of the right channels of the pairs assigned to the other CPUs. By comparing its own left number with the right numbers of all other CPUs, such double tracklets can be found. The tracklet candidate with the lower number of hits is then rejected (which in the above case will mostly result in rejecting the standalone tracklet). Although this leads to CPUs being idle, no new tracklet candidates will be assigned to.

Since the standalone tracklet is supposed to contain only a subset of all hits of the left tracklet candidate (in case the tracklet information is spread on two channels only), the procedure for avoiding double tracklets can be eased. If the CPUs have identification numbers 0 to 3 and the tracklet candidates with lower number of hits are assigned to the CPUs with higher identification number, it is enough, if a CPU compares its left channel number to the right channel numbers of CPUs with lower identification numbers and rejects its candidate in case of a match. In the above example the standalone tracklet will be assigned to a CPU with higher identification number than the left tracklet candidate. So it will compare its left channel number with the right channel number of the left tracklet. As there will be a match, the standalone tracklet will be rejected (figure 6.12).

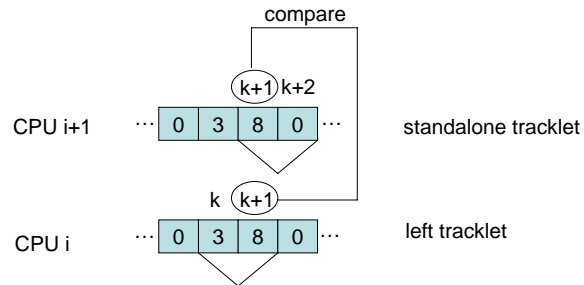


Figure 6.12: Avoidance of the submission of double tracklets: CPUs with higher identification number contain the tracklet candidates with lower number of hits. It compares the left channel number of its tracklet candidate to the right channel numbers of CPUs with lower identification number and rejects its candidate in case of a match.

6.3.2 Merging of the Fit Sums of Channel Pairs

In this step the fit points of the two channels of a tracklet candidate are combined. Up to now all the coordinates of the sums of one channel are expressed in units of the pad width relative to the center of the corresponding pad. In order to merge the fit sums, the coordinates of the right channel have to be transformed into a coordinate system relative to the left channel:

$$(x_{i+1}, y_{i+1})_{\text{channel } i+1} \mapsto (x_{i+1}, y_{i+1} + 1)_{\text{channel } i}.$$

y_{i+1} is the y coordinate of channel $i + 1$, which has to be shifted by one in order to transform it from a coordinate system relative to the right channel to the system of the left one (one pad width away). x is the common time bin number that does not need transformation. The transformation of sums containing the y coordinate has to be performed such, as if the sums had been built in coordinates relative to left channel from begin on. Hence, these sums need to be transformed:

$$\begin{aligned} (Y_{i+1})_{\text{channel } i+1} &\mapsto \left(\sum_{n=1}^{N_{i+1}} (y_{i+1,n} + 1) \right)_{\text{channel } i} = (Y_{i+1} + N_{i+1})_{\text{channel } i} \\ (Y_{i+1}^2)_{\text{channel } i+1} &\mapsto \left(\sum_{n=1}^{N_{i+1}} (y_{i+1,n} + 1)^2 \right)_{\text{channel } i} = (Y_{i+1}^2 + 2 \cdot Y_{i+1} + N_{i+1})_{\text{channel } i} \\ (XY_{i+1})_{\text{channel } i+1} &\mapsto \left(\sum_{n=1}^{N_{i+1}} (x_{i+1} (y_{i+1,n} + 1)) \right)_{\text{channel } i} = (XY_{i+1} + X_{i+1})_{\text{channel } i} \end{aligned}$$

XY_{i+1} is the sum XY in channel $i + 1$. Finally the merged quantities are given by

$$\begin{aligned} N &= N_i + N_{i+1} \\ Q^{(0)} &= Q_i^{(0)} + Q_{i+1}^{(0)} \\ Q^{(1)} &= Q_i^{(1)} + Q_{i+1}^{(1)} \\ X &= X_i + X_{i+1} \\ X^2 &= X_i^2 + X_{i+1}^2 \\ Y &= Y_i + Y_{i+1} + N_{i+1} \\ Y^2 &= Y_i^2 + Y_{i+1}^2 + 2 \cdot Y_{i+1} + N_{i+1} \\ XY &= XY_i + XY_{i+1} + X_{i+1}. \end{aligned}$$

It is clear that if the right hit counter is 0, $N_{i+1} = 0$ (e.g. in case of a standalone tracklet), merging the fit sums will not change the contents of the fit sums of the left channel, because all the sums of the right channel are empty.

6.3.3 Calculation of Offset and Slope

From the merged fit sums and by (6.4) and (6.5), offset and slope can be calculated. In order to have only one division, the denominator is calculated first:

$$\Gamma = \frac{1}{N \cdot X^2 - X \cdot X}.$$

The nominators are given by

$$\begin{aligned}\theta &= N \cdot XY - X \cdot Y \\ \hat{Y} &= X^2 \cdot Y - X \cdot XY.\end{aligned}$$

The parameters slope and offset are then given by multiplications instead of divisions, which is faster. In total one division is saved.

$$\begin{aligned}\vartheta &= \theta \cdot \Gamma \\ \hat{y} &= \hat{Y} \cdot \Gamma + (i + \frac{1}{2}).\end{aligned}$$

i is the channel number on the TRAP, $i \in [0, 17]$. Thus, adding i transforms the offset from relative to the left channel to a system relative to channel 0 on the MCM. Still the offset is given relative to the pad center. The addition of $\frac{1}{2}$ shifts the coordinate system to the border of the pad. Thus in total, \hat{y} is given in coordinates relative to the edge of the MCM, or more precisely, the edge of channel 0 on the MCM (channel number i refers to the counting of the original 18 PASA channels of an MCM).¹⁰

6.3.4 Electron Probability

The electron probability $P_{electron}$ will most probably be a function of the mean charge per cluster. As there is only one hit counter N , the mean charge per cluster can only be calculated if $Q^{(0)}$ and $Q^{(1)}$ cover exactly the whole fit range. Then the mean charge per cluster is given by $\bar{Q} = \frac{Q^{(0)}+Q^{(1)}}{N}$ and

$$P_{electron} = P_{electron}(\bar{Q}).$$

As N is at most the number of time bins in the fit range \hat{N}_{fit} , $N \leq \hat{N}_{fit}$, in order to save the division by N it is convenient to store the \hat{N}_{fit} needed values of $\frac{1}{N}$ in a LUT of the configuration. Then $\bar{Q} = \frac{Q^{(0)}+Q^{(1)}}{N}$ turns into a multiplication: $\bar{Q} = (Q^{(0)} + Q^{(1)}) \cdot \frac{1}{N}$.

Also the values for the electron probability will be stored in a LUT with 2048 entries of 8 bits each. The LUT can be steered by a quantity that is calculated from $Q^{(0)}$, $Q^{(1)}$ and possibly other information.

On GTU level, these tracklet probabilities of each layer can be combined to an overall probability for the corresponding track to be an electron.

Up to now a measure for the electron probability is not implemented. Some more details on the issue of electron pion separation methods can be found in the last chapter.

¹⁰If a tracklet is spread over three channels, there might be a tracklet candidate without hits in the first time bins (figure 6.13). Then the tracklet fit might give a line, that hits the pad plane (offset, time bin 0) outside the two channels of the tracklet candidate. Hence $\hat{Y} \cdot \Gamma$ does not need to fulfill $\hat{Y} \cdot \Gamma \in [-\frac{1}{2}, \frac{3}{2}]$. However, if a tracklet is spread over two channels (which occurs most frequently), then of course $\hat{Y} \cdot \Gamma \in [-\frac{1}{2}, \frac{3}{2}]$ holds for the offset.

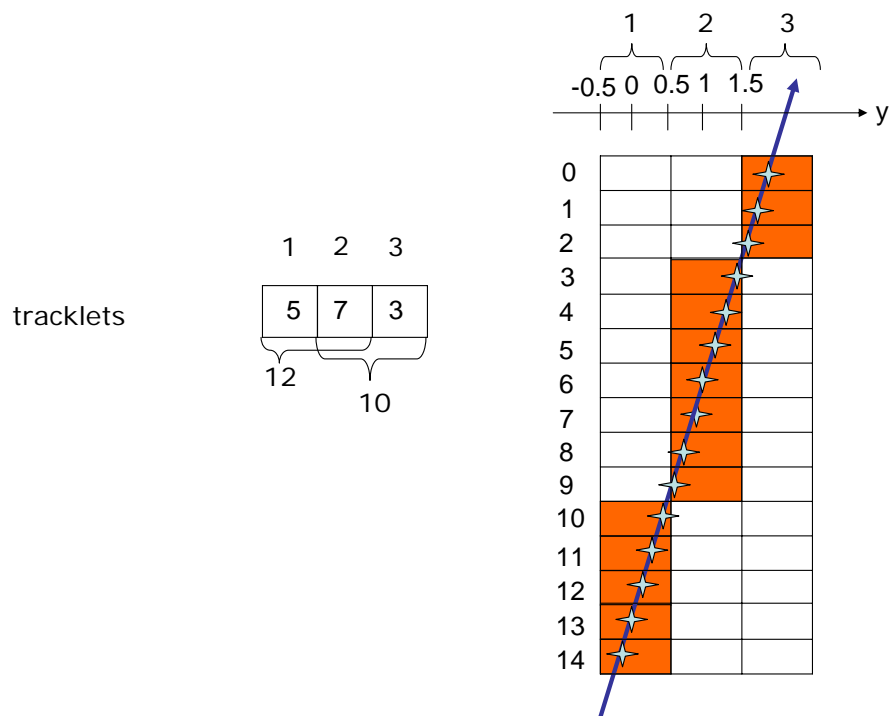


Figure 6.13: A tracklet spread over three channels. The channels (1,2) can build a tracklet candidate with no hit in the first three time bins. Therefore, the offset (intersection of the blue line with the y axis) in local coordinates of the left channel (channel 1) lies at $y > 1.5$. The blue stars denote the centroids of the sampling charges, the channels in red are the corresponding central channels.

6.3.5 Preparing for GTU

Before the information about the tracklets are combined to the 32 bit integer tracklet word that is submitted to the GTU, slope and offset have first to be scaled, transformed and corrected:

$$\begin{aligned}\tilde{\vartheta} &= m^{(\vartheta)} \cdot \vartheta + c^{(\vartheta)} \\ \tilde{\hat{y}} &= m^{(\hat{y})} \cdot \hat{y} + c^{(\hat{y})}.\end{aligned}$$

In the following, the contents of the four quantities $m^{(\vartheta)}$, $c^{(\vartheta)}$, $m^{(\hat{y})}$ and $c^{(\hat{y})}$ are discussed. The definition of offset and deflection in an idealized implementation, where the offset is defined on the readout plane, is shown in figure 6.14. The deflection will be discussed in the text below.

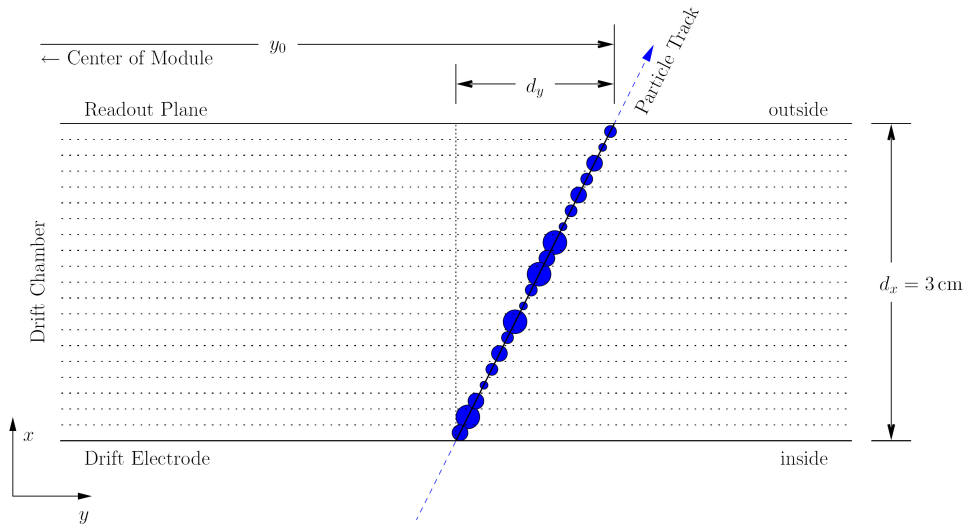


Figure 6.14: Offset and deflection of a tracklet [dC03]

$m^{(\vartheta)}$

The factor $m^{(\vartheta)}$ contains the scaling of the slope to a deflection length and the matching to the GTU metric system.

The slope ϑ is given in units of pad widths per time bin. It is convenient for the GTU, if this number is turned into a deflection between the starting point of the tracklet and its endpoint, i.e. the total distance in y direction, gained within the fit time range with its \hat{N}_{fit} time bins (figure 6.15). Thus one part of $m^{(\vartheta)}$ consists of the factor $\tilde{m}_{fit}^{(\vartheta)} = \hat{N}_{fit} \cdot W_{pad}$. W_{pad} is the width of the pads in the current chamber (the value of W_{pad} is especially layer dependent). In the simulation, the slope is turned to a deflection in y between the entrance and the exit of the drift chamber, replacing \hat{N}_{fit} by the number of time bins $\hat{N} \geq \hat{N}_{fit}$, that would cover the drift region. At a drift velocity of $v_{drift,x} = 1.5\text{cm}/\mu\text{s}$ and a sampling every 100ns , this results in $\hat{N} = 20$ time bins covering a drift volume of 30mm height. Then: $\tilde{m}^{(\vartheta)} = \hat{N} \cdot W_{pad}$. The slope expressed as a deflection $d_y = \hat{N} \cdot W_{pad} \cdot \vartheta = \tilde{m}^{(\vartheta)} \cdot \vartheta$ is expected by the GTU (still d_y has to be corrected for two distortions, which are subsumed

under $c^{(\vartheta)}$). Before the (corrected) deflection is written into the tracklet word, it is scaled to some granularity. This granularity is determined by a maximum deflection and the needed resolution.

For particles with transverse momentum of $p_t = 2.3\text{GeV}/c$ (corresponding to lower the limit for the reconstructed p_t value below which the tracklet is not sent to the GTU, see below) at a magnetic field $B = 0.4T$, the maximum deflection angle from the vertex direction becomes $\alpha = 6.38^\circ$. If this angle is added to the maximum angle between vertex direction and chamber normal of 10° , this would lead to a maximum deflection between the entrance and end of a drift volume of $3.00\text{cm} \cdot \tan 16.38^\circ \approx 0.881\text{cm}$. This can happen in positive and negative direction, hence $d_y \in [-0.881\text{cm}, 0.881\text{cm}]$ ($d_y = \tilde{m}^{(\vartheta)} \cdot \vartheta$). Note, that a track from the primary vertex can only be detected by a chamber, if the angle w.r.t. chamber normal is smaller than 10° . This means, that defining the deflection range by an angle of 16.38° leaves enough margin (figure 6.15). The resolution of the detector limits the resolution of d_y to about $\delta d_y \approx 400\mu\text{m}$. d_y is only needed for the GTU as a criterion for the comparison of tracklets, that have been projected onto a middle plane, but not for reconstruction itself. A variation of α within 10% leads to a deviation from 0.881cm by $370\mu\text{m}$. It is desirable to improve the accuracy considerably as compared to the detector resolution, in order to make quantization errors negligible. Conceding 6 bit for the absolute value of the scaled deflection, the resolution can be chosen $[\tilde{\vartheta}] = \frac{1}{140\mu\text{m}}$ (because $\frac{0.881}{1.4 \cdot 10^{-2}} \approx 62.9 < 2^6$). One bit is used for encoding the sign by two complement representation, thus in total 7 bits are used for the deflection. Finally

$$m^{(\vartheta)} = \frac{\tilde{m}^{(\vartheta)}}{[\tilde{\vartheta}]} = \frac{\hat{N} \cdot W_{pad}}{[\tilde{\vartheta}]}.$$

$m^{(\hat{y})}$

Also the offset is measured in units of the pad width.

For the discussion of the word length, similar arguments as above are applied: As the p_t resolution will depend on the accuracy of the y position, it is necessary to allow for a high resolution. An accuracy of $\delta_y \approx 400\mu\text{m}$ of the detector is assumed. Thus a resolution of better than $\frac{1}{200\mu\text{m}}$ would ensure, that quantization errors do not reduce the accuracy to below $400\mu\text{m}$. Geometrically, the y coordinate covers maximal $y \in [-64.32\text{cm}, 64.32\text{cm}]$ for the outermost layer. The inner layers have smaller dimensions, however the same word length is granted for the offset in all of the layers. Thus the outer layer is the restricting one. Because $\frac{0.6432}{2 \cdot 10^{-4}} = 3216 > 2^{11}$, at least 12 bits are needed. To exploit the 12 bits, the resolution can be improved to $\frac{1}{160\mu\text{m}}$ ($\frac{0.6432}{1.6 \cdot 10^{-4}} = 4020 < 2^{12}$). Because again, another bit is needed to encode the sign via the two-complement of the value, in total 13 bits are used for encoding the offset, scaled to $[\tilde{\hat{y}}] = 160\mu\text{m}$. In total:

$$m^{(\hat{y})} = \frac{W_{pad}}{[\tilde{\hat{y}}]}.$$

$c^{(\hat{y})}$

To transform the offset to a SM system with the y-coordinate being 0 in the middle of the pad plane, a correction $c^{(\hat{y})}$ has to be applied. One pad row (144 pads) is covered by

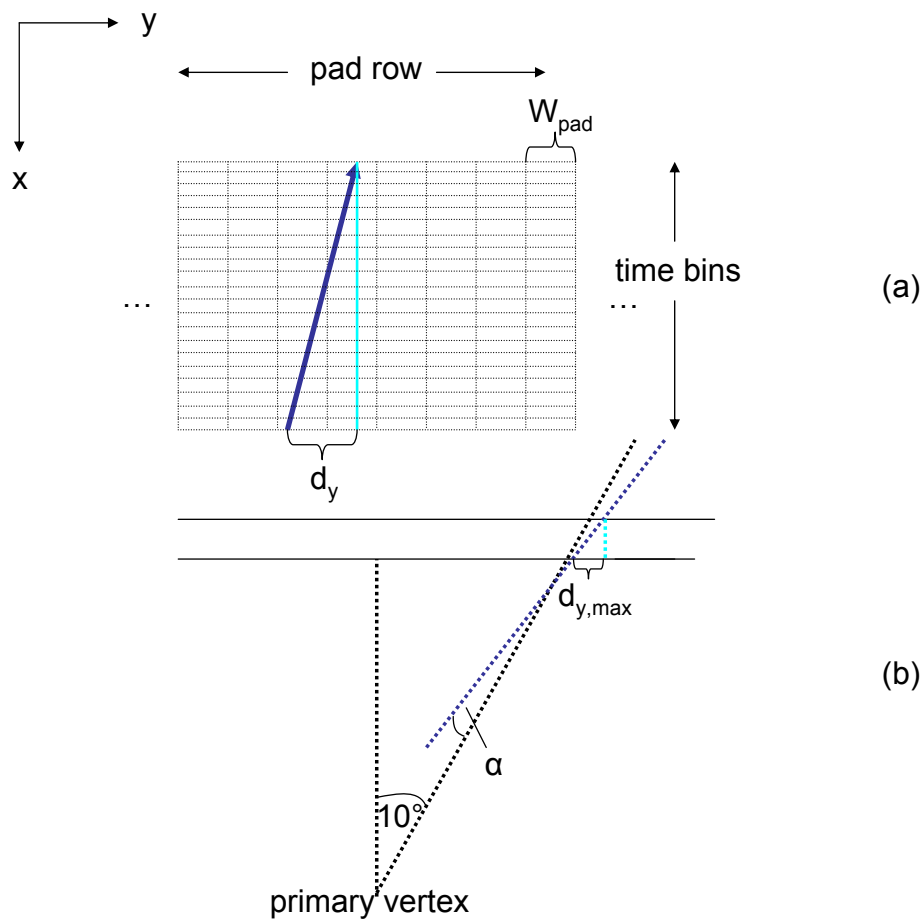


Figure 6.15: The deflection. (a): Definition of the deflection for a tracklet. (b) Calculation of the maximum deflection

8 MCMs of which each incorporates 18 pads. The pad row is distributed over two ROBs (figure 3.7). If the MCMs of a pad row are counted from 0 to 7 in direction of increasing ϕ , and the pads accordingly from 0 to 143 in the same direction, then $y = 0$ lies between MCM 3 and MCM 4 and there between their outer pads 71 and 72. If the current MCM is the n^{th} one in this counting, then the correction is given by

$$c^{(\hat{y})} = ((n - 4) \cdot 18) \frac{W_{pad}}{[\hat{y}]}$$

Here it is exploited that within this MCM, the offset has already been transformed to coordinates relative to the border of the outermost pad with lowest channel number. Of course the correction has to be given in the same format as the offset, thus the multiplication by $\frac{W_{pad}}{[\hat{y}]}$ is necessary.

$c^{(\vartheta)}$

The correction to the slope deflection $c^{(\vartheta)}$ contains two contributions: The first one corrects for the inclination of the drift direction with respect to the chamber normal due to a homogeneous magnetic field perpendicular to the electric drift field. Second, a correction due to the tilting of pads by a small angle is performed. Because they need some explanation, these two topics are granted the following two sections.

6.4 Lorentz Angle Correction

If a homogeneous magnetic field is superimposed on the homogeneous electric drift field, the drift direction of the electrons is influenced and inclined w.r.t. the chamber normal. The inclination angle Ψ_L (also called Lorentz angle) is connected to the magnetic field strength $|\vec{B}|$ and the mean time between two collisions of a drifting electron with gas molecules τ (which depends on the gas, pressure and electric field strength $|\vec{E}|$) by

$$\begin{aligned} \tan(\Psi_L) &= \omega\tau \\ \tan(\Psi_L) &= \frac{e\tau B}{m_e} \end{aligned}$$

$\omega = \frac{v_t}{r} = \frac{eB}{m_e}$ for electrons. For $B = 0.4T$ as foreseen in the TRD, one obtains $\Psi_L \approx 7.7^\circ$. Up to now it was assumed that the drift was parallel to the electric field. Thus the inclination of the real drift introduces an error on the estimation of the position of the cluster (figure 6.16). This error does not depend on the inclination of the incident track.

In an idealized implementation it is assumed that the drift velocity in the amplification region is infinitely high ($\tau \rightarrow 0$) and hence there is no inclination ($\Psi_L \rightarrow 0$). So for the correction only the time bins in the drift volume are of importance. It is further assumed that the linear fit time range incorporates the whole drift volume.

The coordinates of the points for the linear fit are extracted from the pad plane (pad position via charge sharing) and from the time bin in which the signal on the pad plane occurs. Hence, the reconstruction of a point is not sensitive to the inclination of the drift direction and the correction must be exercised explicitly. If one assumes that the combined

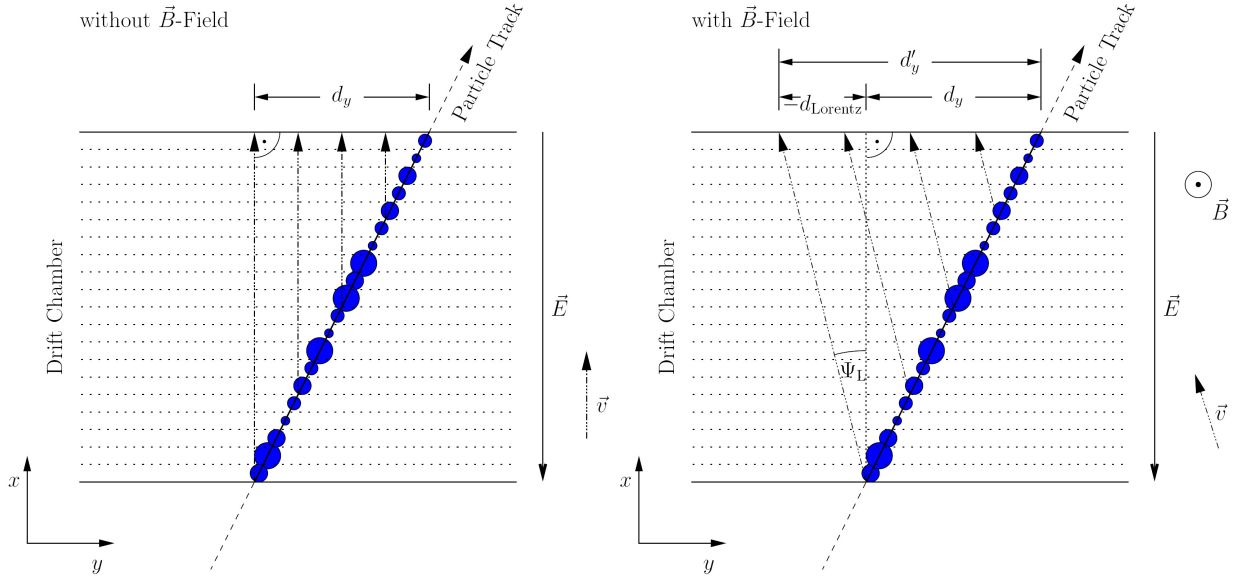


Figure 6.16: Correction for the deflection due to Lorentz drift. On the left, the cluster drift without magnetic field is depicted, on the right the inclination by the Lorentz angle Ψ_L with field is shown [dC03]

action of the magnetic and electric drift field adds a component to the drift velocity in $\vec{E} \times \vec{B}$ direction orthogonal to the x direction ($\parallel \vec{E}$) but leaves $v_{drift,x}$ approximately unchanged, then no correction on the time coordinate will be necessary. Hence, the Lorentz drift biases the real y position of a cluster by a value, that depends on the time bin in which the cluster produces its signal on the pad plane. However for all tracks and a given time bin the correction is a constant.

In the ideal implementation, the offset is given at time bin 0 which corresponds to the x position of the cathode wire plane. Clusters starting to drift from this position will directly enter the amplification region and hence there is no error in the offset estimation.

However, clusters from increasingly later time bins will experience an increasing deflection, since their drift paths grow. A cluster from the n^{th} time bin is radially $\delta x_n = n \cdot 100ns \cdot 1.5cm/\mu s$ away from the cathode wire plane. The error on the estimation of its y position thus becomes $|d_{Lorentz,n}| = \delta x_n \cdot |\tan \Psi_L|$.

It should be noted, that by applying a magnetic field also the drift velocity in x direction changes slightly. In TRD case it decreases to the fraction $\frac{1}{1+(\tan \Psi_L)^2} \approx 0.985$. Thus, 20 time bins, whose samples are $100ns$ distinct, will only cover $29.55mm$ of the drift region. This effect is up to now neglected when scaling the slope to a deflection length between entrance and exit of a drift chamber.

The error in the deflection d_y of the tracklet, $d_{Lorentz}$, is determined by the last time bin in the drift volume and the Lorentz drift contribution to the deflection of its cluster. Thus, the constant Lorentz correction additive for each tracklet, independent of its inclination, becomes:

$$d_{Lorentz} = -d_x \tan \Psi_L \approx -4.056mm.$$

$d_x = 30.0mm$ is the height of the drift volume. $\tan \Psi_L$ changes the sign if either the

direction of the \vec{B} field changes or the charge sign is swapped. To the calculated deflection $d_{y,raw} = \hat{N} \cdot W_{pad} \cdot \vartheta = \tilde{m}^\vartheta \cdot \vartheta$, the Lorentz correction has to be added in order to obtain the deflection, that is only disturbed by the tilted pads influence, d'_y :

$$d'_y = d_{y,raw} + d_{Lorentz}.$$

In a more realistic scenario, the drift velocity in the amplification region is not infinite. Moreover the linear fit time range does not cover the whole drift region, hence there is also an error on the offset position. Some more about this can be found in the following chapter.

6.5 Tilted Pads Correction

In order to improve the z resolution in the offline tracking (to become better than the actual pad length), the pads of a layer are tilted by a small angle $\beta_{tilt} = \pm 2^\circ$. Thus they are no longer exact rectangles but rather parallelograms. The sign of the tilting angle is varied layer by layer. In this way the z and y coordinate, as defined in the SM coordinate system, are no longer independent (figure 6.17). By comparing the track positions in different layers, this can be used for sub pixel estimates on the z position. In the online analysis,

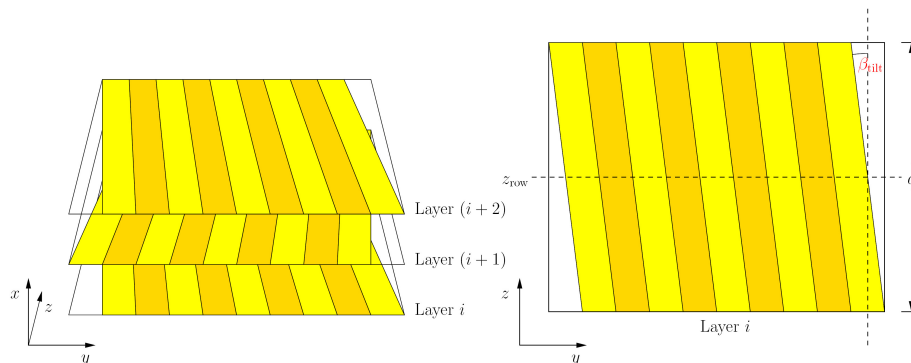


Figure 6.17: The tilting of pads in subsequent layers (left). Definition of the coordinate z_{row} in the middle of a pad row (right) [dC03]

tilted pads are not included in track(let) reconstruction.

However it is tried to account for the correlation of the y and z coordinates (depending on z , the same y coordinate can belong to different pads) that are introduced by the tilting.

Let (y', z') be coordinates in the system of the tilted pads of a row. The row has to be chosen such, that the origin of the tilted pads system coincides with the origin of the local SM system. The pad coordinate system is rotated by β along the x axis w.r.t. the SM system. The sub pixel y coordinates, that were obtained by charge sharing, are given in the tilted pads coordinate frame, and therefore are y' coordinates.

The transformation to coordinates (y, z) in the SM system from coordinates (y', z') in the tilted pads system, is described by the inverse rotation matrix R^{-1} :

$$\begin{pmatrix} y \\ z \end{pmatrix} = R^{-1} \cdot \begin{pmatrix} y' \\ z' \end{pmatrix}$$

where

$$R^{-1} = \begin{pmatrix} \cos \beta & \sin \beta \\ \sin(-\beta) & \cos \beta \end{pmatrix}.$$

Thus

$$\begin{aligned} y &= y' \cos \beta + z' \sin \beta \\ z &= -y' \sin \beta + z' \cos \beta \end{aligned}$$

This yields for $y(y', z)$:

$$y(y', z) = y' \cdot \cos \beta (1 + \tan^2 \beta) + z \cdot \tan \beta.$$

For small angles β (here in radian units $\beta \frac{2\pi}{360^\circ}$), $\sin \beta \approx \beta$, $\cos \beta \approx 1$, $\tan \beta = \frac{\sin \beta}{\cos \beta} \approx \beta$. Neglecting all quadratic terms in β ($\beta^2 \ll \beta$), this finally yields:

$$y \approx y' + z \cdot \tan \beta. \quad (6.6)$$

Severely spoken, the transformation only holds, if (y', z') are coordinates in a pad row, which is contacted by the y axis. If a different pad row is considered, the origins of both coordinate systems have to be shifted to there. This is, because different pad rows in a layer are independent from each other, concerning charge sharing. For the following discussion it is assumed, that this was respected.

If d denotes the projected length of a tilted pad onto the z direction and z_{row} is the z coordinate in the middle of the pad row at $\frac{d}{2}$, the maximum error in y, $(y' - y)_{max}$, relative to z_{row} , amounts to $(y' - y)_{max} = ((z_{row} \pm \frac{d}{2}) - z_{row}) \cdot \tan \beta_{tilt} = \pm \frac{d}{2} \tan \beta_{tilt}$. For $d \approx 10cm$ this yields $(y' - y)_{max} \approx 1.8mm$. Of course, this is again only true, if the origins of both systems have been shifted to z_{row} .

As for the transformation of a calculated y' position (such as the offset) to a y position additionally the z coordinate of the fit point would be needed (which is not known), an offset correction cannot be applied.

Nevertheless the y deflection can be corrected for the influence of the tilted pads (y and z are not independent). Because the deflection is the difference between two y positions, also the contribution by the z coordinates is reduced to a difference Δz . This difference can be estimated by assuming, that the incident track came from the primary vertex.

First, the measured positions due to the tilted pads are given by means of (6.6) (if the origins of the coordinate systems are situated on z_{row}):

$$y' = y - (z - z_{row}) \tan \beta_{tilt}.$$

Thus the measured deflection $d'_y = y'_{exit} - y'_{entrance}$ (y'_{exit} and $y'_{entrance}$ are the y'-coordinates of the exit and the entrance to the drift volume, respectively, as obtained by charge sharing) can be expressed as a function of the deflection in (y, z) coordinates, $d_y = y_{exit} - y_{entrance}$:

$$\begin{aligned} d'_y &= y'_{exit} - y'_{entrance} \\ &= (y_{exit} - (z_{exit} - z_{row}) \tan \beta_{tilt}) - (y_{entrance} - (z_{entrance} - z_{row}) \tan \beta_{tilt}) \\ &= d_y - (z_{exit} - z_{entrance}) \tan \beta_{tilt} \\ &= d_y - \Delta z \cdot \tan \beta_{tilt} \end{aligned}$$

Assuming now the incident track coming from the primary vertex, the particle will follow a path that tends to bend around the magnetic field in z direction. The projection onto the xz plane will thus have the form of a sin function, starting in the vertex. For particles with large p_t which fly into the acceptance of the TRD, assuming $v_t \gg v_{\parallel}$ is a good approximation. Assuming further $v_x \gg v_z$, the sin in the xz plane will still be on its rising flank (at small phases) when entering a TRD chamber, within which the influence of bending is small. The phase shift of the sin between entrance and exit of the chamber will be so small, that the track of the particle inside the TRD chamber in the xz plane can be assumed to be straight (figure 6.18).

From geometry one can then deduce

$$\frac{d_x}{\Delta z} \approx \frac{x_{layer,exit}}{z_{exit}} \approx \frac{x_{layer,exit}}{z_{row}}$$

Here $d_x = 30.0mm$ is the height of a drift chamber, z_{row} is the z coordinate of the middle of a pad row and $x_{layer,exit}$ the x coordinate of the cathode wire plane of this chamber. Since the actual z coordinate of the intersection of the track with the pad row, z_{exit} , is unknown, z_{row} was introduced to characterize the pad row. Since it is the central z coordinate of the pad row, it will introduce the smallest average error on the quantity $\frac{x}{z}$. Because $z \ll x$, the error will nevertheless be small. One finally obtains for the deflection correction:

$$d_{tilt} = d'_y - d_y = -\frac{z_{row} \cdot d_x}{x_{layer,exit}} \tan \beta_{tilt} = \pm 1.048mm \cdot \frac{z_{row}}{x_{layer,exit}}$$

This correction is constant for a certain pad row in a given chamber. So it is enough to precalculate these corrections and, together with the constant Lorentz correction, add to the measured deflection:

$$d_y = d'_y + d_{tilt} = d_{y,row} + d_{Lorentz} + d_{tilt}$$

The final value of $c^{(\vartheta)}$ is then given by

$$\begin{aligned} c^{(\vartheta)} &= \frac{d_{Lorentz} + d_{tilt}}{[\tilde{\vartheta}]} \\ &= -\frac{d_x \cdot \tan(\Psi_L) + \frac{z_{row} \cdot d_x}{x_{layer,exit}} \cdot \tan(\beta_{tilt})}{[\tilde{\vartheta}]} \end{aligned}$$

6.6 Sending of the Tracklet Words

The final tracklet word combines all relevant information from the tracklet calculation into a 32 bit word. Before the tracklet words are sent to the GTU, first a cut on their p_t is applied. This will be the topic of the next section. As the trigger is supposed to look for particles with large transverse momenta, the cut is currently set to $p_t \geq 2.3GeV/c$. It is important to note again, that this only works properly for tracks coming from the primary vertex. However, that was one of the basic assumptions for the functionality of the tracklet algorithm. This cut is expressed in limitations on the y deflection, again relying on the

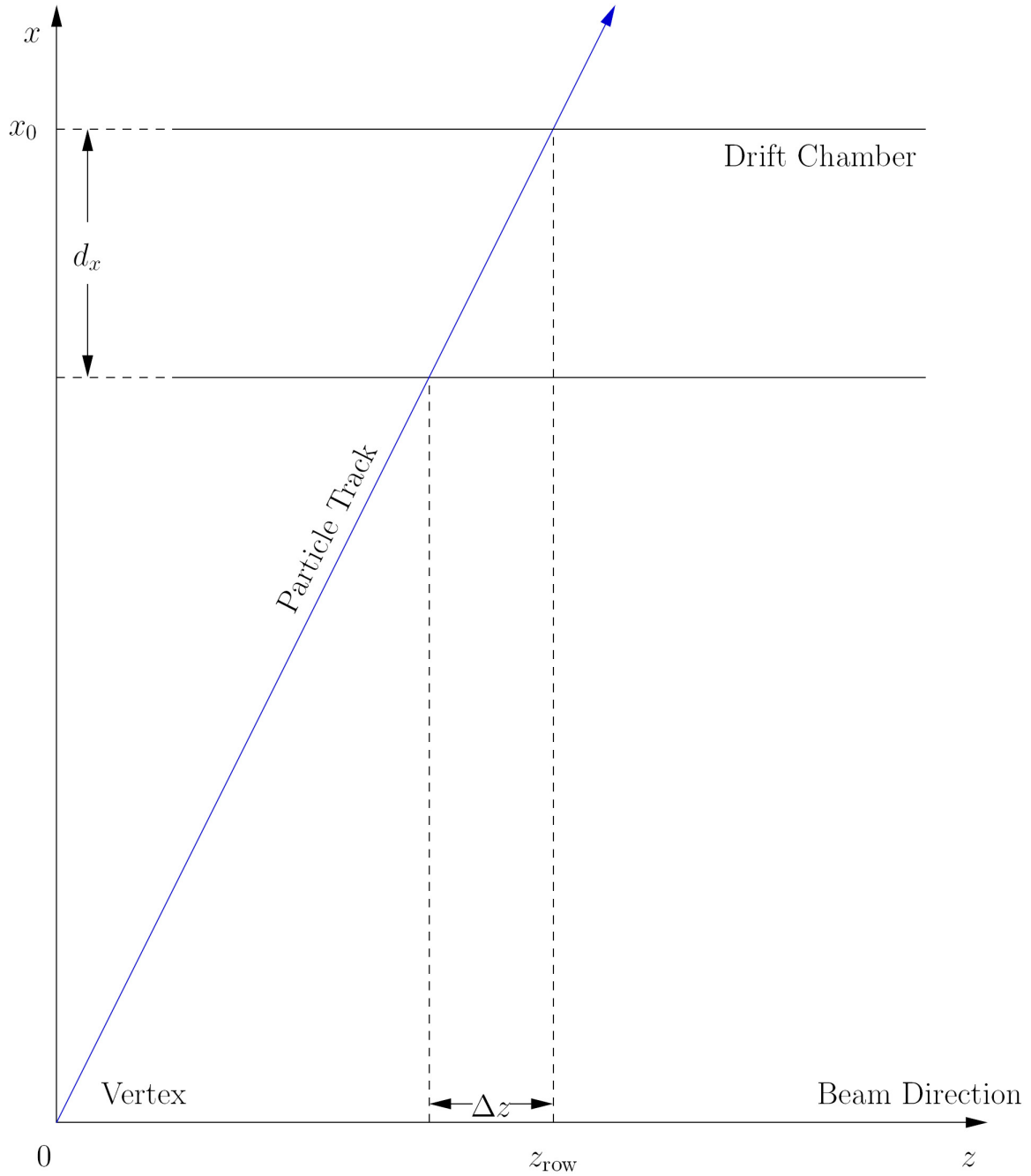


Figure 6.18: The projected track onto the xz -plane under the assumption, that the track comes from the primary vertex. The track is treated as a straight line in the xz -plane. z_{row} was already used for z_{exit} (see text) [dC03]

slope having been transformed to a deflection between entrance and exit of the drift volume. Thus a tracklet is only sent, if its scaled and corrected slope ϑ fulfills

$$T_i^{min} < \tilde{\vartheta} \cdot [\tilde{\vartheta}] < T_i^{max}.$$

Here, the comparators T_i^{min} and T_i^{max} are given at the granularity of pads i .

The tracklet word is then sent to the GTU via the readout tree. All the tracklets of one half chamber are sent by one optical fiber. The GTU collects all the tracklets of one stack, i.e. of six layers and in each layer of two half chambers. Because the tracks, that are under consideration after the p_t cut, are supposed to be stiff enough, they will in the most cases not cross the border between two stacks. Hence, no communication or exchange of tracklets between stacks is foreseen. By the readout tree, which defines the order in which the tracklet words arrive at the GTU, it is intrinsically clear from which sector, stack and layer (even half chamber) they come from.

6.6.1 Cut on the Transverse Momentum

Tracks in a magnetic field travel along a circle whose radius is a measure for the transverse momentum. Of course the primary vertex lies on the circle. Particles of different p_t travel on trajectories of different radii and enter the detector at different positions. Particles with large transverse momenta are characterized by a small angle deviation from the vertex direction at the entrance point. The straight vertex direction of a tracklet at a given point would correspond to a particle with infinitely high p_t traveling to this point, since it would not be bent inside the magnetic field ($\vec{B} = (0, 0, B_z)$, $p_t = \sqrt{p_x^2 + p_y^2}$). In general there is a unique mapping between the deflection angle α of the tracklet (which is a straight line fit but in general not necessarily the tangent to the circle) w.r.t. the vertex direction and the transverse momentum p_t . A minimum p_t corresponds to a maximum angle α_{max} , which can be related locally to a minimal and a maximal deflection length, $d_{y,min}$ and $d_{y,max}$. This relation is deduced in the following.

First, the relation between the minimum transverse momentum and maximum deflection angle is inspected. Let (x_m, y_m) be a representative coordinate for a tracklet, e.g. the coordinate of a cluster from a central time bin in the SM system. For the following discussion it is assumed, that the tracklet corresponds to the tangent of the circle through the touch point (x_m, y_m) (which is an idealization) (figure 6.19). The distance to the vertex is then given by

$$d = \sqrt{x_m^2 + y_m^2}.$$

Let further the radius of the bent track of the particle in the magnetic field be r and the imaginary center of the circle M . Then the opening angle of the triangle (M,vertex, (x_m, y_m)) at M is denoted by α . Because the triangle is isosceles ((x_m, y_m) is a point on the circle), drawing the height through M will cut it into two identical rectangular triangles and divide the distance d equally. Hence the following relation is fulfilled in each of the rectangular triangles:

$$r = \frac{d}{2 \sin \alpha}.$$

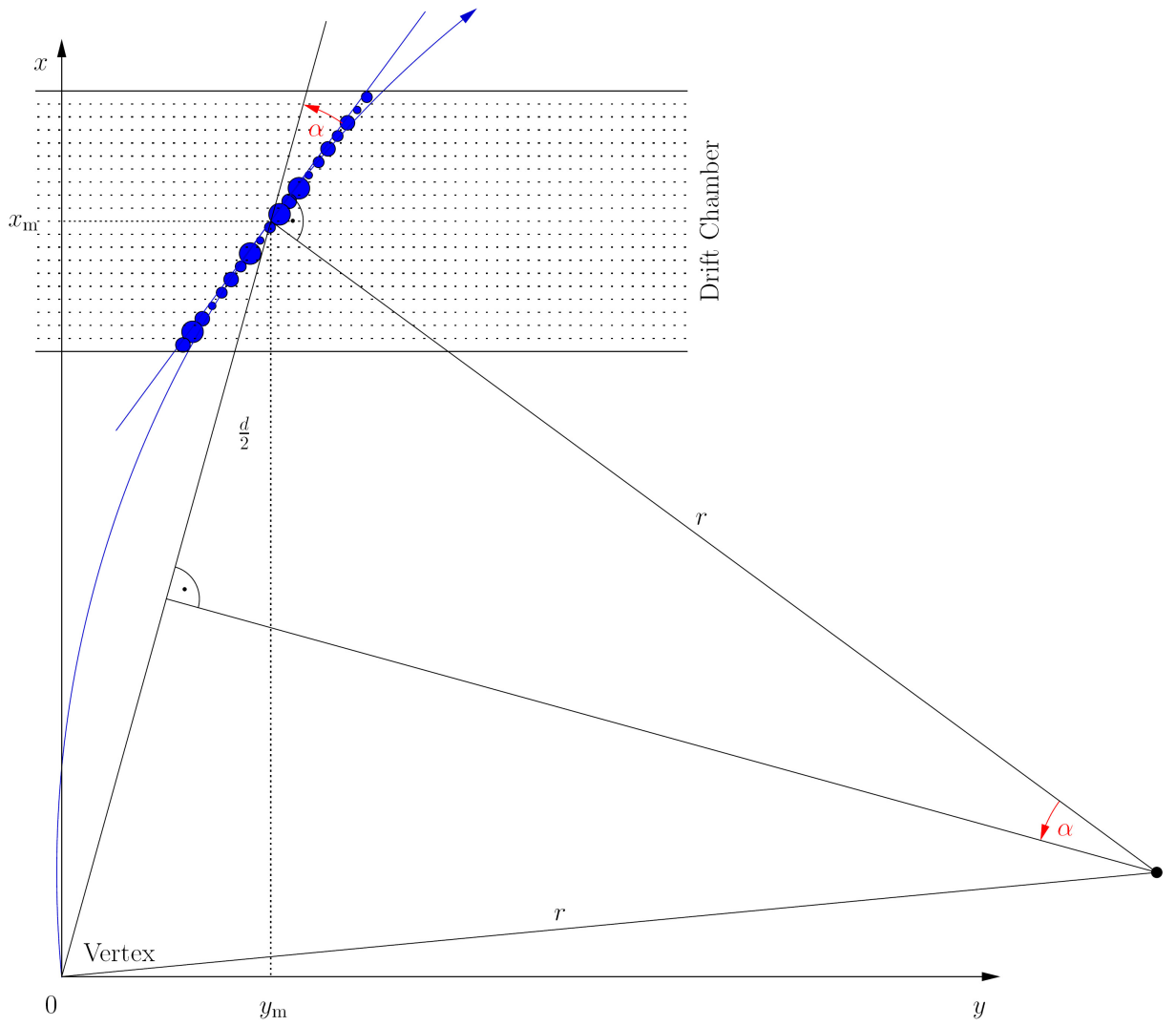


Figure 6.19: The bending of a track in the magnetic field and the connection between the vertex deflection angle α to geometrical quantities [dC03]

Note, that α defines also the angle between vertex direction and tracklet direction (tangent to the circle in (x_m, y_m)). Since the particle is moving on a circle in the xy plane perpendicular to \vec{B} due to the Lorentz force, by setting the Lorentz force equal to the centripetal power, one can express the transverse momentum as a function of the radius:

$$\frac{mv_t^2}{r} = qv_t B$$

$$p_t = mv_t = qrB.$$

The bending direction depends on the charge sign. In case of electrons or pions, which are the particles mostly detected by the TRAP, $q = e$.

Combining yields:

$$\alpha = \arcsin\left(\frac{\sqrt{x_m^2 + y_m^2} \cdot qB}{2p_t}\right).$$

Note, that the deflection angle of the track from the primary vertex direction depends on the position. Using $q = e = 0.30 \frac{GeV/c}{m \cdot T}$, $x_m \leq 3.6m$, $y_m \leq 0.65m$ yields $\frac{\sqrt{x_m^2 + y_m^2} \cdot qB}{2p_t} = \frac{0.22GeV/c}{p_t}$. For the region in which $p_t \geq 1GeV/c$, arcsin is therefore a monotone growing, inversely symmetric function and it follows

$$\alpha_{max} = \arcsin\left(\frac{\sqrt{x_m^2 + y_m^2} eB}{2 \cdot p_{t,min}^{LTU}}\right)$$

for the relation between the maximum deflection angle α_{max} and the minimum transverse momentum of tracklets in the LTU, $p_{t,min}^{LTU} = 2.3GeV/c$. This yields a maximum deflection angle for a pad in the outermost layer on the edge of a pad plane of around 5° .

In the next step the relation between the deflection d_y (for $d_x = 30.0mm$) and the angle α to the vertex direction is investigated. For this, one needs the x coordinate of the entrance to the drift volume, $x_0 = x_{layer,enter}$, and the y position of the tracklet when entering the drift volume, $y_0 = y_{layer,enter} = \hat{y} \cdot [\hat{y}] - d_y$. Let further φ_{track} denote the angle between the tracklet and the chamber normal and φ_{vertex} the angle between the vertex direction and the chamber normal (figure 6.20).

Then the following relations are given by the geometry:

$$\tan(\varphi_{vertex}) = \frac{y_0}{x_0}$$

$$\tan(\varphi_{track}) = \frac{d_y}{d_x}.$$

For the angle α it follows

$$\alpha = \varphi_{track} - \varphi_{vertex}$$

$$= \arctan\left(\frac{d_y}{d_x}\right) - \arctan\left(\frac{y_0}{x_0}\right).$$

Using the relation between α and p_t and resolving for d_y , one can express the deflection as a function of p_t :

$$d_y = d_x \cdot \tan\left[\arctan\left(\frac{y_0}{x_0}\right) + \alpha\right]$$

$$d_y = d_x \cdot \tan\left[\arctan\left(\frac{y_0}{x_0}\right) + \arcsin\left(\frac{\sqrt{x_m^2 + y_m^2} \cdot qB}{2p_t}\right)\right].$$

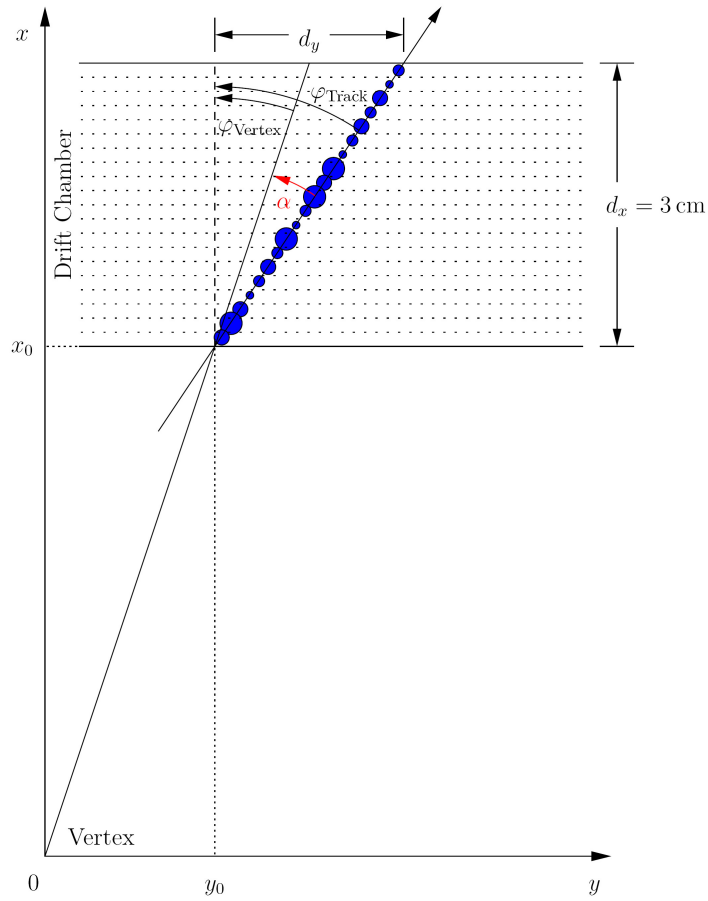


Figure 6.20: Definition of angles φ_{track} (angle of tracklet w.r.t.chamber normal), φ_{vertex} (angle of vertex direction w.r.t.chamber normal) and α (angle of tracklet w.r.t.vertex direction) [dC03]

Now, a particle of negative charge is bent reversely. Hence α can also become negative due to the charge sign and $\alpha_{max} \geq 0$ turns into $\alpha_{min} \leq 0$:

$$\begin{aligned}\alpha_{min} &= \arcsin\left(\frac{\sqrt{x_m^2 + y_m^2}(-e)B}{2 \cdot p_{t,min}^{LTU}}\right) \\ &= -\arcsin\left(\frac{\sqrt{x_m^2 + y_m^2}(e)B}{2 \cdot p_{t,min}^{LTU}}\right) \\ &= -\alpha_{max}.\end{aligned}$$

Since tan is a monotone growing, inversely symmetric function, inserting α_{max} yields a maximum deflection, α_{min} a minimum deflection:

$$\begin{aligned}d_{y,min} &= d_x \cdot \tan\left(\arctan\left(\frac{y_0}{x_0}\right) - \alpha_{max}\right) \\ d_{y,max} &= d_x \cdot \tan\left(\arctan\left(\frac{y_0}{x_0}\right) + \alpha_{max}\right).\end{aligned}$$

As the sign of a charged particle is not known in the TRAP, a constraint on lower and upper deflection has to be imposed. In both cases, $d_y < d_{y,min}$ and $d_y > d_{y,max}$, the tracklet would have too small p_t , i.e. its deflection angle from the vertex would be too large. Therefore one can identify (figure 6.21)

$$\begin{aligned}d_{y,min} &= T_i^{min} \\ d_{y,max} &= T_i^{max}.\end{aligned}$$

Four variable quantities occur: x_0 , y_0 , x_m and y_m . The error is small when setting $x_m = x_0$ and $y_m = y_0$, thus

$$\begin{aligned}d_{y,min} &= d_x \cdot \tan\left(\arctan\left(\frac{y_0}{x_0}\right) - \arcsin\left(\frac{\sqrt{x_0^2 + y_0^2}eB}{2 \cdot p_{t,min}^{LTU}}\right)\right) \\ d_{y,max} &= d_x \cdot \tan\left(\arctan\left(\frac{y_0}{x_0}\right) + \arcsin\left(\frac{\sqrt{x_0^2 + y_0^2}eB}{2 \cdot p_{t,min}^{LTU}}\right)\right)\end{aligned}$$

x_0 is constant for each chamber, since it corresponds to the radial position of the entrance to the drift volume. y_0 , which denoted the y position of the tracklet at x_0 ¹¹, is individual for each tracklet. However it is sufficient to provide y_0 in granularities of pad widths (e.g. center y coordinate of each pad). Hence for each chamber, 144 values for T_i^{min} and T_i^{max} , each, can be precalculated and stored in some configuration buffer. Depending on the pad number i with the coordinate y_0 , the appropriate pair (T_i^{min}, T_i^{max}) has to be chosen for each tracklet to compare with its deflection. In the tracklet simulator things were eased even a bit more by using the coordinates of the left channel of the original tracklet candidate. Thus i denotes this channel number and y_0 its (central) pad y coordinate¹².

¹¹The angle α between tracklet and primary vertex direction depends on the position. Looking at a certain layer fixes x_0 . Then α is determined by the y-coordinate, at which the track enters the layer, y_0 .

¹²Of course now i counts the channels of one pad row, $i \in [0, 143]$. Hence the channel number on a MCM, i' , has to be mapped to the pad row channel number. If the MCM is the n^{th} one, counted from 0 to 7 on a row, this mapping is given by $i = i' + n \cdot 18$

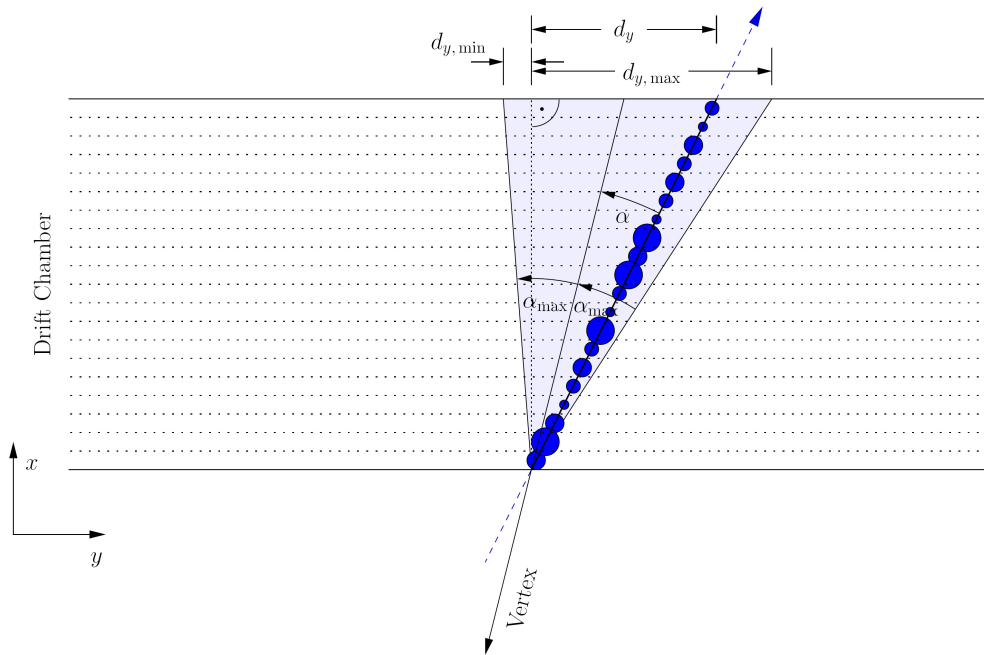


Figure 6.21: Minimum and maximum deflection of a tracklet (whose track comes from the primary vertex), that are applied as a cut, in order to assure $p_t \geq 2.3\text{GeV}/c$ [dC03]

6.6.2 Structure of a Tracklet Word

As 13 bits are used by the offset, 7 by the deflection and 4 bits are used for the pad row number (depending on the chamber, there are between 12 and 16 pad rows), 8 bits are left to encode the electron probability into 2^8 values with an accuracy of 2^{-8} (since the LUT provides 8 bits for each of its entries and $P_{electron} \leq 1$).

Table 6.2: The Tracklet Word

tracklet parameter	symbol	granularity	range	bits
pad position	\tilde{y}	$160\mu\text{m}$	$[-643.2\text{mm}, 643.2\text{mm}]$	13
deflection length	\tilde{v}	$140\mu\text{m}$	$[-8.8\text{mm}, 8.8\text{mm}]$	7
pad row		1	$[0, 15]$	4
electron probability	$P_{electron}$	$3.91 \cdot 10^{-3}$	$[0, 1]$	8

First the electron probability is written (outermost left part of the 32 bit word). Then follow the pad row, deflection length and pad position (outermost right part of the bit word). The order of the words as given in the table thus determines the obtained sequence, when decoding the tracklet word. All quantities are given in two complement representation.

7 Implementation and Results

In this chapter some information concerning the implementation is provided as well as a selection of results from tracklet reconstruction.

An introduction into the ROOT framework is provided by [ROO07], an overview over AliRoot is given in [Off07]. A ROOT code documentation can be found on the ROOT homepage [ROO], an AliRoot code documentation on the Offline Pages [Off]. For elementary C++ issues the tutorial [Dan] was addressed, for advanced topics [LL03]. An overview about issues in information technology are summarized in [RP02]. Some ideas for the reconstruction plots were suggested by [ALI01]. The ALICE detector performance is presented in [ALI06].

The object oriented framework AliRoot, within which the ALICE detector and hence also the TRD is simulated, is based on the ROOT package. ROOT provides a data analysis platform, combined with input/output procedures and a graphical user interface. The frameworks are based on C++.

The simulation environment provides a number of abstract classes as common interface to all detector systems. They enclose the particle production, particle transportation through the detectors, digitization and detector response. For particle production a number of generators are available, which parameterize particle abundance, momentum and rapidity distributions, flow, jets and other physical quantities as they are supposed to occur in special event types (e.g. pp collisions, PbPb collisions,...). The particle transport steers the transport of particles from the primary vertex and their decay products through the detector, producing the energy losses, which are also called hits. All the mother-daughter histories as well as information about particle identity, primary vertex position and primary momenta, are stored in the so called kinematics tree, whose information is available through the class AliStack. For each hit the full information about the track producing it, is kept. During the digitization, the treatment of the effects, which were mentioned in the chapter about Signal Creation, is included. Also noise is added on this level. Alternatively, an intermediate stage, the summable digits, can be produced. They are of importance, if a signal event shall be merged with a background event. Then, the digits of the signal and the background event are produced together. The same background event can be used for several signal events, e.g. for efficiency tests, resulting in a reduction of computing time and storage place.

Finally raw data production takes into account the detector readout peculiarities and electronics. At the stage of raw data, it must be possible to interchange simulated and real data. Like that, the following reconstruction and analysis algorithms can be tested with simulated data, before applying and comparing them to real data.

Through the class AliSimulation, the user can steer the simulation. A macro Config.C, in which it is determined, which detector systems are involved, what generator cocktail is chosen, what particle features (momentum ranges, rapidity intervals, decay products, angle distributions,...) are to be used, what interaction effects between particles and detector

matter shall be included, etc., has to be provided in addition.

7.1 Implementation Issues

The implementation of the tracklet calculation as described in the previous chapter, has been added to the `AliTRDmcmSim` class. This class is intended to simulate the electronics of the MCM chip. As the digitization is already performed by `AliTRDdigitizer`, the MCM simulator starts the simulation from the filter stage on. An implementation of the pedestal filter as well as the tail cancellation filter can be found. Moreover zero suppression mapping is done and the preparation of the raw data is performed. The MCM simulator class can thus be seen as the class, which transforms digits to raw data. It is instantiated and initialized by the class `AliTRDrawData`.

Because tracklet calculation is performed on the MCM chip as well, for the implementation it was chosen to add this functionality to the `AliTRDmcmSim` class. It was intended to simulate the electronics as close as possible. Therefore it was necessary to stick close to the tracklet calculation algorithm as presented in the previous chapter. Also the data word widths that are used by the digital electronics, had to be respected and simulated.

In order to make the code maintainable, all the operations related to arithmetics with floating bit values were encapsulated in a new class, called `AliTRDtrapAlu`. The idea was, to define for each bit-like value its granularity at the beginning by an initialization. The user sets the number of bits before and after the comma and all arithmetics is done within these limits. That means, that if one number is defined to have n bit after the comma, another one to have m , multiplying these two numbers will result in a number with an accuracy of $2^{-\min(m,n)}$. In order to speed up the calculations, not the common operator overloading methods were used. These require to create in the function an instance of the class, whose data members carry the result of the calculation. This instance is then returned by the operator function and has therefore to be copied to a higher scope, such that it is visible e.g. for the assignment operator. Instead of this procedure, a static instance of the class is created and all operator overloading functions were written such, that they vary the members of this static instance directly and return a reference to it. Like that the additional copy to higher visibility scope is omitted. This makes the code much faster but causes a compiler warning, which can be ignored.

Using this `AliTRDtrapAlu` class, also a new version of the tail cancellation filter was written. This was necessary in order to treat the digitized ADC values consistently, which are enlarged from 10 bit to 12 bit in the filter by adding two bits after the comma.

The output from the filter stage of 12 bit is then given to the tracklet calculation. From here on, the preprocessing algorithms are run through. ADC data is only processed if it belongs to samplings in the linear fit range.

During implementation, a number of problems have shown up, which were well hidden and difficult to find. Therefore, they shall be mentioned shortly. One of them was, that in the online code, the numbering of ADCs on a MCM runs reversely to the numbering of the pads on a pad row. Therefore, in order to come to the situation of channel numbering as assumed in the previous chapter, the data array containing the ADC values had to be reversed, before applying the algorithms. In order to be consistent to the online numbering, the reversing had to be inverted in the end.

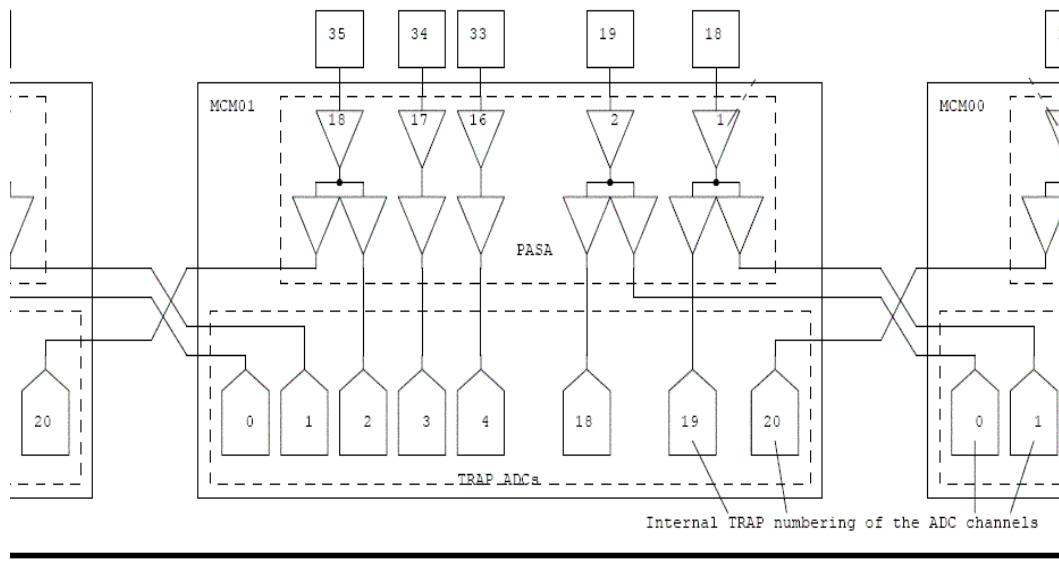


Figure 7.1: The reversed TRAP ADC channel numbering, as it is also implemented in AliRoot [WIK]

Another problem was, that the radial positions of the drift volumes are slightly different in the online geometry as compared to the values in the Technical Design Report. The values in table 7.1 for different layers were obtained by exploiting the coordinate values of hits from the hit tree.

Table 7.1: Radial coordinates in mm of the outer drift chamber plane

layer 1	3003.0
layer 2	3129.0
layer 3	3255.0
layer 4	3381.0
layer 5	3507.0
layer 6	3633.0

For the comparison of the cluster charges to the cluster charge threshold, it is necessary to subtract the baseline. As the baseline is subject to tail filtering, the value to be subtracted depends on the time bin. Therefore the time response of the tail filter to the baseline had to be precalculated and stored. This is different to the procedure described in [TRA06].

In order to do the selection of the four channels with maximum cluster charge correctly, a sorting algorithm based on a linked list was implemented. This sorting method was also used for the selection of a maximum of four tracklets from tracklet candidates later during the processing.

The calculation of the fit sums for the chosen preprocessor channels requires an information about the cluster position relative to the central pad. For this purpose charge sharing is used. From the calibration database (access via AliTRDcalibDB), a sampling of the Pad Response Function for pads from each layer is available. These functions were then linearly interpolated between the given sampling points in order to increase accuracy, before reversing the discrete functions. From the reversed functions the entries for the position correction LUT could be obtained in the requested granularity. In figure 7.2 the estimated position as a function of the real position, $|y^{est}|(y) = \frac{1}{2} \frac{PRF(y-1) - PRF(y+1)}{PRF(y)}$, obtained after linear interpolation of the PRF, is shown in (a). (b) shows the reversed function, $y(|y^{est}|)$, for which $|y^{est}|(y)$ was linearly interpolated, too. Figure 7.3 shows the correction $y(|y^{est}|) - |y^{est}|$ to the estimated position. (a) with fine granularity, (b) discretized, as in the position correction LUT ($|y^{est}|$ with a granularity of 2^{-7} , $y(|y^{est}|) - |y^{est}|$ as five bit value). For each channel, an independent fit sum is reserved which counts the number of hits and which is updated for each time bin during the preprocessing (if no hit was found, the sum is left unchanged). Here, in contrast to reality, all the ADC values for each of the time bins are already calculated and stored in a two dimensional array. The digitization has already finished, when tracklet calculation starts. In reality, preprocessing is done in parallel to data acquisition.

When all the time bins were processed and the fit sums are updated, the real TRAP chip changes into processing mode (steered by an internal clock). The fit sums are merged and tracklet candidates are sought. By means of the above mentioned sorting algorithm, they are sorted with respect to their total number of hits. A maximum of four channels with the largest hit sum are chosen as tracklets. For them, offset and slope is calculated, the slope is turned into a deflection, Lorentz and tilted pads corrections are applied, the quantities are

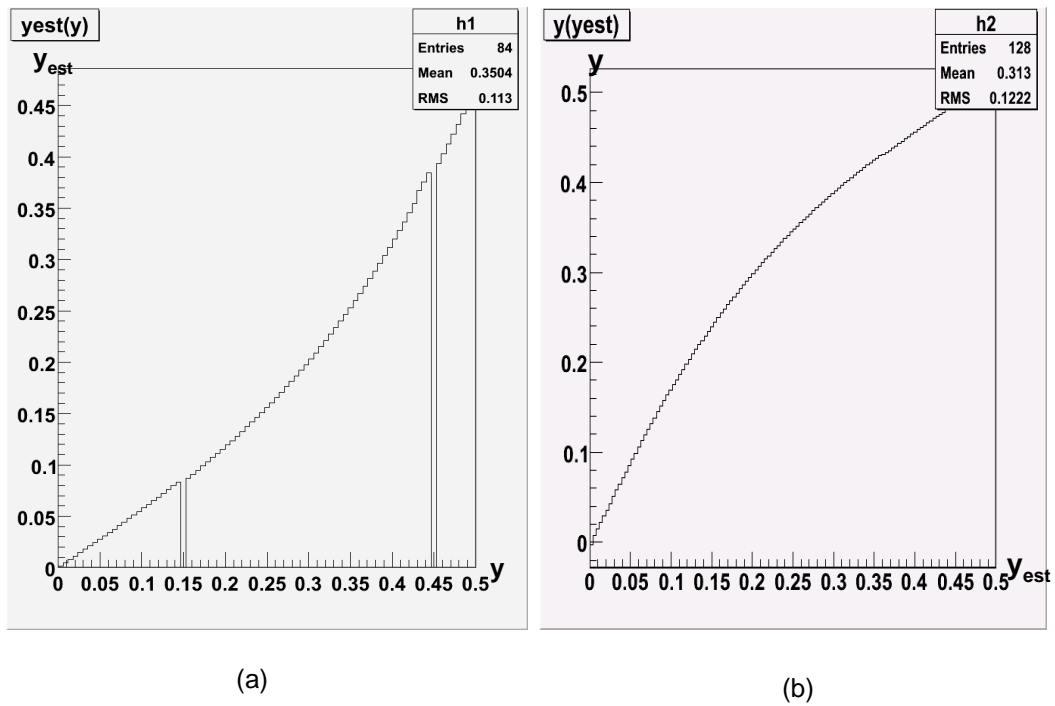
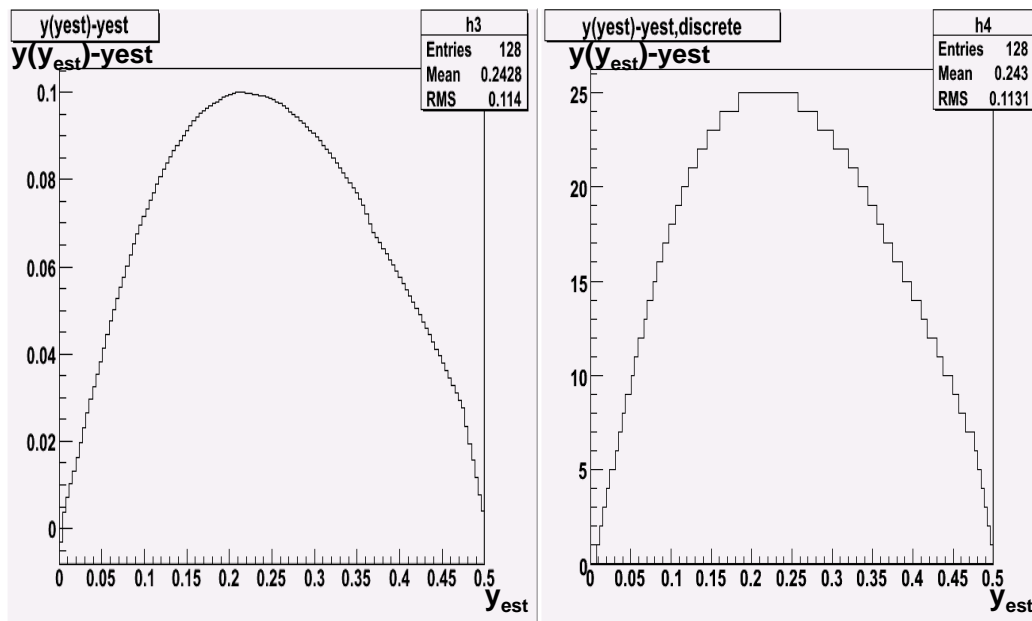


Figure 7.2: Estimated position as function of the real position (a) and the reversed function (b)



(a)

(b)

Figure 7.3: The position correction values: (a) with fine granularity, (b) discretized for the position LUT

turned to the GTU coordinate and metric system and a cut on $p_t = 2.3\text{GeV}/c$ is applied, based on maximum and minimum deflection.

Finally, the 32 bit tracklet words are sorted in ascending y order (according to the offset) and stored. The raw data class collects all tracklet words from a half chamber and writes them one after the other in front of the HC header, as long as the header does not overflow (maximum of 40 tracklets per HC). In a high multiplicity environment, where a buffer overflow can occur, it depends on the sorting, which of the tracklets are sent to the GTU.

Alternatively to this "official" way of storing the tracklets, a .root output format has been created, which stores additionally all the information down to the channel, from which the tracklet occurs. This makes it possible to match the tracklet with the track that created it and by this to check the resolution of deflection and offset. For such performance analysis a voluminous macro (TrackletReader.C) has been written.

The new or changed AliRoot classes have been integrated into the framework and submitted to SVN. The code of the TrackletReader.C macro can be found on the CD, which is part of the thesis. In total, more than 4500 lines of code have been produced.

In 7.2, some data variables used for tracklet calculation, which were generated to be of AliTRDtrapAlu type, are listed, together with their number of pre- and past-comma bits, the granularity, range and their meaning. It is possible to limit the range of a bit word by indicating the scaled upper limit. Note that only positive integer or double values can be assigned to a variable of type AliTRDtrapAlu. A sign has to be set explicitly. Therefore only the non negative ranges are given in the table below. However, in arithmetics and assignments to other AliTRDtrapAlu typed variables, the sign is considered.

There is another peculiarity which has to be thought of, when using the AliTRDtrapAlu class: Let a, b and c be of type AliTRDtrapAlu. Imagine a and b to have 1 pre- and 8 past-comma bits, which is denoted in the following way: $a : (1, 8)$ and $b : (1, 8)$. Let $a, b < 1$. The product $a \cdot b$ produces a bit word, whose number of past-comma bits is limited to 8. However, if $c : (1, 16)$ and $c = a \cdot b$, one would expect c to have 16 valid past comma bits. But this would mean to leave the number range of a and b (with 8 past-comma bit) and therefore c will be limited to an accuracy of 2^{-8} (rest of bits filled by 0). In order to solve this, one has to declare $d, e : (1, 16)$, which means, that d and e are treated with 16 bits after the comma. Doing $d = a$ and $e = b$ and then $c = d \cdot e$ will produce a bit word with a granularity of 2^{-16} .

The unused bits listed in table 7.2 occur, because the corresponding quantities are involved in a multiplication, where the result has finer granularity than the factors (see above example for this peculiarity).

7.2 Offset Correction

In the first part of this section, a correction to the offset due to the inclination of the drifting clusters toward the chamber normal by the Lorentz angle, is discussed. This correction becomes necessary, as the actual implementation of the tracklet calculation includes some peculiarities, which were not foreseen in the ideal case.

In the second part it is discussed, why the offset cannot be corrected for the influence of the tilted pads and how this influences the offset performance.

Table 7.2: AliTRDtrapAlu variables used for tracklet calculation

name	declaration	granularity	range	explanation
data	(10,2)	2^{-2}	full	takes over filtered ADC values
filPed	(10,2)	2^{-2}	full	takes over tail filtered baseline
cQTAlu	(1,10)	2^{-10}	$[0, 2^{-4} - 2^{-10}]$	cluster quality threshold (not set)
cTHAlu	(12,2)	2^{-2}	full	cluster charge threshold
qsumAlu	(12,2)	2^{-2}	full	charge sum
dCOGAlu	(1,7)	2^{-7}	full ($[0, 1 - 2^{-7}]$)	center of gravity $COG = \frac{R-L}{C}$
yrawAlu	(1,8)	2^{-8}	full	$\frac{COG}{2}$
yAlu	(1,16)	2^{-8}	$[0, 1 - 2^{-8}]$	y position update; 8 bit unused
xAlu	(5,8)	1	$[0, 2^5 - 1]$	time bin update; 8 bit unused
xxAlu	(10,0)	1	full	X^2 update
yyAlu	(1,16)	2^{-16}	full	Y^2 update
xyAlu	(6,8)	2^{-8}	full ($[2^6 - 2^{-8}]$)	XY update
XAlu	(9,0)	1	full	fit sum: X
XXAlu	(14,0)	1	full	fit sum: X^2
YAlu	(5,8)	2^{-8}	full	fit sum: Y ; without sign bit
YYAlu	(5,16)	2^{-16}	full	fit sum: XY
XYAlu	(8,8)	2^{-8}	full	fit sum: XY ; without sign bit
QT0Alu	(15,0)	1	full	accumulated charge
QT1Alu	(16,0)	1	full	accumulated charge
inverseNAlu	(1,8)	2^{-8}	full	samples $\frac{1}{N}$
TotalChargeAlu	(17,8)	2^{-8}	full	$(Q^{(0)} + Q^{(1)})\frac{1}{N}$
MeanChargeAlu	(8,0)	1	full	mean cluster charge in 8 bit

7.2.1 Offset Lorentz Correction

The tracklets are a linear fit to the track between $[t_{FS}, t_{FE}] \in [t_{drift,S}, t_{drift,E}]$, where $t_{drift,S}$ is the time bin corresponding to the boundary of the drift volume at larger radii and $t_{drift,E}$ to its boundary at smaller radii. With a drift velocity of $v_{drift,x} = 1.5\text{cm}/\mu\text{s}$ and a sampling frequency of 10MHz , $[t_{drift,S}, t_{drift,E}]$ covers 20 time bins. In the ideal implementation it is assumed that $[t_{FS}, t_{FE}] = [t_{drift,S}, t_{drift,E}]$ and that the pad plane adjoins directly upon the position of t_{FS} . Therefore all clusters drift to the pad plane in this picture. The offset, which is given as a function of the fit sums, corresponds to the y-position at t_{FS} . That means that a cluster produced at t_{FS} does not need to drift and that therefore the offset does not need any Lorentz correction. This situation is sketched in figure 7.4.

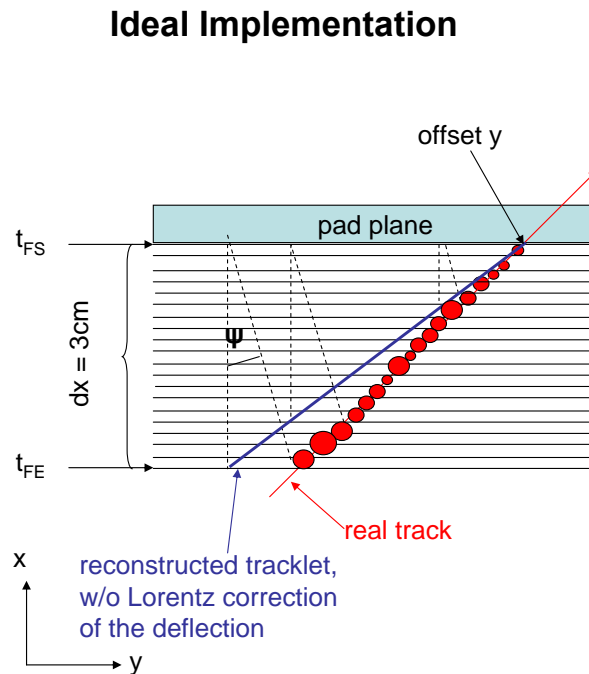


Figure 7.4: Ideal implementation, with no offset Lorentz correction needed.

However in the current settings of the simulation, there are 24 time bins which cover together the amplification and the drift region and additionally some time bins after drift. Since the drift velocity is not constant but increases significantly when approaching the anode wire, it is not possible any more to assign a position to a time bin. Even worse, the drift path depends on the z-position of a cluster, which determines the distance to the next anode wire. The total drift time then depends on the actual drift path, showing that $v_{drift,x}(t) = f(\vec{x}_{init})$ is time dependent and a function of the initial position of a cluster. For this reason, also the number of time bins, that sample clusters from the amplification region (in the following referred to as amplification time bins), may vary.

From an average pulse height spectrum, one can approximately determine the number of amplification time bins, since there the measured charge exceeds the cluster charge of drift time bins for two reasons: First, the drift velocity is larger and therefore more charge reaches the anode wire between two samplings. This corresponds to a larger spatial distance corresponding to an amplification time bin compared to a drift time bin. Second, charge from both sides (3.5mm from cathode wire plane to anode wire plane, 3.5mm from anode wire plane to pad plane) of the anode wire is amplified and measured within the same time bin. One can think of the amplification time bins being mirrored at the anode wire and doubled in size.

It shows up, that between two and three time bins belong to the amplification region, where one time bin will acquire charge clusters from both, the amplification and the drift region. In case of a constant drift velocity in the amplification region of $v_{drift,x}^{amp} \approx 3.5\text{cm}/\mu\text{s}$, the whole charge of the amplification region would even be absorbed within one time bin. Additionally to the mentioned complications, a small offset t_0 can be added (fraction of a time bin) to arbitrarily shift the spectrum. However, this offset can be neglected for the offset correction. In order to be save, one should assume three amplification time bins (also accounting for a possible inefficiency of the tail filter, since the amplification clusters produce large tails).

Now the linear fit start time, t_{FS} , can be chosen arbitrarily, as long as $t_{FS} \geq t_{drift,S}$. Therefore also the offset position varies. Note that the deflection obtained from the linear fit is always (never mind the fit range) scaled to a deflection length for a drift chamber height of 30.0mm (20 time bins), before it is written into the tracklet word. For the offset, such a scaling (e.g. projection to a position at the pad plane) is not possible, because the radial position of time bin t_{FS} , at which the offset is defined, is not known (because drift velocities vary from case to case).

In a simplified picture (sketched in figure 7.5¹), it is assumed, that the drift velocity in the amplification region increases so much, that the Lorentz inclination angle of the drifting clusters can be neglected there ($v_{drift,x}^{amp} \propto \frac{1}{1+(\tan \Psi)^2}$). In the drift region, the drift velocity $v_{drift,x}$ is constant. Then, the error on the offset due to the Lorentz drift only depends on $t_{FS} - t_{drift,S}$:

$$(\delta y)_{err,Lor} = v_{drift,x} \cdot (t_{FS} - t_{drift,S}) \cdot \tan \Psi_L.$$

This introduces a constant shift with constant sign, independent of the charge sign (and thus the bending direction) of the particle track. The only unknown quantity is $t_{drift,S}$, the first time bin that accumulates clusters from the drift region. However, by estimating the number of amplification time bins to be less or equal to three, $t_{drift,S} \leq 3$, and by setting $t_{FS} = 5$ for example, one is left with $t_{FS} - t_{drift,S} \geq 2$. Therefore such a correction of the offset fulfills

$$(\delta y)_{corr,Lor} = v_{drift,x} \cdot 2 \cdot \tan \Psi_L \leq (\delta y)_{err,Lor}$$

and can reduce the shift, if it is subtracted from the offset:

$$y_{corr,Lor} = y - (\delta y)_{corr,Lor}.$$

A correction to the offset value has been implemented in the tracklet simulator.

¹Note that the "reconstructed tracklet" shown here, is not corrected for the Lorentz deflection. Applying this correction would make the tracklet parallel to the track but not change the offset position. The reconstructed tracklet and the real track coincide at $t_{drift,S}$.

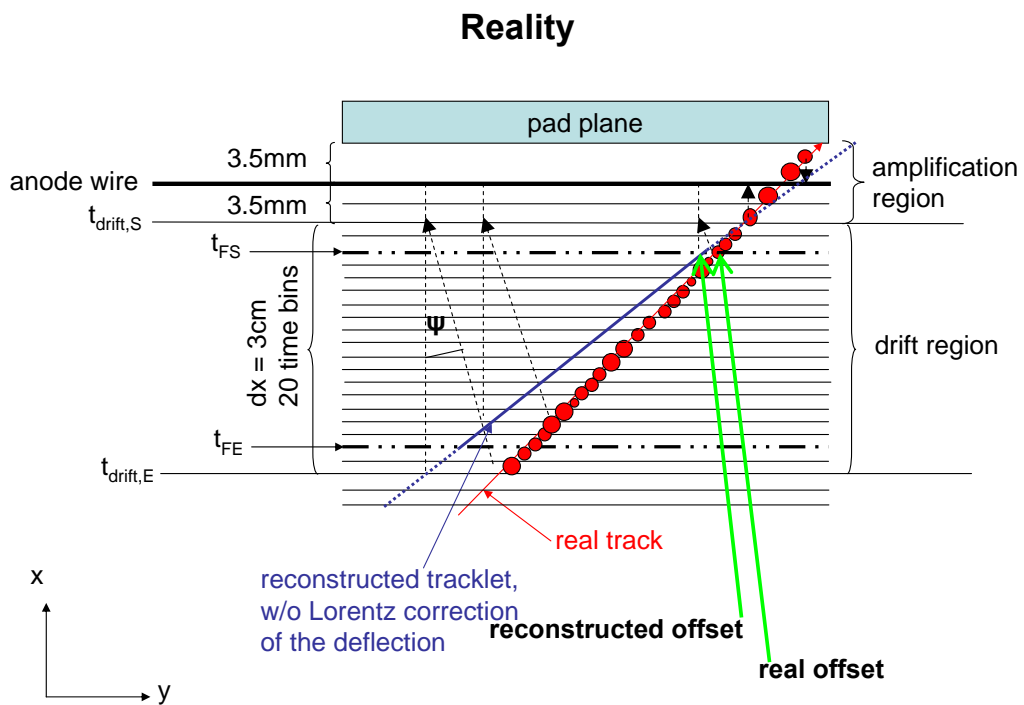


Figure 7.5: Why a offset Lorentz correction is needed.

If the Lorentz angle is supposed to be the only source for a shift of the offset performance distribution (offset performance: $\delta y = y_{tracklet} - y_{MC}$), from the measured shift $(\delta y)_{err,Lor}$, one can deduce the first drift time bin, $t_{drift,S}$:

$$t_{drift,S} = t_{FS} - \frac{(\delta y)_{err,Lor}}{v_{drift,x} \cdot \tan \Psi_L}.$$

From early runs without applied offset Lorentz correction, the measured average mean of the offset performance distributions was around $0.49mm$: $\langle \delta y \rangle \approx 0.49mm$. Assuming that this mean is due to the offset shift $\langle \delta y \rangle \approx (\delta y)_{err,Lor}$, one obtains for $t_{FS} - t_{drift,S}$:

$$t_{FS} - t_{drift,S} \approx \frac{0.049cm}{1.5cm/\mu s \cdot \tan(7.7^\circ)} \approx 0.24\mu s.$$

This corresponds to 2.4 time bins and justifies the assumption $t_{FS} - t_{drift,S} \geq 2$, used above.

Here it should also be noted, that the choice of t_{FE} depends on the estimate Δt_{est} of the number of drift time bins, that occurred before t_{FS} , $\Delta t_{est} \leq t_{FS} - t_{drift,S}$. Because the drift time incorporates 20 time bins, one must take care to choose t_{FE} such, that it lies within the fit range, $t_{FE} \leq t_{drift,E}$, hence $t_{FE} \leq t_{FS} + 20 - \Delta t_{est}$. On the other hand, t_{FE} should be chosen close to $t_{drift,E}$, in order to make sure, that Transition Radiation clusters are accounted for. Otherwise this would cut on the electron-pion separation power.

7.2.2 Offset Tilted Pads Correction

In the following, the notation from chapter 6, section 6.5 is used.

Unlike the deflection, the offset cannot be corrected for the influence of the tilted pads. The measured y coordinate of the offset, which is obtained from charge sharing, is measured in the oblique coordinate system of the pads, hence it is a y' coordinate. In order to correct the error, the offset coordinate must be transformed to the local SM system. For that purpose, the z coordinate of the offset would have to be known (either in the pad system or the local SM system, which would not make a large difference), which is not the case. However, one can estimate the influence of the error. For this, the position of the y axis plays a crucial role. It is important to know, at which height the y axis contacts the pad row. When calculating the correction to the deflection, it was enough to assume, that the y axis contacts the pad row in its middle, hence z_{row} was the z coordinate of the middle of a pad row and the origins of the coordinate systems were situated there. Since the fraction $\frac{z_{row}}{x_{layer}}$ was considered, and $x_{layer} \gg z_{row}$, the exact position of z_{row} would not influence the correction much.

Since the number of pad rows in a chamber is even (12 or 16), also the number of pad rows in one layer of a SM is even. Therefore the y axis in the local SM system runs between two pad rows, only touching their borders (see figure 7.6). It is therefore not correct, to shift the origin of the two coordinate systems to the middle z coordinate of a pad row, to estimate the errors. Note, that the different tilted pad rows of a layer (same tilting angle) are independent of each other. If z_{row} denotes the z position of the pad row borders in the SM system, $z_{row} = n \cdot d$, $n \in \mathbb{Z}$ (d is the projected length of a pad onto the z-axis; d grows toward outer layers), the origin of the SM system and the tilted pads system has to be shifted to $z = z_{row}$, in order to be able to transform coordinates (y', z') into coordinates

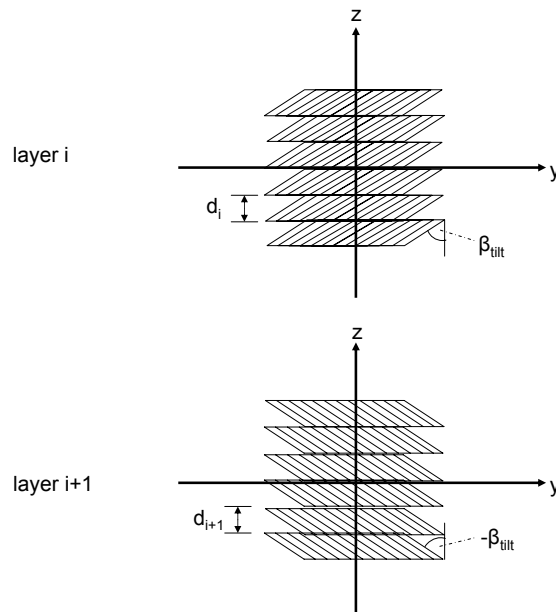


Figure 7.6: Tilted pad rows for two successive layers. The y axis passes between two rows.

(y, z) by a rotation. All the errors on the offset coordinate in one layer have then the same sign. The sign of the error changes layer by layer, since the tilting angle sign alternates. Note, that the error in the offset coordinate can take both signs, if z_{row} is chosen to be the z coordinate in the middle of a pad row. Therefore also the range of the error is different. While the error for $z_{row} = \frac{d}{2} + n \cdot d$, $n \in \mathbb{Z}$ is in the range $[-\frac{d}{2} \tan \beta_{tilt}, \frac{d}{2} \tan \beta_{tilt}]$, this becomes

$$|(\delta y)_{err,tilt}| \in [0, d \cdot |\tan \beta_{tilt}|]$$

in reality, where $z_{row} = n \cdot d$, $n \in \mathbb{Z}$. With $d \approx 100mm$ and $\beta_{tilt} = 2^\circ$, one obtains a maximum error of $|(\delta y)_{err,tilt,max}| \approx 0.35mm$. The actual error depends on the z' position of the offset.

When measuring the offset resolution $y_{offset} - y_{MC}$ (y_{MC} is the corresponding y position of the Monte Carlo track), one compares in fact y' coordinates of the tracklet offset with y coordinates (given in the local SM system) of the track offset. In order to have enough statistics, different layers were included. Due to the large errors by the non correctable tilted pads influence, the distributions will be broadened. As different layers are taken into account, the errors occur with both signs, hence the distributions are broadened in both directions relative to the maximum. Additionally, a constant shift should be seen in case of a non Lorentz corrected offset (a smaller one for a Lorentz corrected offset).

7.3 Results

In this section, some results from tracklet simulation shall be presented. The strategy was to simulate three sets of 200 signal events each. Additionally, three background events at different multiplicities were simulated. The signals of each set of signal events were merged

with one of the background events on sdigits level. Like that, the raw data and tracklet calculation were done for both, the signal and the background event. However, since only particles of the signal events are on the stack, only for them Monte Carlo information (such as track label and particle ID) is available and therefore the background events were used to be able to study the performance of the tracklet algorithms under different detector loads.

Each simulated event consists of 200 e^+ and 200 e^- , which were created by the generator "AliGenBox" with a flat p_t distribution between $3.0\text{GeV}/c \leq p_t \leq 5.0\text{GeV}/c$ (figure 7.7). They were shot into the TRD acceptance in θ , $45^\circ \leq \theta \leq 135^\circ$. The inner barrel detectors

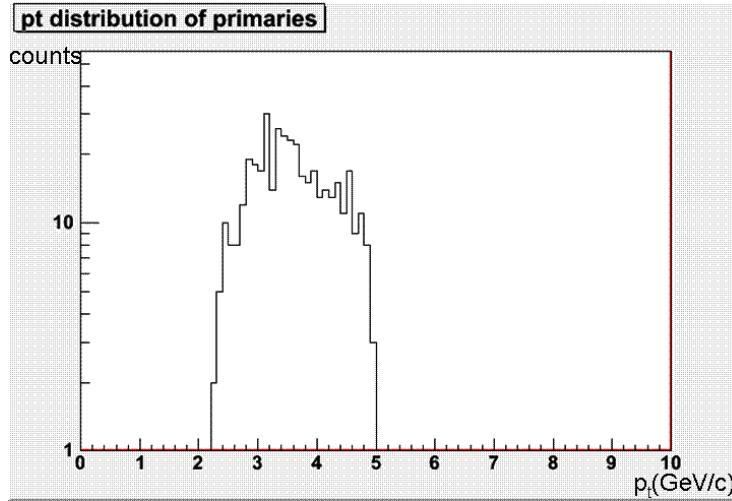


Figure 7.7: Transverse momentum distribution of the primaries from the signal events

(ITS and TPC) were activated. The tracklets were simulated with the cut on $p_t \geq 2.3\text{GeV}/c$ enabled.

The background events were produced by "AliGenHIJINGpara", simulating the detector load at PbPb collisions. The multiplicity can be steered explicitly by setting the number of charged particles. The three chosen multiplicities were: $\frac{dN_{ch}}{dy} = 200$, $\frac{dN_{ch}}{dy} = 2200$ and $\frac{dN_{ch}}{dy} = 8000$. The p_t distribution of the primaries from the background event with $\frac{dN_{ch}}{dy} = 8000$ is shown in figure 7.8.

From figure 7.9 it can be seen, that the occupancy (fraction of pad and time bin detector pixels with signal) increases to almost 35% in case of full multiplicity.

For the comparison of tracklets with the original tracks, the macro "TrackletReader.C" was written. The general strategy to obtain and exploit the corresponding Monte Carlo information for a given tracklet, is as follows:

1. Try to reconstruct the track label of the track, that created the tracklet. By using the non-official output format, the MCM and channel number of the tracklet is known. Each raw data digit (i.e. for all channels and time bins) contains three dictionary entries, in which the track labels of particles are stored, which contributed to the signal (e.g. directly, charge sharing, tail). Up to one entry comes from the background signal, however these track labels cannot be exploited since they are not on the stack. The dictionary entries are used to reconstruct the track label of the track, that most probably caused the tracklet. If a track label cannot be reconstructed

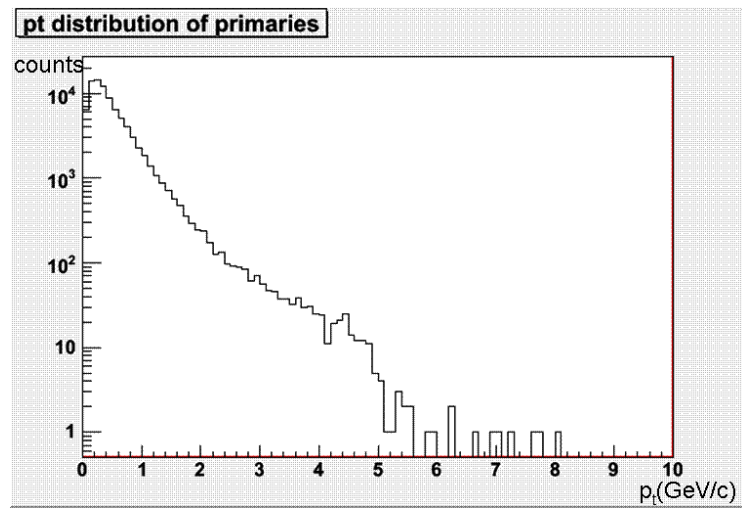


Figure 7.8: Transverse momentum distribution of the primaries from the background event at full multiplicity

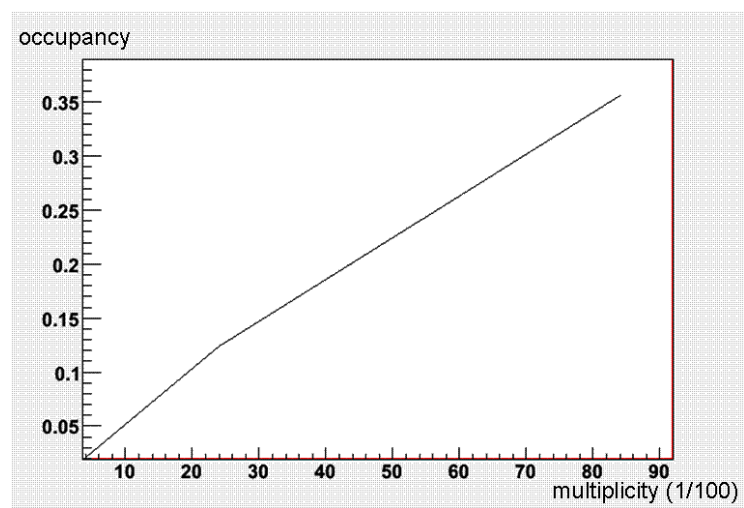


Figure 7.9: Detector occupancy increase with multiplicity

(which is seldom), then the tracklet is not considered any further and the next one is investigated.

2. Only tracklets are considered, that were caused by a primary particle whose transverse momentum at the primary vertex fulfills $p_t \geq 1.0 GeV/c$. Moreover it is required, that the track lost less than 10% of its transverse momentum before the TRD and less than 10% inside: $(\frac{\delta p_t}{p_t})_{before} < 0.1$ and $(\frac{\delta p_t}{p_t})_{inside} < 0.1$. Since ITS and TPC are switched on, this is needed in order to make sure, that the tracks did not change much their original direction before creating the tracklet. Only for those tracks, for which it can be assumed that they come from the primary vertex, the cut on $p_t \geq 2.3 GeV/c$, based on maximum/minimum deflection, works. To obtain the track p_t at the entrance and the exit of the TRD, so called track references are used. By this macro-cut, which is much more efficient than the $p_t \geq 2.3 GeV/c$ tracklet cut, because Monte Carlo information is used (this cut cannot be tricked), a clean tracklet sample is chosen.
3. Try to reconstruct the Monte Carlo information from the track label. Here, hits are used to obtain position information of the original track, to reconstruct offset, deflection, angles, etc. .
4. For each quantity presented, an own algorithm had to be invented and implemented into the TrackletReader, that extracts desired from available information.

In the following first some general results are shown before performance and efficiencies are discussed.

7.3.1 General Results

Dependence of α on p_t

It was shown, that the track angle α with respect to the vertex direction decreases as a function of p_t . The vertex direction corresponds to $p_t = \infty$. In figure 7.11, the calculated angles $\alpha = \arctan \frac{d_y}{d_x} - \arctan \frac{y_{offset}}{x_{offset}}$ (d_y : deflection; $d_x = 30.0 mm$: height of drift volume; (y_{offset}, x_{offset}) : coordinate of the offset in local SM system) from tracklets of all charge signs and from all positions are plotted against their transverse momenta p_t . The two branches belong to the two possible values of the angle for a given p_t and a given vertex direction, depending on the charge sign. The branches are symmetric w.r.t. $\alpha = 0$. Since the vertex direction depends on the tracklet position, also the angle α of the tracklet to the vertex direction shows a dependence on the tracklet position, even for the same momenta. This is explained by the fact that tracks, that are shot from the primary vertex into different directions toward a TRD chamber, have to travel different distances (the TRD chambers are flat). Therefore, even for the same radius of the circle (same p_t), the phase shift of the circle (and thus its bow length) between vertex and entrance point to the TRD chamber, varies (figure 7.10). Since the magnetic field is parallel to the z-axis, only the different possible x and y coordinates of the entry points are relevant. The width of the projected distribution (onto the angle axis) at a given p_t thus is a measure for the ranges of different vertex positions, that can occur within the TRD (all layers are included in the distribution). If the distributions were recorded in a layer sensitive manner, one should observe an increased width toward outer layers, since the width of the pad rows

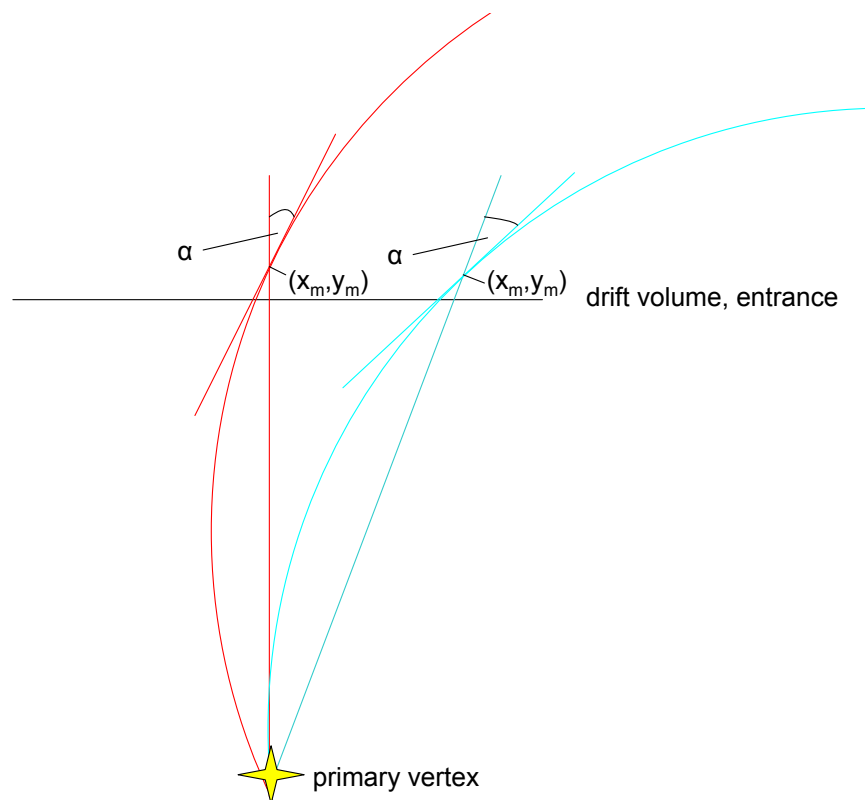


Figure 7.10: Different angles α for the same p_t but different primary vertex directions

increases (together with larger radii, this leads to larger variations of the vertex distance). If a tracklet is thought to be approximately the tangent to the track's circle trajectory with (x_m, y_m) the touch point to the circle in a chamber (characterizing also the primary vertex direction), then one obtains $\alpha = \arcsin\left(\frac{\sqrt{x_m^2 + y_m^2} \cdot eB}{2p_t}\right)$. For small arguments of arcsin (which is the case for the TRD geometry), the angle α increases with the distance to the vertex. Since all layers are included in the plot, one can observe the following of α for $p_t = 2.3\text{GeV}/c$: The maximum angle belongs to the outer layer ($x \approx 3.6\text{m}$) at the chamber edge ($y \approx 0.65\text{m}$). This yields $|\alpha_{max}(p_t = 2.3\text{GeV}/c)| \approx 5.5^\circ$. The smallest possible value for α is obtained for the innermost layer ($x \approx 3\text{m}$) and centrally on a chamber ($y = 0$). Then $|\alpha_{min}(p_t = 2.3\text{GeV}/c)| \approx 4.5^\circ$. Note, that due to the momentum distribution of the primaries, the choice of the tracklets and the $p_t \geq 2.3\text{GeV}/c$ cut (which is efficient for the chosen primary vertex tracklets), the number of entries in the distribution levels off at around $p_t \approx 2.2\text{GeV}/c$.

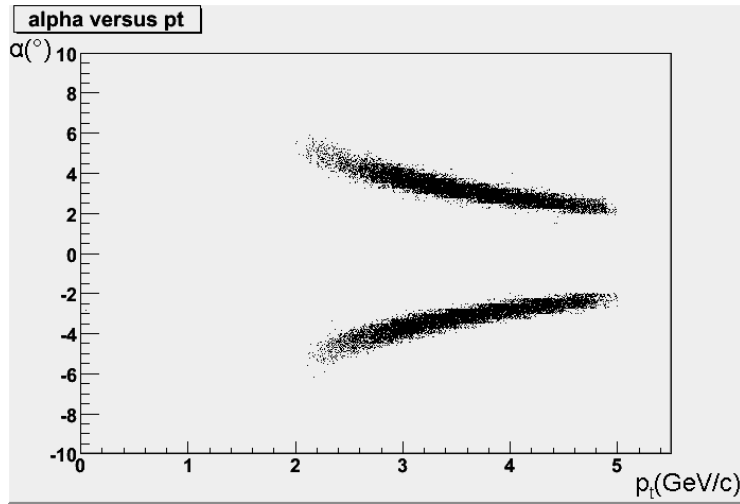


Figure 7.11: Decrease of the angle α with increasing transverse momentum. For multiplicity 2200.

Cluster Quality Measure

The result presented here (figures 7.12 and 7.13) is obtained from a simulation as above, however with the tracklet cut $p_t \geq 2.3\text{GeV}/c$ switched off, in order to have more statistics (even though only 100 events are taken into account for each multiplicity). The cluster quality measure is described by $\frac{L \cdot R}{C^2}$. Here, the distribution of this measure is shown. Note, that the ADC counts were not baseline corrected² and that the distributions are not normalized. However, the general trend is clearly visible: The quantity of the measure in case of clean clusters (which have only contributions from one track) is concentrated

²Let b be the baseline. The measure shown is then approximately (neglecting the time dependence of the baseline correction): $\frac{(L+b)(R+b)}{(C+b)^2} = \frac{LR + (L+R+b)b}{C^2 + (2C+b)b}$. Assuming $L, R, C, b \ll C^2$, the denominator can be simplified: $\frac{1}{C^2 + (2C+b)b} \approx \frac{1}{C^2} - \frac{(2C+b)b}{C^4}$. Thus: $\frac{(L+b)(R+b)}{(C+b)^2} \approx \frac{LR}{C^2} \left(1 - \frac{(2C+b)b}{C^2}\right) + \frac{(R+L+b)b}{C^2} \left(1 - \frac{(2C+b)b}{C^2}\right) \approx \frac{LR}{C^2}$. This holds the better, the larger C is.

at small values, whereas for spoiled clusters the value is distributed over the whole range $[0, 1]$. In order to have enough spoiled clusters, the background event with $\frac{dN_{ch}}{dy} = 8000$ was chosen.

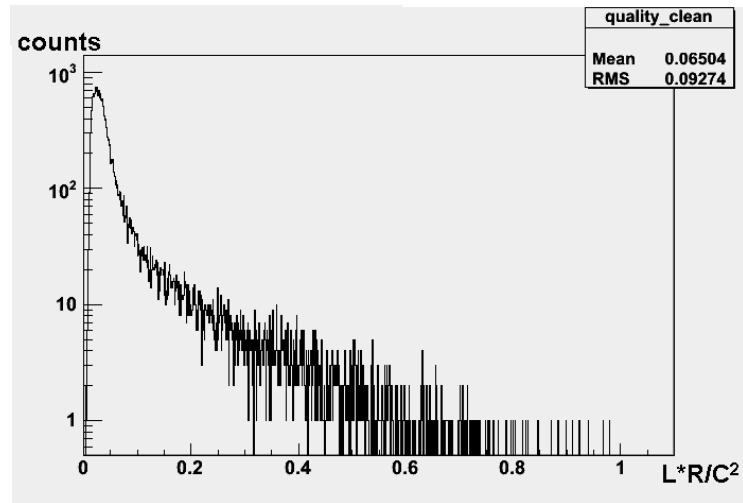


Figure 7.12: Cluster Quality for clean clusters. Multiplicity 8000.

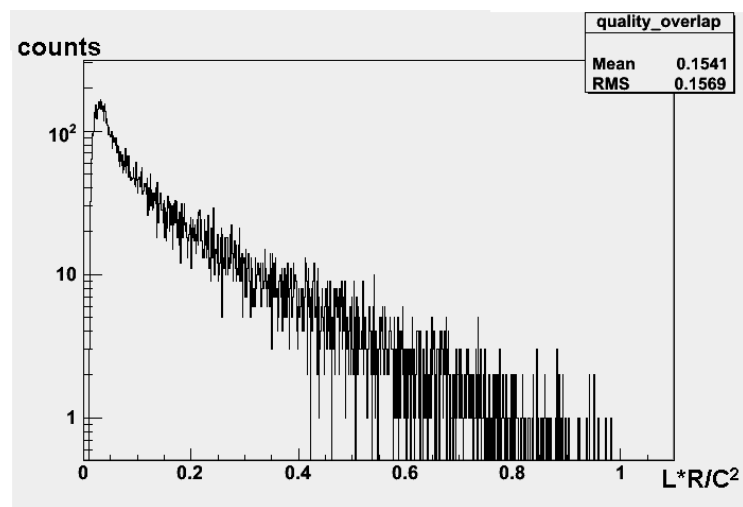


Figure 7.13: Cluster Quality for overlapping clusters. Multiplicity 8000.

Theta Efficiency

Here again, a result from a simulation without a tracklet p_t cut is presented for statistics reasons, figure 7.14. It is evaluated, how many tracks can be reconstructed as a function of the angle θ w.r.t. to the z axis. Since only primary tracks are taken into account which fulfill condition 2 of the macro strategy, it is supposed that their θ has not changed significantly. Note that the magnetic field ($\vec{B} = (0, 0, B_z)$) only bends the track in ϕ , yet not in θ . The z positions at the entrance and the exit of the TRD are independent of the

magnetic field. A track is called reconstructible, if at least four of its tracklets could be found. There is no restriction on the layer (i.e. a track would be called reconstructible in this sense, even if four tracklets in only three layers were found. This is not what is called a reconstructible track in the GTU sense, where the tracklets have to come from different layers). From the figure it can be seen, that there are dips at $\theta = 60^\circ$ and $\theta = 80^\circ$ and less

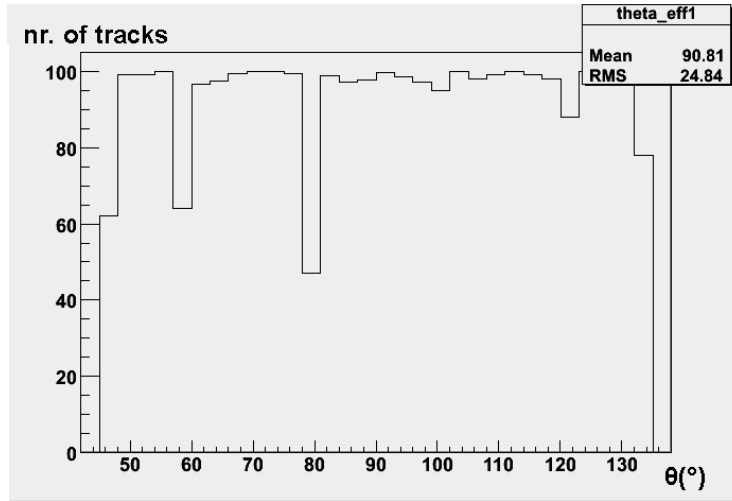


Figure 7.14: Found number of reconstructible tracks (see text) as function of angle

pronounced ones at $\theta = 100^\circ$ and $\theta = 120^\circ$. Otherwise the efficiency is almost uniformly distributed. The dips belong to the inner boundaries of the five stacks of a SM, which are situated at these angles (in all layers, due to the projective geometry of the TRD). Therefore also at $\theta = 100^\circ$ and $\theta = 120^\circ$ deep dips are expected. The dips should be more pronounced for the two intermediate angles, as for these tracks the distance to the TRD is smallest and the probability, that the track is not deflected and flies through the dead region, where no tracklets are reconstructed, is largest. This could explain the deeper dip at $\theta = 80^\circ$ as compared to the one at $\theta = 60^\circ$. It should be noted, that the depth of the dips is also limited by the fact, that always 3° are packed into one bin. However, the fact that the dips at the both large angles are almost missing completely, hints, that even under the severe cuts of strategy condition 2, the tracks can still undergo significant deflections, which bring them out of the dead zone. Some tracks in the vicinity of the dead zones might still lose a tracklet there, however mostly there are at least four other tracklets left. Of course this does not explain the asymmetry of the plot.

The asymmetry could be explained by geometrical distortions. For example, if for $\theta > 90^\circ$, there is additional material between primary vertex and TRD as compared to $\theta \leq 90^\circ$. Then, tracks coming from the primary vertex with $\theta = 100^\circ$ or $\theta = 120^\circ$ are likely to be scattered off their direction. Due to the projective geometry (dead zones only at discrete angles), there would be hardly any tracks having less than 4 tracklets. Almost all tracks would be reconstructible in the above sense and the dip would be missing. However, as will be shown in the next section, the dips at large angles occur, if tracks are considered, that cross pad rows. This hints, that the missing dips in the theta efficiency plot are not due to geometry.

Tracks Crossing Pad Rows

For each track generating at least one tracklet, it is checked, whether this track changes a pad row within the linear fit range. The number of those tracks is evaluated for different angles θ . A tracklet that occurs from a track crossing a pad row within the linear fit range, might have been built with only a fraction of all possible hits. Hence its total cluster charge will be over- or underestimated, depending on the part of the fit range, to which the tracklet belongs. For further information consult the next chapter.

It shows up (figures 7.15 and 7.16), that tracks with oblique incidence (small and large angle θ w.r.t. the z axis) tend to cross pad rows more frequently than tracks with almost normal incidence (arriving at the central stack). The dips are clearly visible here at all

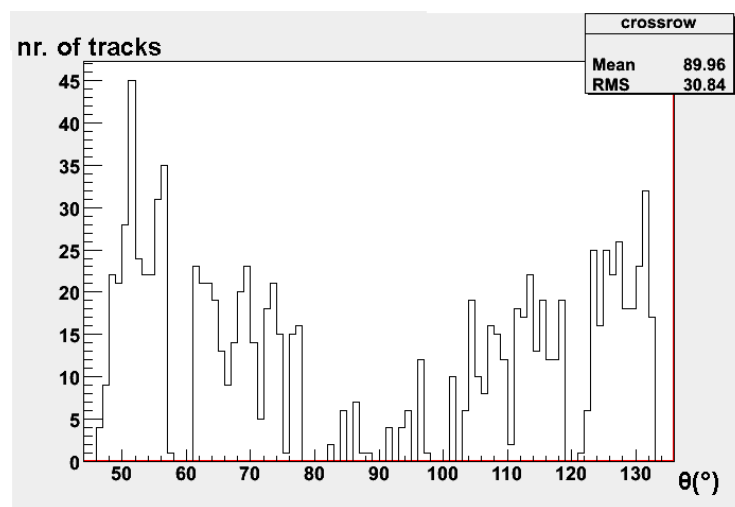


Figure 7.15: Number of tracks with at least one tracklet, crossing a pad row within the linear fit time range, as function of theta

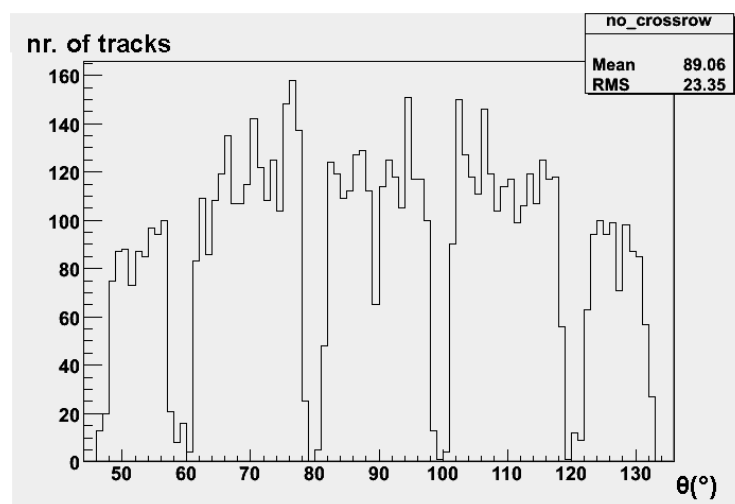


Figure 7.16: Number of tracks with at least one tracklet, that do not cross a pad row within the linear fit time range, as function of theta

four angles. They occur for the tracks that cross pad rows as well as for those, which do not. This suggests, that at these angles no tracklets are found, for whose tracks the pad row crossing could be investigated. Hence it is likely, that the missing dips in the theta efficiency are not a geometry problem.

Mean Cluster Charge

Finally, also for the background event at $\frac{dN_{ch}}{dy} = 8000$ alone, the tracklets were calculated, once with $p_t \geq 2.3\text{GeV}/c$ cut, once without. In a magnetic field of $B = 0.4\text{T}$ and a distance from the primary vertex to the TRD of $d \approx 3\text{m}$, according to $p_t = e \cdot B \cdot r$, a track needs $p_t \geq 0.2\text{GeV}/c$ to reach the TRD instead of being curled up, if no intermediate processes would happen (in the limit, the track would describe a half-circle between primary vertex and the touch-point with the TRD, with a radius of $r \approx 1.5\text{m}$). As it can be seen from figure 7.8, the bulk of all primaries is released at transverse momenta of $p_t \leq 2\text{GeV}/c$. Therefore, a significant number of primaries do not even reach the TRD. Among the primary tracks, there were 471585 electrons and 89410 pions. Looking at the number of found tracklets, the numbers are almost equilibrated: 42434 electron tracklets and 41540 pion tracklets were found. This suggests, that many of the entries at low p_t in the distribution are due to electrons, that do not reach the TRD.

From the run without cut, the mean cluster charge distributions for electrons and pions were recorded for all of their found tracklets (there were no requirements by the macro, concerning track- p_t or momentum changes). Applying the $p_t \geq 2.3\text{GeV}/c$ cut here would leave the good tracklets in the sample, which emerged from tracks with $p_t \geq 2.3\text{GeV}/c$, for which the primary vertex assumption holds. But also tracklets, whose incident angle is per accident such, that they pretend to have $p_t \geq 2.3\text{GeV}/c$, would not be rejected. Therefore, even with the cut, one would not get a clean sample of high p_t tracklets, thus the cut was omitted for the distribution record of the mean cluster charge. Of course, the distinction between the electron and the pion mean cluster charge distributions then decreases, as electrons with $p_t \leq 20\text{MeV}/c$ are no longer on the Fermi plateau of the energy loss and therefore assimilate the electron distribution to the pion distribution. Also, not all of the electrons produce TR (e.g. Bremsstrahlungs electrons produced inside the drift volume, or low energetic δ electrons), making the mean cluster charge of these electron tracklets even more similar to the one of an intermediate- p_t pion tracklet. Moreover, a clear distinction between the distributions of electron mean cluster charge and pion mean cluster charge could only be expected, if tracklets with transverse momenta within a small range were considered. This can be seen in 7.17 and 7.18, where the difference between the two particle species is hardly visible. The mean of the charge distribution for electrons ($\bar{q} = 43.3$) is slightly shifted to a higher value than for pions ($\bar{q} = 40.42$). Since the number of entries is rather large, it can be assumed that this is not a statistical effect. The charge accumulators of the tracklets were set such, that the total charge Q deposited during the fit time is accumulated. The total charge is then scaled by the number of hits $q = \frac{Q}{N}$ and discretized in a 8 bit value. The large entry at bin 255 is due to overflows and subsumes all entries at $q \geq 255$. However, it shows up that even for electrons, less than 200 entries out of more than 42000 (less than 0.5%) were found with mean cluster charge larger than 255. Similar for pions. This justifies to quantize the mean charge with a 8 bit value.

Here it should be mentioned, that also other charged and energetic particles, especially

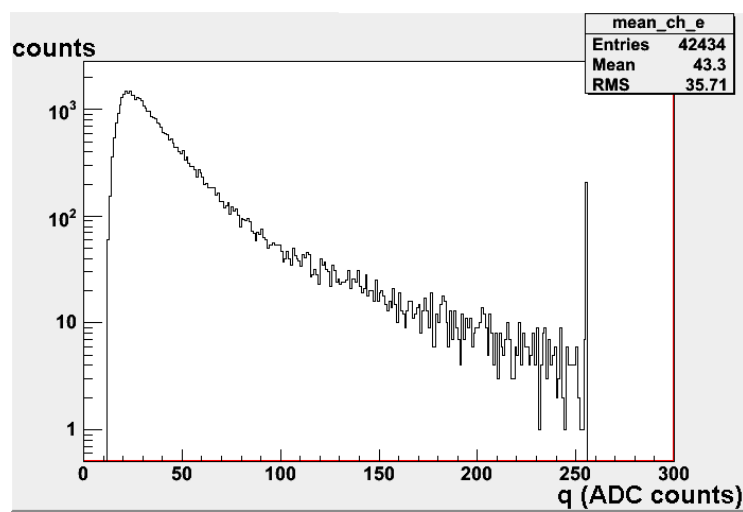


Figure 7.17: Mean cluster charge distribution for electrons for the full multiplicity background event

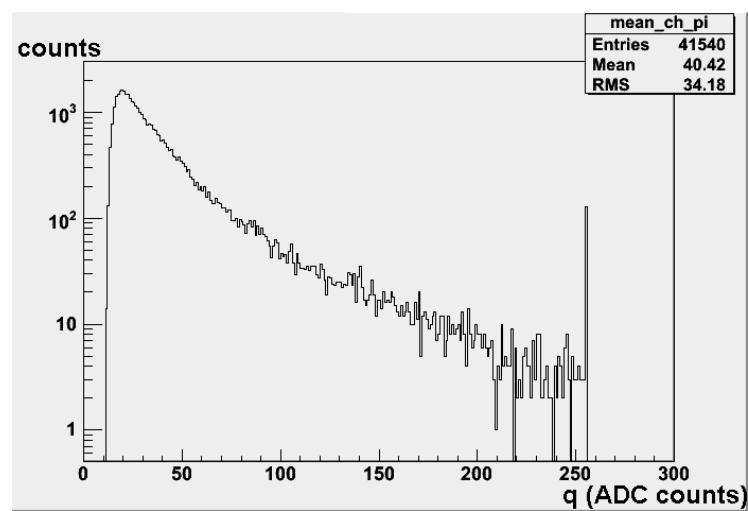


Figure 7.18: Mean cluster charge distribution for pions for the full multiplicity background event

protons, kaons and muons, form tracklets as well. If they are identified as pion tracklets and treated the same way, this poses no problem. A problem only occurs, if there is a significant probability of misidentifying these tracklets as electrons, since then the trigger might urge the event to be read out, although it does not contain enough interesting high- p_t electrons in reality. In the following table 7.3, the amount of tracklets, not belonging to an electron or pion track, is listed, as found in the full multiplicity background event. As can be seen, the fraction is not negligible. By only applying the cut $p_t \geq 2.3\text{GeV}/c$,

Table 7.3: Tracklet identities

particle	nr. of tracks	nr. of tracklets without cut	nr. of tracklets with cut
total	960749 (100.0%)	104800 (100.0%)	13110 (100.0%)
electron	471585 (49.1%)	42434 (40.5%)	6459 (49.2%)
pion	89410 (9.3%)	41540 (39.6%)	4440 (33.9%)
other	399754 (41.6%)	20826 (19.9%)	2211 (16.9%)

the absolute tracklet abundance drops significantly and the fraction of electron tracklets is increased, mostly on cost of pion tracklets.

7.3.2 Performance Results

In this section, some results concerning the performance of the tracklet calculation shall be presented. Here, all results are obtained from event merging with applying the $p_t \geq 2.3\text{GeV}/c$ cut.

Deflection Performance

The performance of the deflection was evaluated by looking at the difference between tracklet deflection and the track deflection, that was obtained by Monte Carlo information: $\delta(d_y) = (d_y)_{\text{tracklet}} - (d_y)_{MC}$. The deflection was offset and tilted pads corrected. The result for an event multiplicity of $\frac{dN_{ch}}{dy} = 2200$ and for tracks having at the primary vertex a value of $p_t \in [3.3\text{GeV}/c, 3.7\text{GeV}/c]$ is shown in figure 7.19.

Only negatively charged particles were taken into account. The Gaussian shape occurs, because the reasons, why the deflection is not reconstructed accurately, are manifold. Here, digitization issues enter as well as, for example, cluster spread due to diffusion (but sampling only on the point) or inefficiencies in reconstructing the positions due to charge sharing. Hence, the error δd_y on the reconstruction is a sum of many independent, small effects, and the distribution of δd_y approaches a normal distribution, according to the central limit theorem. However, since no obvious significant additional broadening of the distribution beyond the detector resolution of $\delta d_y \approx 400\mu\text{m}$ or shifting is visible, it can be assumed, that the sources of the main distortions (tilted pads, Lorentz drift) are known and corrected for in a satisfactory manner.

The distribution has Gaussian shape, however with a tail, suggesting that the deflection is sometimes overestimated by the tracklets. Possibly this can be explained by the applied p_t cut: It will happen frequently, that a track, that does not come from the primary vertex

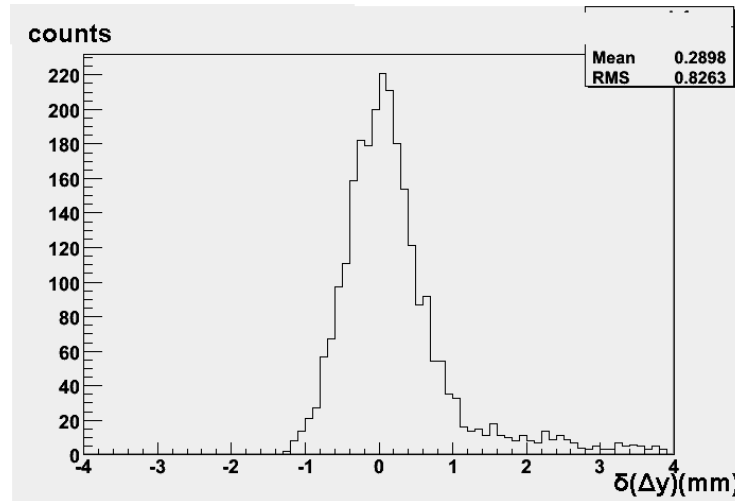


Figure 7.19: Deflection performance for 3.5 GeV/c tracklets at moderate multiplicity

and only pretends to have high p_t , is left in the sample. On the other hand, a track, which in fact has large p_t but is scattered off the primary vertex direction too much, such that its reconstructed p_t is too small, is removed from the sample. This means, that the tail probably corresponds to an overestimation of the transverse momenta of the tracklets in the sample³. Imagine a coordinate system, whose positive z axis points vertically into the plane of your paper (in direction of your view) and whose positive x axis runs along the paper plane toward the upper edge of the paper. The positive y axis then points to the right side of the paper. Now a magnetic field shall be applied, pointing in direction of the positive z axis. A negatively charged particle moving perpendicular to the magnetic field direction along the the positive x axis, will experience a Lorentz force in positive y direction. The trajectory will be a circle on your paper, opened to the right. Now imagine two lines parallel to the y axis, drawn on the paper. If a particle's p_t is large enough, it will intersect the two lines. The difference in the y coordinate of the upper line with respect to the lower one is the deflection: $d_y = y(x_{up}) - y(x_{low})$, $x_{up} > x_{low}$. As p_t increases ($p_t = \sqrt{p_x^2 + p_y^2}$), the deflection decreases (the particle moves closer to the vertex direction, counter clock wise. The vertex is situated in the origin). An overestimation of the track's p_t would thus correspond to a negative value of $\delta(d_y)$. The trajectory circle of a positively charged particle on the other hand would be opened to the left. Increasing p_t urges the track to move closer to the vertex direction clock wise. Hence, its deflection increases. Overestimated p_t leads to a positive value of $\delta(d_y)$. Because one observes the tail for positive values of $\delta(d_y)$ and only negative charged tracks were selected, the magnetic field must be orientated in reverse, pointing into negative z . This is of course only true, if one believes the tail to be due to generally overestimated p_t .

From the previous discussion it also follows, that the tail should appear at negative values of $\delta(d_y)$, if positively charged particles were taken under consideration.

³Tracks, whose p_t is underestimated significantly, are likely to be removed from the sample by the $p_t \geq 2.3\text{GeV}/c$ cut. Tracks, whose p_t is largely overestimated however, are left in the sample.

Angle Performance

Here, the performance of the angle α of the tracklet w.r.t. the vertex direction is considered. The quantity $(\delta\alpha) = \alpha_{tracklet} - \alpha_{MC}$ versus p_t is entered into a scatter plot (7.20). The cuts at $p_t \leq 2\text{GeV}/c$ and $p_t \geq 5\text{GeV}/c$ are due to the rapidly decreasing number of electrons in these momentum ranges (compare with the distribution in figure 7.7; note, that only primaries with small loss of p_t are taken into account). The projection onto the α axis for three bins of p_t (1 bin corresponds to $\Delta p_t = 0.1\text{GeV}/c$) for two different p_t is shown in figures 7.21 and 7.22. Everything for a multiplicity of $\frac{dN_{ch}}{dy} = 2200$.

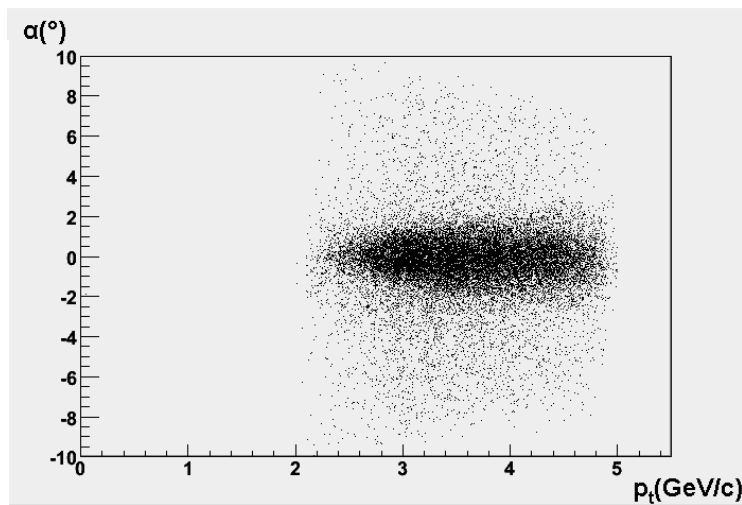


Figure 7.20: Performance of the tracklet angle w.r.t. vertex direction, plotted against transverse momentum

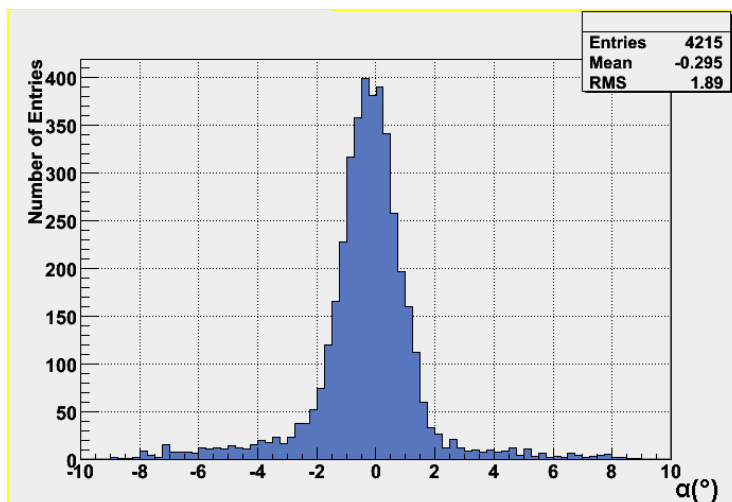


Figure 7.21: Performance of the tracklet angle w.r.t. vertex direction at a transverse momentum of $3.5\text{GeV}/c$

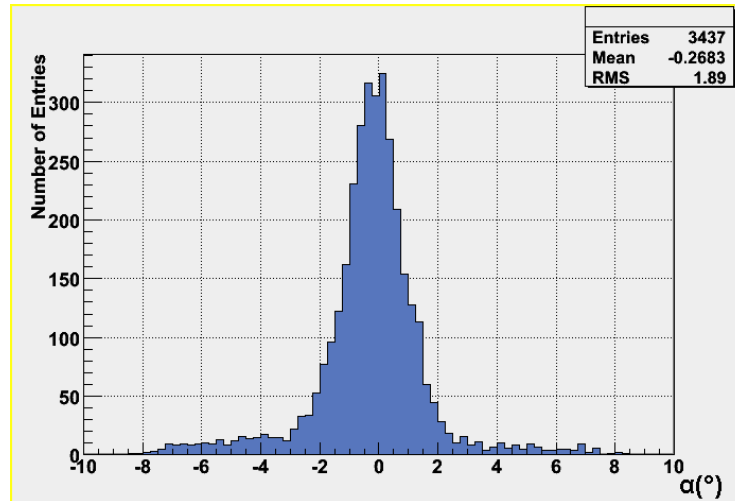


Figure 7.22: Performance of the tracklet angle w.r.t. vertex direction at a transverse momentum of 4.0GeV/c

Offset Performance

Here, the offset performance is presented (figure 7.26). The investigated quantity is $(\delta y) = y_{tracklet} - y_{MC}$. Only negatively charged particles are taken into account. There are several effects, leading to odd distributions:

- Uncertainty of the Lorentz drift correction. This was already explained above. As it is not known exactly, how many of the time bins before linear fit start time t_{FS} belong to the drift region, this number had to be guessed and the offset Lorentz correction only can improve the shift in y , but not totally correct for it. Therefore, the distributions still show a slight shift.
- No tilted pads correction. Since the z coordinates of the tracklets are not known, the influence of the tilted pads cannot be corrected for. Therefore the offset coordinates are actually given in the tilted pads coordinate system (see above). It can be seen from the broad distributions, that the number of counts level off at around $\pm 3.5mm$. As tracklets from all six layers were taken into account, this is in correspondence with the assumption, that the y coordinate runs between the border of two pad rows instead of running through one of them.
- Parallel projection of the tracklet offset (figure 7.23). Since the tracklet offset is given at some height x corresponding to the t_{FS} time bin, it is projected onto the plane (perpendicular to x), where the MC offset is given. This plane varies from case to case but can, in the granularity of the time bin resolution of $\delta x = \Delta t_{sample} \cdot v_{drift,x} = 0.1\mu s \cdot 1.5cm/\mu s = 1.5mm$, be identified with the cathode wire plane. Since the deflection is corrected for all known irregularities (Lorentz angle, tilted pads), one can assume the tracklet to be parallel to the original track. Hence, a projection of the offset along the tracklet direction does not change (δy) . However, since the exact x position of the offset is not known, also its distance to the cathode wire plane is

only an estimation. Depending on the error in x , the distance of the tracklet offset to the MC offset is additionally enlarged by this constant, yet unknown x component.

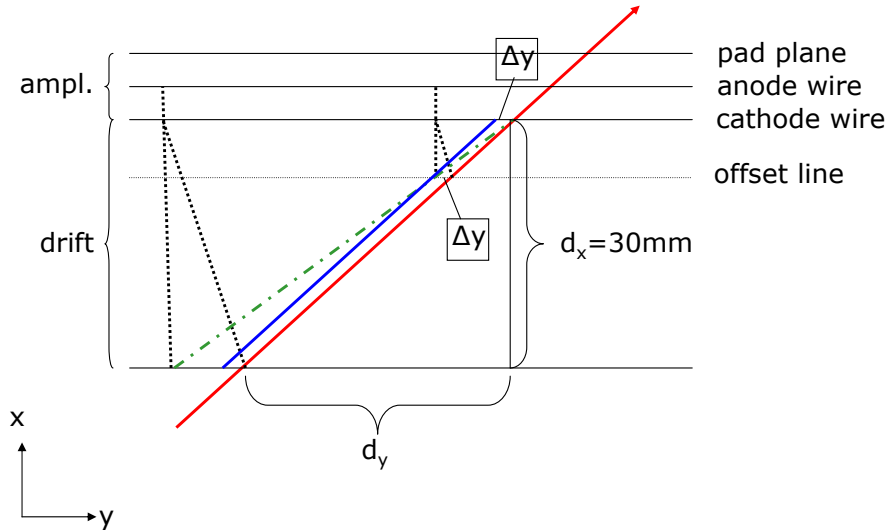


Figure 7.23: Parallel projection of the tracklet offset to the cathode wire plane. Red: The MC track. Green: The reconstructed tracklet, before the Lorentz drift and tilted pads corrections were applied to the deflection. Blue: The reconstructed tracklet after the corrections on the deflections but without Lorentz correction on the offset.

- Tracklets under different conditions are taken into account for one distribution: different θ , different layers, relatively broad p_t intervals (width of $0.4\text{GeV}/c$). Although the effect was not clearly visible in case of the deflection performance, one can only expect a clear Gaussian distribution if tracklets under (almost) the same conditions are regarded. It can be compared to a probability experiment: the performance of each tracklet serves as probe. A clean Gaussian distribution only occurs, if the experiment is repeated under exactly the same conditions. Probably the assumption "same conditions" was not fulfilled.
- As was mentioned in the previous chapter, the tracklet fit itself introduces deviations. First, it is a linear fit to the track. The error introduced by this assumption is small due to the large radius of the tracks under consideration (maximum deflection between

linear fit and circle: $25\mu m$ for $p_t = 2.3GeV/c$ ⁴.

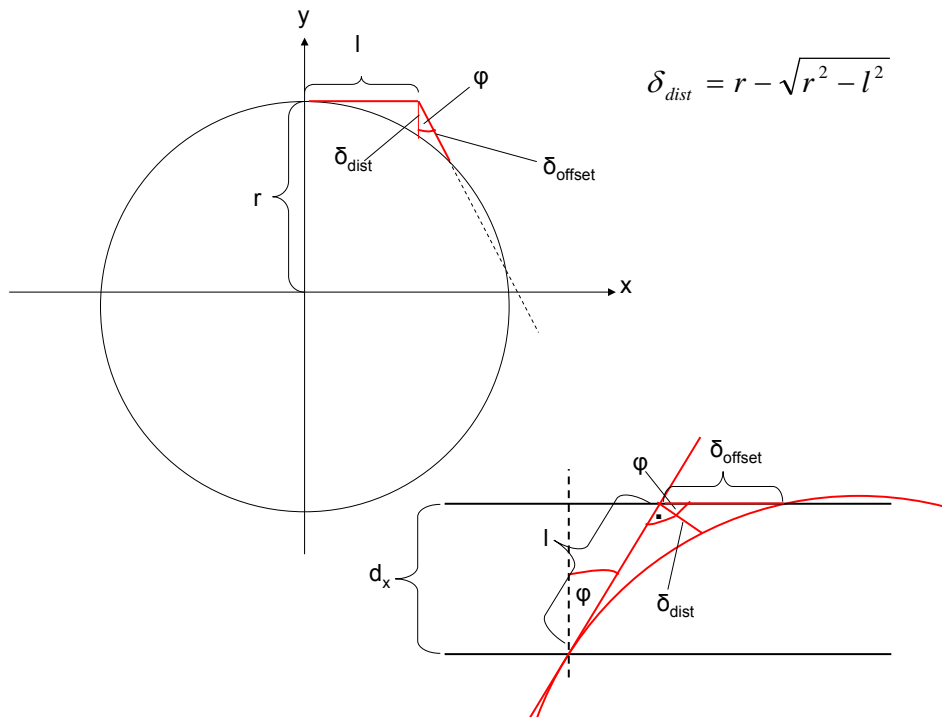


Figure 7.24: The deflection introduced by a linear fit to a circle

Next, each time bin sample incorporates a number of electron clusters, which are spread over a certain distance on the anode wire. The avalanche charge is mirrored onto the pad plane. The y position is obtained by exploiting charge sharing, including the centroid channel and its two neighbors. Since at best the superposition of the mirrored charges from the electron clusters can be measured (with also a slight dependence on the actual arrival time of the individual electron clusters), also the reconstructed y position is at best an average over the positions of the electron clusters within $\Delta t = 100ns$ (corresponding to $\sigma_x = v_{drift,x} \cdot \Delta t = 1.5cm/\mu s \cdot 0.1\mu s = 1.5mm$ of drift length or 5% of the drift volume). The coarseness of the time bin reduces the resolution in y . Therefore, independent of the fit quality, each fit point is afflicted with an error, which translates into an uncertainty of the offset. To get a lower estimate on the

⁴The maximum deflection between linear fit and circle for a $p_t = 2.3GeV/c$ particle is obtained by assuming, that the tracklet is the tangent to the track trajectory (circle) at the entrance point (x_0, y_0) to the drift volume of a chamber. The maximum length of the tracklet within the drift volume (height $d_x = 3.0cm$) is obtained by the maximum incident angle φ_{inc} w.r.t.the chamber normal. For $x_0 = 3.6m$, $y_0 = 0.65m$ on obtains $\varphi_{vertex} \approx 10^\circ$, $\alpha \approx 5^\circ$ and thus $\varphi_{inc} \approx 15^\circ$. The length of the tracklet is given by $l = \frac{d_x}{\cos \varphi_{inc}} \approx 0.031m$. The track radius r is given by $r = \frac{p_t}{eB} \approx 19.2m$. The maximum distance between tracklet and circle is then given by $\delta_{dist} = r - \sqrt{r^2 - l^2} \approx 25\mu m$ (see figure 7.24). However, the offset deflection δ_{offset} ($\delta_{offset} \geq \delta_{dist}$) between tracklet and circle is needed, which, in the ideal implementation, is given as the deflection at the radial height of the drift chamber exit. For large radii $r \gg l$ and small φ ($1 - \cos \varphi \ll 1$, $1 - \cos 15^\circ \approx 0.034$), one can assume $\delta_{offset} \approx \delta_{dist}$.

offset uncertainty, only an error of the fit points in x direction of σ_x is assumed (figure 7.25). For σ_{y1} one obtains: $\frac{\sigma_{y1}}{d_y - \sigma_{y1}} = \frac{\sigma_x/2}{d_x + \sigma_x/2}$ and therefore $\sigma_{y1} = \frac{\sigma_x}{2(d_x + \sigma_x)} d_y \approx 0.021 \cdot d_y$. For σ_{y2} : $\frac{\sigma_{y2}}{d_y + \sigma_{y2}} = \frac{\sigma_x/2}{d_x - \sigma_x/2}$ and therefore $\sigma_{y2} = \frac{\sigma_x}{2(d_x - \sigma_x)} d_y \approx 0.026 \cdot d_y$. Hence, the lower estimate for the error is about 3% of the deflection d_y . With a maximum deflection of $30mm \cdot \tan 15^\circ \approx 8.04mm$ (for a $p_t = 2.3GeV/c$ tracklet: 10° maximum angle between vertex direction and chamber normal, 5° maximum angle between tracklet direction and vertex direction), the maximum of this error estimate corresponds to $\sigma_y \leq 240\mu m$ and is small compared to the error introduced by the tilted pads.

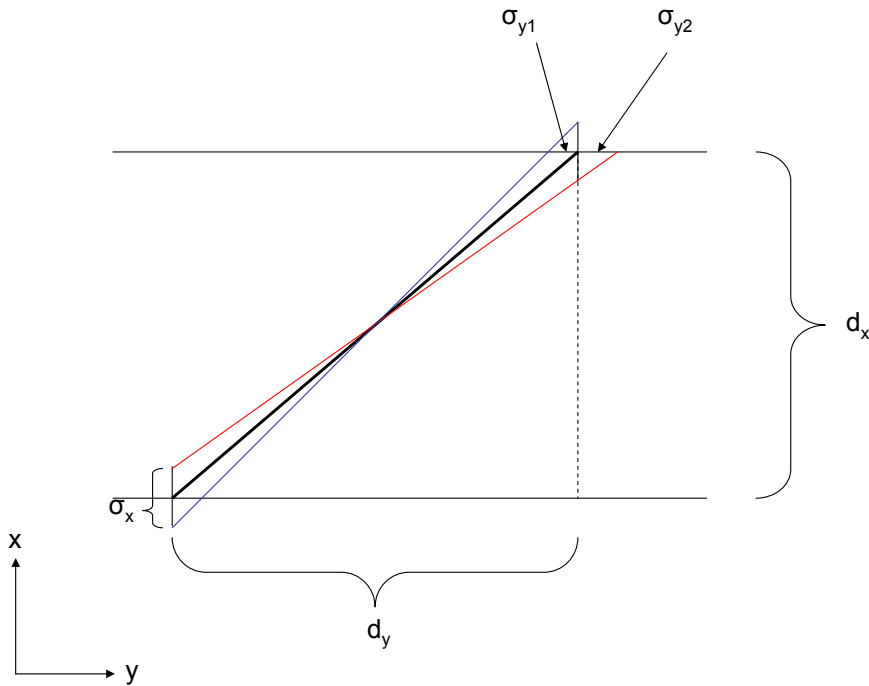


Figure 7.25: Error on the offset introduced by the finite sampling time

- Digitization and granularity restrictions also can lead to deviations of the calculated tracklet offset. During the whole tracklet preprocessing and processing, all data was treated as bit words of limited length. This can easily lead to digitization errors, for which unfortunately no estimation can be given. On the other hand one can assume, that digitization errors together with the scaling of the offset in preparation for the GTU (division by $160\mu m$) will not reduce the resolution below the detector limit of $\delta_y \approx 400\mu m$. The best possible resolution that is allowed by the offset scaling amounts to $160\mu m$. Therefore one can assume, that the digitization and granularity errors are both overwhelmed by the limited detector resolution⁵.

⁵The limited detector resolution can be explained by many effects: Transverse diffusion of the charge

- At large multiplicities, nearby background tracks can spoil clusters, that are used for charge sharing and position reconstruction. This also leads to errors in the offset determination.

These effects lead to a shift and broadening of the distributions. By disentangling tracklets of different conditions (chamber, layer, momentum...), especially the Gaussian shape of the offset performance distribution could have been improved. However, this would have required to simulate runs with large statistics and evaluate the performance. The time for doing so was not available.

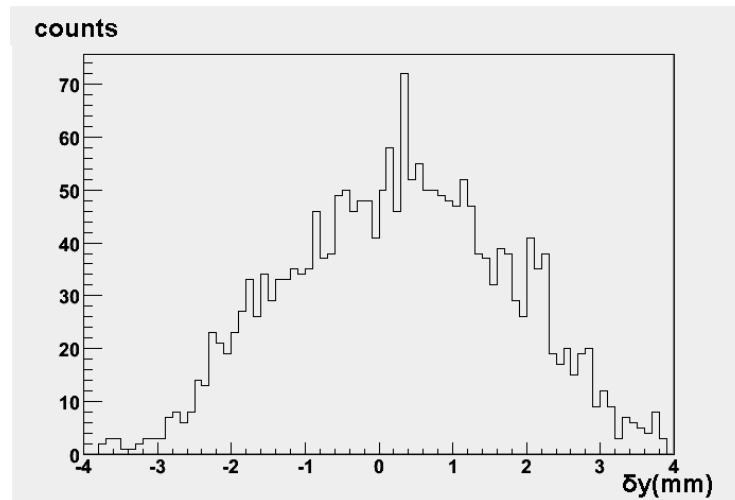


Figure 7.26: Offset performance. $3.8\text{GeV}/c < p_t < 4.2\text{GeV}/c$. Multiplicity 2200.

If the distributions are fitted by a Gaussian (despite their odd shape) and the mean values of the error (δy) for the same p_t intervals at different multiplicities are inserted into a histogram and plotted against multiplicity, one gets a notion for the decrease of the offset performance with multiplicity. Since at higher multiplicities, clusters of different tracks begin to overlap frequently, charge sharing yields no longer the right position of a cluster. Additionally, wrong clusters may be assigned to a track, deteriorating the position measurement further. In figure 7.27, such a fitted distribution for $p_t \in [3.3\text{GeV}/c, 3.7\text{GeV}/c]$ (given as the primary vertex p_t of the track; remember that the track must fulfill condition 2 of the macro's strategy) at $\frac{dN_{ch}}{dy} = 2200$ is pictured. The multiplicity dependence of the offset performance for this momentum range is shown in figure 7.28.

The position performance in z direction is practically independent of multiplicity since the z position is only known on pad row granularity on tracklet basis (tilted pads are not exploited). The anode wires have a distance of 0.5mm from each other in z direction, hence the signal of several anode wires is induced on one pad plane. Since it is not known from which anode wire a signal occurs and no charge sharing between pad rows is applied, the z resolution cannot be improved.

One can also evaluate the offset performance as a function of the incident angle α (angle w.r.t. the chamber normal). Here again, the same arguments apply for explaining the odd shape of the distributions. In addition now, there has been no distinction between

clusters, δ -electrons, inhomogeneous drift field, space charge, etc.

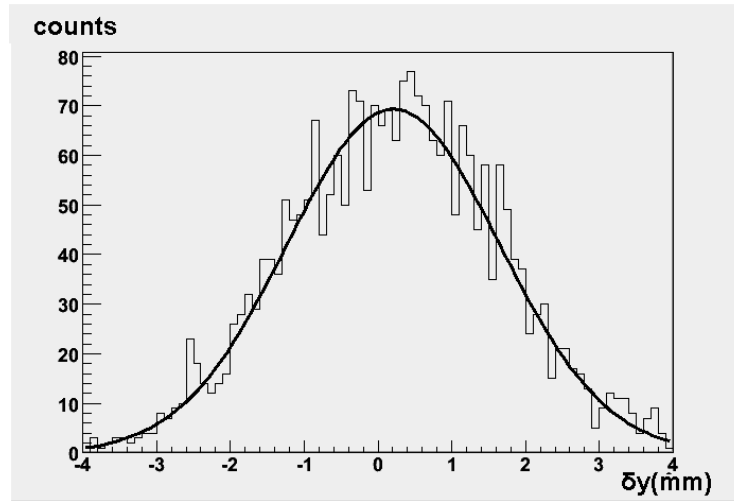


Figure 7.27: Offset performance. $3.3\text{GeV}/c < Pt < 3.7\text{GeV}/c$. Multiplicity 2200.

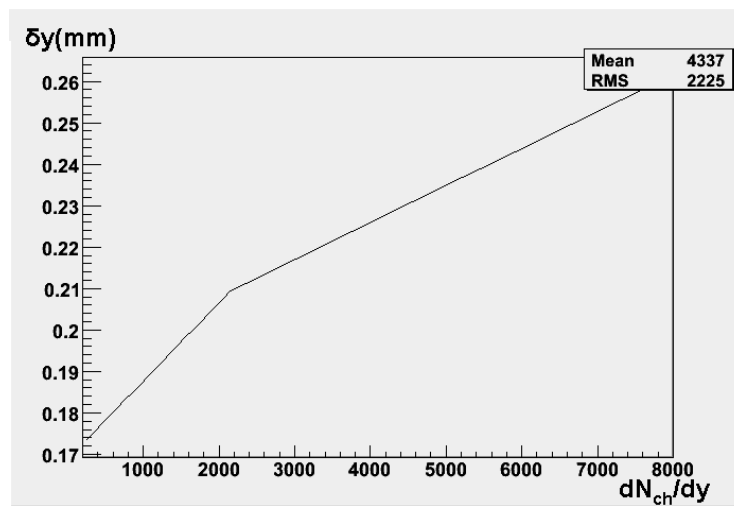


Figure 7.28: Offset performance with multiplicity for $3.3\text{GeV}/c < Pt < 3.7\text{GeV}/c$.

different p_t ranges. First, the (δy) distributions for different incident angles are recorded. Then, they are fitted by a Gaussian (figure 7.29) and their mean is plotted against the corresponding incident angle (figure 7.30). Although, data for smaller angles is missing due to very limited statistics, one can see that the y performance substantially improves, if the incident angle approaches -7° . This angle corresponds to the Lorentz angle Ψ_L . The clusters of tracks entering a chamber under this angle will drift toward one spot on the anode wire. Therefore, there should be no ambiguity about position and deflection of the tracklet. This means, that charge sharing yields the same value of the cluster positions for almost all clusters. The offset y' position in tilted pads coordinates is therefore obtained without ambiguity and the broadening of the distribution only occurs, because the transformation to y coordinates in the local SM system depends on z and is not performed. Yet, the mean of the (δy) distribution for $\alpha = \Psi_L$ is centered around 0. For tracks entering under different angles, charge is spread over a larger region on the anode wire, resulting in a deteriorated position reconstruction already in tilted pads coordinates. With increasing width of the y position range over which the clusters are spread on the wire (at given incident angle, this width is influenced by the Lorentz drift angle), also the mean of the (δy) distribution is shifted. Of course, the shift introduced by incomplete offset Lorentz correction, remains in any case.

A plot of the mean offset performance $\langle \delta y(p_t) \rangle$ against p_t would show a worsening of the performance with decreasing p_t . The position reconstruction performance for a given p_t (the mean of a distribution like in figure 7.27) can be derived from the dependence on the incident angle. Since particles of different transverse momenta enter a chamber under different average incident angles, this influences the position reconstruction accuracy and therefore the mean of the distribution. The lower the momentum of a particle is, the larger is its curvature and therefore its incident angle, such that its charge is spread over a larger region on the wire, resulting in a deteriorated offset performance. It also follows, that the dependence of the offset resolution on the incident angle should follow the same curve, regardless of track momentum.

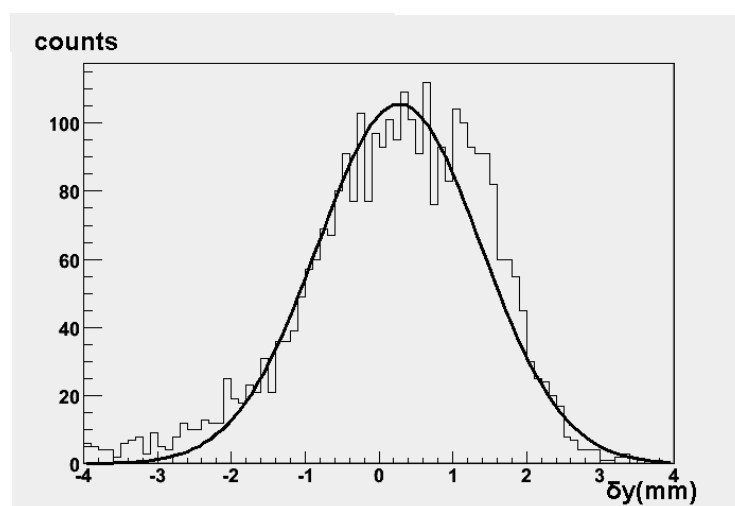


Figure 7.29: Offset performance for all Pt at incident angle of -2°

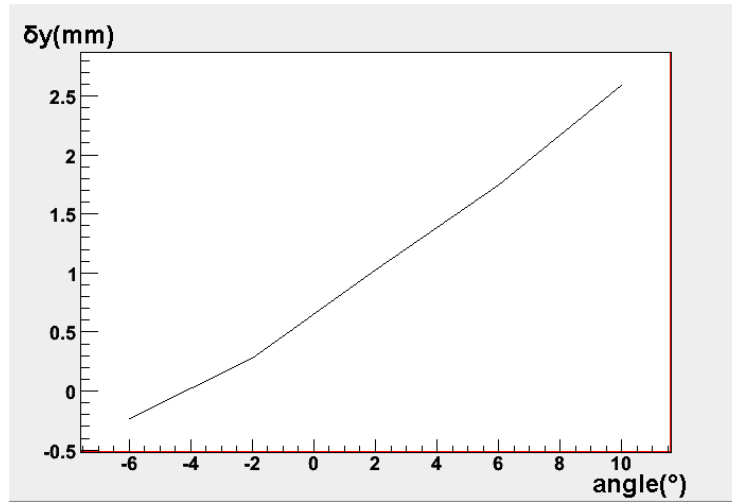


Figure 7.30: Offset performance for all Pt as function of the incident angle

Note that in the previous discussion only the incident angle within the xy -plane was considered. Since the anode wires run in y direction, but are staggered in z with a pitch of 0.5mm , the clusters will drift to the nearest anode wire in z . However, the distribution of the charge on the wire, which is responsible for the offset resolution, is, in ideal case, only a function of the incident angle in the xy -plane (also the Lorentz angle is given in the xy -plane). Therefore the incident angle in the xz -plane was not considered (on tracklet basis, z is unknown nevertheless).

At a height of $x \approx 3.5\text{m}$ and a maximum y coordinate of $y \approx \pm 0.6\text{m}$, it follows for the maximum angle of the primary vertex direction w.r.t. the chamber normal, φ : $\tan \varphi_{max} \approx \frac{0.6}{3.5}$ and hence $\varphi_{max} \approx \pm 10^\circ$. Since the tracklets involved in the considerations occur from negatively charged tracks with a transverse momentum at the primary vertex of $p_t \geq 1\text{GeV}/c$ and a momentum loss of less than 10% of their p_t before and inside the TRD, respectively, the statistics at incident angles lower than $\psi_L = -7.7^\circ$ is limited.

7.3.3 Efficiency Results

In order to check the efficiency of the tracklet algorithm, several approaches were chosen. Generally, the number of tracks were evaluated, for which a given number of tracklets are found. In order to not spoil this number by the macro inefficiency (e.g., non-reconstructible track parameters), the efficiency was evaluated, after a track label could be reconstructed (necessary in order to assign a tracklet to a track) but before the MC information is obtained. The reconstruction of a track label is almost always successful and adds hardly no inefficiency.

Efficiency Strategies

These strategies were followed:

- One first approach was to look at primaries of the signal event, that fulfilled the condition mentioned in point 2 of the macro strategy ($p_t \geq 1\text{GeV}/c$, $\frac{\delta p_t}{p_t} < 0.1$ before and

inside TRD). The tracklets that survive these conditions are called "good" tracklets in the following, as they can be assumed to come from the primary vertex. Since the tracks were chosen to have momenta in the range $3\text{GeV} \leq p_t \leq 5\text{GeV}/c$, the good tracklets should not be subject to the $p_t \geq 2.3\text{GeV}/c$ tracklet cut. In this way, by checking two event samples, one with and one without tracklet cut, one can receive an impression of the inefficiency of the tracklet cut (how many of the good tracklets are rejected). This approach was done for three different background multiplicities.

- A second approach was to modify the macro and take into account only tracks, for which $\frac{\delta p_t}{p_t} > 0.1$. Still, most of the tracks have large momenta (due to the shape of the p_t distribution for the signal primaries, figure 7.7, there would be hardly statistics at $p_t < 2.3\text{GeV}/c$). Hence, this probes the efficiency of the tracklet cut in case of high p_t particles coming not from the primary vertex. This approach was applied for a background multiplicity of $\frac{dN_{ch}}{dy} = 2200$.
- In a third approach, the full multiplicity $\frac{dN_{ch}}{dy} = 8000$ background event was investigated. Here again, the total efficiencies with and without tracklet cut were checked. Additionally, for each case, the efficiencies for tracks with $p_t < 2.3\text{GeV}/c$ and tracks with $p_t > 2.3\text{GeV}/c$ were investigated separately. Here it is assumed, that a track with large p_t at the primary vertex is likely to keep its p_t until the TRD. Then, by comparing the efficiencies with and without tracklet cut at the different p_t ranges, one can estimate how many high p_t tracklets are removed by the cut⁶. Since only one background event was taken into account, the statistics for $p_t > 2.3\text{GeV}/c$ is very limited, as can already be seen from the p_t distribution of the primary background tracks, figure 7.8.

First Approach: Good Signal Tracklets

- Without Tracklet Cut. In table 7.4 the efficiencies for events without tracklet cut and for different multiplicities are given. Here, only 100 events were evaluated. At all

Table 7.4: Tracklet efficiencies. The fraction of tracks with a given number (nr.) of found tracklets is listed. No tracklet cut. Different multiplicities. The fraction of tracks with a number of tracklets is given in %.

multiplicity	nr.	0	1	2	3	4	5	6	7	8	9	10	11	sum for ≥ 4
200		0	0	0	0	0	3	77	18	2	0	0	0	100
2200		0	0	0	0	0	4	73	20	3	0	0	0	100
8000		0	0	0	0	1	10	61	23	4	1	0	0	100

multiplicities, the majority of the tracks have six tracklets. Seven tracklets can occur for example from tracks that cross pad rows. Since the minimum number of hits for a tracklet is set to 8 and the number of time bins in the fit range amounts to 15,

⁶If the cut was 100% efficient, meaning that tracks from the primary vertex were taken out of the sample, if their p_t was exactly smaller than $2.3\text{GeV}/c$, then this approach would be a measure for the number of tracks, that are scattered off significantly their original direction

building a tracklet in each of the row requires, that the track crosses the rows "just in time". I.e., in one time bin the track produces two hits in two different rows, which is rather improbable. Also low p_t tracks, that get curled up in the magnetic field, might produce more than six tracklets, however such tracklets will hardly be part of the clean sample under consideration. A third possibility, which is more likely to happen, takes into account the tracks, that cross the border between two MCMs. They can produce two tracklets in one layer (one of them a standalone tracklet; discussed in the previous chapter), because the double track avoidance mechanism only works within one MCM. At larger multiplicity, together with nearby background tracks, further channels for multiple tracklet production in one layer open, as will be discussed on an example below. Clearly, the fraction of tracks with more than six tracklets should decrease, when applying the tracklet cut.

One can see a clear decrease in the fraction of tracks with 6 tracklets at increasing multiplicity. This comes hand in hand with an increase for 5 and for 7 tracklets.

Reasons, Why a Track Loses a Tracklet at Increasing Multiplicity There are several reasons, why a track may lose a tracklet (hence, why the fraction of tracks with 5 found tracklets increases), if multiplicity is increased:

- There is a close track from the background event which spoils the clusters of another track. The centroids of clusters from the signal track might be smeared (by charge sharing) and not found. Therefore, in the end, not enough hits could have been reconstructed in order to form a signal tracklet. Maybe a tracklet of the background track can be built but it will not be assigned a signal track label by the macro (except, the signal track and the background track overlap and produce dictionary entries at exactly the same digits). Note, that of three adjacent channels only one can be a central hit channel.
- The avoidance of double tracklets, which is supposed to avoid sending the same tracklet from one track inside one TRAP twice, works only in a low multiplicity environment and for tracklets that are spread over two channels at maximum. In a high multiplicity environment, the mechanism could reject a signal tracklet. Such a situation, respecting that in the current simulation the linear fit time range encloses 15 time bins, is shown in figure 7.31. Here, the signal track, that might have crossed a pad row and enters the current row only in time bin 7, produces three hits in channel 4 and five hits in channel 3. This would be enough to build a tracklet. Due to the large momenta of the signal tracks, this tracklet is spread over two channels only. However, a near background track with large incident angle is spread over three pads. Together with the signal track, three tracklets will be built: Tracklet (3,4) with 9 hits, tracklet (2,3) with 13 hits and tracklet (1,2) with 14 hits. In order to avoid double tracklets, tracklet (3,4) (with lowest hit sum) compares its left channel number (3) with the right channel number of tracklet (2,3). Since they are equal, tracklet (3,4) is rejected, because it has the lower number of hits. Consequently tracklet (2,3) compares its left channel number with the right channel number of tracklet (1,2) and is rejected. In the end, only tracklet (1,2) is left, containing no dictionary entries of the

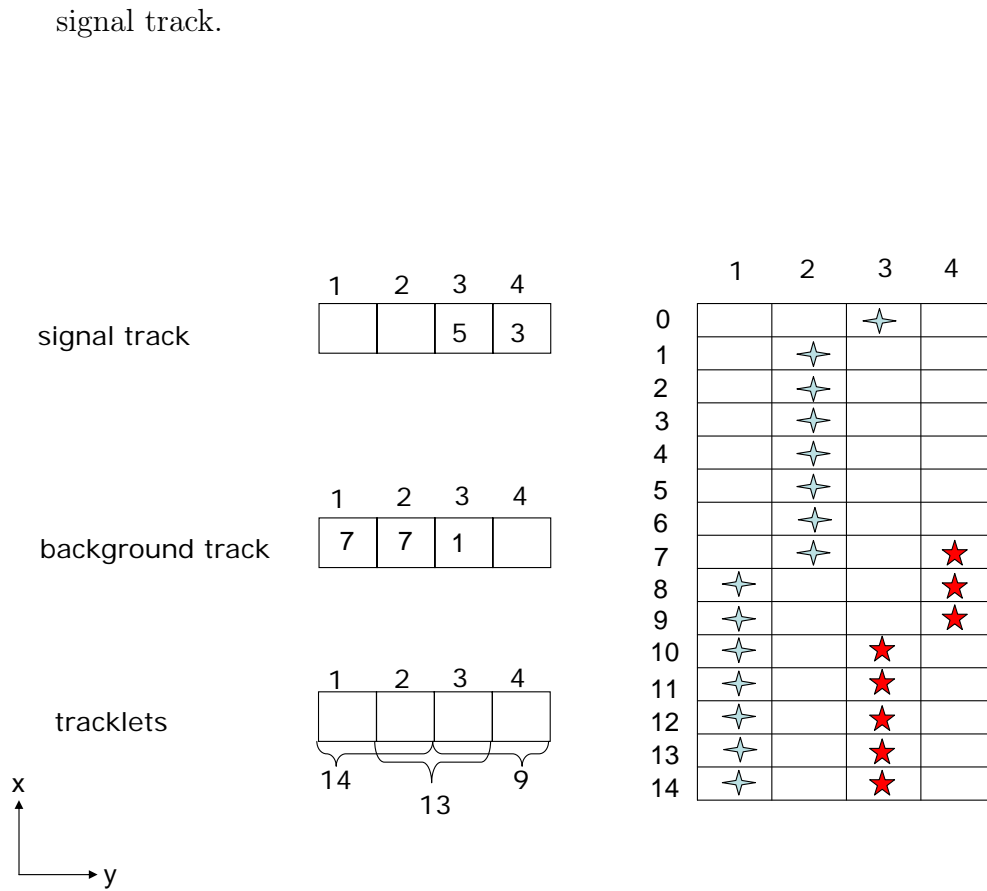


Figure 7.31: Possible constellation for how a tracklet can get lost due to double track avoidance. For channels of one pad row. Blue stars: Hits of the background track in the four channels within the fit range. Red stars: Hits of the signal track.

Rejecting the signal tracklet would not have worked, if the background track was spread over channels 2 and 3 only, e.g. with 8 hits in channel 2 and one in channel 3. The reason is some inefficiency of the macro at high multiplicities: Roughly, the macro counts the number of dictionary entries of a track in the central and its neighbor channels and chooses the most probable one to be the track label to which the tracklet is assigned. However, since the tracklet cannot be assigned to a background track (as it is not found in the stack, no particle ID), it will be assigned to a signal track whenever possible. Since in channel 3 the macro will find 8 dictionary entries (3 created by charge sharing) from the signal track, tracklet (3,4) would be assigned to it.

If the background tracklet had 10 hits in channel 3, only one tracklet (3,4) would occur. Since the background track labels are not considered by the macro, such a tracklet would have been assigned to the signal track as well.

- In a high multiplicity environment, it can happen, that more than four tracklets are found within one MCM. Then some of them will not be sent. Note, that more than four tracklets in one MCM means, that there are probably overlapping

clusters.

- Not more than 40 tracklets from a half chamber are read out. If more occur, they are omitted. This item is not important for the current simulation, as in the used tracklet output tree all tracks, that come out of the MCMs, are considered.

Reasons, Why a Track Gains a Tracklet at Increasing Multiplicity Here some reasons are listed, concerning why a track could gain a tracklet (especially, why the fraction of tracks with seven tracklets increases with increasing multiplicity).

- If a track crosses a pad row, it could build a tracklet in the row containing the later time bins, but in the other it might not have enough hits to produce a tracklet. There, some clusters at later time bins but corresponding channels from a nearby background track might be picked up. In the end, the number of clusters might be sufficient for a tracklet. Due to the TRF, signal clusters from the earlier time bins create dictionary entries at later time bins, where hits were created by the background track. Since enough dictionary entries stem from the signal track, the tracklet is assigned to it by the macro. Hence, two tracklets in one layer from two pad rows are assigned to one signal track.
- Another reason, why two tracklets in the same pad row are assigned to the same signal track, is again the macro inefficiency: Imagine a situation as shown in figure 7.32. Three tracklets can be built: tracklet (1,2), which contains purely signal hits, tracklet (2,3), which is a mixed tracklet and tracklet (3,4), which is purely background. Avoiding double tracklets, tracklet (2,3) compares its left channel number to the right channel number of tracklet (1,2) and is rejected due to its lower hit sum. Tracklet (1,2) and tracklet (3,4) are left. The macro assigns tracklet (1,2) correctly to the signal track. As it finds in channel 3 eight dictionary entries of the signal track and it cannot assign tracklet (3,4) to the background track, again the tracklet will be identified with the signal track. In that way there are two tracklets in one pad row for the same track.

Here it should be noted that these macro inefficiencies also have an impact on the worsening of offset, angle and deflection performance at increasing multiplicity. There, the shown situations might occur frequently due to a large abundance of background tracks. The tracklet quantities are then compared to the wrong MC tracks. However, the macro inefficiency accounts only for a fraction of the efficiency increase of tracks with 5 or 7 tracklets. Since these increases are in the low per cent range themselves, the overall deterioration of the tracklet performance due to the macro inefficiency will be small. Moreover, the situations shown in figures 7.31 and 7.32 only work, if the channels between the centroids of the two tracks (signal and background), that are used for charge sharing and which contain overlapping clusters, do not prevent the creation of the shown centroids⁷ The position reconstruction, however, and by that the offset determination, are spoiled in these cases nevertheless.

⁷This is the case, e.g. if the background and the signal track have similar ADC counts. On the channels between the centroids, charge from charge sharing from both sides is accumulated, which makes up around 13% of the centroid charges, respectively (if the hits of the centroid channels are situated in the center of the channels).

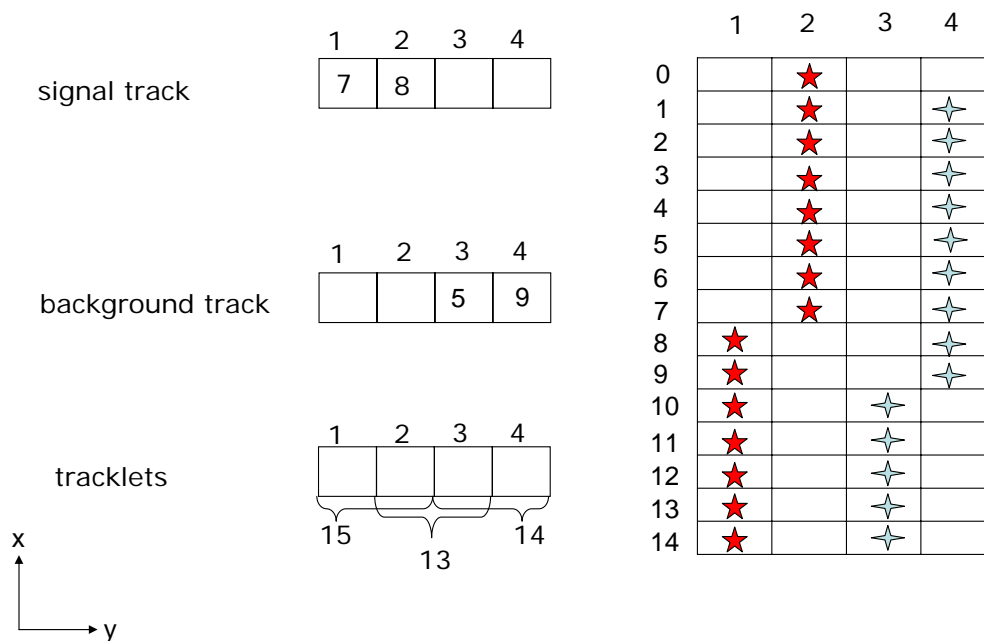


Figure 7.32: Possible constellation for how a tracklet can be gained due to the macro inefficiency. For channels of one pad row. Blue stars: Hits of the background track in the four channels within the fit range. Red stars: Hits of the signal track.

By rejecting also ambiguous background tracklets (which might be assigned to signal tracks), the efficiency increase of tracks with 7 tracklets on cost of the efficiency of tracks with 6 tracklets, could probably have been weakened.

- With Cut. Now, the tracklet cut is applied. 200 events have been simulated (160 for $\frac{dN_{ch}}{dy} = 8000$), since the cut requires to have more tracklets. The efficiency results are given in table 7.5. By comparing these numbers with the case where no tracklet

Table 7.5: Tracklet efficiencies. The fraction of tracks with a given number (nr.) of found tracklets is listed. With tracklet cut. Different multiplicities. The fraction of tracks with a number of tracklets is given in %.

multiplicity	nr.:	0	1	2	3	4	5	6	7	8	9	10	11	sum for ≥ 4
200		0	0	1	4	13	32	45	4	1	0	0	0	95
2200		0	1	3	10	23	34	27	2	0	0	0	0	86
8000		1	5	15	26	29	18	6	0	0	0	0	0	53

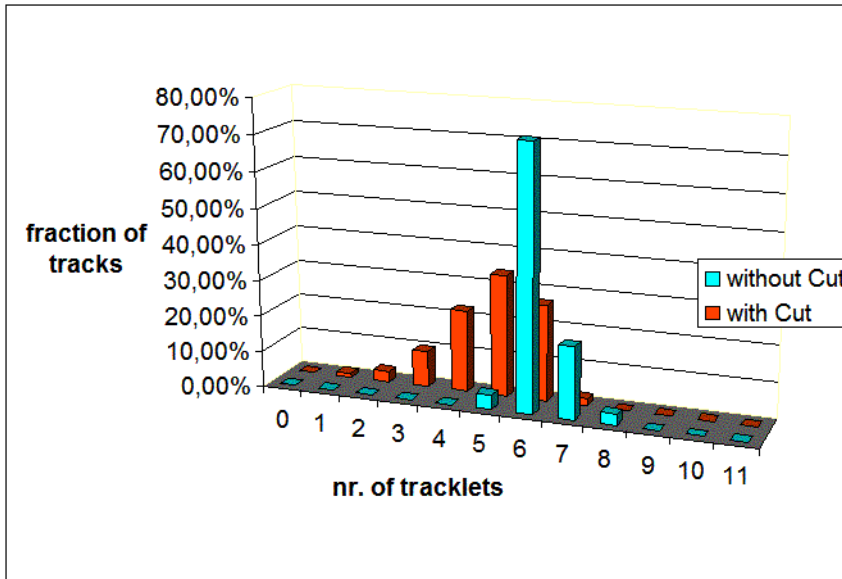


Figure 7.33: Efficiency for signal tracks with (last row) and without (first row) tracklet cut. Multiplicity 2200.

cut was applied (see figure 7.33 for a comparison at $\frac{dN_{ch}}{dy} = 2200$), it shows up, that the cut removes a substantial number of good tracklets. Compared to the non-cut case, the efficiency distribution is broadened toward lower number of tracklets and the maximum is shifted by one tracklet to a lower number (from six to five). Thus, on average, more than one tracklet per track is removed, when switching the cut on. There are hardly any tracks with more than seven tracklets, since in the case without cut, hardly any track had more than eight tracklets. Tracks with seven tracklets previously (before the cut) probably had eight tracklets. In the clean sample used, the tracklet cut will be able to remove tracks, whose $p_t < \frac{2.3GeV/c}{0.9 \cdot 0.9} = 2.84GeV/c$ (this

is the limit, if the track loses exactly 10% before and 10% inside the TRD and is thus still accepted by the macro). Tracks in the sample with $p_t > 2.84 \text{ GeV}/c$ at the primary vertex, which were not subject to significant scattering on their way to the TRD, will survive the tracklet cut. Looking at figure 7.7, tracks with $p_t < 2.84 \text{ GeV}/c$ already make up a substantial amount of all created signal-event tracks. Therefore it can be understood, that the tracklet cut removes about 14% of the tracks with ≥ 4 tracklets from a good sample at $\frac{dN_{ch}}{dy} = 2200$, compared to the case without cut.

The decrease in efficiency for five and six tracklets at increasing multiplicity, leading to an efficiency increase for four or less tracklets, might again be explained by an overload of MCMs with more than four tracklets. Some tracklets are then simply not sent. For others, due to overlapping clusters, the individual cluster position reconstruction is spoiled in a way, that the calculated deflection does not pass the deflection cuts any more (although the tracklets are taken from the good track sample).

Assuming that the tracklets left after the cut are stiff enough and fulfill the conditions to reconstruct a track with them inside the GTU, this goes on cost of the number of tracks with four or more tracklets. For the track reconstruction inside the GTU, at least four tracklets from different layers are required. Assuming no further diminution of the number of tracks with sufficient number of tracklets for reconstruction (hence assuming, that of the left tracklets at least four are found in different layers), one observes a fast degradation of the maximal possible, overall (tracklet and GTU) reconstruction efficiency with multiplicity (assuming a GTU reconstruction efficiency of 100%). While 95% of all tracks can be reconstructed at a multiplicity of $\frac{dN_{ch}}{dy} = 200$ and 86% at $\frac{dN_{ch}}{dy} = 2200$, this number decreases to 53% at $\frac{dN_{ch}}{dy} = 8000$. Hence, just half of the tracks, that were originally in a sample of good tracks, will be reconstructed at large multiplicities. This means, that for about 50% of the high- p_t primary vertex tracks, the tracklet cut will remove at least two tracklets from the sample.

At increasing multiplicity, also the majority of the tracks no longer has six tracklets. The number of tracklets, that occurs most frequently, decreases. This shows, that within the sample of tracklets chosen by the cut, the discussed mechanisms of gaining a tracklet are not efficient any more compared to the effects, that lead to loss of tracklets. Probably a large fraction of the background tracklets are removed, such that the effective abundance of tracklets is reduced and by that also the macro inefficiency (it becomes more unlikely, that constellations as shown in figure 7.32, leading to tracklet gain, are found). This also shows, that a gain in efficiency for tracks with more than six tracklets at increasing multiplicity, would mostly be based on the macro inefficiency. For the tracklet loss mechanisms, this is not the case.

Second Approach: Bad Signal Tracklets

Here, shortly the results of applying a tracklet cut on a sample of high p_t tracklets, which are likely to not come from the primary vertex, are presented (table 7.6). A background multiplicity of $\frac{dN_{ch}}{dy} = 2200$ was chosen.

In case no cut is applied, the majority of tracks produces six or more tracklets, suggesting that in any layer a tracklet occurs. The distribution is broadened with a maximum at 4

Table 7.6: Tracklet efficiencies of a bad tracklet sample. The fraction of tracks with a given number (nr.) of found tracklets is listed. Multiplicity 2200. The fraction of tracks with a number of tracklets is given in %.

state	nr.:	0	1	2	3	4	5	6	7	8	9	10	11
without cut		0	0	1	0	3	8	60	23	4	1	0	0
with cut		7	9	12	16	20	21	14	1	0	0	0	0

and 5 tracklets, if a cut is applied. This equilibration is much more pronounced than in the sample with good tracklets.

Third Approach: Full Multiplicity Background Event

In the following, one $\frac{dN_{ch}}{dy} = 8000$ background event is considered. Here, the number of tracks having no tracklets is so large, that it is not contained in efficiency calculation.

In table 7.7 the results without tracklet cut are shown, in table 7.8 the results with cut.

Table 7.7: Tracklet efficiencies of the full background event. No tracklet cut. The fraction of tracks with a number (nr.) of tracklets is given in %.

state	nr.:	1	2	3	4	5	6	7	8	9	10	11	sum ≥ 4
total		30	18	13	11	10	8	5	3	1	1	0	39
$p_t < 2.3GeV/c$		30	19	13	11	10	7	5	3	1	1	0	38
$p_t \geq 2.3GeV/c$		5	5	8	13	24	29	11	4	1	0	0	82

Table 7.8: Tracklet efficiencies of the full background event. With tracklet cut. The fraction of tracks with a number (nr.) of tracklets is given in %.

state	nr.:	1	2	3	4	5	6	7	8	9	10	11	sum ≥ 4
total		75	18	5	2	0	0	0	0	0	0	0	2
$p_t < 2.3GeV/c$		77	18	4	1	0	0	0	0	0	0	0	1
$p_t \geq 2.3GeV/c$		20	20	30	20	8	2	0	0	0	0	0	30

Since the majority of tracks has $p_t < 2.3GeV/c$, the distributions of all tracks and those with transverse momentum at the primary vertex $p_t < 2.3GeV/c$ look almost identical, even when applying a cut. One observes that tracks with $p_t \geq 2.3GeV/c$ produce on average more tracklets. This hints, that many tracks in case of $p_t < 2.3GeV/c$, produce only a low number of tracklets, which may also occur by accident, e.g. by assigning wrong clusters in the high multiplicity environment. Applying a cut throws away a substantial number of tracklets. In case of $p_t < 2.3GeV/c$ tracks, the overwhelming majority is left with a maximum of two tracklets.

In case of $p_t \geq 2.3GeV/c$, the situation is less dramatic (see figure 7.34). Although the distribution is shifted toward smaller number of tracklets, the weights are distributed

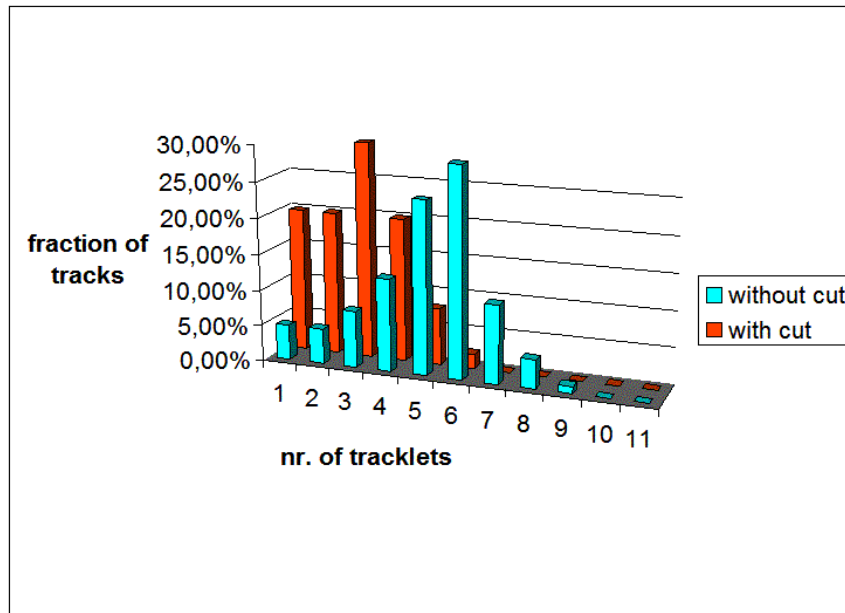


Figure 7.34: Efficiency for background tracks with (last row) and without (first row) tracklet cut. Multiplicity 8000. $P_t > 2.3 \text{ GeV}/c$.

almost equivalently over the range from 1 to 4 tracklets. Still for around 30% of the tracks with $p_t > 2.3 \text{ GeV}/c$, four or more tracklets are found. This suggests, that a significant amount of large p_t tracks arrive at the TRD with almost vertex direction. Comparing the result to the case of the good signal sample, where at a multiplicity of $\frac{dN_{ch}}{dy} = 8000$ only about 50% of the tracks are left with four or more tracklets, a yield of 30% of high p_t tracks, which could be reconstructed by the GTU, is quite astonishing. This means that the additional restriction of $\frac{\delta p_t}{p_t} < 0.1$ before and inside the TRD, respectively, increases the yield by just 20%, as compared to just restricting the sample to $p_t > 2 \text{ GeV}/c$ tracks. Note that in both cases, in the simulation of the background and the signal, ITS and TPC were activated. Almost none of the $p_t < 2.3 \text{ GeV}/c$ tracks could be reconstructed by the GTU.

The tracklet cut therefore relieves the matching for the GTU by taking out tracklets from the sample, which probably could not be merged to a track (tracklets from spoiled clusters, tracklets from curled up tracks (several tracklets in one layer), etc.). On the other hand also promising tracklets are removed, which can lead to the impossibility of reconstructing good tracks or result in a reconstruction of less quality, since less than six tracklets are available.

8 Electron Probability Measure and Pion Rejection Capability

In this chapter, the way to a possible electron identification measure in the TRAP is described. The method is based on the distribution of the mean charge per cluster. After a short introduction into the likelihood method, a simple implementation is proposed.

The particle identification procedure on tracklet basis will only be able to distinguish between two particle species, electrons and pions. Therefore it has to be assumed throughout this chapter, that there are but electron and pion tracklets in the event samples. Otherwise, if a third particle specie was involved, it would be identified as electron or pion and spoil the performance of the pion rejection capability, except its charge distribution had the same shape as that of electrons or pions. But of course, also other charged and energetic particles, e.g. muons, protons or kaons, can form tracklets. Since the trigger is supposed to find promising high p_t electrons, it is of importance, that these tracklets are treated like pions and are not misidentified as electrons.

More about the electron pion separation methods offline, especially a description of a neural network approach, can be found in [Wil04]. Detector performance results, concerning the electron identification, are given in [ALI01], [Ene03] and [Spa04]. An introduction into Stochastic is provided in [Naw94]. Probability issues, concerning the energy loss of particles, are contained in [Kol].

8.1 Electron Probability and Likelihood

Because a measure for the electron probability in the TRAP will have to exploit the deposited charge of the incident particle in some way, the distribution of the mean cluster charge is the foundation of the following discussion. The main purpose of the TRAP is to separate high p_t electrons from the large pion background. Therefore the electron probability measures are aimed to provide a good efficiency in electron detection with a large suppression of the ion background. In order to exploit a large fraction of promising events and to not spoil the chosen samples too much by background pions, a pion rejection factor of greater than 100 is necessary at 90% electron efficiency. That means that on average 90% of all interesting (high p_t) electron tracks have to be found and that less than 1% of these tracks may be misidentified as pions.

8.1.1 1D Likelihood Approach for TRAP

In the following, all discussions are specified for tracklets. The goal is to calculate a measure for the probability, that a given tracklet has been produced by an electron track. In the GTU, when tracklets are combined to tracks, the probability information of the tracklets

are combined to an overall probability for the track to be an electron. Also the mean cluster charge distributions are supposed to be recorded on tracklet basis. The mean charge per cluster is then given as the total charge $Q = Q^{(1)} + Q^{(2)}$ deposited by a tracklet, divided by the number of clusters, N : $q = \frac{Q}{N} = \frac{1}{N} \sum_{i=1}^N (L_i + C_i + R_i)$. The total charge of a cluster is given as the sum over the charges of the central channel and its two neighbors. The accumulated charges $Q^{(1)}$ and $Q^{(2)}$ and thus as the total charge of all clusters, Q , are given without baseline. Since N counts the number of detected clusters in the linear fit range, it is necessary that $Q^{(1)}$ and $Q^{(2)}$ cover together exactly the whole fit range without overlapping or gaps, in order to get a proper mean cluster charge¹.

If the distributions are normalized by their total number of entries, they can be interpreted as the conditional probability to measure the charge q given the knowledge of the particle specie: $P_e(q) = P(q|e)$ for electrons, $P_\pi(q) = P(q|\pi)$ for pions. Note that the distributions considered here are supposed to only contain the charge of tracklets with applied tracklet cut, i.e., whose p_t was found to be larger than $2.3\text{GeV}/c$. This is of course only true if the particles are assumed to come from the primary vertex.

The typical shape of mean cluster charge distributions for electrons and pions is shown in figure 8.1.

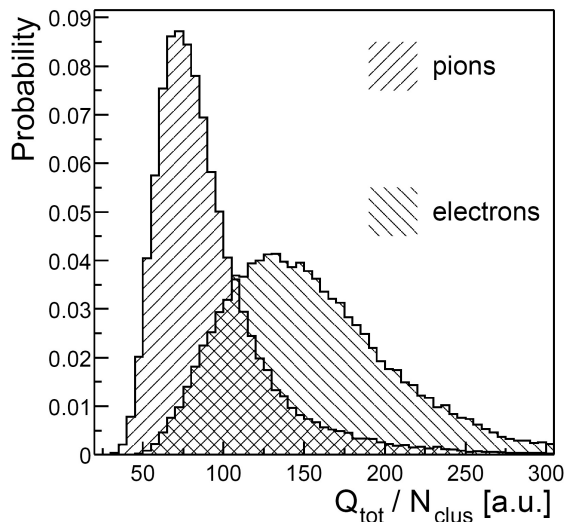


Figure 8.1: Mean cluster charge distributions for electrons and pions [ALI01]

The distribution of electrons is shifted toward larger values of q . This has two reasons. First, high p_t electrons have a large value of $\beta\gamma$ and are already at the Fermi plateau of energy loss. Pions at these momenta on the other hand are still on the relativistic rise.

¹Since one can assume, that a tracklet has a cluster in almost every time bin, the charge accumulation can be set to cover the drift region, whereas the linear fit range can be set to cover the amplification region in addition. This is possible, because the fit range and the charge accumulation range can be set independently. Then, the normalization factor for the mean charge per cluster is given by $N - N_{\text{amplification}} = N - (t_{\text{drift},S} - 1)$ (in every amplification time bin a cluster can be expected), if N is the total number of detected clusters. This is of course only true, as long as a track does not cross pad rows and all the amplification time bins are included in N . To be save, in the following, the fit range and the charge accumulation range are expected to be set equally. Then, the normalization factor is just given by N .

Second, there is additional charge, produced by TR clusters in case of electrons, yet not in case of pions. Therefore, the mean value and the most probable value (MPV) of the distribution are larger for electrons than for pions.

The quantity one would like to extract is the conditional probability, that a measured charge q was created by an electron: $P(e|q)$. Let $P(e)$ be the unconditioned probability that the incident particle was an electron (that the current tracklet was created by an electron track) and $P(q)$ the unconditioned probability to measure the mean charge per cluster q . Clearly, $P(e)$ and $P(q)$ depend on the fraction of electrons and pions in the TRD event (simplifying to the assumption that the event is made up only by electrons and pions, $P(e) + P(\pi) = 1$). Hence, the knowledge of $P(e)$ and $P(q)$ is a global event information, which is not available on MCM level. In the following, A denotes the event, that the tracklet was caused by an electron track and B the event, that the mean cluster charge q is created, $P(e) = P(A)$ and $P(q) = P(B)$. Including global information and using $P(A|B) = \frac{P(A \cap B)}{P(B)}$, one can write for $P(e|q)$:

$$P(e|q) = P(A|B) = P(B|A) \cdot \frac{P(A)}{P(B)}.$$

$P(q)$ can be turned into

$$P(q) = P(B) = P((A \cap B) \cup (\bar{A} \cap B)).$$

$A \cap B$ and $\bar{A} \cap B$ are disjunct events, hence

$$P(B) = P(A \cap B) + P(\bar{A} \cap B).$$

Because $P(A \cap B) = P(B) \cdot P(A|B) = P(A) \cdot P(B|A)$, it follows

$$P(B) = P(A) \cdot P(B|A) + P(\bar{A}) \cdot P(B|\bar{A}).$$

Therefore

$$P(A|B) = \frac{P(B|A) \cdot P(A)}{P(A) \cdot P(B|A) + P(\bar{A}) \cdot P(B|\bar{A})}$$

or in terms of $P(e)$ and $P(q)$

$$P(e|q) = \frac{P_e(q) \cdot P(e)}{P(e) \cdot P_e(q) + P(\pi) \cdot P_\pi(q)}. \quad (8.1)$$

This is the probability that an electron produces the mean cluster charge q .

As no global probabilities are available, one reduces equation (8.1) to its local components:

$$L_e(q) = \frac{P_e(q)}{P_e(q) + P_\pi(q)} = \frac{1}{1 + \frac{P_\pi(q)}{P_e(q)}},$$

with $0 \leq L_e(q) \leq 1$. The quantity L_e is called electron Likelihood and is a function of q . It is used as a measure for the probability, that the charge q was deposited by an electron. It is based only on the charge distributions and can be applied if no information beyond the charge deposition is available.

The following considerations are restricted to tracklets, i.e. to the charge deposit in one layer. By $L_e^i(q)$ the tracklet electron likelihoods are denoted (based on the mean charge q). Given the distributions of $P_e^i(q)$ and $P_\pi^i(q)$, for each q the likelihood $L_e^i(q)$ can be calculated. If, in case of an incident electron, these likelihood values $L_e^i(q)$ are weighted by the corresponding value of $P_e^i(q)$ at charge q and if these weights are filled into a likelihood histogram at the bin of the likelihood value $L_e^i(q)$, one obtains the distribution of the electron likelihood for incident electrons, $L_{e \rightarrow e}^i$ ². The distribution can of course also be obtained by measuring a second time for a large sample of incoming electrons under the same conditions, for which the $P_e(q)$ distributions were recorded, the mean cluster charge q and by increasing the corresponding likelihood bin $L_{e \rightarrow e}^i(q)$. For incoming pions, the likelihood distribution $L_{\pi \rightarrow e}^i$ can be obtained analogously. The $L_{e \rightarrow e}^i$ distribution can be considered as the distribution of the fraction of electrons, that are inferred as electrons. Accordingly $L_{\pi \rightarrow e}^i$ denotes the fraction of pions, that are misidentified as electrons. Note, that each charge q is connected to a likelihood value $L_e(q)$. Just the distribution of the likelihood values depends on the incident particle type (electron or pion). Typical electron likelihood distributions for incoming electrons and pions are shown in figure 8.2.

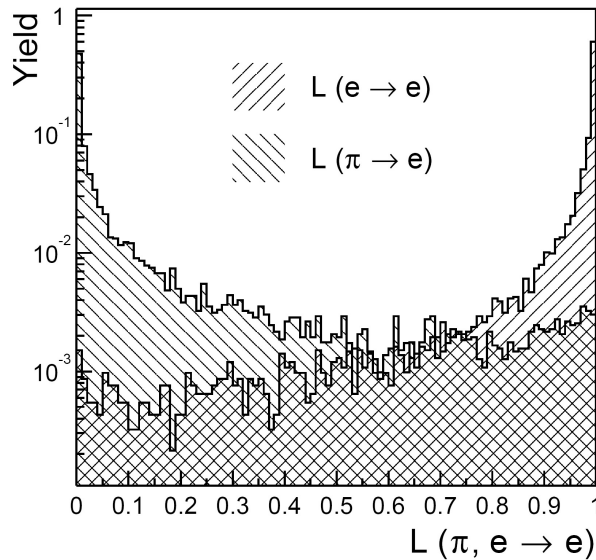


Figure 8.2: Electron likelihood distributions for incoming electrons and pions [ALI01]

The $L_{e \rightarrow e}^i$ distribution shows a strong increase of entries at likelihood values approaching 1. These likelihood values occur for large q , where the mean charge distribution of electrons still shows a considerable fraction of entries, whereas only a very small number of pions deposits that much charge (the number of entries in $L_{\pi \rightarrow e}^i$ decreases for increasing q). On the other hand, the fraction of electrons producing little charges q is small as compared to the fraction of pions depositing this charge. Therefore the number of entries in the $L_{e \rightarrow e}^i$ distribution decreases toward smaller q , while the number of entries increases in the $L_{\pi \rightarrow e}^i$ distribution³.

² q and hence $L_e^i(q)$ are discretized

³For the likelihood to be a pion (which is not used here), $L_\pi^i(q)$, it follows $L_\pi^i(q) = \frac{P_\pi^i(q)}{P_e^i(q) + P_\pi^i(q)} = 1 - L_e^i(q)$.

From the measured mean charge per cluster q , the TRAP is supposed to provide the corresponding likelihood value $L_e^i(q)$, based on the distributions of $P_e^i(q)$ and $P_\pi^i(q)$.

When combining the PID information of the tracklets from different layers, that were merged to one track, the GTU has to make a final decision of whether this track is treated as an electron or a pion track. Assuming that C tracklets are merged to one track, the likelihoods could be merged by building their mean:

$$L_e = \frac{1}{C} \cdot \sum_i L_e^i(q_i),$$

where the sum runs over the the contributing tracklets. q_i denotes the measured mean cluster charge of tracklet i , L_e the average electron likelihood of a track.

Based on the assumption, that the mean charge per cluster distributions and hence the electron likelihood distributions look the same in every layer (for incident electrons and pions; $P_e^i(q) = P_e(q)$, $P_\pi^i(q) = P_\pi(q) \forall i$)⁴, one can now apply a cut on the average likelihood L_e , $L_{e,cut}$. Particles with $L_e \geq L_{e,cut}$ are considered electrons and are kept, particles with $L_e < L_{e,cut}$ are treated as pions and are rejected. The value of the cut is chosen such, that the number of entries in the electron likelihood distribution for an incident electron make up 90% of all entries. If $f(L_{e \rightarrow e})$ ($f(L_{\pi \rightarrow e})$) denotes the functional description of the average electron likelihood distribution for an incident electron (pion)⁵, the cut fulfills the following condition:

$$\int_{L_{e,cut}}^1 f(L_{e \rightarrow e}) dL_{e \rightarrow e} = 0.9.$$

Under this cut about 2% of the entries in the electron likelihood distributions for incident pions are kept:

$$\int_{L_{e,cut}}^1 f(L_{\pi \rightarrow e}) dL_{\pi \rightarrow e} = \varepsilon_\pi.$$

This means that applying this cut will on average keep 90% of the good electrons⁶ (electron efficiency ε_e) and will keep around 2% of the high p_t pions, which are then treated as electrons (misidentified pions, pion efficiency ε_π). A pion efficiency ε_π hence means a pion rejection of $\frac{1}{\varepsilon_\pi}$ (in the example with $\varepsilon_\pi = 0.02$, only every 50th pion is misidentified and a factor 50 pion rejection is achieved).

Therefore the distributions of the pion likelihood for incoming electrons or pions are the mirrored distributions of the respective electron likelihoods (mirrored at $L = \frac{1}{2}$).

⁴Due to this assumption, the average electron likelihood distribution for the tracks can be expected to have the same shape as the likelihood distributions for the individual tracklets (depending on whether incident electrons or pions are considered). If an electron tracklet produces the fraction b of all entries in the $L_{e \rightarrow e}$ -distribution in a likelihood range $[L_{e,min}, L_{e,max}]$, this will also apply for the average distribution. This also makes the average electron likelihood L_e independent of the actual layers i , that are taken into account and additionally independent of the number C of tracklets, which were used to reconstruct the track.

⁵The average electron likelihood distributions for incoming e and π are obtained by inserting the values of L_e for many merged tracks into a likelihood histogram. Due to the assumption $P_e^i(q) = P_e(q)$ and $P_\pi^i(q) = P_\pi(q)$, alternatively it could be assumed, that the average likelihood distributions look the same as the distributions on tracklet basis, $f(L_{e \rightarrow e}) = f(L_{e \rightarrow e}^i)$ and $f(L_{\pi \rightarrow e}) = f(L_{\pi \rightarrow e}^i)$. Then, the cut values could be obtained by using the tracklet likelihood distributions.

⁶electrons with high p_t (on the Fermi plateau and producing TR), that go into the distributions

The approach in the offline reconstruction is different. In order to prevent confusion, the electron identification method used there is shortly presented.

8.1.2 1D Likelihood Approach Offline

The crucial difference in the offline reconstruction is, that the likelihoods are not calculated for each layer. Instead, for each layer the probabilities for measuring the mean charge q under the assumption of an incident electron and of an incident pion are calculated and both given as information to the track reconstruction unit. If the probabilities $P_e^i(q)$ and $P_\pi^i(q)$ are the same for all layers, $P_e^i(q) = P_e(q)$ and $P_\pi^i(q) = P_\pi(q)$ and the amount of charge created in a layer is independent of the charge in any other layer (independent energy losses), one obtains for the probability, that an electron creates the mean charge sequence $\vec{q} = (q_i)_{i \in \{1, \dots, 6\}}$, $P_e^{tot}(\vec{q})$:

$$\begin{aligned} P_e^{tot}(\vec{q}) &= (P^1 \times P^2 \times \dots \times P^6)(q_1 \text{ in layer 1} \cap q_2 \text{ in layer 2} \cap \dots \cap q_6 \text{ in layer 6} | e) \\ &= \prod_{i=1}^6 P_e^i(q_i) = \prod_{i=1}^6 P_e(q_i). \end{aligned}$$

For pions, the total probability for this charge sequence \vec{q} is calculated in the same way:

$$P_\pi^{tot}(\vec{q}) = \prod_{i=1}^6 P_\pi^i(q_i) = \prod_{i=1}^6 P_\pi(q_i).$$

The final electron likelihood for a track is now constructed with these probabilities:

$$\begin{aligned} L_e &= \frac{P_e^{tot}(\vec{q})}{P_e^{tot}(\vec{q}) + P_\pi^{tot}(\vec{q})} \\ &= \frac{\prod_{i=1}^6 P_e(q_i)}{\prod_{i=1}^6 P_e(q_i) + \prod_{i=1}^6 P_\pi(q_i)}. \end{aligned}$$

Therefore, the likelihood distribution has to be recorded for the total probabilities. If less than six layers are used, the products of the total probabilities are modified and therefore also the electron likelihood definition. Under the assumption, that the likelihood distribution only depends on the total number, not on the specific identity of the participating layers, for each possible number of involved layers, an individual distribution has to be recorded. If less than six layers are available for measurements, the pion efficiency results from less than six layers (e.g. measurements for one, two, ..., five involved layers) can be extrapolated to six layers.

The decision of whether a track is considered an electron or a pion is again chosen by a cut, allowing for 90% electron efficiency.

The reason, why this approach is not feasible for tracklets, is rather technical. For the measure of the electron probability of a tracklet, only 8 bits are available. The offline approach would require to send to the GTU the values $P_e^i(q_i)$ and $P_\pi^i(q_i)$. Having only 8 bit available for both values would restrict the accuracy of the final likelihood estimation very much. Therefore the approach of calculating the likelihood locally for each tracklet in the TRAP, will probably be the more accurate method.

It would however be possible, that for each tracklet the mean cluster charge q , encoded in 8 bit⁷, is written into the electron probability part of the tracklet word and sent to the GTU. Then all the probabilities would be calculated within the GTU and the offline likelihood method just described could be applied. This would mean, that the electron charge distribution, the pion charge distribution as well as the likelihood distribution would have to be stored in LUTs of the GTU. Moreover the GTU would be confronted with additional bunches of calculations⁸, although timing is already very tough. Additionally, since on GTU level the actual MCM, from which a tracklet comes from, is not known (only the half chamber is known), the mean cluster charge of a tracklet q , would have to be tracklet length corrected (see below) on LTU level before transmission to the GTU nevertheless (otherwise the tracklet length correction could only be done with have-chamber accuracy, incorporating between 24 and 32 MCMs). As it is not clear technically if the GTU approach would be possible, it is not followed any further here.

8.1.3 2D Likelihood Approach Offline

Up to now only one information about the deposited charge was used for electron pion separation, namely the mean cluster charge. Because of TR in case of electrons, which arrives preferentially toward later time bins and forms large charge clusters, an additional information can be exploited by recording also the arrival time of the largest detected charge cluster. The distribution is sketched in figure 8.3. The time distribution of the

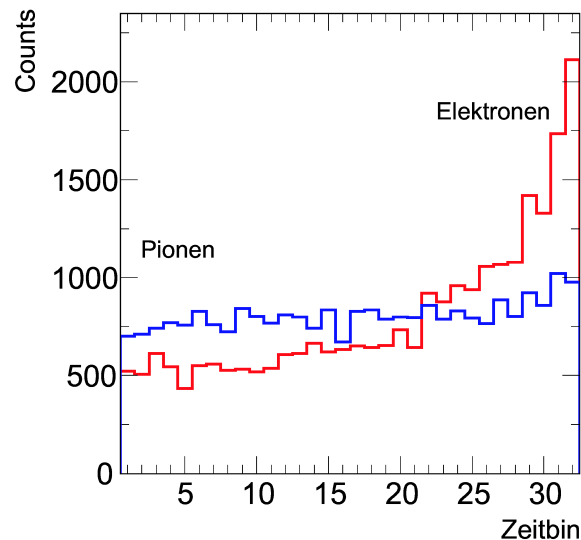


Figure 8.3: Time bin distribution of the largest cluster for electron and pion tracks [Wil04]

⁷Already by restricting q to 8 bit, throws away a significant part of the electron charge distribution (overflow for values $\geq 2^8$, projected to the $2^8 - 1$ bin of the distribution). Taking the first 8 bit of the n bit value q instead of the last ones on the other hand, restricts the resolution to 2^{n-8} . Smaller values are projected to this bin of the distribution.

⁸10 multiplications for the electron and pion charge probabilities, one addition and one division compared to 5 additions and one multiplication by a constant $\frac{1}{C}$ in case of the method described in the previous section

largest charge is almost uniform for pions. For electrons, the probability for the largest charge to arrive at small times is lower than for pions, however the probability is strongly increasing toward later time bins because of the additional TR clusters.

Let T_i be the time of the maximum charge of a cluster in layer i and let $\tilde{P}_e^i(T_i) = \tilde{P}^i(T_i|e)$ the probability for arrival time T_i in case of an electron ($\tilde{P}_\pi^i(T_i) = \tilde{P}^i(T_i|\pi)$ for a pion). Again the distributions are assumed to not differ in different layers, $\tilde{P}_e^i(T) = \tilde{P}_e(T)$ ($\tilde{P}_\pi^i(T) = \tilde{P}_\pi(T)$). Then, as the mean charge q and the time position T of the largest cluster are independent, one obtains for the probability for electrons:

$$\begin{aligned} P_e^{tot}(\vec{q}, \vec{T}) &= (P_e^1 \times \dots \times P_e^6 \times \tilde{P}_e^1 \times \dots \times \tilde{P}_e^6)((q_1 \cap T_1) \cap \dots \cap (q_6 \cap T_6)) \\ &= \prod_{i=1}^6 P_e(q_i) \cdot \prod_{i=1}^6 \tilde{P}_e(T_i). \end{aligned}$$

For pions:

$$P_\pi^{tot}(\vec{q}, \vec{T}) = \prod_{i=1}^6 P_\pi(q_i) \cdot \prod_{i=1}^6 \tilde{P}_\pi(T_i).$$

Similarly to the likelihood method for the charge q , one can define an electron likelihood for the position of the largest cluster by

$$\begin{aligned} \tilde{L}_e(\vec{T}) &= \frac{\tilde{P}_e(\vec{T})}{\tilde{P}_e(\vec{T}) + \tilde{P}_\pi(\vec{T})} \\ &= \frac{\prod_{i=1}^6 \tilde{P}_e(T_i)}{\prod_{i=1}^6 \tilde{P}_e(T_i) + \prod_{i=1}^6 \tilde{P}_\pi(T_i)} \end{aligned}$$

If less than six layers are included, the according products just run over the involved layers. Also for the total probability measure, an electron likelihood can be defined. Since this likelihood depends on two measures, \vec{T} and \vec{q} , it is also called 2D likelihood.

$$\begin{aligned} L_e^{tot}(\vec{q}, \vec{T}) &= \frac{P_e^{tot}(\vec{q}, \vec{T})}{P_e^{tot}(\vec{q}, \vec{T}) + P_\pi^{tot}(\vec{q}, \vec{T})} \\ &= \frac{\prod_{i=1}^6 P_e(q_i) \cdot \prod_{i=1}^6 \tilde{P}_e(T_i)}{\prod_{i=1}^6 P_e(q_i) \cdot \prod_{i=1}^6 \tilde{P}_e(T_i) + \prod_{i=1}^6 P_\pi(q_i) \cdot \prod_{i=1}^6 \tilde{P}_\pi(T_i)}. \end{aligned}$$

Applying the 2D likelihood method for incident electrons and pions, the pion rejection factor at 90% electron efficiency can be significantly increased. Unfortunately, from the TRAP no information about the time position of the largest cluster of a tracklet is available and therefore a 2D likelihood approach is not considered any further.

Another method, a neural network approach, tries to use the full information for electron pion separation, namely which charge was deposited when. However, a description of this method would lead too far.

8.2 The Energy Loss Distribution

In this section different aspects, that influence the mean cluster charge distributions, are shortly discussed. It is assumed that the total energy loss of a track within the fit range of

a layer is proportional to the mean cluster charge of the corresponding tracklet. Moreover, it is assumed that the shapes of both, the energy loss distribution and the mean cluster charge distribution are Landau like. A justification is given in the next section.

Because the probability for a mean cluster charge $q = \frac{Q}{N}$ is calculated from the corresponding distributions, one has first to define the conditions, under which the detector will be run, before recording the reference distributions. These conditions determine the values of q , that can occur and to which a probability has to be assigned. Moreover it should be noted, that the mean cluster charges for tracklets are considered, that have already passed a cut on the momentum of the tracklets at $p_t = 2.3 \text{ GeV}/c$. So it is assumed, that mostly stiff tracklets from the primary vertex are in the sample ($\frac{Q}{N}$ is obtained from such clusters). The mean cluster charge distributions, used for the electron probability in the TRAP, should be recorded under this condition.

8.2.1 Average Pulse Height Spectrum and Electron Pion Separation Power

The course of the averaged (over many measurements) signal height with time for electrons and pions is shown in figure 8.4. The time range considered also covers the amplification region. As a measure for the electron pion separation power, the fraction of the average signal of electrons and pions at a defined time t can be used:

$$R_{e,\pi} = \frac{\text{average signal of electrons at time } t}{\text{average signal of pions at time } t}.$$

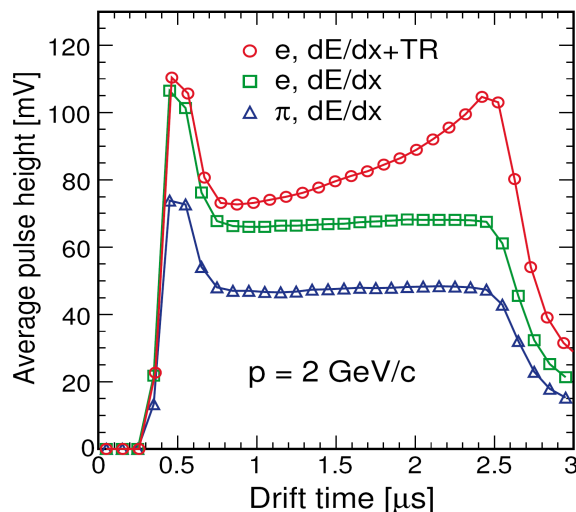


Figure 8.4: Average pulse height spectrum as function of the drift time [Pos04]

The first peak in the pulse height spectrum, which is on average twice as high as the height of the plateau, is due to charge clusters from the amplification region, which arrive

from below and above at the anode wire within the same time bin⁹.

With the arrival of clusters from the drift volume, the average pulse height decreases considerably and only slightly increases with drift time. This increase comes from overlappings of the long tails due to the slow ion drift of preceding avalanches. If a tail filter is applied, this slight increase could be used as a measure of its efficiency.

After drift time the average signal decreases exponentially, which again is due to the gradual decay of the long tails from the last clusters.

In case of electrons, the average height of the plateau is larger than in the pion pulse height spectrum, because electrons are already at the Fermi plateau of ionization while pions are at the relativistic rise. Moreover the contribution of TR clusters (which are preferentially absorbed at the entrance of the drift volume) makes the plateau values increase considerably toward the end of drift time. Therefore it is sensible to choose for $R_{e,\pi}$ a time t toward the end of the drift.

If electrons and pions are not separated and both are used for the average pulse height spectrum, the increase due to TR clusters is hardly visible, since the average effect suffers from the large ion background.

8.2.2 Some Features Influencing the Mean Cluster Charge Distributions

- δ -rays. They mostly influence the tail of the distribution. It is hence important to decide, how δ -rays are treated: Whether they are tracked and their energy loss is added to the energy loss of the tracklet or if one does not account for δ -electrons (low energetic ones might get curled up in the magnetic field) and hence only the energy deposit of the tracklet is considered. To characterize the mean charge per cluster distribution, it is of advantage to take the MPV instead of the mean, since the MPV is less affected by the tail.
- Tracks that are crossing pad rows. As there is no communication between pad rows on TRAP level, tracklets of such tracks have biased mean cluster charge. If a tracklet is produced of clusters from early time bins, the contribution of TR for electrons is missing and hence the mean cluster charge is too small and closer to the values for pions. This decreases the electron pion separation capability. If, on the other hand, an electron tracklet is formed of clusters from later time bins only, due to the overestimated TR contribution its mean cluster charge becomes too large, hence increasing the separation capability¹⁰. Because stiff tracks are considered (small deflection from

⁹Due to the higher drift velocity and the low drift distance of these clusters, the time shape of the individual signal caused by them is hardly influenced by transverse diffusion but is almost exclusively given by the PASA shaping and the time response of the amplification (slow ion drift away from anode wire). Hence the individual signal of an amplification cluster approaches the shape of the time response function (time response to a delta shape like charge cluster at the anode wire)

¹⁰Due to the shape of the individual energy release spectrum ($\delta E \propto \frac{1}{(\delta E)^2}$), there will be only few electron clusters with large energy content produced by one track (and hence only few detected clusters with large charge; a detected cluster is composed of the signal of several electron clusters). If a track with such a large detected cluster crosses a pad row, its mean cluster charge will be underestimated in one row and overestimated in the other. Underestimated mean cluster charge of electrons as well as overestimated mean cluster charge of pions will also reduce the separation capability.

the vertex direction), tracks that cross pad rows are mainly an issue at large angles between the vertex direction and the chamber normal in the xz -plane, e.g. at the outer stacks of a sector. While in the central stack rows are only crossed, if the stiff track enters close to a pad row boundary (happening only for a small angular region), in the outer stacks, due to the larger inclination of the tracks w.r.t. the chamber normal, the angular region, permitting row-crossing, becomes broad. For a sample of tracks from the primary vertex with no preferred direction, this means, that the probability for pad row crossing increases with the longitudinal z -distance from the vertex. Because a SM is seen at an opening angle of 90° from the primary vertex, the maximum deflection of vertex direction to chamber normal is 45° . Crossing a pad row means, that on the flight through the drift volume (linear fit range), where clusters are created, the boundary between pad rows is crossed. Because the maximum deflection in z , $\Delta z = \tan 45^\circ \cdot 3.0\text{cm} = 3.0\text{cm}$, is considerably smaller than the pad lengths (7cm to 10cm), a maximum of one pad row is crossed per layer. The number of pad rows covered by the opening angle, is the same for all of the layers (the pad length is increased layer by layer to cover the larger area, figure 8.5), hence the probability to cross a pad row should not be layer dependent.

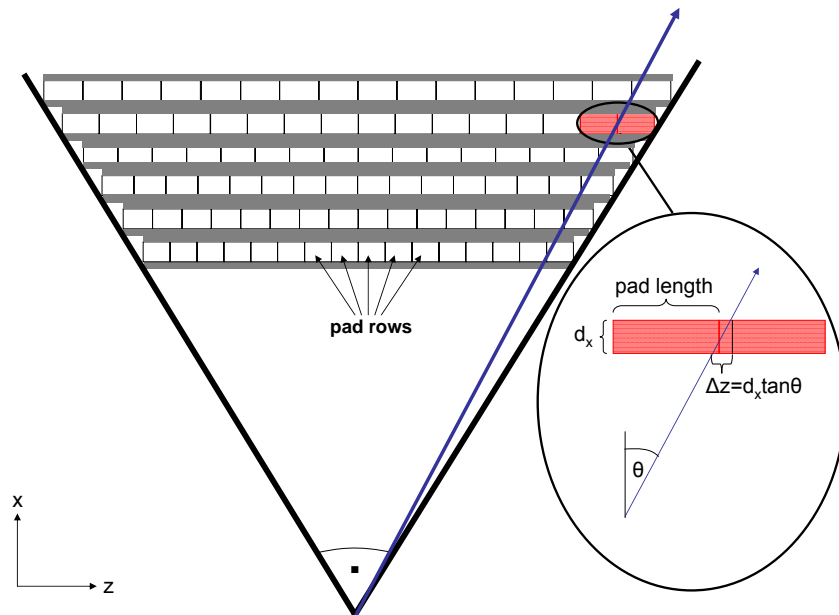


Figure 8.5: Projective geometry of the TRD in the xz -plane. Stack with 16 pad rows.

- **Momentum.** Since pions are on the relativistic rise of energy loss and electrons are on the Fermi plateau, the mean charge per cluster will increase with momentum for pions, yet not for electrons. Therefore the electron pion separation (pion rejection at 90% electron efficiency) decreases with momentum. At large momenta, for the separation the contribution of TR is crucial.

As a measure for the separation of e from π one could use the truncated mean of

the mean cluster charge distribution (by not counting entries in the distributions at charges above a threshold; also used for discriminating particles with no TR contribution) or the MPV, which is less affected by the tail and therefore more stable. However, to determine the MPV requires to fit the measured energy loss by a convolution of a Gaussian with a Landau distribution and derive the MPV from that. The Gaussian describes the limited detector energy resolution, leading to a smearing of the actual energy losses. The smeared energy loss is then weighted by a Landau distribution. Thus the convolution of the two effects yields the observed distributions.

Assuming that the energy transfer spectrum remains unchanged ($\delta E \propto \frac{1}{(\delta E)^2}$), a larger energy loss of pions at larger momenta is induced by a greater number of primary inelastic collisions (the mean of the Poisson distribution, \bar{N} , grows). The effect on the mean cluster charge distribution is then comparable to what happens, if the path length through the detector is enlarged. This means for the distribution of the tracklet energy deposit $\Delta E = \sum_{i=1}^N \delta E_i$, that the MPV grows. Also the tail becomes less pronounced, because the probability for large energy losses or the production of δ -rays does not increase proportional to the number of energy losses. Moreover the FWHM, normalized to the MPV, $\frac{FWHM}{MPV}$, decreases. More entries in the sum (entries all distributed according to $\delta E \propto \frac{1}{(\delta E)^2}$) allow for an easier balance of the sum's value and thus makes it more stable with less fluctuations. Hence the FWHM of the distribution, normalized to \bar{N} or MPV, decreases. By increasing \bar{N} , the Landau distributions should then gradually approach a normal distribution.

For electrons, no momentum effects on the energy loss by ionization should be visible. However, the mean energy loss for electrons is composed by two parts: the energy loss due to ionizations and the loss because of Bremsstrahlung:

$$\left(\frac{dE}{dx}\right) = \left(\frac{dE}{dx}\right)_{\text{ion}} + \left(\frac{dE}{dx}\right)_{\text{brems}}.$$

While $\left(\frac{dE}{dx}\right)_{\text{ion}}$ is almost independent of the energy E (electrons are at Fermi Plateau at the considered momentum scale), $\left(\frac{dE}{dx}\right)_{\text{brems}}$ increases proportional to E . As the energy loss spectrum for Bremsstrahlung is rather broad with a different mean value as compared to the energy loss due to ionization, its increasing contribution at growing momentum would add fluctuations to $\left(\frac{dE}{dx}\right)$ and might enlarge the FWHM of the total energy loss distribution (with Bremsstrahlung included).

- Effective detector thickness. If the incident angle of the track w.r.t. the chamber normal is different from 0° , also the effective path length through the radiator and the detector increases. This increases again \bar{N} and has to be taken into account when using a recorded energy loss distribution, by applying a corresponding normalization.
- Detector constants. The energy loss depends on features like the gas composition, pressure, electric field strengths, drift velocity ... Therefore one has to define the environment under which the detector will be run, before recording the reference energy loss distributions.
- Space charge. The average pulse height increases exponentially with gas gain. However, at large gas gains, space charge reduces the gain especially for later time bins.

For the amplification region, as there are no preceding avalanches, space charge has no influence. For later times the plateau of the average pulse height spectrum becomes attenuated. The strength of this effect however depends on the incident angle of the track (becomes more marked toward normal incidence, since all charge becomes concentrated on a small area). Moreover the effect of space charge is more pronounced for electrons than for pions due to their larger signal (more drifting positive ions after the avalanche). Hence also the electron pion rejection power $R_{e,\pi}$ decreases toward normal incidence.

Because space charge is a local effect, it varies the gas gain locally. Therefore it would be of advantage to reduce space charge as much as possible. As already mentioned, space charge is reduced at larger incident angles. However the increase in $R_{e,\pi}$ for larger angles is also positively influenced by the thicker effective radiator and detector, which leads to more TR and more energy loss. Another way to reduce space charge is to reduce the gas gain (by reduction of anode voltage), resulting in a ion cloud of less density.

- Linear fit range. This issue was already mentioned in the previous chapter. If the linear fit end time t_{FE} is not chosen close enough to the real drift end time, $t_{drift,E}$, the Transition Radiation clusters are not properly taken into account. This influences the mean cluster charge distribution of electrons and reduces the electron-pion separation capability.
- Multiplicity (e.g. pp run, PbPb run). In an environment with very many tracks, there are a number of effects which influence the mean cluster charge distribution:
 - Clusters not found. Because the probability for finding several very close tracks is large in a high multiplicity event, it can easily happen that position reconstruction of a cluster due to charge sharing is influenced by nearby clusters. Then the reconstruction algorithm might no longer be able to assign the cluster to the right track or even might not find some clusters and as a consequence some tracks could end up with too low mean cluster charge assigned to them.
 - Assigning wrong clusters to a track could either reduce or enlarge the cluster charge, assigned to the track
 - Cluster pick up. Also for stiff tracklets (distributed only over 2 or 3 pads) it is very common, that a track picks up clusters from other tracks. An overlapping cluster for example cannot be disentangled before it is assigned to a track. In this way, one track picks up clusters, which were built by several tracks, resulting in an exaggerated mean charge per cluster. Since the mean of the charge distributions grow with multiplicity, cluster pick up seems to be the overwhelming effect.

That also means, that the values of the pulse height spectrum increase. However, this effect is more pronounced for pions than for electrons, because for pions the value of $\frac{dE}{dx}$ is smaller and TR is missing. Therefore cluster pick up reduces the electron pion separation power $R_{e,\pi}$ and thus the pion rejection at given electron efficiency.

A possibility to reduce the influence of high multiplicity on the mean cluster charge distribution and on $R_{e,\pi}$, could be the usage of the cluster quality measure. Only if a cluster is considered clean, it is counted as a fit point and the charge counter Q and the hit counter N are increased. Of course, if the measure is used in the run, also for the reference distributions it must be applied.

In a high multiplicity environment, where almost 30% of all detector pixels (pad and time bins) are occupied, using the quality measure could lead to a substantial decrease of counted clusters. This could either reduce the number of tracklets (because not enough clusters are available to build a tracklet) or to a wrong charge measure. A usual track is supposed to produce clusters in almost every time bin it traverses in the fit range. However, the quality measure could take out clusters from time bins arbitrarily, in which clusters are found to occur from crossing tracks (overlapping clusters). If nevertheless a tracklet is built (tracklet with holes), it could happen that its clusters are concentrated around some time bins and a collection of holes is found around other time bins (where tracks have crossed). Like that, the mean charge of the tracklet can easily be under- or overestimated (by excluding TR or excluding ranges without TR). Because there is no time bin information on the participating clusters, there is no way to find out, whether one can rely on the mean charge measurement of a tracklet or how often the mean charge of tracklets is determined considerably false.

8.3 Proposal for the Implementation of a Likelihood Measure into the TRAP

In this section a possible implementation of an electron probability measure for the TRAP is presented, respecting the technical conditions.

8.3.1 Technical Conditions

The final electron identification measure of a tracklet, which, as was discussed in the first section, will be a likelihood, will be stored as part of the tracklet word, encoded as 8 bit, with a granularity of 2^{-8} . To store the likelihood values for different mean cluster charges q , a LUT with place for 2047 entries of 8 bit each is available on the TRAP. The LUT is steered by a 11 bit word, which contains the address of the entry in the LUT, that is chosen as electron probability.

8.3.2 The Reference Distribution

In the following, all quantities that are related to the reference distribution will be marked by the index 0 or are given as a function of the reference tracklet length in the fit range, l_0 (specified later). l_0 is assumed to correspond to the N_{fit} time bins of the fit range (and is determined by the incident angle of the track).

The first observation is, that a minimum ionizing particle (MIP) produces on average (Poisson mean) around 50 hits per cm track length. In the whole drift volume of 3.0cm , on average 150 hits can be expected and this amounts to around 7 hits per time bin (20 time

bins in drift volume). Thus, the signal that is observed at sampling time, can be made up from the contributions of several hits.

Let a tracklet be made up of N clusters, where it is assumed that N almost is given by the number of time bins from the fit range, $N \leq N_{fit}$, which are usually chosen to be all situated in the drift volume of one chamber (if the tracklet is not spread over several pad rows). The assumption is, that the track produces a cluster in almost every time bin it flies through, which is justified by the fact, that a cluster is made up from the contribution of several hits. The mean cluster charge can be written

$$q(l_0) = \frac{Q(l_0)}{N} = \frac{1}{N} \sum_{j=1}^N q_j(l_0).$$

By $q_j(l_0) = L_j + C_j + R_j$, the cluster charge of the j^{th} counted cluster (with subtracted baseline) is denoted (the charge is spread over neighbored pad due to charge sharing). l_0 is the tracklet length.

Now it can be further assumed, that the detected cluster charge is proportional to the energy content ε of the cluster,

$$q_j(l_0) = m \cdot \varepsilon_j(l_0) + c.$$

$c = 0$ because $\varepsilon_j(l_0) = 0 \Leftrightarrow q_j(l_0) = 0$. m is given by the gas gain amplification and the PASA contribution. That's why the following considerations will be based on energy.

In a simplified picture, where the spatial distances between the hits contributing to a cluster as well as the distance of the PASA-shaped signal maximum from the sampling time is neglected, it can be assumed, that the detected cluster signal at sampling time is directly proportional to the sum of the energy deposits as stored in the hits. In terms of the energy signal, this means:

$$\begin{aligned} \varepsilon_j(l_0) &= \sum_{i=1}^{M_j} \delta E_i \\ q_j(l_0) &= m \sum_{i=1}^{M_j} \delta E_i. \end{aligned}$$

M_j is the number of hits contributing to the j^{th} cluster and δE_i is an individual energy transfer. Since the number of hits per cluster, M_j , is Poisson distributed with mean $\bar{M}_j(l_{tb})$, depending on the effective length of a time bin, l_{tb} (and hence on the tracklet length by $l_{tb} = \frac{l_0}{N_{fit}}$), and the energy transfer δE_i is approximately distributed as $\frac{1}{\delta E_i^2}$, $\varepsilon_j(l_0)$ is the energy transfer in a thin detector (effective thickness of a time bin) and is Landau distributed. Also the effective length of all fit time bins corresponds to a thin detector and hence the total energy loss in the fit time range,

$$\sum_{j=1}^N \sum_{i=1}^{M_j} \delta E_i,$$

should also be Landau distributed. This can be seen by rewriting

$$\sum_{j=1}^N \sum_{i=1}^{M_j} \delta E_i = \sum_{k=1}^{M_{tot,l_0}=M_1+M_2+\dots+M_N} \delta E_k.$$

Again, δE_k is $\frac{1}{\delta E_k^2}$ distributed. Since the sum of Poisson distributed variables is again Poisson distributed (see Appendix), M_{tot,l_0} is Poisson distributed. Because the individual mean values for an effective time bin length l_{tb} (depending on the incident angle), $\bar{M}_j(l_{tb})$, are the same for each time bin j , $\bar{M}_j(l_{tb}) = \bar{M}(l_{tb})$, one obtains for the mean of M_{tot,l_0} :

$$\bar{M}_{tot,l_0} = N \cdot \bar{M}(l_{tb}).$$

\bar{M}_{tot,l_0} corresponds to a larger effective path length $N \cdot l_{tb}$, however not necessarily to $l_0 = N_{fit} \cdot l_{tb}$, since $N \leq N_{fit}$, therefore $\bar{M}_{tot,l_0} \leq \bar{M}(l_0)$ ($\bar{M}(l_0) = N_{fit} \cdot \bar{M}(l_{tb})$).

Because of the above considerations for the distribution of the mean cluster charge q (which is the charge distribution normalized by N), a Landau shape can be expected.

8.3.3 Tracklet Length Correction

Because it is not possible to record reference distributions for all geometrical positions of MCMs, the reference mean cluster charge distribution is instead adjusted to different lengths of the tracklets inside the fit range due to the different geometrical positions. The tracklet length depends for example on the position of the MCM (direction to primary vertex) and the momentum of the tracklet (together yielding the deflection d_y). In this section it shall be first inferred, how the reference distribution can be adjusted to a different effective tracklet length, before the various contributions to the path length are discussed.

Adjustment of the Reference Distribution to Different Tracklet Lengths

Let the fit range $[t_{FS}, t_{FE}]$ be totally covered by the drift region. It is assumed, that the reference distribution was recorded for an effective tracklet length l_0 inside the fit range and that an adjustment to the actual tracklet length l shall be performed. The number of fit time bins, N_{fit} , is supposed to be the same. The question is, how the reference distribution can still be used in case of different effective path lengths. Or, in other words: If a tracklet, that travels the distance l , produces the mean cluster charge $q(l)$, is there a scaling to obtain the charge $q(l_0)$ in the reference distribution for the case, the tracklet had traveled the distance l_0 ? In both cases one can assume that the number of clusters N is equal and approximately equal to the number of fit time bins, $N \approx N_{fit}$ ($N \leq N_{fit}$).

In the following it is again assumed, that the distribution of the individual energy transfers remains unchanged. The difference in the mean cluster charge for different tracklet lengths is then due to a changing number of energy transfers. The mean cluster energy can

be expressed by

$$\begin{aligned}\varepsilon(l_0) &= \frac{1}{N} \sum_{k=1}^{M_{tot,l_0}} \delta E_k \\ \varepsilon(l) &= \frac{1}{N} \sum_{k=1}^{M_{tot,l}} \delta E_k.\end{aligned}$$

If the distance l_0 is split into $G_0 \gg 1$ basic parts of length $\delta l = \frac{l_0}{G_0}$, the number of hits produced on this basic length $M(\delta l)$ is Poisson distributed with mean $\bar{M}(\delta l)$ (possibly the mean is ≤ 1). Then, due to the fact that the sum of Poisson distributed variables are again Poisson distributed, one obtains

$$\begin{aligned}\bar{M}_{tot,l_0} &= G_0 \cdot M(\delta l) \\ \bar{M}_{tot,l} &= \frac{l}{\delta l} \cdot M(\delta l) \\ &= \bar{M}_{tot,l_0} \frac{l}{l_0}.\end{aligned}$$

Hence, $\bar{M}_{tot,l} \propto l$ with the proportionality constant $\frac{\bar{M}_{tot,l_0}}{l_0}$.

As an assumption, one can expect the average value of the energy transfer to an individual hit not to change with increasing tracklet length:

$$\frac{1}{M_{tot,l}} \sum_{k=1}^{M_{tot,l}} \delta E_k \approx \frac{1}{M_{tot,l_0}} \sum_{k=1}^{M_{tot,l_0}} \delta E_k.$$

Then

$$\sum_{k=1}^{M_{tot,l}} \delta E_k \approx \frac{M_{tot,l}}{M_{tot,l_0}} \sum_{k=1}^{M_{tot,l_0}} \delta E_k.$$

Now, it can be assumed that $\bar{M}_{tot,l} \gg 1$ and $\bar{M}_{tot,l_0} \gg 1$, since they are the mean values of the number of energy transfers for the whole tracklet. Assuming further that there is a large probability that $M_{tot,l}$ does not deviate much from $\bar{M}_{tot,l}$, one can write $M_{tot,l} = \bar{M}_{tot,l} + x$ with $x \ll \bar{M}_{tot,l}$, and correspondingly $M_{tot,l_0} = \bar{M}_{tot,l_0} + y$ with $y \ll \bar{M}_{tot,l_0}$. Then

$$\begin{aligned}\frac{M_{tot,l}}{M_{tot,l_0}} &= \frac{\bar{M}_{tot,l} + x}{\bar{M}_{tot,l_0} + y} \\ &= \frac{\bar{M}_{tot,l} + x}{\bar{M}_{tot,l_0} \left(1 + \frac{y}{\bar{M}_{tot,l_0}}\right)} \\ &\approx \frac{\bar{M}_{tot,l} + x}{\bar{M}_{tot,l_0}} \left(1 - \frac{y}{\bar{M}_{tot,l_0}}\right) \\ &\approx \frac{\bar{M}_{tot,l}}{\bar{M}_{tot,l_0}}.\end{aligned}$$

Therefore

$$\sum_{k=1}^{M_{tot,l}} \delta E_k \approx \frac{l}{l_0} \sum_{k=1}^{M_{tot,l_0}} \delta E_k$$

and

$$\begin{aligned} \varepsilon(l) &\approx \frac{l}{l_0} \varepsilon(l_0) \\ \Rightarrow q(l) &\approx \frac{l}{l_0} q(l_0). \end{aligned}$$

This means, the mean cluster charge is proportional to the tracklet length. The normalized mean cluster charge distribution for tracklet length l is obtained from the reference distribution by:

$$P(q|l) = P\left(\frac{l_0}{l} \cdot q|l_0\right), \quad (8.2)$$

where q is the measured charge for tracklet length l and $\frac{l_0}{l} \cdot q$ the corresponding charge from the reference distribution in case of tracklet length l_0 .

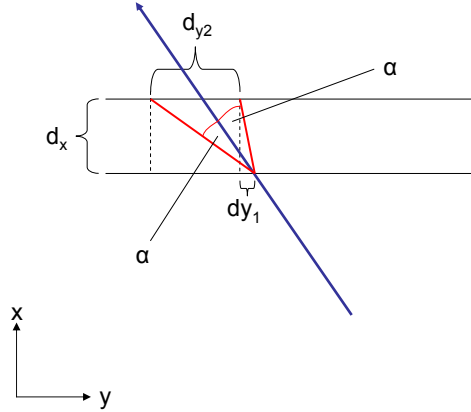
Tracklet Length Ingredients

The tracklet length is directly given by the incident angle with respect to the chamber normal (which is determined by the direction to the primary vertex and the finite value of p_t), where the inclination in y and in z direction have to be considered. The angle depends on the geometrical position of the track and on its transverse momentum p_t . There are several assumptions:

- The track comes from the primary vertex.
- The track does not change pad rows.
- The charge sign is not known on TRAP level.
- Each MCM knows its coordinates.
- For each momentum a specific reference distribution is recorded. Of course, this is idealistic but its implications will be exploited.

As the mean cluster charge distributions are stored in each MCM, each one must be configured individually. The geometry impact of the z coordinate to the tracklet length can only be given on pad row granularity. The quantity d_y , which is known for each tracklet and which denotes the deflection length, contains the combined influence of geometry and momentum. A first difficulty is visible immediately: As the charge sign is not known, the sign of the angle between tracklet direction and vertex direction in the xy-plane is unknown. Since the deflection d_y for a specific track angle is asymmetric w.r.t. the charge sign (figure 8.6), for each momentum two distributions have to be stored, each normalized by the appropriate tracklet length, corresponding to the two different charge signs.

The contributions of the individual coordinates to the tracklet length are as follows:


 Figure 8.6: The asymmetric d_y ranges for different charge signs

- x coordinate. In x direction the tracklet length is restricted by the number of fit time bins. If ν is the sampling frequency, one obtains:

$$l_x = (t_{FE} - t_{FS}) \frac{v_{drift,x}}{\nu}.$$

- y coordinate. In y direction the deflection is directly given by d_y (given as a number with dimension), which contains the geometrical input as well as the momentum contribution:

$$l_y = d_y.$$

Note that the part of the deflection, that occurs due to momentum, d_{y,p_t} ¹¹, depends on the charge sign. Due to the inclined vertex direction (relative to chamber normal), these two values of deflection d_{y,p_t} are asymmetric with respect to the vertex direction $p_t = \infty$ ($d_{y,p_t=\infty} = 0$). For the lowest value of p_t that should occur according to the applied cut, $p_{t,min} = 2.3 GeV$, together with a maximum vertex direction of $\phi_{vertex} = 12^\circ$ in the xy-plane (corresponding to $x = 3m$, $y = 0.65m$), one obtains the two values of deflection (geometry and momentum), $d_{y,min} \approx 4.0mm$ and $d_{y,max} \approx 8.9mm$. Therefore two distributions have to be stored for each momentum (range), one for each charge sign.

¹¹ $d_{y,p_t} = \pm \arcsin\left(\frac{\sqrt{x_m^2 + y_m^2} eB}{2p_t}\right)$ and $d_y(p_t) = d_x \cdot (\tan(\arctan(\frac{y_m}{x_m}) + d_{y,p_t}))$

- z coordinate. The tracklet length in z direction depends on the path length in x direction, l_x . Let ϑ be the angle in the xz-plane between track direction and chamber normal, then (figure 8.7)

$$l_z = l_x \cdot \tan \vartheta.$$

Let now z_m denote the z coordinate in the middle of the pad row on which the MCM

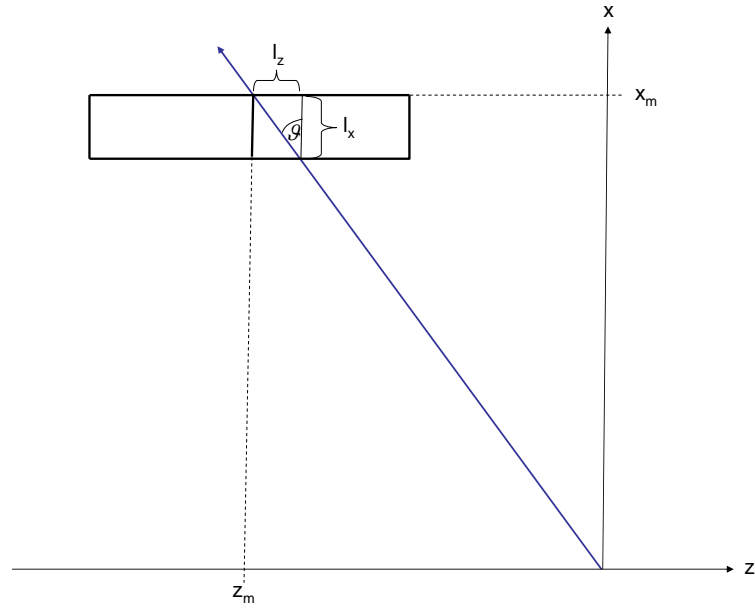


Figure 8.7: The dependence of l_z on l_x

is situated and x_m the height of the corresponding pad plane. Using this yields

$$\begin{aligned} \tan \vartheta &= \frac{z_m}{x_m} \\ \Rightarrow l_z &= l_x \cdot \frac{z_m}{x_m}. \end{aligned}$$

Combining yields

$$\begin{aligned} l &= \sqrt{l_x^2 + l_y^2 + l_z^2} \\ &= \sqrt{l_x^2 \left(1 + \frac{z_m^2}{x_m^2}\right) + d_y^2}. \end{aligned}$$

For d_y , the following expressions were obtained:

$$\begin{aligned} d_{y,min}(p_t) &= d_x \cdot \tan \left(\arctan \left(\frac{y_m}{x_m} \right) - \arcsin \left(\frac{\sqrt{x_m^2 + y_m^2} eB}{2 \cdot p_t} \right) \right) \\ d_{y,max}(p_t) &= d_x \cdot \tan \left(\arctan \left(\frac{y_m}{x_m} \right) + \arcsin \left(\frac{\sqrt{x_m^2 + y_m^2} eB}{2 \cdot p_t} \right) \right) \end{aligned}$$

For a given p_t , $d_{y,min}$ is obtained for one charge sign, $d_{y,max}$ for the other. Here, a new problem occurs. Since all distributions are in the configuration of one MCM, also the correction factor for the tracklet length has to be precalculated. As there is not enough space to store distributions that are corrected on pad granularity, the only way is to calculate the correction factor in granularity of MCMs. Therefore y_m denotes the central y position of the 18 pads belonging to one MCM. x_m is specific for a layer. If it is clear for what p_t ranges the reference distributions are recorded, also the corresponding d_y and hence l can be calculated for each MCM. Because all arguments of the trigonometric functions are small, one can approximately write for d_y (error in the low % range and smaller than the error introduced by restricting the granularity to MCMs):

$$d_{y,min}(p_t) \approx d_x \cdot \left(\left(\frac{y_m}{x_m} \right) - \left(\frac{\sqrt{x_m^2 + y_m^2} eB}{2 \cdot p_t} \right) \right)$$

$$d_{y,max}(p_t) = d_x \cdot \left(\left(\frac{y_m}{x_m} \right) + \left(\frac{\sqrt{x_m^2 + y_m^2} eB}{2 \cdot p_t} \right) \right)$$

Specifying now the conditions for the reference distribution means to choose the MCMs, for which the mean cluster charge distributions for tracklets within a given p_t range are recorded. This defines the geometrical quantities needed to calculate l_0 in MCM granularities. Here, the chamber in the lowest layer 1 and middle stack 2 is chosen. There, the four central MCMs are picked (number of pad rows is even and $\frac{\text{number of pads in a row}}{18} = \frac{144}{18} = 8$ is also an even number, figure 8.8). For those MCMs one can approximately set $y_m \approx 0$,

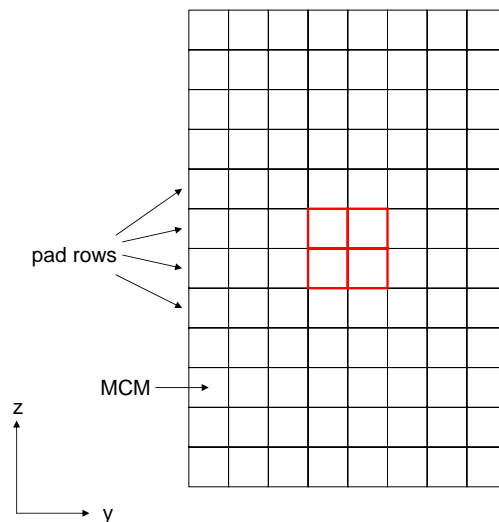


Figure 8.8: The four chosen central MCMs in a chamber with 12 pad rows

$z_m \approx 0$. Then,

$$l_{0,max} \approx \sqrt{l_x^2 + d_x^2 \frac{x_{m,layer\ 1}^2 e^2 B^2}{4p_t^2}}$$

$$l_{0,min} \approx \sqrt{l_x^2 - d_x^2 \frac{x_{m,layer\ 1}^2 e^2 B^2}{4p_t^2}}.$$

p_t can be given as the central momentum of recorded p_t range. Of course, using only 4 MCMs will result in a very long time needed to record the distributions with enough statistics. Using instead more than 4 MCMs (e.g. combining different layers or a complete pad row) will on the other hand reduce the resolution of l_0 and thus the correction factor from MCM granularity to pad row or stack granularity. In this sense, achieving higher statistics will reduce accuracy. In the following however, it is assumed that the tracklet length is given in MCM granularity and that one gains enough statistics nevertheless.

For the correction factor $\frac{l_0}{l}$ according to (8.2), one obtains:

$$\frac{l_0}{l} = l_0 \cdot \frac{1}{l_x \sqrt{1 + \frac{z_m^2}{x_m^2}}} \sqrt{\frac{1}{1 + \delta}}$$

$$\delta = \frac{d_y^2}{l_x^2 (1 + \frac{z_m^2}{x_m^2})}.$$

Now, as it has already been shown, $d_{y,max} \leq 8.9mm$. With $l_x \leq 30.0mm$, approximately $d_y^2 \ll l_x^2$ and hence $d_y^2 \ll l_x^2 (1 + \frac{z_m^2}{x_m^2})$ holds. Thus

$$\sqrt{\frac{1}{1 + \delta}} \approx 1 - \frac{1}{2}\delta.$$

Denoting $l_{xz} = \sqrt{l_x^2 + l_z^2} = l_x \sqrt{1 + \frac{z_m^2}{x_m^2}}$, for $\frac{l_0}{l}$ this finally yields:

$$\frac{l_0}{l} = \frac{l_0}{l_{xz}} \left(1 - \frac{1}{2} \frac{d_y^2}{l_{xz}^2}\right). \quad (8.3)$$

For a given p_t (central value of the p_t range, the distributions were recorded for), two distributions are needed, one for each charge sign. According to a measured d_y it must be possible to decide, which distribution (for which charge sign) has to be chosen to look up the probability corresponding to the measured mean cluster charge q . Since there is no time left to calculate the quantity $\frac{l_0}{l} \cdot q(d_y)$ for each tracklet, the distributions have to be precalculated and stored. To obtain the two tracklet length-normalized distributions, one could record two reference distributions, one for each charge sign. These distributions then have to be normalized by the appropriate factors: $\frac{l_{0,min}}{l_{xz}} (1 - \frac{1}{2} \frac{d_{y,min}^2}{l_{xz}^2})$ or $\frac{l_{0,max}}{l_{xz}} (1 - \frac{1}{2} \frac{d_{y,max}^2}{l_{xz}^2})$. Instead, it would be enough to record one reference distribution for one charge sign. To obtain the two normalized distributions, that will be stored in the MCM, one has then to normalize the reference distribution by two different tracklet lengths: $\frac{l_0}{l_{xz}} (1 -$

$\frac{1}{2} \frac{d_{y,min}^2}{l_{xz}^2}$) and $\frac{l_0}{l_{xz}} (1 - \frac{1}{2} \frac{d_{y,max}^2}{l_{xz}^2})$. $l_0 = l_{0,min}$ or $l_0 = l_{0,max}$, depending on whether the reference distribution was recorded for positively or negatively charged particles. Recording the reference distribution for one charge sign requires of course, that the energy loss mechanisms are independent of the charge sign. As long as the energy loss is determined by ionization, this is fulfilled. However, for simplification, for the rest of this chapter the approach of recording two reference distributions for each p_t is followed. But of course one can easily switch to the other approach.

The correction factor has to be precalculated for each MCM and each distribution individually. To obtain the entry for the mean cluster charge q in the distribution that will be stored in a MCM, the entry at the charge $\frac{l_0}{\gamma} q$ (expressed in the granularity of q) from the reference distribution has to be taken. Since $\frac{l_0}{\gamma} \leq 1$ for a reference distribution under the mentioned conditions (shortest possible value of l_0), it can happen, that different entries in the distribution of this MCM come from one entry of the reference distribution. Typical values for $\frac{l_0}{\gamma}$ are between 0.95 and 1.

8.3.4 Implementation

Before discussing quantization issues, a possible way for implementation shall be presented.

In the first place, all distributions have to be recorded and corrected for each MCM. Then the likelihood has to be calculated from the distribution for each value of q . Looking at the range of ADC values occurring for $q = \frac{Q}{N}$ in the distribution, it can be seen, that 7 bit are not enough to cover the whole dynamical range. At least 8 bit are needed to sufficiently represent the values showing up with some probability and hence having entries in a record with high statistics (in order to make the range fit into 8 bit, q and not Q is chosen as measure)¹². However, even 8 bit are only enough, if the overall amplification factor (gas gain, PASA amplification) is chosen sufficiently small. The LUT with 2047 entries (available in each MCM) will be used to store the likelihoods¹³. However, it will also be used to return for a given d_y the address of the corresponding bunch of likelihoods (not the probabilities) (obtained from the correct tracklet length adjusted distribution, according to p_t and charge sign, inferred from d_y). For each q -distribution at least 8 bit are necessary and therefore also 8 bit are needed to store the likelihoods from this distribution ($L_e = L_e(q)$ is a function of q). Hence, since $\frac{2^{11}-1}{2^8-1} = 8$, a maximum of three momentum ranges can be chosen. Note, that for each momentum there are two distributions. Then $(2^{11} - 1) - 6 \cdot (2^8 - 1) = 517$ entries can be used to find out the address of a likelihood bunch from d_y . Therefore all 7 bit of d_y can be encoded in the LUT. If there was a one to one relation between d_y and p_t (which is not the case, as will be described in the next section), in order to be able to assign the right distribution to d_y , the central p_t values, for which the reference distributions were recorded, should be distinct enough, such that d_y changes by at least 1 bit.

Once all likelihoods are calculated and stored for each MCM and the problem of assigning to d_y the right distribution (and thus the right likelihood bunch) is solved, the following

¹²If the overall gain (gas gain and PASA) was increased too much, also Q and $q = \frac{Q}{N}$ would increase. 8 bit are therefore only enough, if the gain is sufficiently low.

¹³Since each stored likelihood distribution occupies 255 entries of the LUT (since the LUT is steered by the 8 bit mean cluster charge q), it is not possible to store a distribution for every of the possible 18 tracklet channels of one TRAP. The same distributions have to be used by all of the TRAP channels.

strategy of steering the LUT could be chosen. First, d_y is given to the LUT. As d_y shall be stored at the end of the LUT, the corresponding 11 bit LUT steer word (giving the position in the LUT) would look like 1111& d_y , meaning, that the largest four bits are filled by 1. The corresponding 8 bit entry in the LUT is only filled with a 3 bit number, denoting the address of the corresponding likelihood bunch. These 3 bit are subsequently written onto the first three bit of the LUT steer word. The last 8 bit are filled with the value of q , where q has been cut at a value of $2^8 - 1$. Hence, the following words will be formed:

$$\begin{aligned} &000\&q, 001\&q \\ &010\&q, 011\&q \\ &100\&q, 101\&q. \end{aligned}$$

The largest address number in the LUT occupied by the likelihoods will thus be $2^{10} + 2^8 + (2^8 - 1) = 1535$. It should be again emphasized, that the LUT is steered by two quantities in this approach: q and d_y . At the corresponding LUT address, the 8 bit value of the electron likelihood is stored, which can immediately be used to fill the 8 bit electron probability part of the 32 bit tracklet word.

8.3.5 Assigning Momentum to Deflection

Since it is necessary to assign to d_y a momentum in order to choose a distribution, this issue shall be discussed in an own section.

If a deflection d_y is measured for a tracklet, this is done on pad granularity (x coordinate of the drift chamber entrance, y coordinate of the pad, on which the tracklet was found). That means, that the direction to the primary vertex of this tracklet was given with pad width resolution. As the assignment of d_y to p_t happens on MCM basis¹⁴, tracklets with 18 different vertex directions occur. For a given value of p_t , there are 18 different deflections d_y on one MCM for each charge sign. Since the the tracklet word does not carry information about the angle or deflection of the primary vertex direction, without an additional offset information a one to one representation of d_y to p_t is not possible any more. As was mentioned in the last section, 517 entries in the LUT (9 bit) are available for d_y and possibly another quantity, being suitable to define a tracklet's vertex direction. However, since the pad width in the outermost layer amounts to $0.8cm$, a MCM, incorporating 18 pad widths, ranges over $18 \cdot 0.8cm = 14.4cm$. Because $\frac{144mm}{0.16mm} = 900$ ($160\mu m$: offset granularity), this means, that only to obtain the pad information from the offset, at least 10 bit of the 13 bit offset word would be needed. For each MCM, one would have to determine, which 10 out of the 13 bit are necessary. However, since only 9 bit in total are available in the LUT, this approach of using offset information is not followed here.

Imagine all tracklets in one MCM that have a common value $p_{t,1}$. Their deflections span a range in the $d_{y,min}$ and $d_{y,max}$ values:

$$\begin{aligned} &[d_{y,max}^{min}(p_{t,1}), d_{y,max}^{max}(p_{t,1})] \\ &[d_{y,min}^{min}(p_{t,1}), d_{y,min}^{max}(p_{t,1})]. \end{aligned}$$

The $d_{y,min}$ range is due to tracks of the opposite charge sign than those producing the $d_{y,max}$ range. The same holds of course for tracklets of $p_{t,2}$ and $p_{t,3}$. $d_{y,min}^{min}(p_{t,1})$ and $d_{y,max}^{min}(p_{t,1})$

¹⁴because each MCM has only got one LUT to store the distributions

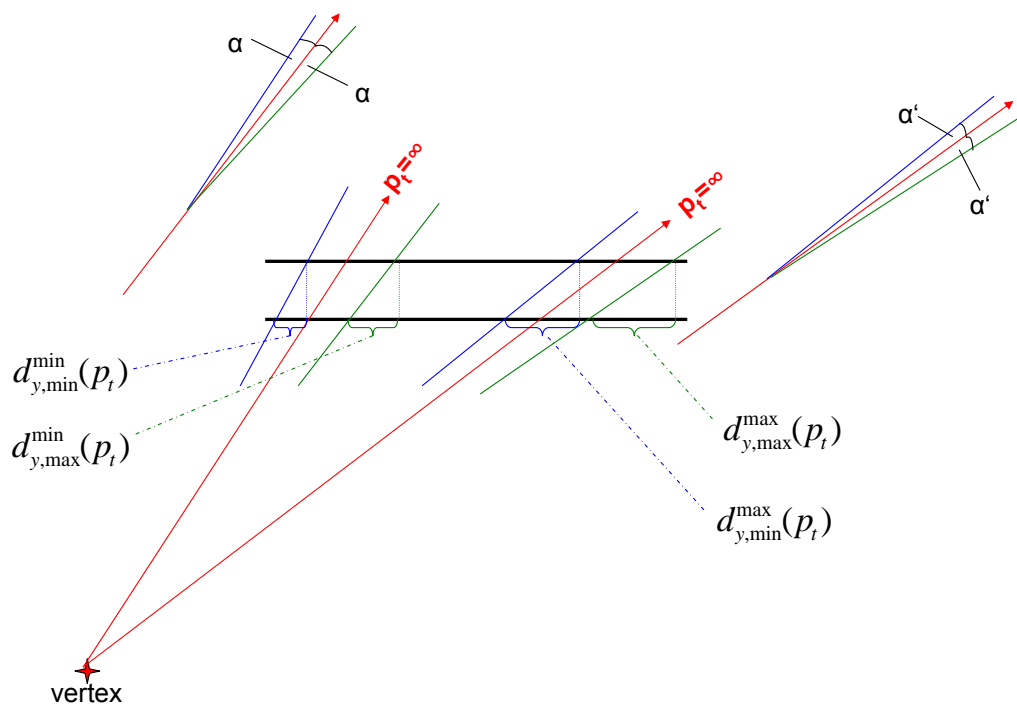


Figure 8.9: Ranges of possible tracklet deflections within one MCM

are the deflections of primary vertex tracklets on one edge of the MCM, $d_{y,min}^{max}(p_{t,1})$ and $d_{y,max}^{max}(p_{t,1})$ on the other edge. The linear fits to the corresponding tracks through the MCM edges, surround the vertex direction at these positions. As p_t increases, the tracks will increasingly nestle to the vertex direction, resulting in a decrease of $d_{y,max}^{min}(p_t)$ and $d_{y,max}^{max}(p_t)$ and an increase of $d_{y,min}^{min}(p_t)$ and $d_{y,min}^{max}(p_t)$. Note that at $p_t = \infty$ the track lines will be identical to the vertex direction.

From these observations it can be shown, that $d_{y,min}$ and $d_{y,max}$ ranges do not overlap, even for different p_t . This means, that it is always possible to decide for a given d_y , to which class of range it belongs (corresponding to a charge sign). If also a p_t could be inferred from d_y , finally a distribution could be assigned to d_y . To show that $d_{y,min}$ and $d_{y,max}$ ranges do not overlap for three chosen p_t values $p_{t,1} < p_{t,2} < p_{t,3}$, because of the above observations it is enough to show, that still at $p_{t,3}$

$$d_{y,max}^{min}(p_{t,3}) \geq d_{y,min}^{max}(p_{t,3}) \quad (8.4)$$

holds. Using now again the approximated expressions for d_y and evaluating $\sqrt{x^2 + y^2} \approx x \cdot (1 + \frac{y^2}{2x^2})$ since $y^2 \ll x^2$, and inserting for y the coordinates of the MCM edges (y_m : y coordinate of MCM center, $\Delta y = 9 \cdot \text{pad width}$: half of MCM width), one obtains:

$$d_{y,max}^{min}(p_{t,3}) \approx d_x \left(\frac{y_m - \Delta y}{x_m} + \frac{1}{2p_{t,3}} eBx_m \left(1 + \frac{(y_m - \Delta y)^2}{2x_m^2} \right) \right)$$

$$d_{y,min}^{max}(p_{t,3}) \approx d_x \left(\frac{y_m + \Delta y}{x_m} - \frac{1}{2p_{t,3}} eBx_m \left(1 + \frac{(y_m + \Delta y)^2}{2x_m^2} \right) \right).$$

Resolving (8.4) for $p_{t,3}$, yields:

$$p_{t,3} \leq \frac{eB(2x_m^2 + y_m^2 + \Delta y^2)}{4\Delta y}.$$

The condition, that $d_{y,min}$ and $d_{y,max}$ ranges are separate, is fulfilled for all MCMs if $p_{t,3} \leq 9\text{GeV}/c$ is chosen. Hence,

$$[d_{y,min}^{min}(p_{t,1}), d_{y,min}^{max}(p_{t,3})] \cap [d_{y,max}^{min}(p_{t,3}), d_{y,max}^{max}(p_{t,1})] = \emptyset.$$

The strategy is now as follows: First choose the three values of p_t , e.g. $p_{t,1} = 2.5\text{GeV}/c$, $p_{t,2} = 4.0\text{GeV}/c$, $p_{t,3} = 6.0\text{GeV}/c$. Determine for each MCM in a pad row the range of $d_{y,min}$ and $d_{y,max}$ values for each individual p_t (MCMs at according y yet different z can be treated equally for this discussion). There will be overlapping parts of the ranges $[d_{y,max}^{min}(p_t), d_{y,max}^{max}(p_t)]$ for the different p_t (also for the $d_{y,min}$ ranges). It can be achieved that only ranges belonging to the neighbored p_t values are overlapping (hence, d_y ranges belonging to $p_{t,1}$ do not overlap with those belonging to $p_{t,3}$), by requiring

$$d_{y,max}^{min}(p_{t,1}) \geq d_{y,max}^{max}(p_{t,3})$$

$$d_{y,min}^{min}(p_{t,3}) \geq d_{y,min}^{max}(p_{t,1}).$$

The first condition yields

$$p_{t,3} \geq \frac{p_{t,1}eB(2x_m^2 + (y_m + \Delta y)^2)}{eB(2x_m^2 + (y_m - \Delta y)^2) - 8\Delta yp_{t,1}}$$

for

$$p_{t,1} \leq \frac{eB}{8\Delta y}(2x_m^2 + (y_0 - \Delta y)^2).$$

which is fulfilled for all MCMs, if $p_{t,1} \leq 4.5\text{GeV}/c$ is chosen. Accordingly, the second condition yields

$$p_{t,3} \geq \frac{p_{t,1}eB(2x_m^2 + (y_m - \Delta y)^2)}{eB(2x_m^2 + (y_m + \Delta y)^2) - 8\Delta y p_{t,1}}$$

for

$$p_{t,1} \leq \frac{eB}{8\Delta y}(2x_m^2 + (y_0 + \Delta y)^2).$$

which again is globally fulfilled for $p_{t,1} \leq 4.5\text{GeV}/c$.

Evaluating these two conditions for all MCMs, it shows up that for $p_{t,1} = 2.5\text{GeV}/c$ one has to choose $p_{t,3} \geq 5.7\text{GeV}/c$. That's why $p_{t,3} = 6\text{GeV}/c$ was proposed.

In total, the ranges look like:

$$\begin{array}{ccc} [d_{y,\min}^{\min}, d_{y,\min}^{\max}] & p_{t,1} & [d_{y,\max}^{\min}, d_{y,\max}^{\max}] \\ [d_{y,\min}^{\min}, d_{y,\min}^{\max}] & p_{t,2} & [d_{y,\max}^{\min}, d_{y,\max}^{\max}] \\ [d_{y,\min}^{\min}, d_{y,\min}^{\max}] & p_{t,3} & [d_{y,\max}^{\min}, d_{y,\max}^{\max}] \end{array}$$

In case of overlapping ranges for two adjacent values of p_t , this means that there are a number of values of d_y for which the assignment to a p_t is not unique. For these, a definite strategy has to be developed, that assigns these d_y to one of the p_t 's (there is no preferred p_t). For example, half of the overlapping range could be assigned to one p_t , the other half to the other p_t . Or the assignment could be done such, that all p_t values incorporate a possibly similar number of the 255 d_y values.

In case there is a gap between the ranges of two values of p_t , this means there are a number of d_y values, which are not assigned to any p_t . For these an unique assignment to one p_t value has to be chosen, similarly to the strategy in case of overlapping ranges.

Still there might be unused d_y , e.g. $d_y \leq d_{y,\min}^{\min}(p_{t,1})$, $d_y \geq d_{y,\max}^{\max}(p_{t,1})$ or $d_{y,\min}^{\max}(p_{t,3}) \leq d_y \leq d_{y,\max}^{\min}(p_{t,3})$ (as the $d_{y,\min}$ and $d_{y,\max}$ ranges are disjunct). For $d_y \leq d_{y,\min}^{\min}(p_{t,1})$ and $d_y \geq d_{y,\max}^{\max}(p_{t,1})$, d_y should be assigned to $p_{t,1}$. If $d_{y,\min}^{\max}(p_{t,3}) \leq d_y \leq d_{y,\max}^{\min}(p_{t,3})$, d_y should be assigned to $p_{t,3}$. Because of this it could be of advantage to assign a large part of overlapping d_y or gap d_y to $p_{t,2}$.

In the end, inside each MCM each of the 255 d_y values is assigned to one of the six distributions, which means, d_y has been assigned to the $d_{y,\min}$ or the $d_{y,\max}$ range and to one out of the three p_t values. Therefore, tracklets inside a MCM of same p_t yet different directions to the primary vertex, can be assigned to different distributions. However, in any case, tracklets are correctly assigned to one of the three distributions that correspond to their charge sign (which is unknown in the TRAP but expresses itself by different d_y ranges).

The effect, that this assignment strategy might lead to different relative statistics of the reference distributions recorded in a small sample of MCMs, is not further investigated. Although it would be more sensible to record for each MCM its own reference distributions, this is technically impossible.

8.3.6 Mean Cluster Charge Distributions and Likelihood Distributions in view of the Quantization Issue

The topic to be discussed in this section concerns the likelihood calculation from the recorded reference $q = \frac{Q}{N}$ distributions. It is assumed, that the range of q with significant statistics can be sufficiently covered by a 8 bit value. Moreover it is expected that the shape of the distributions resemble that of a Landau distribution, which, beyond the position of the MPV ($q > q_{MPV}$), gradually approaches 0 with a long tail. For $q < q_{MPV}$ the distribution is supposed to be monotonely increasing, for $q > q_{MPV}$ monotonely falling. Under all conditions it is assumed, that the normalized distributions for electrons and pions have exactly one point of intersection. For q smaller than the intersection point, $p_\pi > p_e$ and for larger values of q , $p_e > p_\pi$. These assumptions are the foundation of the model, that is used in the following.

Mean Cluster Charge Distributions

The first step is to collect entries for the reference distributions under the conditions, which will govern the later run. Since 3 p_t ranges are governed, six distributions are recorded, 2 for each p_t . The reason for that has been explained in previous sections. In short, this is related to the two possible charge signs of a track, resulting in two different deflections for the same p_t . Hence, also the tracklet length depends on the charge sign. The p_t values are chosen such, that all possible deflections that can occur within the TRD due to one charge sign, are separated from the deflections, that can occur for the other charge sign. Therefore, depending on their d_y , which is a direct measure of their charge sign (although the actual sign cannot be inferred, unless the orientation of the magnetic field is known), the tracklets can immediately be assigned to one of the two categories.

Of course, although this was not explicitly mentioned above, mean cluster charge distributions have to be recorded for electrons and pions under the given conditions. Therefore in total one has 12 reference distributions for the implementation proposed in this chapter. Recording the distributions requires knowledge about the particle identity (up to the sign; it is enough to know whether it is a $\pi^{+,-}$ or a $e^{+,-}$). Hence, either recording is done in simulation with real events where one gets the Monte Carlo information of each particle or with a real detector. Then the sample of particles, that is used, has to be known (e.g. one can use a beam of purely electrons or purely pions). From the e and π distributions, finally the likelihood is calculated (which is the topic of this section). This likelihood is stored within the LUTs in the different MCMs. These likelihoods, being the result of two distributions, were sometimes referred to as "likelihood bunches" or as "distributions".

A tracklet with mean cluster charge q makes an entry in its distribution at the corresponding bin. For the record, the bin range should cover values beyond $2^8 - 1 = 255$, e.g. from 0 to 300 (none of the entries should be rejected; the bin range might also depend on the chosen conditions, e.g. p_t , multiplicity (cluster pick-up), gain...). Later, the likelihoods are calculated for bin 0 to 255. Roughly, the total number of entries should be chosen such, that the relative abundance of each bin (also those with only few entries) does not change much any more, when acquiring more statistics.

After filling of the histogram, it must at some point be normalized by the total number of entries, to obtain the probabilities $P_\pi(q)$ and $P_e(q)$. However, normalizing immediately

means to discretize the distribution (even representing the result of the division with a float is a discretization). In the following, some issues, that should be respected when choosing the discretization granularity, are mentioned.

Likelihood Distributions

The quantity needed in the following, is the electron likelihood. It is most convenient to express it as

$$0 \leq L_e(q) = \frac{P_e(q)}{P_e(q) + P_\pi(q)} \leq 1. \quad (8.5)$$

Hence the likelihood is based on the discretized probability values. The first observation is, that in order to be consistent, the granularity for representing the probabilities should not be worse than 2^{-8} , since the likelihood values, that are calculated from them, will be given in this resolution as well (8 valid bit after the floating point). To reduce errors on the 8th likelihood bit after floating point, it would be of advantage, if the probabilities could even be given at a granularity of 2^{-9} .

When discretizing with a given granularity, the likelihood values that are obtained, do not necessarily govern the whole possible range $[0, 1 - 2^{-8}]$. Here again, one can see an argument for covering the mean cluster charge range by at least a 8 bit counter. Otherwise it would not even be possible to obtain all of the 256 possible likelihood values (for each q , possibly a different likelihood value occurs). From (8.5) it can be seen, that a value of 0 can only occur, if $P_e(q) = 0$, $P_\pi(q) \neq 0$. The value 1 on the other hand occurs, if $P_\pi(q) = 0$, yet $P_e(q) \neq 0$. Due to the shape of the distributions, this hints, that $L_e(q)$ will approach 0 most likely for small q and 1 for large q .

Values of q , which have no entry, neither for the electron distribution nor for the pion distribution, are expected to show up only on the very first bins (and possibly the last bins) but not somewhere in between, as enough statistics is supposed to be accumulated. Because for these bins the likelihood calculation would result in $\frac{0}{0}$, one has to assign to these bins a likelihood manually. If empty bins occur for low q , they are assigned $L_e = 0$, in case q is large, $L_e = 1$ can be assigned. This will not influence the likelihood distributions $L_{e \rightarrow e}$ and $L_{\pi \rightarrow e}$, since empty bins in the mean cluster charge distributions contribute no entries to the likelihood distributions. Remember that the electron likelihood distribution for incoming electrons can be obtained by calculating for each bin of q the likelihood $L_e(q)$ and add the bin content in q to the content of bin $L_{e \rightarrow e}(q)$ in the likelihood distribution histogram. For incoming pions, the electron likelihood distribution can be obtained by adding to the $L_{\pi \rightarrow e}(q)$ -bin the number of entries in bin q of the pion mean cluster charge distribution.

As it can be assumed, that there are empty early bins in the mean cluster charge distributions of electrons¹⁵, the likelihood value $L_e(q) = 0$ appears, however with perhaps no entries in the $L_{e \rightarrow e}$ distribution.

Since the likelihood distribution $L_{e \rightarrow e}(q)$ should contain most of its entries for $L_e \rightarrow 1$, it would be appropriate to ensure, that the discretization is chosen such, that for some q also $L_e(q) = 1$ appears. Because $L_e \rightarrow 1$ for large q , especially the last bins have to be taken

¹⁵or bins, whose normalized probability value becomes 0, because the granularity of the chosen discretization is not fine enough; especially the case if much statistics was accumulated

into account for choosing the granularity. The more entries have been accumulated, the more stable the probabilities become due to the statistical law of large numbers. Therefore the distribution should follow the course of a smooth Landau distribution in this case and be almost monotone falling for $q > q_{MPV}$ (of course this is highly idealistic). Moreover, $P_\pi(q) < P_e(q)$ in this regime. Then, if the discretization is chosen such, that $L_e(q = 255) = 1$, this is true also for all bins $q > 255$ ($L_e(q \geq 255) = 1$). As these bins probably have a significant number of entries, cutting on $q = 255$ without overflow would cut on the $L_e = 1$ entries in the likelihood distribution.

Therefore here it is proposed to use the original (not overflowed) number of entries in bin $q = 255$ to determine the quantization granularity (such, that $L_e(q = 255) = 1$). Then, in order to determine the likelihood distribution, the bin entries from $q > 255$ are projected into the bin $q = 255$ (overflow bin). Thus it is ensured to not lose statistics for $L_e = 1$ in the $L_{e \rightarrow e}$ likelihood distribution, which otherwise would deteriorate the determination of the separating likelihood value (cut), above which 90% of all entries are found. This again shows that it is necessary, to take into account more than 255 bins for q , when accumulating the reference distributions, especially if one wants to extract the corresponding likelihood distributions from the mean cluster charge distributions at the same time.

However, on GTU level, when tracklets are combined to tracks, it is no longer known from which distributions the likelihood values of the individual tracklets were obtained (tracklets of the same track in different layers may be assigned to different p_t 's, according to their d_y). Nevertheless the tracklet likelihoods are averaged, $L_{e,track} = \frac{1}{C} \sum_i L_i$ and upon the resulting value it is judged, whether the track was an electron or a pion ($L_{e,track} > L_{e,cut}$: electron, $L_{e,track} \leq L_{e,cut}$: pion). To obtain $L_{e,cut}$ one could think of many strategies. The easiest and fastest would be to calculate $L_{e,cut}$ for each of the electron likelihood distributions for incident electrons, as obtained from the reference mean cluster charge distributions for electrons. This yields $L_{e,cut}^k$. Taking the average, regardless of momentum and charge sign (since for the tracklets on GTU level it is not known, which p_t - and charge sign-distributions led to their likelihood values): $L_{e,cut} = \frac{1}{K} \sum_{k=1}^K L_{e,cut}^k$ (K : total number of considered likelihood distributions)¹⁶. Since d_y is part of the tracklet word, the GTU could find out, to which category of charge sign a tracklet belongs. Then the cut value $L_{e,cut}$ could be obtained by averaging only over those cut values of a layer, which belong to the category of the corresponding tracklet (this would require to precalculate the cut values due to all possible combinations and store them in a LUT. To steer the LUT, a 42 bit word would be needed, containing the up to six d_y values of tracklets, that are merged to a track). If on average the number of tracklets assigned to the different distributions, according to their d_y , is equally distributed, then averaging the individual cut values could be a feasible method.

Alternatively one could build the distribution of $L_{e \rightarrow e,track}$, where the likelihoods are given by $L_{e,track}$ (the averaged likelihoods of those tracklets, that are merged to the track) and the corresponding histogram entries are only filled, if the incident track-particle was an electron (known by Monte Carlo). The cut is chosen such, that 90% of all $L_{e \rightarrow e,track}$ histogram entries are kept on its application.¹⁷

¹⁶In the proposed implementation, each layer incorporates six reference distributions for electrons. Therefore $K = 36$ for all layers.

¹⁷It should be noted that building the likelihood distributions from the mean cluster charge distributions directly, could result in not every likelihood bin having an entry. Because there are only 255 values of

As another way to determine a cut, it would also be possible to accumulate in a test run, where the individual tracklet particle identity is known, again a mean cluster charge distribution for electrons and pions with possibly higher accuracy than a 8 bit integer range in q . Here, all tracklets contribute with their accumulated charge, distinctless of their p_t or other conditions. From these mean cluster charge distributions, the electron likelihood values could be calculated in a similar way as described above and in case of an incident electron, it is inserted into a electron likelihood distribution histogram $L_{e \rightarrow e}$. Finally, after having filled this likelihood distribution $L_{e \rightarrow e}$, the cut value is obtained (likelihood value for incident electrons, such that 90% of all entries lie above). By building the $L_{\pi \rightarrow e}$ distribution also for incident pions, one can immediately infer the corresponding pion rejection capability at the chosen cut¹⁸.

To obtain a confident measure for the actual electron efficiency on tracklet basis, one should compare the number of electrons in the tracklet sample to the number of electron tracklets, that were detected as electrons, according to the likelihood assignment in the MCM and the cut $L_{e,cut,j}$. Accordingly the corresponding pion rejection capability can be obtained (by looking at pion tracklets, that were identified as electrons in the MCM). This could be done in simulation or in an experiment, where the particle identities are known.

To obtain an overall estimate of the electron probability procedure, the electron and

q , a maximum of 255 likelihood values $L_e(q)$ can occur (probably less, because the same value of $L_e(q)$ can come up for different q ; bins $q \leq 255$ were chosen to have $L_e = 1$), corresponding to the maximum number allowed by the granularity of 2^{-8} . Hence, there might be empty bins in the $L_{e \rightarrow e}$ likelihood distribution. If there are several adjacent empty bins which would all be valid values for the likelihood cut $L_{e,cut}$ (90% of all entries above these values), then the largest of those bins should be chosen as the cut. Then it is assured, that the less possible entries in the $L_{\pi \rightarrow e}$ distribution for incident pions are considered for $L_e \geq L_{e,cut}$, which might improve the pion rejection. To obtain the theoretical pion rejection capability at 90% electron efficiency, first the electron likelihood distribution for incident pions is built from the mean cluster charge distribution for pions. Then the fraction of entries in $L_{\pi \rightarrow e}$ at $L_e \geq L_{e,cut}$ w.r.t. the total number of entries is obtained. Note that the $L_{\pi \rightarrow e}$ distribution does not necessarily have entries for $L_e = 0$ (although pions accumulate there), as this is not required in the quantization scheme (where the incident electrons were in the focus)

¹⁸In a very simplified approach, the decision, of whether a track has been released by an electron or a pion, could already be performed for each tracklet individually. This approach might be an option, if the GTU needs to be relieved. The electron likelihood cut values $L_{e,cut}^k$, as obtained from the reference likelihood distributions (hence on tracklet basis), could be stored in addition to the corresponding likelihood bunches within the LUTs of each MCM. After the likelihood has been looked up and written into the 8 bit electron probability word, the lookup address of the LUT steer word would be changed to the position of the likelihood cut, belonging to the used likelihood bunch. The 8 bit likelihood value in the electron probability word is compared to the cut value. In case, the decision is "pion", the 8 bit word is overwritten by 0, in case of "electron" by 1. This decision D^i ($D^i \in \{0,1\}$) is sent to the GTU. The GTU then only has to decide upon a maximum of 6 binary values D^0, \dots, D^5 of the merged tracklets, whether the track is to be considered as electron or as pion. E.g., if C tracklets are involved, then the decision "electron track" could be made, if more than $\lceil \frac{C}{2} \rceil$ tracklets are found with 1, hence if $\sum_{i=1}^C D^i \geq \lceil \frac{C}{2} \rceil$.

If the electron likelihood distributions for incoming electrons are built for each of the reference mean cluster charge distributions, for each of those the electron likelihood cut value $L_{e,cut}^k$ can be deduced. The next consequent step would then be, to not store the likelihood values in the LUTs of the MCMs, but directly 0 or 1 (0, if $L_e^k < L_{e,cut}^k$, 1 if $L_e^k \geq L_{e,cut}^k$) instead. Then, by looking up the entry, that belongs to the tracklet parameters d_y and q (by which the LUT is steered), the decision "electron tracklet" or "pion tracklet" can be obtained without the additional comparison of the likelihood value with the likelihood cut. In this way, one comparison can be saved for each tracklet.

pion efficiencies should be obtained on track basis. Then, the detected particle identity of the reconstructed track is compared to the real particle identity. Here, the inefficiencies of the MCM likelihood assignment, of the GTU combination of the individual likelihoods, of the likelihood cut estimate as well as the inefficiency of the track reconstruction enter (if a track is combined of wrong tracklets, a confident decision of the particle identity cannot be expected; also the corresponding Monte Carlo track might not be found then).

Quantization

Finally, the quantization shall be discussed more quantitatively. As it was mentioned above, the granularity should be 2^{-8} or better. Here, only bin $q = 255$ is considered and it is assumed, that at least for the electron mean cluster charge distribution, there is an entry. If not, then, according to the model, upon which these discussions are based, also the pion mean cluster charge distribution has no entry at $q = 255$ ($P_\pi(q = 255) < P_e(q = 255)$) and $L_e(q = 255) = 1$ is assigned "manually". Otherwise the quantization is chosen such, that due to the quantized probabilities, $L_e(q = 255) = 1$. It is convenient to use the following form for the likelihood:

$$0 \leq L_e(q) = \frac{1}{1 + \frac{P_\pi(q)}{P_e(q)}} \leq 1.$$

By "relative weight" (r.w.) of bin $q = 255$, the float value of

$$r.w. = \frac{\text{number of entries in bin } q=255}{\text{total number of entries in the histogram}}$$

will be denoted. Thus, $r.w.$ tries to approach a non discretized version of the probability $P(q)$ (exploiting, that the granularity of a float is much better than 2^{-8}). Then, according to the value of $r.w.$, the following cases can occur:

1. $r.w.(\pi) < 2^{-b} \wedge r.w.(e) \geq 2^{-b}$ for $b \geq 8$.

Then choose the granularity 2^{-b} for the maximum value of b , for which the conditions can be fulfilled. It follows: $P_\pi(q = 255) = 0$, $P_e(q = 255) \neq 0$ and therefore $L_e(q = 255) = 1$.

2. $2^{-(b+1)} \leq r.w.(\pi) < r.w.(e) < 2^{-b}$ for a $b \geq 8$.

Then $r.w.(e) - r.w.(\pi) = \delta < 2^{-(b+1)}$. Choose a $r > b + 1 \geq 9$ with $2^{-r} < \delta$. Then a smallest M exists, for which $r.w.(\pi) \leq M \cdot 2^{-r} < r.w.(\pi) + \delta = r.w.(e)$. Of course the choice of M depends on r . Generally the smallest choosable M increases with increasing r . For this M and r one obtains: $\frac{r.w.\pi}{M} \leq 2^{-r} < \frac{r.w.(e)}{M}$. Note that $M \neq 2^n, n \in \mathbb{N}$ as otherwise $2^{-(b+1+n)} \leq \frac{r.w.(\pi)}{M} < \frac{r.w.(e)}{M} < 2^{-(b+n)}$ and the problem would remain. In the continuous case, dividing the probabilities of both distributions by an additional factor M does not change the likelihood values. This is exploited here. Before quantizing, calculate the float values of $\frac{r.w.(\pi)}{M}$ and $\frac{r.w.(e)}{M}$. Then discretize with a granularity of 2^{-r} . In order to be consequent, all probability entries have to be divided by M before quantizing them. In the continuous case, dividing or not would make no difference for the likelihood. In the discrete case, dividing before discretizing can mean changing the likelihood value (an entry in the mean cluster charge distribution possibly becomes 0 under quantization. This has exactly happened for bin $q = 255$).

By dividing the probabilities by M , accuracy is lost very fast, because the scaled probabilities approach the granularity border very fast. Hence, for consistency, all float values of both distributions have to be divided by M before quantizing and calculating the likelihood, because the division changes the fraction of the quantized probabilities at given q and therefore the likelihood. The value of M should be kept as low as possible (meaning r to be kept as small as possible, on cost of resolution).

3. $r.w.(\pi) > 2^{-b} \wedge r.w.(e) > 2^{-b} \forall b \geq 8$.

Then, in order to obtain a likelihood $L_e(q = 255) = 1$ at a granularity of at least 2^{-8} , one has no other choice but dividing by gradually increasing numbers $M > 1, M \in \mathbb{N}$, until case 1 or case 2 occur. By this, M is automatically chosen as small as possible, which is necessary due to the reasons listed in case 2.

It was assumed, that $q_{MPV} < 255$ for electrons and pions and that at bin $q = 255$ the number of entries in the pion distribution is smaller than in the electron distribution ($r.w.(\pi) < r.w.(e)$), because otherwise $L_e(q = 255) = 1$ cannot be reached. If $r.w.(\pi) \geq r.w.(e)$ should occur despite its low probability, one can simply choose a granularity of 2^{-8} .

8.4 Recipe for an Electron Probability

This section is a short summary of this chapter, revising again the most important ingredients on the way to an electron probability measure under the technical constraints.

Configuration

- Define the run conditions.
- Define the three p_t ranges.
- Accumulate the reference distributions for electrons and pions of defined track length (defined incident angle w.r.t. chamber normal) in a simulation or during a (test) run with at least 255 entries (8 bit).
- After normalizing the distributions, quantize them and calculate the likelihoods.
- Merge the tracklets to tracks and calculate the final track likelihood distributions, e.g. based on the averaged likelihood $L_{e,track} = \frac{1}{C} \sum_i L_e^i$ (L_e^i : tracklet likelihood).
- Store the likelihoods in the LUTs of the different MCMs, respecting the tracklet length correction.
- Define for each MCM which tracklet deflection d_y is assigned to which bunch of likelihoods and store the corresponding addresses also in the LUT.

¹⁹As an example, imagine two float numbers, $a_f = 0.40$ and $b_f = 0.0625$. In 2^{-8} representation: $0.40 \rightarrow a_2 = 2^{-2} + 2^{-3} + 2^{-6} + 2^{-7}$, $0.0625 \rightarrow b_2 = 2^{-4}$. If a_f and b_f are divided by 9, one obtains: $\tilde{a}_f = 0.0\bar{4} \rightarrow \tilde{a}_2 = 2^{-5} + 2^{-7} + 2^{-8}$ and $\tilde{b}_f = 6.9\bar{4} \cdot 10^{-3} \rightarrow \tilde{b}_2 = 2^{-8}$. It is $\frac{a_f}{b_f} = 6.4 \approx \frac{\tilde{a}_f}{\tilde{b}_f}$ but $\frac{\tilde{a}_2}{\tilde{b}_2} = 2^2 + 2^1 + 2^{-1} + 2^{-2} = 6.75 \neq \frac{\tilde{a}_2}{\tilde{b}_2} = 2^3 + 2^1 + 2^0 = 11$.

- Define the likelihood cut $L_{e,cut}$ from the distribution of the final electron likelihood for incident electrons on track level, $L_{e \rightarrow e, track}$ and tell the GTU.

Run

- For each tracklet accumulate Q and N.
- Get d_y from the tracklet.
- Feed the LUT with d_y and get the address of the likelihood bunch.
- Together with the address and the mean cluster charge (discretized into 8 bit), feed the LUT and look up the electron likelihood (8 bit, granularity 2^{-8}) at position q .
- Use that likelihood as the 8 bit electron probability.
- GTU: Combine likelihoods from tracklets that were assigned to a track, to the track likelihood, e.g. by averaging: $L_{e, track} = \frac{1}{C} \sum_i L_e^i$.
- GTU: Depending on $L_{e, track}$ make decision if electron ($L_{e, track} > L_{e, cut}$) or pion ($L_{e, track} \leq L_{e, cut}$). Possibly remove ion samples.

The efficiency of this electron probability measure can be estimated by investigating the pion rejection factor at 90% electron efficiency. As the presented algorithm has to fit into technical conditions and should not increase the overall calculation time of the trigger, surely a rejection factor of 100, as suggested in the Technical Design Report, will by far not be reached. At all, the suggested proceeding should be understood more as an idea than a serious proposal.

Summary and Conclusions

The Transition Radiation Detector (TRD) of the heavy ion experiment ALICE at LHC (CERN) is embedded into the ALICE trigger system. An important part of the TRD trigger calculation is based on a local linear fit (tracklet) to the trajectory of an incident particle track. The calculations are performed during data acquisition by the Tracklet Processing (TRAP) chips, which are integrated on the detector. Due to the segmentation of the TRD into six layers, up to six tracklets are produced from one track in parallel. Each tracklet contains information about its position and the slope, which is used as a measure for the transverse momentum p_t . The tracklets are merged to a track by the Global Tracking Unit (GTU). The goal of the trigger is to detect electrons with large transverse momenta.

In order to understand the results and inaccuracies of the tracklet calculation, it is of importance to have in view the signal processing path. Therefore, the whole way from the signal creation to digitization is described within this diploma thesis. If a charged particle traverses the active area of the detector, it deposits energy by ionization, leading to the formation of electron clusters. In the applied homogeneous electric drift field, these clusters travel to an anode wire grid, where they are amplified in an avalanche process. During drift, several effects can occur, which may have an effect on the finally measured signal, e.g. diffusion, recombination, distortions of the electric drift field, distortions of the gas gain due to space charge, etc.

The amplified charge is then processed by the detector electronics. First, the charge signal is shaped and turned into a voltage by the PASA. Then the signal is sampled. The subsequent Analog Digital Converters (ADCs) digitize the signal. Digital filters try to reduce the influence of disturbing effects or correlations. The slow ion drift, for example, leads to a correlation between the sampled signals in adjacent time bins. The tail cancellation filter tries to reduce this correlation by approaching the tail with an exponentially decaying function. All the electrical processing takes place in parallel to the drift of the electron clusters.

The signal that comes out of the filter stage is then used for tracklet calculation. The algorithm of obtaining relevant fit points from the track and the subsequent linear fitting are described as well as the deduction of the desired parameters offset and deflection. The complete tracklet calculation was integrated into the detector simulation framework AliRoot, with special emphasis on a close-to-electronics implementation.

There are two main sources of distortions, influencing the offset and deflection: The Lorentz angle of the drift and the tilted pads. In an ideal implementation, the deflection can be corrected for both effects whereas the offset does not need Lorentz correction, since it is situated on the exit of the drift volume. Due to the conditions in the simulation, where the sampling also covers the amplification region, this is no more true. Although the radial position of the offset is not precisely known, a Lorentz correction can at least improve the shift, introduced on the offset performance distributions. It was shown, that for the width of these distributions, mainly the non-correctable tilted pads influence is to blame.

A selection of results obtained from comparing the tracklets with the corresponding Monte Carlo tracks was discussed. For these comparisons a macro has been developed. It showed up, that most of the distortions on tracklet level can be understood, yet many of them cannot be corrected for. Nevertheless, the accuracy will be sufficient to provide a reliable trigger on high- p_t electrons. Some efficiencies of the tracklet cut, aimed to select $p_t \geq 2.3\text{GeV}/c$ electrons, have been evaluated. Depending on multiplicity, the number of good electron tracks, that can be reconstructed by the GTU, drops to 50% in the worst case. Since the GTU will only reconstruct a track, if it finds more than four tracklets to be assigned to the track and based on the assumption, that a usual high- p_t track produces a tracklet in each of the layers, this means, that at large multiplicities, the tracklet cut removes in 50% of the cases more than two good tracklets from the sample.

Finally, issues concerning the implementation of an electron-pion separation method on TRAP basis, are discussed. Since the GTU has tough timing restrictions, most of the calculations should be done on the Local Tracking Unit (LTU). The method will probably be based on a 1D likelihood approach, using the mean cluster charge of a tracklet. Since only 8 bit are available to encode the electron probability, it is convenient to encode the tracklet likelihood directly. In order to obtain the likelihood, reference distributions must be recorded, which are then scaled by a factor, depending on the tracklet length, which varies with the position of a MCM. Since the deflection d_y is the only applicable measure for p_t and charge sign, the p_t values, for which the reference distributions are recorded, should be chosen such, that the assignment of d_y to p_t and to a charge sign is as unique as possible. The problem is, that on each TRAP only one LUT is available to store the scaled distributions. However, d_y is given in pad width granularity. Therefore, a given value of p_t creates a range of 18 different d_y values for each charge sign on one MCM. By choosing three p_t values for the reference distributions, which fulfill some restrictions, it is possible, to infer from a given d_y at least the charge sign category (the actual sign is unknown, unless the magnetic field direction is taken into account) and to make sure, that for the assignment there is an ambiguity between a maximum of two p_t values.

Since the trigger is supposed to select high- p_t electrons from a large pion background, its functionality crucially depends on the implementation of an electron probability measure.

A Appendix

A.1 Kinematics

For reference see [Kra06]. Throughout this section $\hbar = c = 1$. Therefore all velocities are given as fraction of the light speed and are smaller than 1: $v \leq 1$.

A.1.1 Collision and Decay

Collision

Imagine two particles A and B colliding. Their 4-vectors before the collision are denoted by $P_A = \begin{pmatrix} E_A \\ \vec{p}_A \end{pmatrix}$ and $P_B = \begin{pmatrix} E_B \\ \vec{p}_B \end{pmatrix}$. P'_A and P'_B are the corresponding 4-vectors after the collision. Let further $P' = \begin{pmatrix} E' \\ \vec{p}' \end{pmatrix}$ denote the 4-vector belonging to the center of mass system after the collision ($\vec{p}' = 0$). Due to 4-vector conservation it follows

$$P_A + P_B = P'_A + P'_B.$$

Due to Lorentz invariance of 4-vector inner products:

$$(P'_A + P'_B)^2 = P'^2.$$

Therefore

$$\begin{aligned} (P_A + P_B)^2 &= E'^2 \\ (E_A + E_B)^2 - (\vec{p}_A + \vec{p}_B)^2 &= E'^2. \end{aligned}$$

- Fixed targeted experiment, $P_B = \begin{pmatrix} m_B \\ 0 \end{pmatrix}$ ($\vec{p}_B = 0$). Then

$$\begin{aligned} (E_A + m_B)^2 - (\vec{p}_A)^2 &= E'^2 \\ m_A^2 + m_B^2 + 2E_A m_B &= E'^2. \end{aligned}$$

For $m_A, m_B \ll E_A$ (thus $E_A \approx |\vec{p}_A|$) it follows:

$$\begin{aligned} E' &\approx \sqrt{2E_A m_B} \\ E' &\approx \sqrt{2|\vec{p}_A| m_B}. \end{aligned}$$

The center of mass energy increases with the square root of the particle energy E_A .

- Collider experiment, $\vec{p}_A = -\vec{p}_B$. For $m_A = m_B$, this yields

$$E' = 2E_A.$$

The center of mass energy increases proportional to the energy of the colliding particles E_A .

Decay

Imagine a two body decay. Suppose the 4-vector of the mother particle given by $P = \begin{pmatrix} E \\ \vec{p} \end{pmatrix}$, and the 4-vectors of the daughter particles A and B by $P_A = \begin{pmatrix} E_A \\ \vec{p}_A \end{pmatrix}$ and $P_B = \begin{pmatrix} E_B \\ \vec{p}_B \end{pmatrix}$. Due to 4-vector conservation

$$P^2 = (P_A + P_B)^2.$$

Hence, the invariant mass of the mother particle can be obtained from the kinematical quantities of the daughter particles:

$$m = \sqrt{(E_A + E_B)^2 - (\vec{p}_A + \vec{p}_B)^2}.$$

A.1.2 Observables

In chapter 1 it was mentioned, that the transverse energy distribution of the daughter particles emerging from a collision contains information about quantities of the reaction, like for example the energy density. The transverse energy E_t of a particle with rest mass m_0 is defined accordingly to the total energy $E = \sqrt{\vec{p}^2 + m_0^2}$:

$$E_t = \sqrt{p_t^2 + m_0^2}.$$

If two particles collide at $(0, 0, 0)$ (position of the primary vertex), in a local coordinate system one usually lies the z axis tangentially to the beam line through $(0, 0, 0)$ ¹. In this coordinate frame, the momenta of the two colliding particles have but a p_z -component at the instance of collision. After collision, the daughter particles have gained transverse momentum p_t , which is defined by

$$p_t = \sqrt{p_x^2 + p_y^2}.$$

Hence,

$$E^2 = E_t^2 + p_t^2.$$

If a particle of rest mass m_0 moves with the velocity $\vec{v} = (v_x, v_y, v_z)$ ($\beta = |\vec{v}|$) w.r.t. an observer, its rapidity y is defined by

$$\begin{aligned} y &= \frac{1}{2} \ln\left(\frac{E + p_z}{E - p_z}\right) \\ &= \frac{1}{2} \ln\left(\frac{1 + v_z}{1 - v_z}\right). \end{aligned}$$

If $v_z = 0$, also $y = 0$ and y increases with v_z ($y \rightarrow \infty$ for $v_z \rightarrow 1$). Thus, the rapidity is a measure for the longitudinal velocity. It responds linearly to a Lorentz transformation. Here, just a boost in z-direction is considered:

$$\begin{pmatrix} E' \\ p'_z \end{pmatrix} = \begin{pmatrix} \gamma' & -\beta'\gamma' \\ -\beta'\gamma' & \gamma' \end{pmatrix} \cdot \begin{pmatrix} E \\ p_z \end{pmatrix}$$

¹Due to the large radius of the LHC collider ring as compared to the dimensions of the TRD experiment, it is justified to say, that the z-axis locally runs parallel to the beam line.

Therefore

$$\frac{E' + p'_z}{E' - p'_z} = \frac{1 - \beta' E + p_z}{1 + \beta' E - p_z}.$$

This yields for the rapidity after Lorentz transformation, y' :

$$\begin{aligned} y' &= \frac{1}{2} \ln\left(\frac{1 - \beta' E + p_z}{1 + \beta' E - p_z}\right) \\ &= \frac{1}{2} \ln\left(\frac{1 - \beta'}{1 + \beta'}\right) + \frac{1}{2} \ln\left(\frac{E + p_z}{E - p_z}\right) \\ &= y + \frac{1}{2} \ln\left(\frac{1 - \beta'}{1 + \beta'}\right). \end{aligned}$$

This means, that a rapidity distribution of particles is shifted by the constant value $\frac{1}{2} \ln\left(\frac{1 - \beta'}{1 + \beta'}\right)$ after a Lorentz transformation.

Because E often is unknown (e.g. because the particle specie and hence m_0 is unknown) but the momentum might be easier to determine (bending radius of a charged particle in a magnetic field), an additional quantity, the pseudorapidity η , is introduced. It is defined by

$$\eta = \frac{1}{2} \ln\left(\frac{|\vec{p}| + p_z}{|\vec{p}| - p_z}\right).$$

For large $|\vec{p}|$ ($m_0 \ll |\vec{p}|$), the rapidity y approaches the pseudorapidity η . If θ denotes the angle w.r.t.the z-axis, one can write

$$\tan \theta = \frac{p_t}{p_z} = \frac{\sqrt{p^2 - p_z^2}}{p_z}.$$

Since $\tan\left(\frac{\theta}{2}\right) = \frac{-1 + \sqrt{1 + \tan^2 \theta}}{\tan \theta}$, it follows:

$$\begin{aligned} \tan \frac{\theta}{2} &= \sqrt{\frac{|\vec{p}| - p_z}{|\vec{p}| + p_z}} \\ &= \left(\frac{|\vec{p}| + p_z}{|\vec{p}| - p_z}\right)^{-\frac{1}{2}}. \end{aligned}$$

Therefore

$$\eta = -\ln\left(\tan\left(\frac{\theta}{2}\right)\right).$$

In the following, $\cosh y = \frac{e^y + e^{-y}}{2}$ and $\sinh y = \frac{e^y - e^{-y}}{2}$ are used. Inserting y yields

$$\begin{aligned} \cosh y &= \frac{1}{2} \left(e^{\frac{1}{2} \ln\left(\frac{E+p_z}{E-p_z}\right)} + e^{-\frac{1}{2} \ln\left(\frac{E+p_z}{E-p_z}\right)} \right) \\ &= \frac{1}{2} \left(\sqrt{\frac{E+p_z}{E-p_z}} + \sqrt{\frac{E-p_z}{E+p_z}} \right) \\ &= \frac{E}{\sqrt{E^2 - p_z^2}} \\ &= \frac{E}{E_t}. \end{aligned}$$

Accordingly

$$\begin{aligned}
 \sinh y &= \frac{1}{2} \left(e^{\frac{1}{2} \ln \left(\frac{E+p_z}{E-p_z} \right)} - e^{-\frac{1}{2} \ln \left(\frac{E+p_z}{E-p_z} \right)} \right) \\
 &= \frac{1}{2} \left(\sqrt{\frac{E+p_z}{E-p_z}} - \sqrt{\frac{E-p_z}{E+p_z}} \right) \\
 &= \frac{p_z}{\sqrt{E^2 - p_z^2}} \\
 &= \frac{p_z}{E_t}.
 \end{aligned}$$

It follows,

$$\begin{aligned}
 E &= E_t \cosh y, \\
 p_z &= E_t \sinh y.
 \end{aligned}$$

If the rest mass m_0 of a particle is known (or negligibly small as compared to $|\vec{p}|$), one needs at least two momentum components and the energy of all three momentum components to describe its kinematics: (m_0, p_i, p_j, E) or (m_0, \vec{p}) ($i \neq j$). Alternatively, the kinematics can be described by another set of observables: (m_0, y, p_t, ϕ) . ϕ is the azimuthal angle and is defined as

$$\phi = \arctan \frac{p_y}{p_x}.$$

Invariant Mass, Expressed in Different Observables

The invariant mass

$$m = \sqrt{(E_A + E_B)^2 - (\vec{p}_A + \vec{p}_B)^2}$$

can also be expressed in the new set of observables (m_0, y, p_t, ϕ) . First, one can rewrite m as

$$m = \sqrt{m_A^2 + m_B^2 + 2E_A E_B - 2(p_{x,AP_{x,B}} + p_{y,AP_{y,B}} + p_{z,AP_{z,B}})},$$

where $E^2 - \vec{p}^2 = m^2$ was used. Now, $2E_A E_B = 2E_{t,A} E_{t,B} \cosh y_A \cosh y_B$. Since $\cosh x \cdot \cosh y = \frac{1}{2}(\cosh(x+y) + \cosh(x-y))$, this yields

$$2E_A E_B = E_{t,A} E_{t,B} (\cosh(y_A + y_B) + \cosh(y_A - y_B)).$$

Also, $p_{z,AP_{z,B}} = E_{t,A} E_{t,B} \sinh y_A \sinh y_B$. Because $\sinh x \cdot \sinh y = \frac{1}{2}(\cosh(x+y) - \cosh(x-y))$, it follows

$$2p_{z,AP_{z,B}} = E_{t,A} E_{t,B} (\cosh(y_A + y_B) - \cosh(y_A - y_B)).$$

Therefore

$$2E_A E_B - 2p_{z,AP_{z,B}} = 2E_{t,A} E_{t,B} (\cosh(y_A - y_B)).$$

Next, $p_t^2 = p_x^2 + p_y^2$ and $p_y^2 = p_x^2 \tan^2 \phi$. This yields $p_x^2 = \frac{p_t^2}{1 + \tan^2 \phi}$ and hence $p_x = p_t \cos \phi$. For p_y one obtains $p_y = p_t \sin \phi$. This yields

$$\begin{aligned}
 2p_{x,AP_{x,B}} + 2p_{y,AP_{y,B}} &= 2p_{t,AP_{t,B}} (\cos \phi_A \cos \phi_B + \sin \phi_A \sin \phi_B) \\
 &= 2p_{t,AP_{t,B}} (\cos(\phi_A - \phi_B)),
 \end{aligned}$$

because of the trigonometrical addition theorems. Putting everything together, one obtains

$$m = \sqrt{m_A^2 + m_B^2 + 2E_{t,A}E_{t,B}(\cosh(y_A - y_B)) - 2p_{t,A}p_{t,B}(\cos(\phi_A - \phi_B))}.$$

Denoting $\Delta y = y_A - y_B$ and $\Delta\phi = \phi_A - \phi_B$ and assuming $m_A \ll |\vec{p}_A|$, $m_B \ll |\vec{p}_B|$, one can neglect the mass terms $m_A^2 + m_B^2$ and $E_{t,A} \approx p_{t,A}$, $E_{t,B} \approx p_{t,B}$. Moreover, y can be approached by η , $\Delta y \approx \Delta\eta$. This finally yields

$$m \approx \sqrt{2p_{t,A}p_{t,B}[\cosh(\Delta\eta) - \cos(\Delta\phi)]}.$$

A.2 The Maximum Energy Transfer to a Scattered Electron

In this discussion c and \hbar are set to 1.

A charged particle of mass M is assumed to scatter against an electron with mass m_e being originally at rest. Assume that the 4-vectors before the scattering of the incident particle and the electron are $P = \begin{pmatrix} E \\ \vec{p} \end{pmatrix}$ and $p = \begin{pmatrix} m_e \\ 0 \end{pmatrix}$, respectively. After the scattering the 4-vectors are given by $P' = \begin{pmatrix} E+m_e-E' \\ \vec{p}-\vec{p}' \end{pmatrix}$ and $p' = \begin{pmatrix} E' \\ \vec{p}' \end{pmatrix}$ where energy and momentum conservation were already exploited. Using 4-vector conservation $(P+p)^2 = (P'+p')^2$ and the Lorentz invariance of the inner product (resulting in $P^2 = P'^2 = M^2$ and $p^2 = p'^2 = m_e^2$) one obtains

$$P \cdot p = P' \cdot p'.$$

Evaluating this yields:

$$\begin{aligned} Em_e &= (E - E')E' + m_e E' - (\vec{p} - \vec{p}')\vec{p}' \\ 0 &= (E - E')E' + m_e(E' - E) - \vec{p}\vec{p}' + p'^2 \\ 0 &= (E - E')(E' - m_e) - \vec{p}\vec{p}' + E'^2 - m_e^2. \end{aligned}$$

Here it was used that $E'^2 = \vec{p}'^2 + m_e^2$. In the following p^2 or p'^2 denotes the squared 3-momentum. Writing $E'^2 - m_e^2 = (E' - m_e)(E' + m_e)$ and introducing the angle θ between the direction of the incident particle before scattering and the electron after scattering with $\vec{p} \cdot \vec{p}' = pp' \cos \theta$ one can further calculate

$$\begin{aligned} 0 &= (E' - m_e)(E + m_e) - pp' \cos \theta \\ p^2(E' - m_e)(E' + m_e) \cos^2 \theta &= (E' - m_e)^2(E + m_e)^2 \\ p^2 \cos^2 \theta(E' + m_e) &= (E' - m_e)(E + m_e)^2. \end{aligned}$$

Solving this for E' yields:

$$E' = \frac{m_e((E + m_e)^2 + p^2 \cos^2 \theta)}{(E + m_e)^2 - p^2 \cos^2 \theta}.$$

Obviously E' becomes maximal if $\cos^2 \theta = 1$. Thus

$$E'_{max} = \frac{m_e((E + m_e)^2 + p^2)}{(E + m_e)^2 - p^2}.$$

If the energy of the particle is much larger than the rest energy of the electron, $E \gg m_e$ this can be simplified to

$$E'_{max} \approx \frac{m_e(E^2 + p^2)}{E^2 - p^2}$$

$$E'_{max} \approx \frac{m_e(E^2 + p^2)}{M^2}$$

where $E^2 = p^2 + M^2$ was inserted. So the maximum energy transfer to the electron $\Delta E'_{max} = E'_{max} - m_e$ is given by

$$\Delta E'_{max} = \frac{m_e(E^2 + p^2 - M^2)}{M^2}$$

$$\Delta E'_{max} = \frac{2m_e p^2}{M^2}$$

$$\Delta E'_{max} = 2m_e \beta^2 \gamma^2$$

with $\beta\gamma = \frac{p}{M}$.

A.3 Sum of Two Poisson Distributed Variables

For reference see [Naw94]. Assume $\zeta_1 \geq 0$ and $\zeta_2 \geq 0$ Poisson distributed variables with

$$P_{\lambda_1}(\zeta_1 = m) = \frac{\lambda_1^m}{m!} e^{-\lambda_1}$$

$$P_{\lambda_2}(\zeta_2 = m) = \frac{\lambda_2^m}{m!} e^{-\lambda_2}.$$

$P(\zeta_1 + \zeta_2 = m)$ is given by the convolution of P_{λ_1} with P_{λ_2} . Using

$$(\lambda_1 + \lambda_2)^m = \sum_{k=0}^m \binom{m}{k} \cdot \lambda_1^k \lambda_2^{m-k}$$

and

$$\binom{m}{k} = \frac{m!}{k!(m-k)!}.$$

one obtains:

$$P(\zeta_1 + \zeta_2 = m) = \sum_{k=0}^m \frac{\lambda_1^{m-k}}{(m-k)!} e^{-\lambda_1} \cdot \frac{\lambda_2^k}{k!} e^{-\lambda_2}$$

$$= \frac{(\lambda_1 + \lambda_2)^m}{m!} e^{-(\lambda_1 + \lambda_2)}$$

which is a Poisson distribution with mean $\lambda_1 + \lambda_2$.

A.4 How the Kinematics Tree is built

Because the way the kinematics tree is built caused some confusion in the beginning, it shall be explained by a simple example. The principle is that for each particle, that is currently transported through the detector system and which decays or produces other particles, e.g. delta electrons, first all its daughter particles are transported. Only after all the daughter particles have been transported, a particle is assigned a track number. Thus, the kinematics tree is built recursively.

For each primary particle an own tree can be built. Let each particle be represented by a node. The root of the tree in level 0 is defined by one of the primary particles (from the primary vertex). Its direct daughters have their nodes in level 1, etc. The algorithm for assigning a track number to the particles can be described as follows, starting from an arbitrary particle on level m :

- Get all the direct daughters of the particle (delta electrons, Bremsstrahlungs photons, decay products,...) in the order of their production (maybe first a delta electron is produced, before a particle decays; order of decay products is arbitrary).
- Take the daughter produced first and build a node for it on level $m + 1$.
- Get all the daughters from this node.
 - In case there are no more daughters, name the node by the current track label counter. Increase the counter by 1. Go to the mother node on level m and replay the algorithm for the next daughter.
 - Otherwise take the daughter produced first and replay the whole algorithm for the next level (replacing m by $m + 1$, $m + 1$ by $m + 2$).

For each node, one can assign a first daughter and a last daughter track label, defined by the range of track labels, that are assigned to the daughter nodes in higher levels. The first-last daughter ranges are always continuous (without a track label missing in between). The primary particles, which are not daughters of any particles, are only assigned a track label, after they all have been transported. Thus, the largest track labels belong to primaries.

In the picture A.1, a tree with assigned track labels is shown for the case, that each particle has exactly two daughters (e.g. a two-particle decay).

A.5 Two-Complement Representation

Since it is not possible to store negative binary numbers, a representation has to be chosen, which assigns a negative value to a certain range of positive values. In the two-complement representation, the highest bit is treated as sign-bit. For a k bit number, the representation is given by

$$a_{k-1} \cdot 2^{k-1} | a_{k-2} \cdot 2^{k-2} | a_{k-3} \cdot 2^{k-3} | \dots | a_1 \cdot 2^1 | a_0 \cdot 2^0$$

with $a_i \in \{0, 1\}$. $a_{k-1} = 0$ denotes a non-negative value, $a_{k-1} = 1$ denotes a negative value. Given the representation, the signed value b is obtained by

$$b = -a_{k-1} \cdot 2^{k-1} + a_{k-2} \cdot 2^{k-2} + \dots + a_1 \cdot 2^1 + a_0,$$

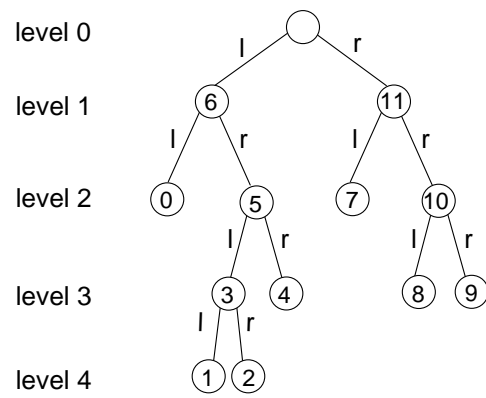


Figure A.1: Kinematics tree for two-particle decays and for one primary particle

hence the largest bit is signed. This definition leads to an asymmetric range:

$$b \in [-2^{k-1}, 2^{k-1} - 1].$$

Note, that $b = 0$ is treated as positive value, since then $a_i = 0 \forall i$, especially $a_{k-1} = 0$.

Quantitatively speaking, b is assigned to another bit number c according to the following definition:

$$\begin{aligned} b &\mapsto c \\ b &= -a_{k-1} \cdot 2^{k-1} + a_{k-2} \cdot 2^{k-2} + \dots + a_1 \cdot 2^1 + a_0 \\ c &= a_{k-1} \cdot 2^{k-1} + a_{k-2} \cdot 2^{k-2} + \dots + a_1 \cdot 2^1 + a_0. \end{aligned}$$

Therefore, $c \in [0, 2^k - 1]$. If $b < 0$, hence $a_{k-1} = 1$, $c = b + 2^k$. For $b \geq 0$ ($a_{k-1} = 0$): $c = b$. In this sense,

$$b = c \pmod{2^k}.$$

From a given value b one obtains $-b$ by inverting all bits and adding 1, $-b = \bar{b} + 1$: For

$$b = -a_{k-1} \cdot 2^{k-1} + a_{k-2} \cdot 2^{k-2} + \dots + a_1 \cdot 2^1 + a_0$$

inverting yields:

$$\begin{aligned} \bar{b} &= -\bar{a}_{k-1} \cdot 2^{k-1} + \bar{a}_{k-2} \cdot 2^{k-2} + \dots + \bar{a}_1 \cdot 2^1 + \bar{a}_0 \\ &= -2^{k-1}(1 - a_{k-1}) + 2^{k-2}(1 - a_{k-2}) + \dots + 2(1 - a_1) + (1 - a_0) \\ &= -2^{k-1} + (2^{k-1} - 1) - b \\ &= -b - 1. \end{aligned}$$

Therefore, adding 1 yields $\bar{b} + 1 = -b$.

For more details about binary numbers, see for example [RP02].

Acknowledgment

Representative for many people to whom I am indebted, I would like to express my gratitude to Prof. Dr. Johanna Stachel for providing me with this interesting topic and to Dr. Ken Oyama for his valuable support. I also would like to thank Dr. Kai Schweda for his critical reading.

Moreover I would like to thank my family for encouraging me throughout my study. I am grateful to my coinhabitant for all the motivating conversations.

Contents of the CD

The CD contains the `AliTRDmcmSim` class, of which the `Tracklet()` method was implemented as the tracklet simulator. The class `AliTRDtrapAlu`, which was developed to treat bit-like numbers, is added, as well as the macro for the performance evaluation, `TrackletReader.C`. Finally, also the PDF version of the diploma thesis is appended.

Bibliography

- [ALI01] ALICE Collaboration: *ALICE Technical Design Report of the Transition Radiation Detector*, 2001.
- [ALI04] ALICE Collaboration: *ALICE: Physics Performance Report, Volume I*, 2004.
- [ALI06] ALICE Collaboration: *ALICE: Physics Performance Report, Volume II*, 2006.
- [ALI08] ALICE Collaboration: *ALICE Experiment at the CERN LHC, Technical Paper I*, 2008.
- [And] Andronic, Anton: *The alice transition radiation detector*. <http://www.alice.gsi.de/TRD>. presentation.
- [BMW07] Braun-Munzinger, P. and J. Wambach: *The phase diagram of strongly-interacting matter*. International Journal of Modern Physics E, Volume 16, Issue 03, part1, pp.867-878, 2007.
- [Dan] Dankert, J.: *C++ fuer C Programmierer*. <http://www.fh-hamburg.de/rzbt/dankert>.
- [dC03] Cuveland, Jan de: *Entwicklung der globalen Spurrekonstruktionseinheit für den ALICE-Übergangsstrahlungsdetektor am LHC (CERN)*, 2003. Ruprecht-Karls-Universitaet Heidelberg, Fakultaeet fuer Physik und Astronomie.
- [Dem99] Demtroeder, Wolfgang: *Experimentalphysik2*. Springer, 2. Auflage, 1999.
- [Ems06] Emschermann, David: *The TRD numbering convention*. <http://www.physi.uni-heidelberg.de/~demscher/alice/numbering/more>, 2006.
- [Ene03] *Energy loss of pions and electrons of 1 – 6GeV/c in drift chambers operated with Xe, CO₂(15%)*. www.sciencedirect.com, 2003.
- [FHV05] Ferreira, Ix B García, J Garía Herrera und L Villasenor: *The Drift Chambers Handbook, introductory laboratory course*. <http://www.iop.org/EJ/abstract/1742-6596/18/1/010>, 2005. Journal of Physics: Conference Series.
- [Gut02] Gutfleisch, Marcus: *Digitales Frontend und Preprozessor im TRAP1-Chip des TRD-Triggers fuer das ALICE-Experiment am LHC(CERN)*, 2002. Ruprecht-Karls-Universitaet Heidelberg, Fakultaeet fuer Physik und Astronomie.
- [Gut06] Gutfleisch, Marcus: *Local Signal Processing of the ALICE Transition Radiation Detector at LHC (CERN)*. PhD thesis, Ruprecht-Karls-Universitaet Heidelberg, Fakultaeet fuer Physik und Astronomie, 2006.

- [Hun04] Hunklinger, Siegfried: *Festkoerperphysik*, 2004. Vorlesungsskript.
- [Jae02] Jaehne, Bernd: *Digitale Bildverarbeitung*. Springer, 5. Auflage, 2002.
- [Kle84] Kleinknecht, Konrad: *Detektoren fuer Teilchenstrahlung*. B.G. Teubner, 1984.
- [Kol] Kolanoski, Hermann: *Detektoren in der Elementarteilchenphysik*. <http://www-zeuthen.desy.de/~kolanosk/det07/skripte/>. Vorlesungsskript.
- [Kra06] Kramer, Frederick: *Studie zur Messung von Quarkonia mit dem ALICE-TRD und Aufbau eines Teststandes fuer seine Ausleseammern*, 2006. Johann Wolfgang Goethe-Universitaet Frankfurt a.M., Fachbereich Physik.
- [LL03] Lippman, Stanley B. und Josée Lajoie: *C++*. mitp, 1. Auflage, 2003.
- [Naw94] Nawrotzki, Kurt: *Lehrbuch der Stochastik*. Harri Deutsch, 1. Auflage, 1994.
- [Off] *Aliroot code documentation*. <http://aliceinfo.cern.ch/static/aliroot-new/html/roothtml/index.html>.
- [Off07] *The ALICE Offline Bible*, 2007. aliceinfo.cern.ch/export/download/OfflineDownload/OfflineBible.pdf.
- [PDG02] *Particle physics booklet*, July 2002. Particle data group.
- [Phy06] Physikalisches Fortgeschrittenen Praktikum der Johann Wolfgang Goethe-Universitaet Frankfurt a.M.: *Funktionsweise einer Spurendriftkammer(TPC)*, 2006.
- [Pos04] *Position reconstruction in drift chambers operated with Xe, CO₂(15%)*. www.sciencedirect.com, 2004.
- [PRSZ04] Povh, Bogdan, Klaus Rith, Christoph Scholz und Frank Zetsche: *Teilchen und Kerne*. Springer, 6. Auflage, 2004.
- [ROO] *Root code documentation*. <http://root.cern.ch/root/html/ClassIndex.html>.
- [ROO07] *ROOT Users Guide 5.16*, 2007. <http://root.cern.ch>.
- [RP02] Rechenberg, Peter und Gustav Pomberger (Herausgeber): *Informatik-Handbuch*. Hanser, 3. Auflage, 2002.
- [Spa04] *Space charge in drift chambers operated with the Xe, CO₂(15%) mixture*. www.sciencedirect.com, 2004.
- [TRA06] *ALICE TRAP User Manual*, 2006.
- [WIK] *ALICE TRD Wiki Pages*. http://wiki.kip.uni-heidelberg.de/ti/TRD/index.php/Main_Page.
- [Wil04] Wilk, Alexander: *Elektronen-Pionen-Separation im ALICE TRD*, 2004. Westfaelische Wilhelms-Universitaet Muenster, Insitut fuer Kernphysik.
- [Y⁺05] Yagi, K. *et al.*: *Quark-Gluon Plasma*. Cambridge University Press, 2005.

Selbstaendigkeitserklaerung:

Hiermit versichere ich, dass ich die Arbeit selbstaendig verfasst und nur die angegebenen Quellen und Hilfsmittel verwendet habe.

Heidelberg, den